

**SCHOOL OF ENGINEERING AND SCIENCE
VICTORIA UNIVERSITY, MELBOURNE, AUSTRALIA**

**FLOW FIELDS AND HEAT TRANSFER OF LIQUID
FALLING FILM ON HORIZONTAL CYLINDERS**

**BY
FARIAL A. JAFAR**

**THIS THESIS IS PRESENTED FOR THE DEGREE OF
DOCTOR OF PHILOSOPHY
OF
VICTORIA UNIVERSITY
August 2011**

DECLARATION

I, Fariar Jafar, declare that the PhD thesis entitled “Flow Fields and Heat Transfer of Liquid Films Falling on Horizontal Cylinders” is no more than 100,000 words in length including quotes and exclusive of tables, figures, appendices, bibliography, references and footnotes. This thesis contains no material that has been submitted previously, in whole or in part, for the award of any other academic degree or diploma. Except where otherwise indicated, this thesis is my own work.

Signature:



Date:

8 August 2011

ABSTRACT

A liquid film flowing over horizontal cylinders is of great importance as a high rate of heat transfer exists between the falling liquid film and the horizontal cylinders. For this reason falling film is widely used in chemical and food process industries and in refrigeration equipment where high rates of heat transfer are important.

The flow field and heat transfer processes that occur in such configurations are generally calculated by means of empirical relationships amongst dimensionless groups. Trickle bed chemical reactors and equipment used to cool horticultural produce usually involve three phase porous media. The fluid dynamics and heat transfer processes that occur are generally quantified by means of empirical relationships between dimensionless groups. The research reported in this thesis is motivated by the possibility of using detailed numerical simulations of the phenomena that occur in beds of irrigated porous media to obviate the need for empirical correlations. Numerical predictions are obtained using the power of computational fluid dynamics (CFD) code – FLUENT[®] for 2D and 3D configurations of three horizontal plain cylinders. In the numerical predictions, the mathematical approach is based on the volume of fluid (VOF) method where the primary phase is represented by air and the secondary phase by the liquid.

The objective of this research is to use numerical predictions, following experimental verification, to study the flow field and heat transfer to better understand the heat transfer processes that occur in beds of irrigated horticultural produce. Also to refine the traditional methods of analysing heat transfer in three-phase porous media by modelling the transport process in much finer detail. This objective relevant, to hydrocooler where warm produce is cooled directly by spraying it with chilled water, the process is known as hydrocooling. Other similar systems, is achieved by formulating the equations that govern heat transfer on the scale of the pieces of horticultural produce, and the spaces between them.

In this research, flow and heat transfer predictions are presented of a single slot liquid jet. The flow field of droplet, jet and sheet modes have been investigated.

The effects of Reynolds number, nozzle to plate spacing, nozzle width and target surface configuration, cylinder diameter, cylinder separation have been investigated. The spatial placement of cylinder on droplet mode, have also been studied. The Reynolds number range studied in this research is, 50 to 3000 where the liquid medium is water.

The results show that Reynolds numbers, nozzle to plate spacing and nozzle width, cylinder diameter and cylinder separation have a significant effect on the flow field and heat transfer characteristics; whereas the target surface configuration at the impinging area has no substantial impact. The numerical results are in good agreement with the experimental results. The use of a numerical tool has resulted in a detailed investigation of these characteristics, which has not been available in the literature previously.

The novelty of this work is the contribution of the phenomena associated with three phase of flow, also, the research contributes to validation of numerical predictions against experimental results and to provides an in- depth qualitative understanding of the qualitative results presented in both the literature and this research towards reducing energy and cooling water requirements in cooling horticultural produce. This research can also help future engineers in designing hydrocoolers that are more energy and water efficient.

ACKNOWLEDGEMENTS

I wish to express my deepest appreciation to my academic supervisors, Professor Graham Thorpe and Association Professor Özden Turan, for their guidance, support, understanding and encouragement throughout my graduate years and for making the completion of this study achievable.

I am very grateful to Dr Eren Semercigil for his support, valuable comments, and willingness to assist me during my study. I also would like to thank Dr Rainer Seidel and Xun Xu from Auckland University in New Zealand for their support and assistance.

Special thanks to my good friend Andrew Antiohos for his support, a particular thank also to Jenny Fafeita for providing valuable suggestions. Also a special thanks to Jack Jakupec for his involvement in the project and help in setting up the apparatus. Again a special thank to Tien Do for his continuous assistance and also to Earl Gunn for his participation in the first year of this study.

Very special thanks to a very special person in my life, Debbie Thomas for her assistance in the most critical time of my life. I am grateful to the CEO, Managing Director of NHP Electrical Engineering Products Pty Ltd, Lloyd Thomas for his support and kindness. Many thanks for all NHP employees for their encouragement and friendship.

I am grateful to my beloved husband, Mytm Hassin whose constant encouragement, patience, love, and care has made it possible for me to carry the research to the end. I would also like to thank my three gorgeous children, Ebrahim, Zahraa and Noor without their love and smiles I would have never been able to get to this point.

Finally, I would like to thank my mum, for her support and encouragement even though she is half way across the world. I am also grateful for my brothers and sisters for their encouragement and love. I would like to thank the sprit of my dad for the determination and the strength that he gave me and would like to tell him, that your encouragement is a whisper in my ears for all the times I thought I wouldn't make it, this work is a small piece of my appreciation for everything you've done for me and allowed me to do. Thank you for always being there.

TABLE OF CONTENTS

TABLE OF CONTENTS	Page
LIST OF TABLES	x
LIST OF FIGURES.....	xi
NOMENCLATURE.....	xxi
CHAPTER	
1. INTRODUCTION.....	1
2. NUMERICAL MODEL AND EXPERIMENTAL SETUP.....	10
2.1 The Problem and Computational Domain.....	11
2.2 Mesh Generation and Model Validation.....	16
2.2.1 Grid Independence.....	16
2.2.2 Time Independence.....	16
2.3 Design Consideration.....	18
2.4 Apparatus.....	20
2.4.1 Flow Field Experimental Apparatus.....	21
2.4.2 Heat Transfer Apparatus Modification.....	25
2.5 Flowmeters.....	30
2.6 Data Reduction Procedure and Uncertainty Analysis.....	33
2.7 Scope of Experiments.....	34
2.8 Conclusion.....	35
3. FLOW FIELD OF LIQUID JET IMPINGING SURFACE WITHOUT AND WITH HEAT TRANSFER	36
3.1 Introduction.....	36
3.2 Mathematical Analysis.....	43
3.3 Computational Details.....	45
3.4 Flow Field Analysis.....	46
3.4.1 Effect of Reynolds Number, Re (Case study 1).....	46
3.4.2 Effect of Nozzle to Plate Spacing, S (Case study 2).....	52
3.4.3 Effect of Nozzle Width, W (Case study 3).....	58
3.4.4 Effect of Different Surface Configuration (Case study 4)...	62

3.5	Thermal Characterization of Liquid Jet.....	64
3.5.1	Effect of Reynolds Number, Re on Heat Transfer.....	66
3.5.2	Effect of Nozzle to Plate Spacing S/D on Heat Transfer....	71
3.5.3	Effect of Nozzle Width on Heat Transfer at Impinging and Wall Jet Regions.....	75
3.5.4	Effect of Surface Configuration on Heat Transfer.....	75
3.6	Analysis of Heat Transfers Characteristics.....	76
3.6.1	Heat Transfer at Stagnation Point ($X/D = 0$).....	76
3.6.2	Heat Transfer in Impinging Region ($0 < X/D < 0.25$).....	76
3.6.3	Heat Transfer in Transition Region ($0.25 < X/D < 0.5$).....	76
3.6.4	Heat Transfer in Wall Jet Region ($X/D > 1$).....	77
3.7	Conclusion	77
4.	FLOW VISUALIZATION AND FALLING FILM MODES.....	79
4.1	Introduction.....	81
4.2	Experimental Setup.....	87
4.3	Numerical Model.....	88
4.4	Flow Mode Visualization.....	92
4.4.1	Droplet Mode.....	92
4.4.2	Droplet-Jet Mode.....	93
4.4.3	Jet Mode.....	93
4.4.4	Jet-Sheet Mode.....	93
4.4.5	Sheet Mode.....	93
4.5	Measuring the Flow Behaviour.....	94
4.5.1	Effect of Flow Rate on Droplet Mode.....	94
4.5.2	Effect of Spatial Placement of Cylinder on Droplet Mode..	95
4.5.3	Effect of Cylinder Diameter.....	96
4.5.4	Effect of Vertical Spacing Distance between Cylinders, Separation.....	96
4.6	Hysteresis of Falling Film Transition.....	97
4.7	Conclusion.....	110

5.	HEAT TRANSFER IN FALLING LIQUID FILM.....	111
5.1	Introduction.....	111
5.2	Experimental Setup and Numerical Model.....	114
5.3	Interpretative Framework.....	118
5.4	Design of Heat Transfer in Liquid Film.....	120
5.4.1	Jet Impingement Region.....	120
5.4.2	Developing Thermal Boundary Layer Region.....	122
5.4.3	Fully Developed Region.....	124
5.5	Effect of Falling Film Modes on Heat Transfer Characteristics.....	125
5.5.1	Heat Transfer Coefficient for the Droplet Mode.....	125
5.5.2	Heat Transfer Coefficient for Jet Mode.....	125
5.5.3	Heat Transfer Coefficient for Sheet Mode.....	126
5.6	The Effects of Operating Conditions and Geometry on the Heat Transfer.....	128
5.6.1	Liquid Flow Rate, Γ and Reynolds Number, Re	128
5.6.2	Height of Feeder.....	137
5.6.3	Cylinder Diameter.....	140
5.6.4	Heat Flux.....	141
5.7	Conclusions.....	142
6.	PERFORMANCE OF HYDROCOOLING SYSTEMS.....	143
6.1	Introduction.....	143
6.2	Types of Hydrocoolers.....	145
6.2.1	Continuous Flow Hydrocooler.....	145
6.2.2	Immersion Hydrocooler.....	146
6.2.3	Truck Hydrocooler.....	147
6.2.4	Batch Hydrocooler.....	148
6.3	Design and Operation a Smart Water Hydrocooler.....	149
6.3.1	Realization of a Practical Commercial Hydrocooler.....	149
6.4	Water Distribution and Treatment in the Hydrocooler.....	158
6.5	Determining Hydrocooling Rates.....	161
6.5.1	Cooling Rate of Product (Broccoli).....	162
6.6	Water and Electricity Consumption.....	164
6.7	Modifications to the Hydrocooler.....	165

6.7.1 Simplify the Design of the Hydrocooler.....	165
6.7.2 Materials of Construction.....	166
6.8 Conclusion.....	167
7. SUMMARY AND CONCLUSIONS.....	168
APPENDIX A.....	172
A.1 Discussion of Design Consideration.....	176
APPENDIX B.....	195
Falling Film over Cylinders in Random, Rectangular Pitch Arrangement and up to Ten Horizontal Cylinders: Flow Field.....	195
APPENDIX C.....	200
Falling Film over Cylinders in Random, Rectangular Pitch Arrangement and up to Ten Horizontal Cylinders: Heat Transfer.....	200
REFERENCES.....	205

LIST OF TABLES

TABLE	Page
2.1 Computation results for grid independence for 2D.....	18
2.2 Computation results for grid independence for 3D.....	18
2.3 Computation results for time step independence for 2D.....	18
2.4 Computation results for time step independence for 3D.....	18
2.5 Definition of the Dimensionless physical parameters.....	34
2.6 Experimental Scope.....	35
3.1 Summary of relevant studies of jet impingement.....	40
3.2 The parameters used in this study.....	42
3.3 Analytical results of heat transfer for jet impingement.....	67
4.1 Overview of the experimental and numerical scope.....	80
4.2 Values of the transition constant, K , reported by Honda et al. (1987) compared with those from the present study.....	83
4.3 Total grid elements of the three 3D geometries.....	91
5.1 FLUENT [®] 2D simulation settings for half domain.....	117
5.2 Numerical conditions.....	117
5.3 Constant parameters.....	118
6.1 Principal dimensions of the Smart Water hydrocooler.....	149
A.1 Simulations used for the design of the experimental setup.....	173

LIST OF FIGURES

FIGURE	Page
1.1 Basic 2D geometry for a round nozzle with diameter of D or a slot nozzle with width W	8
2.1 Typical values of the VOF function near a free surface. 1.0 represents the cell containing liquid, 0.0 represents the cell containing air. The cell which contains liquid and gas indicates the presence of a free surface.....	12
2.2 The 2D flow field model: a) boundary conditions of the domain with three phases, including the three solid horizontal cylinders, b) tracking interface in 2D of the liquid (red colour) over the three horizontal cylinders and the surrounding gas (blue colour). The scale on the left denotes 1 for water and 0 for air. The scale on the left denotes 1 for water and 0 for air.....	13
2.3 The 2D heat transfer model: a) grid domain which consists three phases of liquid, gas, and solid, b) tracking interface for 2D of the liquid (red colour) over three horizontal cylinders and the surrounding gas (blue colour), d) heat distribution of water (liquid phase) and cylinders (solid phase).....	14
2.4 The 3D flow field model; a) grid domain of three horizontal cylinders which consists two phases of liquid and gas, b) tracking interface for 3D of the liquid (red colour) over three horizontal cylinders and the surrounding gas (blue).....	15
2.5 Zooming out the top cylinder showing the boundary layer technique at different grid elements; a) 50,708, b) 24,600 and c) 15,020	17
2.6 Size function technique for half domain of 3D.....	17
2.7 Sheet of water falls over a heated tube.....	19
2.8 Irrigated tube is idealized by dividing it into three regions.....	19
2.9 Photograph of the flow field apparatus.....	22
2.10 Sketch of the flow field experimental setup.....	23
2.11 Photograph of the flow field apparatus. 1) water tank; 2) test tubes; 3) reservoir; 4) water pump; 5), 6), 7) valves; 8) low flow rate flow meter; 9) high flow rate flow meter; 10) bypass line; 11) digital camera	24
2.12 Schematic diagram of the flow field experimental setup.1) water tank; 2) test tubes; 3) reservoir; 4) water pump; 5), 6), 7) valves; 8) low flow rate flow meter; 9) high flow rate flow meter; 10) bypass line; 11) digital camera	24
2.13 Sketch of the thermocouple placements.....	25
2.14 Sketch of thermocouple placement and heater; a) heater element, b) Aluminium tube which located outside the cylinder, c) Aluminium cylinder.....	26
2.15 Sketch of inner and outer part of Bakelite insulation caps.....	26
2.16 photograph of one cylinder with element heater and inner part of the Bakelite insulation cap.....	27

2.17	Sketch of cylinder with element heater and two part of Bakelite cap insulation.....	27
2.18	Photograph of the three cylinders with element heaters inside and Bakelite at both sides of the cylinders.....	28
2.19	Photograph of water distributor. The water flows from the Flowmeters to the inner diameter and then to the spherical groove through the vertical holes and then drop down to the cylinders through the vertical holes.	29
2.20	Sketch of water distributor where inner diameter connected with the outer diameter by drilling twenty four hols.....	29
2.21	Sketch of the heated setup; a) the front view of three Aluminium cylinders and water distributor; b) side view of the set up.....	30
2.22	Flowmeter; a) MPB Series 1200B flowmeter, b) a photograph of the two Flowmeters used in the apparatus.....	31
2.23	Completed setup on the right connected with the computerized data acquisition system.....	32
2.24	Schematic diagram of heat transfer setup. 1) water tank; 2) cylinders; 3) reservoir; 4) water pump; 5), 6), 7) valves; 8) low flow rate flow meter; 9) high flow rate flow meter; 10) bypass line; 11) digital voltmeter; 12) electric power meter; 13) digital camera; 14) computerize collected data; 15) thermocouples.....	32
3.1	A schematic of liquid jet impinging on a flat surface.....	37
3.2	A schematic of liquid jet impinging on a curved surface.....	37
3.3	2D impinging jet flat surface where water is in red colour, air in blue and target surface is green.....	42
3.4	2D impinging jet curved surface where water is red colour, air in blue and target surface is green	42
3.5	Grid for the flat surface.....	46
3.6	Grid for the curved surface	46
3.7	Flow field developing from a nozzle to a plate for a range of Reynolds numbers.....	49
3.8	Non-dimensional water film thickness in the horizontal direction at different Reynolds numbers for $S/D = 2.5$	50
3.9	Flow field for impinging zone. (a) $Re = 500$, (b) $Re = 700$, and (c) $Re = 1900$	50
3.10	Flow field for wall jet zone. (a) $Re = 500$, (b) $Re = 700$, and (c) $Re = 1900$	50
3.11	Wall pressure coefficient for different Reynolds number.....	51
3.12	Wall friction coefficients for different Reynolds number.....	51
3.13	Non-dimensional U velocity for different Reynolds number.....	51
3.14	Hydraulic jump at different Reynolds number of 250 and 100.....	52
3.15	Geometry of impinging jet at different nozzle plate spacing.....	53
3.16	Velocity field for the three flow regions coloured by volume fraction (red is water and blue is air) for a Reynolds number of 1900, for S/D , a) = 12.5; b) = 5; c) = 2.5; and d) = 1.25.....	54
3.17	Non-dimensional horizontal velocity U at $Re = 1900$, with different jet nozzle to plate spacing.....	55

3.18 Non-dimensional y-direction velocity V at same Reynolds number of 1900, with different jet nozzle to plate spacing.	55
3.19 Distribution of wall shear stress at different nozzle to plate spacing S/D at $Re = 1900$	55
3.20 Velocity profile for impingement region for same Reynolds number of 1900, slot jet $W = 4\text{mm}$, $D = 8\text{ mm}$ at different jet nozzle plate spacing S/D . (a): 12.5, (b): 5, (c): 2.5, and (d): 1.....	56
3.21 Velocity field in stagnation and wall flow regions for same Reynolds number of 1900, slot jet $W = 4\text{mm}$, $D = 8\text{ mm}$ and $S/D = 12.5, 5, 2.5$ and 1.25 for (a), (b), (c), and for (d) respectively....	56
3.22 Flow visualization of 1900 Re , $S/D = 5$. (a) Free jet region at 0.02 s, (b) impingement region at 0.045 s and (c) wall jet region at quasi state.....	57
3.23 Flow visualization of 1900 Re and $S/D = 1.25$. (a) Free jet region at 0.01 s, (b) impingement region at 0.018 s and (c) wall jet region at quasi state.....	57
3.24 Case study 3: Effect of jet nozzle width with the same $S = 100\text{ mm}$, plate length $L = 50\text{ mm}$ and $Re = 1800$. (a) jet nozzle width $W = 4\text{ mm}$ and (b) $W = 2\text{ mm}$	59
3.25 Velocity profile colored by volume fraction (red is liquid) at 1800 Re (a) $W = 4\text{mm}$ and (b) $W = 2\text{ mm}$	59
3.26 Flow visualization of 1800 Re , $S = 100\text{mm}$ and $W = 4\text{ mm}$ (a) Free jet region at time of 0.04 s, (b) at 0.06 s, (c) Impingement region at 0.09 s and (d) wall jet region at quasi state.....	60
3.27 Flow visualization of $Re = 1800$, $S = 100\text{ mm}$ and $W = 2\text{ mm}$ (a) Free jet region at time of 0.02 s, (b) at 0.04 s, (c) after impingement region at 0.06 s and (d) wall jet region at quasi state.....	60
3.28 Non-dimensional velocity for x-direction at the impinging and wall jet regions	61
3.29 Non-dimensional velocity for y-direction at the free and impinging regions	61
3.30 Water film thickness at the wall jet region for different nozzle width compared with the literatures at $Re = 1800$	61
3.31 Non-dimensional water film thickness at impinging region for circular and flat surface at Reynolds number = 250.....	62
3.32 Flow visualization (water is red and air is blue) over a flat surface. (a) liquid flow at 0.15 s, (b) Impinging flow at 0.3 s and (c) at quasi state.....	63
3.33 Flow visualization (water is red and air is blue) over a circular surface. (a) liquid flow at 0.15 s, (b) Impinging flow at 0.3 s and (c) at quasi state.....	63
3.34 Local Nusselt number at free jet, impinging and wall jet regions for different Reynolds numbers at $S/D = 12.5$	68
3.35 Local Nusselt number at wall jet region for different Reynolds numbers at $S/D = 12.5$	68
3.36 Stagnation Nusselt number for different Reynolds numbers at nozzle plate spacing S/D of 12.5.....	69
3.37 Stagnation Nusselt number for Re of 500 compared with literature at $S/D = 12.5$	69

3.38	Flow field of liquid jet over heated surface for free, stagnation and wall jet regions coloured by volume fraction (red is water and blue is air) at 12.5 of S/D and Reynolds number of a) = 500, b) = 700, c) = 1900.....	70
3.39	Zooming in the stagnation area coloured by volume fraction at 12.5 of S/D and Re of a) = 500, b) = 700, c) = 1900.....	70
3.40	The stagnation Nusselt number for different jet nozzle to plate distances of Re of 1900.....	72
3.41	The stagnation Nusselt number for different jet nozzle to plate distances of different Re	73
3.42	The stagnation Nusselt number variation with Reynolds number at different jet nozzle to plate spacing.....	73
3.43	Effect of different nozzle to plate spacing on heat transfer at 1900 Reynolds number. a) $S/D = 1.25$, b) = $S/D = 2.5$, c) $S/D = 5$ and d) $S/D = 12.5$	74
3.44	Zooming in the stagnation area at 1900 Reynolds number and different nozzle to plate spacing. a) $S/D = 1.25$, b) = $S/D = 2.5$, c) $S/D = 5$ and d) $S/D = 12.5$	74
3.45	The influence of nozzle width on Nusselt number.....	75
3.46	Local thermal boundary condition on stagnation region for convex and flat surfaces at $Re = 250$	76
4.1	Schematic of the three main flow modes. (a) Droplet, (b) jet, and (c) sheet mode after Mitrovic (1986).....	87
4.2	Schematic of droplet flow for the present study.....	87
4.3	Geometry of 2D used to model three phases of (1) liquid, (2) gas and (3) solid phase.....	89
4.4	Geometry of 3D used to model three phases of (1) liquid, (2) gas and (3) solid phase	90
4.5	Three 3D geometries for the three lowest cylinder diameters. The two upper cylinders have diameters of 0.1 m, and the lowest cylinder diameters are 0.1 m, 0.05 m and 0.02 m. The lower row of figures indicate the finite volume mesh used in each case.....	91
4.6	Experimental visualization of flow modes; a) droplet, b) droplet-jet, c) inline jet, d) staggered jet, e) jet-sheet, f) sheet mode.....	98
4.7	Contours of volume fraction (phase water) the flow visualization of 2D falling liquid film between two cylinders a) droplet mode; b) droplet-droplet jet mode; c) jet mode; d)jet-jet sheet mode; e)jet sheet-sheet mode; f) sheet mode. Red colour indicates water which is equal to 1 and blue is air which is equal to 0.....	99
4.8	Contours of volume fraction (phase water) for flow visualization of 3D falling liquid film; a) droplet mode; b) jet mode and c) sheet mode. Red colour indicates water which is equal to 1 and blue is air which is equal to 0.....	100
4.9	The experimental and numerical principal flow modes compared with the literature.....	101
4.10	The experimental transition modes compared to Roques and Thome (2007).....	102

4.11	Effect of film Reynolds number on the frequency of droplet detachment for the middle cylinder.....	103
4.12	Effect of increasing and decreasing film flow rate variation on the frequency of small droplet detachment for middle cylinder....	103
4.13	Effect of increasing and decreasing film flow rate variation on the distance between small droplet producing sites for the middle cylinder.....	103
4.14	Effect of spatial placement of a cylinder in the column on the frequency of large droplet detachment.....	104
4.15	Effect of spatial placement of cylinders in the column on the distance between drop producing sites, the present results and those of Hu and Jacobi (1998).....	104
4.16	Effect of bottom cylinder diameter on the frequency of drop detachment.....	105
4.17	Effect of bottom cylinder diameter on the distance between drop producing sites.....	105
4.18	Four geometries of two cylinders with different separation distance, \bar{s} . a) $\bar{s} = 0.001$ m, b) $\bar{s} = 0.01$ m, c) $\bar{s} = 0.03$ m and d) $\bar{s} = 0.05$ m.....	106
4.19	Separation distance between two cylinders. a) $\bar{s} = 0.001$ m, b) $\bar{s} = 0.01$ m, c) $\bar{s} = 0.03$ m and d) $\bar{s} = 0.05$ m.....	106
4.20	Zooming out of separation distance between two cylinder. a) sheet mode; b) Sheet mode; c) droplet-jet mode and d) droplet at $\bar{s} = 0.001$ m, 0.01 m, 0.03 m and 0.05 m respectively.....	107
4.21	Transition as a function of relative spacing. (a) droplet and droplet-jet modes; (b) jet and droplet-jet modes; (c) jet-sheet and jet modes; (d) sheet and jet-sheet modes.....	108
4.22	Flow visualization of falling liquid over three cylinders at different times. a) at time of 0.45 s, b) at 0.6 s; and c) at 0.675 s, d) at time of 0.75 s, e) at 0.825 s; and f) at 0.9 s, g) at time of 0.975 s, h) at 1.2 s; and i) at 1.275 s and J) at (quasi state) after 1.8 s at $Re = 1200$	109
5.1	The physical configuration of the system.....	116
5.2	Details of the grid in the vicinity of the cylinder surface.....	116
5.3	Model for falling liquid film on two heated horizontal cylinders...	120
5.4	Distribution of velocity in the jet impingement region for $Re = 500$ where U is the main velocity, V_j is the liquid jet velocity, x is the distance along the heated surface and d is the nozzle diameter.....	121
5.5	Variation of liquid film thickness around the cylinder with respect to angular position at liquid mass flow rate of 0.6 kg/ms.....	123
5.6	Temperature profile development over time of liquid film in thermal boundary layer development region. Where y is the location in x-axis, δ is the water film thickness, T_Y is the local temperature in water film thickness and T_j is the liquid jet temperature at $Re = 1200$	124
5.7	Average Nusselt number for droplet, jet and sheet modes at different Reynolds numbers.....	127

5.8	The variation of local heat transfer coefficient as a function of the angle ϕ at sheet mode of at Re of 3000.....	128
5.9	Effect of the cooling water velocity on the average heat transfer coefficient.....	131
5.10	Effect of the liquid flow rate and Re on heat transfer coefficient for the top cylinder of 0.1 m diameter.....	131
5.11	The effect of the liquid flow rate and Re on the heat transfer coefficient for the middle cylinder of 0.1 m diameter.....	132
5.12	The effect of the liquid flow rate and Re on the heat transfer coefficient for the bottom cylinder of 0.1 m diameter.....	132
5.13	The distribution of the local heat transfer coefficient around the circumference of the cylinder at Re = 500, cylinder diameter 0.022 m.....	133
5.14	The distribution of heat transfer coefficient around the circumference of a cylinder diameter of 0.132 m, Re = 1300, compared with Ouldhadda <i>et al.</i> (2000).....	133
5.15	The effect of Reynolds number on the average heat transfer coefficient or the average Nusselt number and the position of the cylinder.....	134
5.16	Impinging wall temperate for the top, middle and bottom cylinders where $\phi = 0$ at different Reynolds numbers.....	134
5.17	Temperature distributions in the top, middle and bottom cylinders at different Reynolds numbers. (a) Re = 50; (b) Re = 100; (c) Re = 250 and (d) Re = 500. (e) Re = 800; (f) Re = 1300; (g) Re = 2000 and (h) Re = 3000.....	135
5.18	Thermo photographs of temperature distributions in the top, middle and bottom cylinders at different Reynolds numbers. (a) Droplet mode; (b) jet mode; and (c) sheet mode.....	136
5.19	Three geometries with different nozzle high; a) nozzle height of 0.03 m; b) nozzle high of 0.01 m, and c) 0.005 m.....	138
5.20	Temperature distribution at Re of 3000; a) nozzle height of 0.03 m; b) nozzle high of 0.01 m, and c) 0.005 m.....	138
5.21	Local heat transfer coefficient for the top cylinder at low Re of 50 for three nozzles high of 0.005 m, 0.01 m and 0.03 m.....	139
5.22	Local heat transfer coefficient for the top cylinder at high Re of 3000 for three nozzles high of 0.005 m, 0.01 m and 0.03 m.....	139
5.23	Effect of the cylinder diameter on average heat transfer coefficient.....	140
5.24	Effect of heat flux on average heat transfer coefficient.....	141
6.1	Continuous flow hydrocooler system: a) and b) a photograph and a diagram respectively of a continuous flow hydrocooler showing the cartons of the produce being loaded in the front to pass along the conveyor to enter the cooling bay where the produce is cooled by chilled water, and then removed from other side. c) The cartons of produce enter the shower room. d) the heavy duty cooling coils are suspended above the produce. Boyette <i>et al.</i> (1992) and Anon (2007).....	145
6.2	Immersion hydrocooler system where the boxes of the product are loaded in one end and moved by a submerged conveyor. The	

products are floated in a tank of chilled water and then removed from the other side. (Boyette <i>et al.</i> (1992).....	146
6.3 Truck hydrocooler system which has a tank holding water, pump, valves and pips that delivered shower of chilled water to the product. (Boyette <i>et al.</i> (1992).....	147
6.4 Batch hydrocooler system with a small refrigeration unit to cool the water after it falls over the bulk product bins. Boyette (1992).....	148
6.5 The hydrocooler system has three cooling bays, a pump room and the chemical treatment room. Cooling bay 1 is covered with a blind to reduce the water lost as a result of splashing.....	151
6.6 A general diagram of the hydrocooler, shows the three cooling bays, pump room, chemical treatment room, seven tanks, backwash tank and the provision for the refrigeration plant.....	151
6.7 Water chilling unit supplies the hydrocooler with chilled water and it is transported separately from the hydrocooler.....	152
6.8 A process diagram of the hydrocooler showing the three cooling bays and seven principal circuits.....	152
6.8a Cold water from chilling unit into flows tanks 3 and 6 from which it flows into adjacent tanks that supply the cooling bays. Water returns to the chiller from tank 6. Thorpe (2008).....	153
6.8b The water distribution circuits in the Smart Water hydrocooler. Bays 1 and 3 are each supplied by two pumps, whereas the sprays in the smaller Bay 2 are supplied using only one pump. Thorpe (2008).....	154
6.8c The chemical dosing system in which solid bromo-chloro-dimethylhydantoin (BCDMH) is dissolved in water that has been recycled within the hydrocooler. The treated water is returned to tanks 1 and 4.....	154
6.8d Water is removed from tank 7 on the right of the hydrocooler before passing through a stainless steel strainer. It is then pumped through a sand filter before being returned to tanks 1, 2, 4 and 7. The ORP, temperature and electrical conductivity, and pH of the re-circulated water are measured in the line that leaves the sand filter and leads to the water tanks.....	155
6.8e The backwash circuit in which fresh the water from the tank adjacent to the filter is pumped vertically upward through the sand filter. As a result large pieces of debris that are not removed by the pre-strainers are removed from the filter and discharged from the hydrocooler.....	156
6.8f The chilled disinfected water is mixed by ensuring it flows by gravity into tanks that have overflows, thus making sure the treated water flows into the bases of the cooling bays. The water is returned from the cooling bays to the tanks.....	157
6.8g Fresh water is supplied on demand to the backwash tank and tank 1 by means of two independent ballcocks.....	157
6.9 Water distribution system in the roof of the shipping container. Water goes out of the inverted tee-pieces and the pipe elbows.....	158

6.10	A view of the water distribution system from below. It is supported by a light metal frame.....	159
6.11	Water leaving the distribution system at a rate of about 18 litres per second.....	159
6.12	Water landing in the base of cooling bay of the hydrocooler.....	160
6.13	Chemical treatment system.....	160
6.14	The sand filter.....	161
6.16	The box in which the instrumented pieces of broccoli were placed to measure their rate of cooling.....	162
6.17	The instrumented broccoli in the hydrocooler.....	163
6.18	The rate at which broccoli cools in the Smart Water hydrocooler..	163
6.19	A simplified flow diagram that illustrates that there is only one storage tank for chilled water, a mixing circuit has been eliminated and the amount of piping has been reduced. Thorpe (2008).....	166
A.1	Case 1 from Table A.1. Center wall and two side regions are made of Aluminium at 5° C of center wall region (irrigation temperature) and 25° C two side regions; a) temperature contours for the three regions; b) temperature distribution along the cylinder; c) heat flux along the surface.....	177
A.2	Case 2 in Table A.1. Center wall and two side regions are made of Aluminium at 25° C of center wall region (irrigation temperature) and 25° C two side regions; a) temperature contours for the three regions; b) temperature distribution along the cylinder; c) heat flux along the surface.....	178
A.3	Case 3 in Table A.1. Center wall and two side regions are made of Aluminium at 30° C of center wall region (irrigation temperature) and 25° C two side regions; a) temperature contours for the three regions; b) temperature distribution along the cylinder; c) heat flux along the surface.....	179
A.4	Case 4 in Table A.1. Aluminium center wall region (irrigation) at 5° C and Gypsum two side regions at 25° C; a) temperature contours for the three regions; b) temperature distribution along the cylinder; c) heat flux along the surface.....	181
A.5	Case 5 in Table A.1. Aluminium center wall region (irrigation) at 25° C and Gypsum two side regions at 25° C; a) temperature contours for the three regions; b) temperature distribution along the cylinder; c) heat flux along the surface.....	182
A.6	Case 6 in Table A.1. Aluminium center wall region (irrigation) at 30° C and Gypsum two side regions at 25° C; a) temperature contours for the three regions; b) temperature distribution along the cylinder; c) heat flux along the surface.....	183
A.7	Case 7 in Table A.1. Three regions of center wall and tow side are made of Steel, at 5° C of center wall region (irrigation) and 25° C of the two side region; a) temperature contours for the three regions; b) temperature distribution along the cylinder; c) heat flux along the surface.....	185

A.8	Case 8 in Table A.1. Three regions of center wall and tow side are made of Steel, at 25° C of center wall region (irrigation) and 25° C of the two side region; a) temperature contours for the three regions; b) temperature distribution along the cylinder; c) heat flux along the surface.....	186
A.9	Case 9 in Table A.1. Three regions of center wall and tow side are made of Steel, at 30° C of center wall region (irrigation) and 25° C of the two side region; a) temperature contours for the three regions; b) temperature distribution along the cylinder; c) heat flux along the surface.....	187
A.10	Case 10 in Table A.1. Center wall region (irrigation) is made of Steel at 5° C. Two side regions are made of Gypsum at 25° C; a) temperature contours for the three regions; b) temperature distribution along the cylinder; c) heat flux along the surface.....	188
A.11	Case 11 in Table A.1. Center wall region (irrigation) is made of Steel at 25° C. Two side regions are made of Gypsum at 25° C; a) temperature contours for the three regions; b) temperature distribution along the cylinder; c) heat flux along the surface.....	189
A.12	Case 12 in Table A.1. Center wall region (irrigation) is made of Steel at 30° C. Two side regions are made of Gypsum at 25° C; a) temperature contours for the three regions; b) temperature distribution along the cylinder; c) heat flux along the surface.....	190
A.13	Case 13 in Table A.1. Center wall region (irrigation) is made of Aluminium of 0.04m diameter at 25° C. Two side regions are made of Gypsum at 25° C; a) temperature contours for the three regions; b) temperature distribution along the cylinder; c) heat flux along the surface.....	192
A.14	Case 14 in Table A.1. Center wall region (irrigation) is made of Aluminium of 0.06m diameter at 25° C. Two side regions are made of Gypsum at 25° C; a) temperature contours for the three regions; b) temperature distribution along the cylinder; c) heat flux along the surface.....	193
A.15	Case 15 in Table A.1. Center wall region (irrigation) is made of Aluminium of 0.08m diameter at 25° C. Two side regions are made of Gypsum at 25° C; a) temperature contours for the three regions; b) temperature distribution along the cylinder; c) heat flux along the surface.....	194
B.1	Flow visualization of falling liquid film over random cylinders arrangement, a) the mesh of the geometry and b) liquid film falling over cylinders at $Re = 1300$	196
B.2	Flow visualization of falling liquid film over rectangular cylinders arrangement, a) the mesh of the geometry and b) liquid film falling over cylinders at $Re = 1300$	197
B.3	Flow visualization of falling liquid film over ten cylinders, a) the mesh of the geometry and b) liquid film falling over cylinders at different time at $Re = 1300$	198
B.4	Wetted area for ten horizontal cylinders at different Reynolds numbers.....	199

C.1	Temperature distributions for rectangular pitch cylinders arrangement at different times.....	201
C.2	Temperature distribution for random pitch cylinders arrangement at different time; a) $t = 30$ s; b) $t = 90$ s; c) $t = 150$; d) $t = 200$ s...	202
C.3	Cylinder temperature for the rectangular pitch arrangement. Cylinders 4, 5 and 6 are below the nozzle.....	203
C.4	Cylinders temperature for random pitch arrangement. Cylinders 1 and 4 are below the nozzle.....	203
C.5	Temperature distribution of 2D ten cylinders: a) 90 s, b) 250 s, c) 420 s and d) 950 s.....	204

NOMENCLATURE

List of Symbols

Ar	Archimedes number (dimensionless)
C_p	specific heat, (J/kg.K)
D	nozzle hydraulic diameter, (m)
d	tube diameter, (m)
g	acceleration due to gravity, (m/s ²)
Ga	Galileo number, (dimensionless)
h_ϕ	local heat transfer coefficient, (W/m ² K)
\bar{h}	average heat transfer coefficient, (W/m ² K)
h_0	heat transfer coefficient at stagnation region (W/m ² K)
k	thermal conductivity (W/m K)
\dot{m}	mass flow rate (kg/s)
Nu	local Nusselt number, (dimensionless)
\overline{Nu}	average Nusselt number, (dimensionless)
Nu_0	Nusselt number at stagnation region, (dimensionless)
P	pressure, (Pa)
Pr	Prandtl number, (dimensionless)
q''	heat flux, (W/m ²)
$R_1 R_2$	principal radii of curved at a point on a free surface
Re	Reynolds number, (dimensionless)
\bar{S}	separation, distance between tubes, (m)
S	height of feeder, (m)
T	temperature (°C)
T_m	local mean temperature in water film, (°C)
T_w	local wall temperature, (°C)
V	velocity (m/s)
u	velocity in x direction (m/s)
v	velocity in y direction (m/s)
W	jet nozzle width (m)
X, Y	coordinates from the impingement point (m)

Greek symbols

α	fluid thermal diffusivity (m ² /s)
ρ	fluid density, (kg/m ³)
μ	Newtonian dynamic viscosity, (kg/m.s)
σ	Surface tension, (kg/s ²)
ν	kinematic viscosity, (m ² /s)
τ_w	wall shear stress, (N/m ²)
$\overline{\epsilon}H$	turbulent diffusivity for heat transfer, (m ² /s)

$\overline{\epsilon_{jm}}$	turbulent diffusivity for momentum transfer, (m ² /s)
Γ	mass flow rate of the liquid film per unit length of tube for each side, (kg/ms)
δ	liquid film thickness, m
ξ	capillary constant, (m)
l_c	characteristic length, (m)
λ	instability wavelength, spacing between neighbouring jets or droplets, (m)
λ^*	dimensionless wavelength

Subscripts

A	atmosphere
i	inlet
j	jet
L	liquid
s	surface
x	local value of parameter on target wall
0	stagnation point

CHAPTER ONE

INTRODUCTION

Most fresh fruits and vegetables require immediate cooling after harvesting. This procedure is undertaken to reduce deterioration, to meet market requirements and then, to deliver the best quality product to the consumers. The cooling procedure allows the horticultural produce to retain its flavour, texture and nutritional qualities. When warm produce is cooled directly by spraying it with chilled water, the process is known as hydrocooling, and the cooling device is known as a hydrocooler. Other useful effects of hydrocooling include cleaning horticultural products and delaying fruit decay. These two effects ensure that the surface of the produce will not be subject to any water loss, but on the contrary, the absorbed water will ensure that the fruits and vegetables retain their vibrant freshness and become free of any unwanted dirt. Some of the produce that undergoes cooling in a hydrocooler may include crops such as broccoli, asparagus, carrots and a wide range of summer fruit.

Hydrocooling methods differ in their cooling rates and overall process efficiencies. There are four common types of hydrocoolers. These are continuous flow hydrocoolers, batch hydrocoolers, immersion hydrocoolers and truck hydrocoolers. In this study, the performance of a batch hydrocooler, dubbed the Smart Water Hydrocooler, is examined in detail as an example.

To analyze the equipment used to cool horticultural produce, three-phase porous media need to be considered. The produce represents the solid phase, liquid falling films represent the liquid phase and the surrounding air is the gas phase.

The objective of this work is to refine the traditional methods of analysing heat transfer in three-phase porous media by modelling the transport process in much finer detail. This objective, which is relevant to hydrocooler and other similar systems, is achieved by formulating the equations that govern heat, mass and

momentum transfer on the scale of the pieces of horticultural produce, and the spaces between them. The novel findings of this work can help future engineers in designing hydrocoolers that are more energy and water efficient.

There are several important parameters that need to be addressed in order to design a hydrocooler. These parameters are, the total mass flow rate of water, the size of spray nozzles and the distance between the nozzles and the horticultural produce. To establish these parameters within an intellectual framework, the results of this study are expressed in terms of dimensionless quantities such as Reynolds number, Re , Nusselt number, Nu , dimensionless distance between the spray nozzle and the surface, S/D or S/W where S is the distance between the nozzle and the surface and D and W are the diameter and the width of the nozzle, respectively. A basic geometry is shown in Figure 1.1 to describe the geometric parameters.

In this research, the prediction and description of the rate of heat transfer between the horticultural produce and cooling water in a hydrocooler system are presented. To achieve this goal numerically and experimentally, heat transfer between a liquid film of water and horizontal circular cylinders (solid phase) is investigated. The results for this study provide the fundamental steps for the critical understanding of the configuration of a semi-continuum mathematical model of a hydrocooler system.

Porous media, such as beds of horticultural produce, usually have complicated and random geometries. It is difficult to attack such a problem without first solving the governing equations that apply to simple geometries. The mechanism of heat transfer studied in this research is primarily convection heat transfer. This is due to the heat transfer between the horticultural produce (solid phase) and the falling liquid film (liquid phase).

Heat transfer in liquid films falling over horizontal cylinders is encountered in several other industrial processes such as in chemical engineering (trickle bed chemical reactors), food and polymer processing, as well as in cooling systems, evaporators, distillation, and heat exchangers. Although the heat transfer in liquid films falling on horizontal cylinders is important in engineering applications where

three phases of solid, liquid and gas exist, the complexity of the physical phenomena render it an excellent candidate for an analysis using contemporary multiphase methods.

It is essential that computational fluid dynamics (CFD) simulations are validated against experimental data for temperature distribution, heat transfer characteristic, flow modes and other flow characteristics. The research reported in this thesis contributes to the validation of a commercial CFD package against a significant range of phenomena associated with three-phase flow. These include the modes of the fluid within the system, namely droplet, jet and sheets.

In the numerical predictions, the mathematical approach is based on the volume of fluid (VOF) method where the primary phase is represented by air and the secondary phase by the liquid. A CFD code and proprietary software packages are employed to calculate and illustrate the liquid flow field and the rate of heat transfer in the porous media.

Liquid flow field and heat transfer laboratory experiments have been performed to determine the effect of Reynolds number, cylinder spacing and heat flux. The falling liquid film modes that are characterized with and without heating are also studied. Three horizontal plain cylinders are adjusted to obtain the desired cylinder spacing and water is introduced through a nozzle placed on the water tank or the water distributor. Falling film flow over the cylinders is studied at different flow rates to produce drop, jet and sheet modes. At high liquid flow rates, the falling film represents a sheet mode, with decreasing liquid flow rate the sheet breaks up, forming a sheet-jet mode. Upon decreasing the flow rate further, the falling liquid film passes through jet, jet-droplet and then droplet modes ⁽¹⁾ (superscripts within parentheses in this chapter refer to the publications arising from this thesis, as listed on pages 9). During the course of the laboratory experiments, liquid temperature and the cylinder surface temperature are also measured and recorded.

To complement this study, experiments on the cooling rate of the horticultural produce in a commercial hydrocooler are reported.

In each chapter of this thesis, an introduction and the review of literature, both relevant to the chapter coverage, are presented to place this research in context. The description of the problem, experimental framework, numerical analysis, and finally the computational details are presented. The discussion of results and a conclusive summary are given at the end of each chapter. The tables and figures of each chapter are presented within the text.

Following the overall introduction in Chapter 1, the computational domain, mesh generation, model validation and the experimental setup are explained in detail in Chapter 2.

To understand the phenomena of the falling liquid film, 2D numerical investigations of liquid jet impinging on flat and curved surfaces are presented in Chapter 3. This study is extended to account for heat transfer and for the case when the jet of liquid impinges on the upper surface of a cylinder in Chapters of 4 and 5. A range of Reynolds numbers is employed to study the effects of liquid flow rate or Re , dimensionless nozzle to plate spacing S/D , nozzle width W , and target surface configuration ⁽²⁾ ⁽³⁾. The hydraulic jump at Reynolds number of 250 and 100 is studied, too.

The flow field of an impinging jet is divided into three regions. These are, free jet, impingement, and wall jet regions. It has been found that Reynolds number has a significant effect on the flow field and heat transfer. The heat transfer coefficient in the impinging and wall jet regions is enhanced with increase in Reynolds number. The wall jet region is sensitive to jet to plate spacing due to the shear stress along the wall plate. It has also been found that there is no significant effect due to the surface configuration on the flow field and heat transfer. These findings lead to the understanding of the fundamentals of flow and heat transfer on curved surfaces of the plain cylinders. The numerical outcome of this chapter provides the understanding of the phenomenon of the falling liquid film on flat and curved surfaces for the three regions of free, impinging and wall jet.

In Chapter 4, the work forms part of an experimental and numerical framework in which to study the flow field using the power of computational fluid dynamics

(CFD) to better design beds of irrigated horticultural produce. The objective of the study in this chapter is to use numerical predictions, followed by experimental verification, towards reducing energy and cooling water requirements in cooling horticultural produce. ⁽⁴⁾⁽⁵⁾⁽⁶⁾⁽⁷⁾

The flow visualization and falling film modes are represented experimentally and numerically in 2D and 3D. The behavior of water falling over horizontal cylinders and the definition of flow patterns are reported. The effects of Reynolds number, hysteresis, cylinder diameter, placement of the cylinders (top, middle and bottom) and the vertical separation between the cylinders are studied. The Reynolds number range studied in this chapter is 50 to 2000. The cylinder diameters are 0.1 m, 0.05 m, and 0.02 m.

The frequency and wavelength of the droplet mode are studied in detail in Chapter 4. It has been found that the number of large drops increases relatively slowly as the Reynolds number increases to about 80 and the frequency of the large drops remain about constant as the Reynolds number increases further. For small droplets, Reynolds number has a large impact, such that the frequency increases sharply by a factor of about four as the Reynolds number increases from 20 to about 50. This finding leads to the result of not needing to use a high liquid flow rate or Reynolds number above 80, to conserve both water and energy without sacrificing performance. Unfortunately the situation in a hydrocooler is extremely complicated, and this effect may not be dominant.

It has also been found that hysteresis has no effect as the flow rate increases or decreases. Hysteresis of falling film transitions is studied by examining the Reynolds numbers needed to reach identical modes with increasing or decreasing flow rates. For the cylinder placement, the results show that at the desired Reynolds number, the wavelength is large for the top cylinder, and then, it decreases for the middle and even further for the bottom cylinder. As the film flow rate increases, more sites become simultaneously active. The distance between active sites where droplets are generated is large at low Reynolds numbers and small at high Reynolds numbers for the top, middle and the bottom cylinders. The

placement of the cylinders plays an important role in the irrigation procedure where the top cylinder has a better irrigation than the middle and the bottom.

It is observed that at the same Reynolds number, the flow modes are different at different separation distances between the cylinders, The flow mode tends to be droplet at larger separations, and jet and sheet modes at smaller separations.

Drop detachment from smaller cylinders has been found to stabilize at lower frequencies, and the wavelength decreases with increasing the cylinder diameter.

The numerical results are in good agreement with the experimental results. The use of a numerical tool has resulted in a detailed investigation of these characteristics, which has not been available in the literature previously. The novelty of this chapter is the contribution of the phenomena associated with three - phase flow. Also, the work in this chapter contributes to validation of numerical predictions against experimental results.

The heat transfer between falling liquid films and cylinders is investigated in Chapter 5 ⁽⁸⁾ ⁽⁹⁾. The temperature profile in the liquid film is studied and the local and average heat transfer coefficients around the horizontal cylinders are calculated. The investigation in this chapter is part of an experimental and numerical exploration of heat transfer and falling film modes. Different parameters such as liquid flow rate or Reynolds number, feeder height, cylinder diameters, and heat flux are investigated.

There are three regions of a film flow around a heated cylinder. These are, impingement flow, the thermal development and the fully developed regions. The analysis for this study is based on the assumption of the entire surface of the cylinder being completely wet, and that there is no boiling within the film. The fluid properties remain constant, and the simulations were allowed to continue to a quasi steady-state solution where the results start to repeat themselves.

It has been found that the flow and heat transfer interactions are essentially different for each of the falling film modes. The heat transfer coefficient is most

effective when the sheet mode is apparent. It decreases for jet mode, and further decreases for droplet mode.

Increasing the liquid flow rate results in increasing its velocity, which precipitates a change in the flow mode from drop to jet to sheet modes. Increasing the flow velocity has a corresponding effect on heat transfer. This effect is most clearly seen in the case of the top cylinder.

At the desired Reynolds number, heated cylinders at a short feeder distance are covered with thicker liquid film which helps to remove more heat from the heated cylinder and enhances the heat transfer. For the effect of cylinder diameter, the results show that the heat transfer coefficient is larger for a smaller cylinder diameter over the whole range of liquid flow rate or Reynolds numbers covering the droplet, jet and sheet modes. The effect of cylinder diameter on the heat transfer coefficient is explained in terms of boundary layer development. Since the impingement region occupies a larger portion of the cylinder area, the average heat transfer coefficients are also higher for smaller cylinders. For small cylinder diameters, the surface area is smaller, and the impinging zone is larger than for larger diameters, resulting in a larger average heat transfer coefficient.

The experimental and numerical results indicate that for completely wetted surfaces, the heat flux has no significant impact on the heat transfer coefficient.

The results from the experimental and numerical studies are used to elucidate the effect of heat transfer on the behaviour of falling films. The results reported in this chapter are motivated by the possibility of using detailed numerical simulations of the phenomena that occur in beds of irrigated porous media to obviate the need for purely empirical correlations. The novelty of this chapter is that it provides an in-depth qualitative understanding of the results presented in both the literature and this thesis, towards reducing energy and cooling water requirements in cooling horticultural produce.

The results presented in Chapters 2 to 5 have helped for a better understanding of the flow and heat transfer characteristic. Within this background, in Chapter 6, the

design, construction and the operation of a hydrocooler named Smart Water are discussed in detail. The types of hydrocoolers, design and operation of a Smart Water Hydrocooler are presented. Seven sub-systems that make up a Smart Water Hydrocooler, distribution system and cooling rate of product (broccoli) are given. The conclusions for all chapters are summarized in Chapter 7, along with recommendations for future work.

In Appendix A, the selection of cylinder material used in the laboratory experiments and the different irrigation temperatures have been studied. Aluminium has been chosen to represent the cylinder and Gypsum has been selected as the two ends for the cylinders to avoid the heat lost.

In Appendix B, the numerical simulations of the 2D flow field are studied for random, rectangular pitch-arrangement and up to ten horizontal cylinders. It has been found that better water distribution occurs in the case of a rectangular arrangement. The top cylinder has a better irrigation than the second and the third for the multiple horizontal cylinders. It has been found also that the falling liquid film behaves the same way as in three horizontal cylinders for multiple horizontal cylinders.

In Appendix C, numerical studies of heat transfer coefficients for random, rectangular pitch-arrangement and up to ten horizontal cylinders are reported. The results indicate that the temperature distribution in a rectangular cylinder arrangement is more uniform than in a random arrangement, due to more consistent liquid distribution. For ten horizontal cylinders, the temperature distribution has been monitored and found that the top cylinder cools faster than the bottom ones, due to its closeness to the feeder as expected.

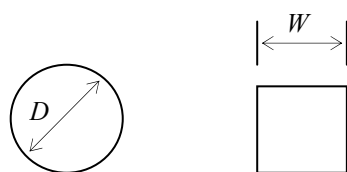


Figure 1.1. Basic 2D geometry for a round nozzle with diameter of D or a slot nozzle with width W

Publications arising from the work to date

- ⁽¹⁾ Jafar, F, Thorpe, G. R. & Turan, Ö. F 2007, 'Liquid Film Falling on Horizontal Circular Cylinders', paper presented to 16th Australasian Fluid Mechanics Conference (AFMC), Gold Coast, Queensland, Australia, 3-7 December.
- ⁽²⁾ Jafar, F. A, Thorpe, G. R & Turan, Ö. F 2009, 'Liquid Jet Impingement without and with Heat Transfer', paper presented to 2009 ASME Summer Heat Transfer Conference, San Francisco, California, USA, 19-23 July.
- ⁽³⁾ Jafar, F. A, Thorpe, G. R & Turan, Ö. F 2011, 'Flow Visualization and Heat Transfer Characteristics of Liquid Jet Impingement', International Journal for Computational Methods in Engineering Science & Mechanics (In print, UCME – 2010 - 0088).
- ⁽⁴⁾ Jafar, F. A, Thorpe, G. R & Turan, Ö. F 2009, 'Flow Mode Characterisation of Liquid Films Falling on Horizontal Plain Cylinders', paper presented to Seventh International Conference on CFD in the Minerals and Process Industries , CSIRO, Melbourne, Australia, 9-11 December.
- ⁽⁵⁾ Jafar, F. A, Thorpe, G. R & Turan, Ö. F 2010, 'Liquid Films Falling on Horizontal Plain Cylinders: Part 1 - Experimental and Numerical Study of Flow Behavior' Computational Thermal Sciences, vol. 3 (2), pp. 145-156.
- ⁽⁶⁾ Jafar, F. A, Thorpe, G. R & Turan, Ö. F 2010, 'Liquid Films Falling on Horizontal Plain Cylinders: Part 2 - Numerical Study of Heat Transfer in Unsaturated Porous Media' Computational Thermal Sciences (under review).
- ⁽⁷⁾ Jafar, F. A, Thorpe, G. R & Turan, Ö. F 2010, 'Falling Film Transitions on Plain Horizontal Horizontal Circular Cylinders' 17th Australasian Fluid Mechanics Conference (AFMC), Auckland, New Zealand, 5-9 December.
- ⁽⁸⁾ Jafar, F. A, Thorpe, G. R & Turan, Ö. F 2009, 'Toward the Detailed Simulation of the Heat Transfer Processes in Unsaturated Porous Media', paper presented to 2009 ASME Summer Heat Transfer Conference, San Francisco, California, USA, 19-23 July.
- ⁽⁹⁾ Jafar, F. A, Thorpe, G. R & Turan, Ö. F 2011, ' Computational Fluid Dynamics Modelling of Liquid Films Falling on Horizontal Cylinder' 3rd World Congress in Applied Computing, Computer Science and Computer Engineering (ACC2011). Kota Kinabalu, Malaysia, 16-17 July.

CHAPTER TWO

NUMERICAL MODEL AND EXPERIMENTAL SETUP

Agricultural scientists tend to compartmentalise their work into technological specialism. This may limit their progress because they are likely to view the use of water to cool horticultural produce, say, as an isolated technology. Engineering scientists are more likely to view the cooling of warm horticultural produce by irrigating it with water as a heat transfer process in a three-phase porous medium. They would then bring the panoply of engineering analytic tools to bear on the problem. These tools are essentially consisting of empirical correlations between the flow rates of water, air and the properties of the three phases. Such an approach is quite contemporary (Thorpe(2006), but it ignores the inexorable tendency of engineering science to consider physical phenomena in increasing detail.

It is likely that at some future time, perhaps several decades from now, empirical correlations of macroscopic heat transfer phenomena in three phases porous media will be defunct. Taking their place will be mathematical descriptions of phenomena that occur on the length scales of the liquid film, the pores and solid particles that constitute a three phase porous system.

This work is motivated by the desire to take some admittedly small steps in this direction. In this chapter, the experimental apparatus is described which is used to study the flow of water over an array of cylinders which can be heated. In addition, the numerical approach is introduced.

Several numerical simulations are conducted to select the material of the cylinders which are used to represent fruits and vegetable produce. In this study, a CFD code, FLUENT[®] has been employed. These simulations are presented next, then, the experimental setup is described first for flow, followed by the modification of

the apparatus for heat transfer experiments. The problem and computational domain, mesh generation and model validation are explained in detail.

2.1 The Problem and Computational Domain

The problem considered is the liquid flow field and the heat transfer to the liquid film falling over horizontal plain cylinders using GAMBIT and the CFD code FLUENT[®]. The volume of fluid (VOF) multiphase modelling capability has been used for the simulations. The gas phase represents the air as the primary phase and the liquid phase represents the water as the secondary phase.

The VOF (volume of fluid) method was established by Hirt and Nichols (1981), when they traced the fluid regions through an Eulerian mesh of stationary cells. The fluid fraction function F is defined to be equal to 1.0 in a liquid cell and 0.0 outside in a gas cell. A free surface is deemed to exist when the cell contains a liquid and gas. The values of the VOF function near free surface are presented in Figure 2.1

The boundary conditions and the tracking of a liquid-gas interface for 2D flow field simulations are shown in Figures 2.2a and 2.2b, respectively. The domain consists of three phases, where gas represents the surrounding air, liquid represents water and the solid phase is the wall for the cylinders which introduces the horticultural produce. In flow field simulations the cylinders are modelled to be hollow and not solid. This is because the study focuses on the liquid flow around the cylinder and not on the inside of the cylinder. This model helps to minimize the domain grid elements for faster FLUENT simulations.

For heat transfer simulations, the domain is modelled so that the temperature distribution can be calculated inside the cylinders to determine the cooling rates for the solid phase which represents the horticulture produce as shown in Figure 2.3. In Figure 2.3a, the boundary conditions are shown for a grid domain where the cylinders represent the solid phase, air represents the gas phase, and falling liquid

film represents the liquid phase. In Figures 2.3b and 2.3c, the liquid-gas interface and the temperature distribution inside cylinders are presented for 2D.

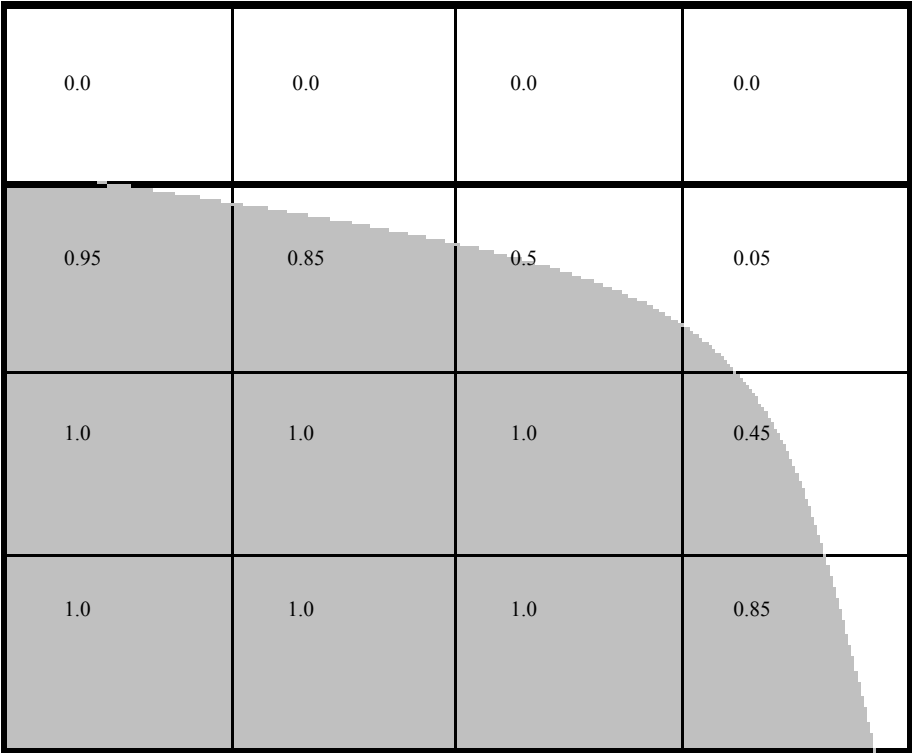
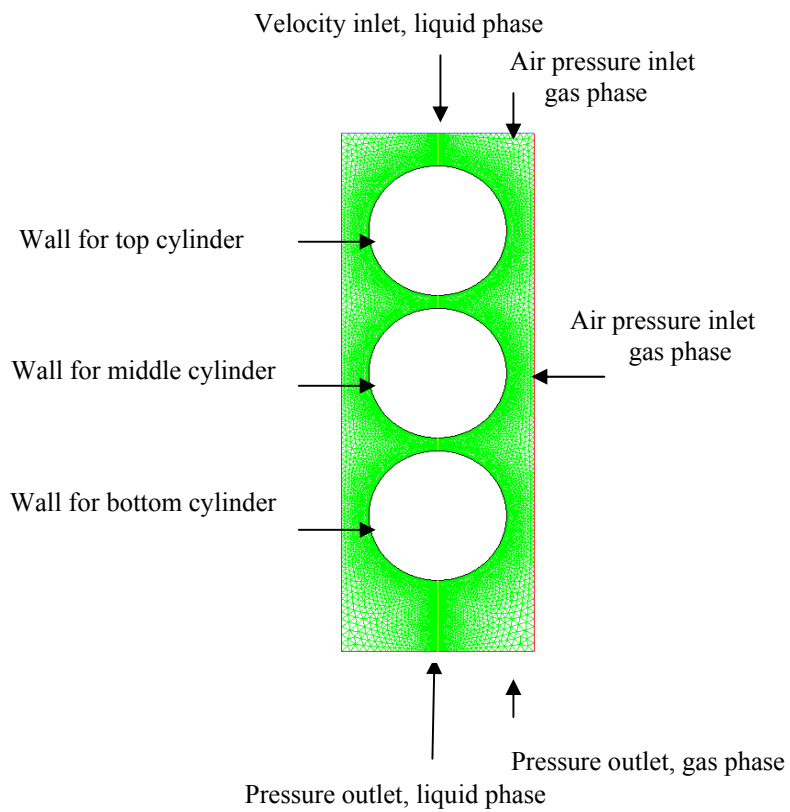
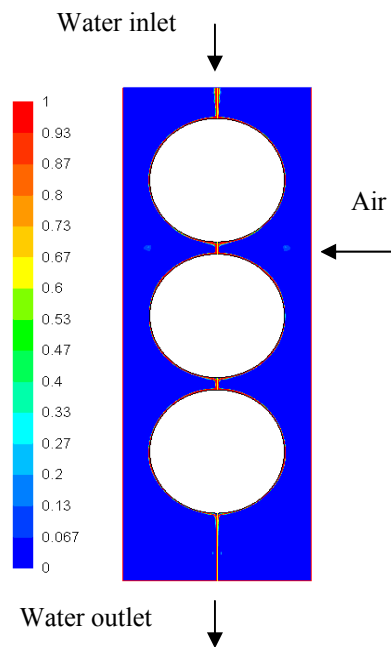


Figure 2.1. Typical values of the VOF function near a free surface. 1.0 represents the cell containing liquid, 0.0 represents the cell containing air. The cell which contains liquid and gas indicates the presence of a free surface.



a



b

Figure 2.2. The 2D flow field model. a) boundary conditions of the domain with three phases, including the three solid horizontal cylinders, b) tracking the interface in 2D of the liquid (red) over the three horizontal cylinders and the surrounding air (blue). The scale on the left denotes 1 for water and 0 for air.

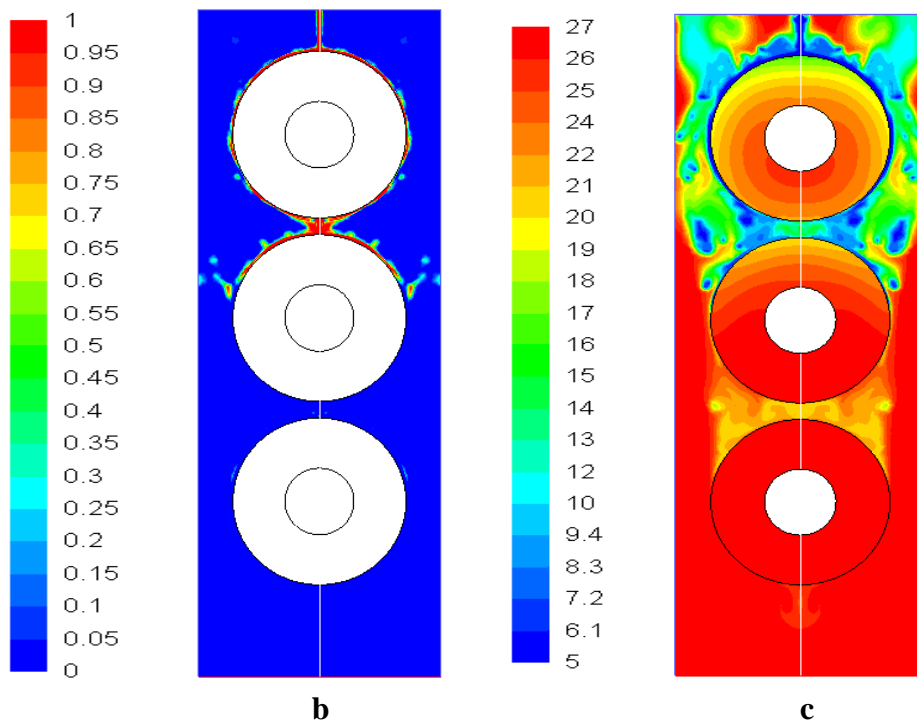
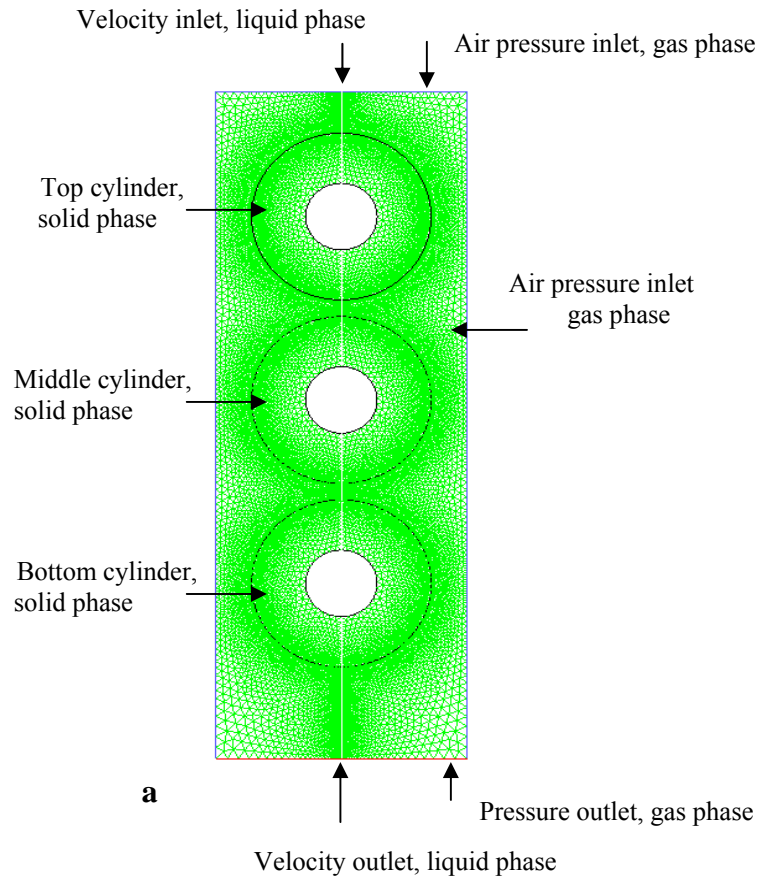
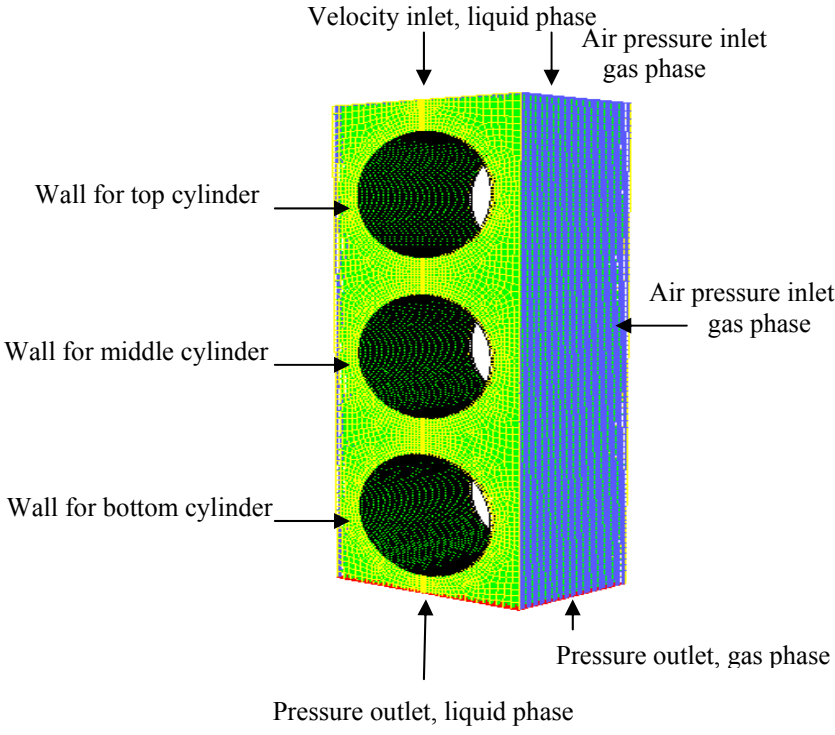
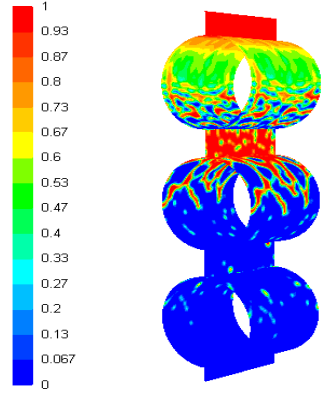


Figure 2.3. The 2D heat transfer model: a) grid domain which consists of the three phases of liquid, gas, and solid, b) tracking interface in 2D of the liquid (red) over the three horizontal cylinders and the surrounding gas (blue), similar to Figure 2.2b, but with heat transfer to be added in Figure 2.3c, c) heat distribution to the water (liquid phase) from the cylinders (solid phase).

3D investigations are limited to studying only the flow field due to impractical run times. Flow field alone has taken up to several weeks even without heat transfer calculations at higher Reynolds number. The geometry which consists of three phases has been modelled to simulate the flow. In Figure 2.4a and Figure 2.4b, the boundary conditions are presented for the 3D model, along with the interface of the liquid over the three horizontal cylinders and surrounding gas. The axial symmetry of the problem allows the 2D and 3D geometries to be used in half for faster simulations.



a



b

Figure 2.4. The 3D flow field model: a) grid domain of three horizontal cylinders which consists of the two phases of liquid and gas, b) tracking interface in 3D of the liquid (red) over the three horizontal cylinders and the surrounding gas (blue).

2.2 Mesh Generation and Model Validation

GAMBIT has been employed to model and mesh the domain of the geometry. A tri pave mesh has been generated for the 2D domain and Hex/wedge elements have been used (Cooper type) for the 3D domain.

The region around the cylinder wall has been carefully meshed by using a boundary layer technique to capture details of the water flow around the cylinder and to precisely calculate the water film thickness as shown in Figure 2.5. A size function technique has been employed. This technique enables starting from a minimal mesh size where flow details are important. The grid size then increases with distance from the cylinder surface, as flow gradients become severe. The size function chosen here is 0.003 m with growth rate of 1.1 to a size limit of 1. The size function technique is illustrated in Figure 2.6.

2.2.1 Grid Independence

To study grid independence, three different grids for the 2D and 3D geometries have been used at a constant liquid flow rate of 0.4 kg/ms. For 2D, the first simulation is with 50,708 elements, the second for 24,600 elements and the third with 15,020 elements as shown in Figure 2.5. The water film thickness is studied for the three simulations and the computation results are shown in Table 2.1. The same simulations have been repeated for 3D with grid elements of 475,000, 170,594 and 105,250. The computational results for 3D are shown in Table 2.2. The results show that using different grid elements has no significant impact on the simulation results. Therefore, a grid size of 24, 600 elements is chosen for the results presented here.

2.2.2 Time Independence

To check for time step independence for 2D and 3D, grids of 24.600 elements and 475.000, respectively have been employed using a mass flow rate of 0.4 kg/ms. The simulations have been run for three time steps of 0.0025, 0.00125, and 0.000625 seconds. The water film thickness results presented in Tables 2.3 and 2.4 for 2D and 3D, respectively, show that changing the time step has no effect on the

results. therefore, a time step of 0.00125 second is chosen for the results presented in this thesis.

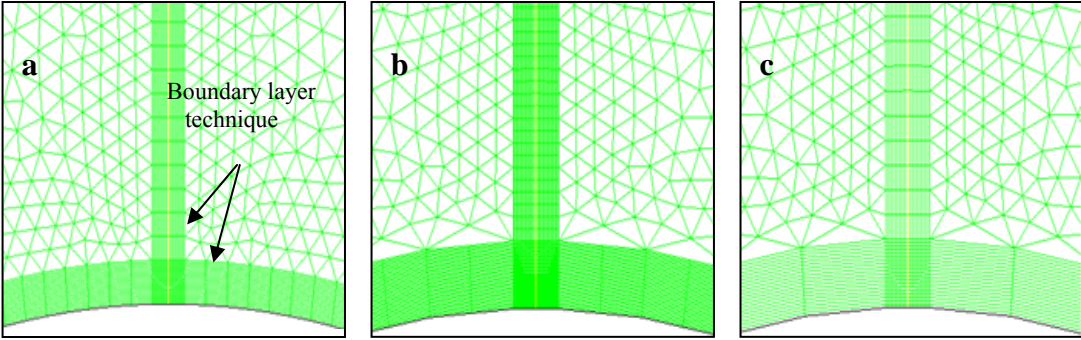


Figure 2.5. Zooming in at the top cylinder showing the boundary layer technique with different grid elements: a) 50,708, b) 24,600 and c) 15,020.

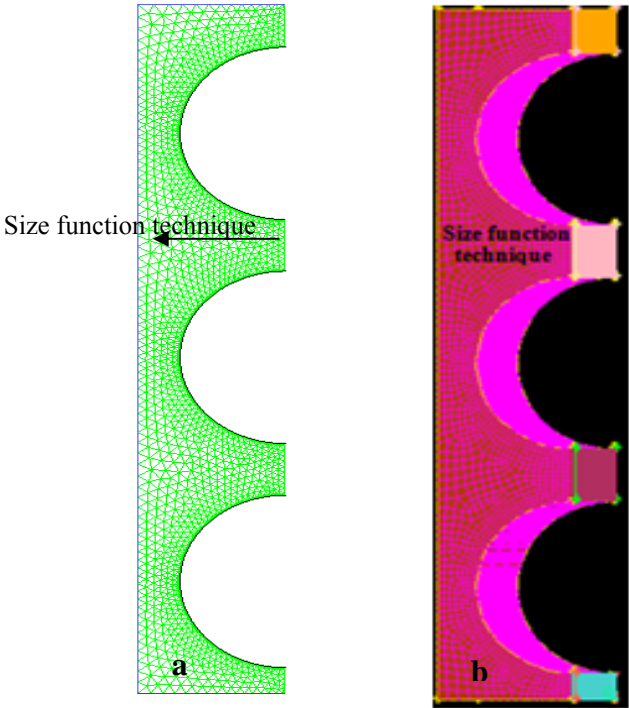


Figure 2.6. Size function technique for half domain: a) for 2 D and b) for 3D.

Table 2.1. Computation results for grid independence for 2D.

Grid (total element)	50,708	24,600	15,020
Water film thickness at $\theta = 90^\circ$, m	0.000402	0.000412	0.000432

Table 2.2. Computation results of grid independence for 3D.

Grid (total element)	475,000	170,594	105,250
Water film thickness at $\theta = 90^\circ$, m	0.000476	0.000491	0.000495

Table 2.3. Computation results of time step independence for 2D.

Time step, s	0.0025	0.00125	0.000625
Water film thickness at $\theta = 90^\circ$, m	0.000412	0.000487	0.000492

Table 2.4. Computation results of time step independence for 3D.

Time step, s	0.0025	0.00125	0.000625
Water film thickness at $\theta = 90^\circ$, m	0.000476	0.000493	0.000497

2.3 Design Consideration

It is essential to ensure in this study that the heat flux is uniform and that there is little loss at the two ends of each cylinder. Thus, the objective is to model a cylinder which has three regions as shown in Figure 2.7, and then to simulate heat transfer at the wall region by applying a heat flux. The two end regions are exposed to air that is at the ambient temperature of 25 °C. FLUENT has been used to investigate the distribution of the heat flux at the surface of the cylinder. The simple boundary conditions discussed here can be easily implemented in FLUENT. It is assumed that the flux is uniform in the central region of the cylinder, and equal to that calculated from the heating element. It is likely that the radial flow of heat will not be uniform along the cylinder. A possible scenario is shown in Figure 2.7. It can be seen that a sheet of water falls over a heated tube and water flows over the

central portion of the cylinder, whereas the outer ends are exposed to air that is essentially stagnant. The configuration shown in Figure 2.8 will result in the ends of the cylinder becoming warmer than the central region causing the measured heat flow from the heating element to be a false reflection of the heat flux at the surface of the tube. However, it is possible that the heat flux near the centre of the cylinder does indeed flow radially, in which case the measured heat flux at the centre of the tube is equal to that at the surface. It can be seen that the irrigated cylinder is idealized by dividing it into three regions. The two ends are exposed to air that has an ambient temperature of 25 °C and the central region is exposed to water that has a temperature of 5 °C. The corresponding heat transfer coefficients are set to be 10 and 1000 W/m² K, respectively.

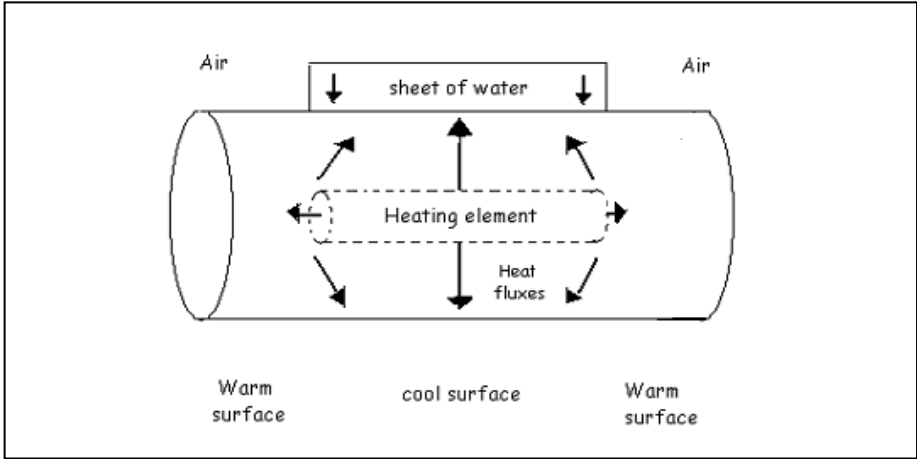


Figure 2.7. Sheet of water falls over a heated cylinder.

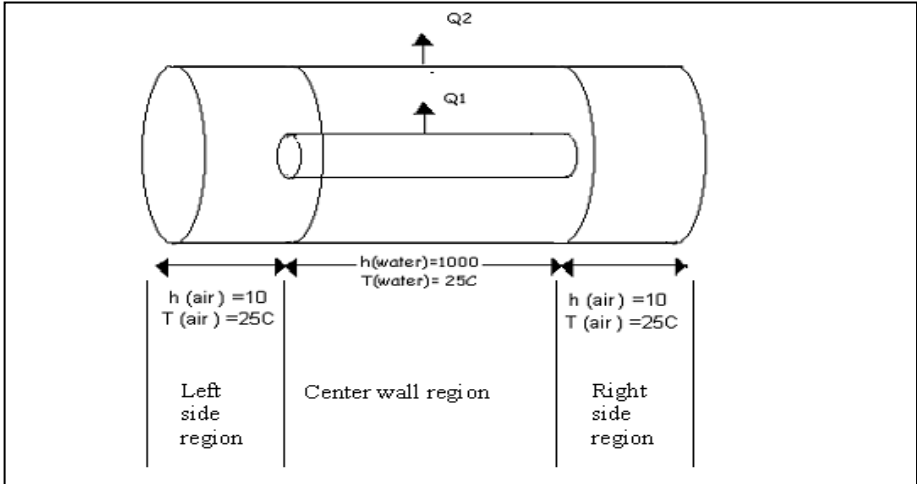


Figure 2.8. Irrigated tube is idealized by dividing it into three regions.

Fifteen simulations have been designed to examine the effect of different materials (to be able to select the correct cylinder material to be used in the laboratory experiments), cylinder diameters and different irrigation temperatures. Aluminium and steel have been chosen to represent the center region. Aluminium, steel and Gypsum have been selected to present the left and right side regions (to be able to select the correct material of the two ends of the cylinder used in the laboratory experiments).

The selection criteria are the minimum heat loss from the ends and the most uniform temperature distribution on the cylinder surface. In reality, the best material which represents horticultural produce as a porous medium is wood, as most woods have thermal conductivity close to that of packed produce. However, due to having to use heating in the laboratory experiments, such a selection is not possible. Gypsum option in FLUENT has the closest thermal conductivity value to that of Bakelite which have been chosen in the laboratory experiments to represent the insulated ends.

These simulations are presented in detail in appendix A. The results given in appendix A indicate that the best material for the core and the ends, respectively, are the Aluminium and Gypsum. The reason for chosen these materials is that the corresponding results presented in Figures A.5 have the most uniform surface temperature distribution among all cases tested numerically.

2.4 Apparatus

2.4.1 Flow Field Experimental Apparatus

To experimentally study the flow field of liquid film falling over the cylinders, the apparatus is made up of seven parts: a water tank, three cylinders, cylinder rack, water collection tub, pump, and elastic hoses as shown in Figures 2.9 and 2.10 with a photograph and a sketch, respectively.

The water tank is rectangular and made of transparent plastic with the dimensions of 0.4 x 0.2 x 0.3 m. Within the tank, there are two copper tubes: a long 0.250 m

outlet tube that prevents overflow by draining excess water down to the collection tub through the hoses, and an inlet tube 0.01 m long that provides water into the tank through a water pump.

The cylinders are used in the laboratory experiments to represent horticultural produce that is curved such as broccoli or apples, fruits and vegetables that will ultimately be cooled in a hydrocooler system. The use of these cylinders is to provide a practical alternative in the simulations using GAMBIT and FLUENT software packages.

Cylinders of 0.3 m length are used in both falling liquid film and heat transfer studies. The rack, which holds the three cylinders, is made up of four vertical columns with three horizontal rods placed horizontally on each side to hold the cylinders. The horizontal rods are fixed with a further set of screw columns. These columns allow rising and lowering of the cylinders to the desired height, thus allowing adjustment of the distance between each cylinder to study the effect of the separation distance \bar{S} . The galvanized water reservoir collects the falling water from the water tank.

Flow field tests are performed to determine the falling film mode characterized without heating. Before starting the test, the cylinders are adjusted to the desired cylinder spacing. Then, the cylinders are carefully levelled to avoid non-uniform liquid distribution. Inclination of the cylinders could drive the liquid flow to one side to cause a non-uniform distribution, and hence, this is an important point.

The liquid flow rate is adjusted to obtain droplet, jet and sheet modes. Liquid flow rates are measured using a container and stop watch. This method involved collecting the liquid with the container while monitoring the time. The flow field experiments have been repeated after two flowmeters are connected; one to obtain a low liquid flow rate and the second for a high liquid flow rate. The type of flowmeters and connected valves are described in detail further in this chapter in Section 2.5. Another photograph and sketch of the flow field setup with the flowmeters are shown in Figures 2.11 and 2.12 respectively.

At high flow rates, the falling film is in sheet mode. With decreasing liquid flow rate the sheet breaks up, exhibiting a sheet-jet mode. Upon decreasing the flow rate further, the falling film goes through jet, jet-droplet and then to droplet mode. It has been possible to accurately record the corresponding flow rates and take flow visualisation photographs. To study the flow patterns, spacing between the jets or droplets, and also the temperature distribution at different flow modes of droplet, jet and sheet modes a photographic Kodak camera of 10.3 mega pixels is utilized along with a thermal imaging camera of Neo Thermo, Tvs-700, and Radiometric UFPA IR Camera specifications.

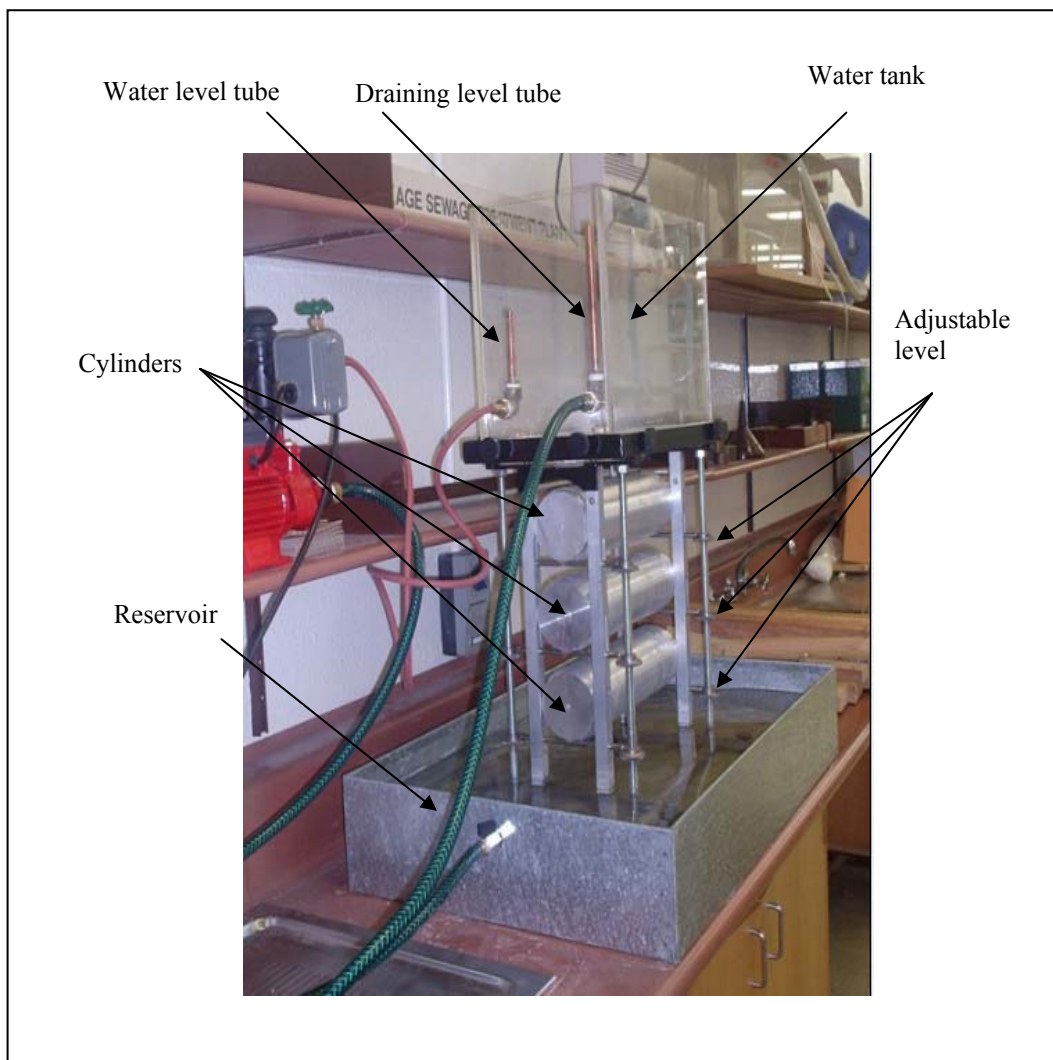


Figure 2.9. Photograph of the flow field apparatus.

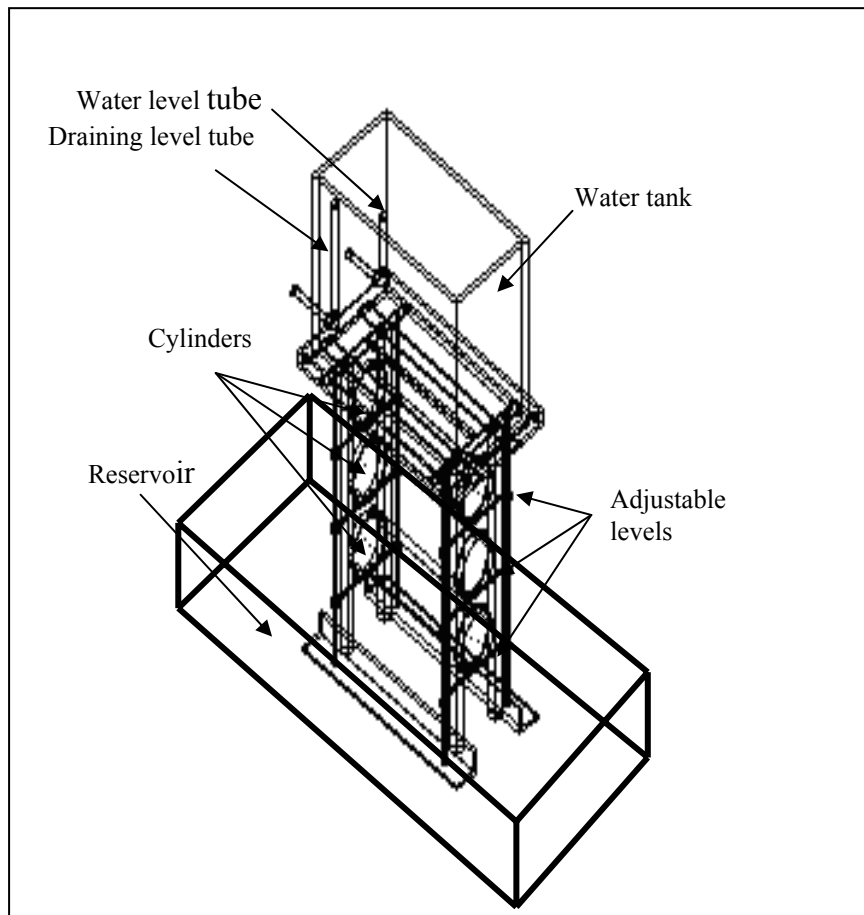


Figure 2.10. Sketch of the flow field experimental setup.

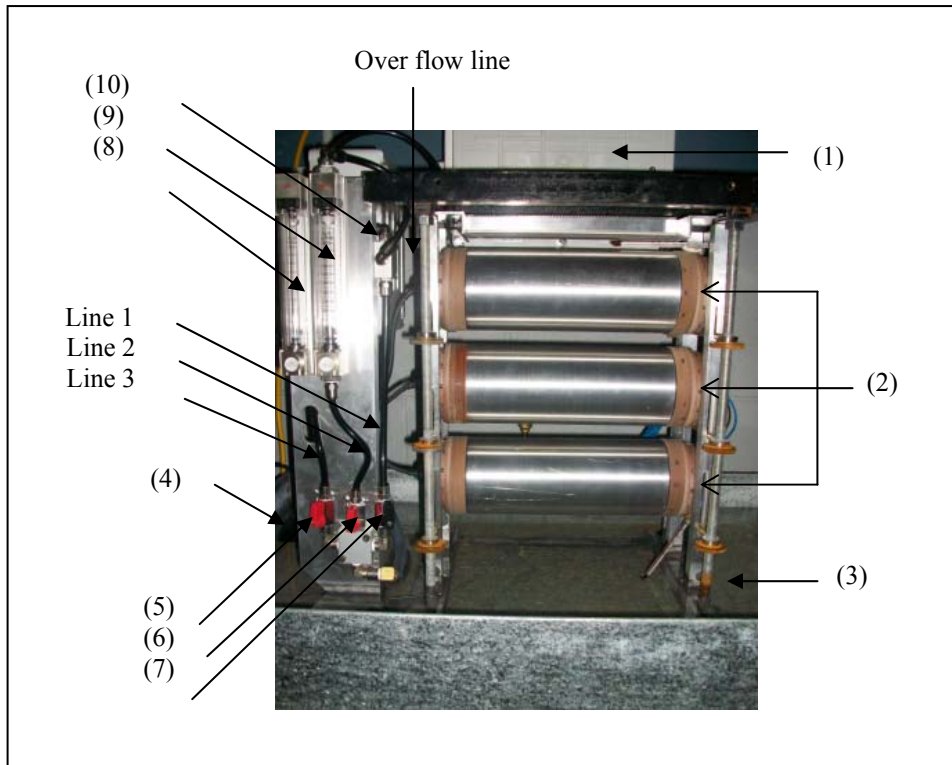


Figure 2.11. Photograph of the flow field experimental setup to show components. 1) water tank, 2) test tubes, 3) reservoir, 4) water pump, 5), 6), 7) valves, 8) low flow rate flow meter, 9) high flow rate flow meter, 10) bypass line, 11) digital camera.

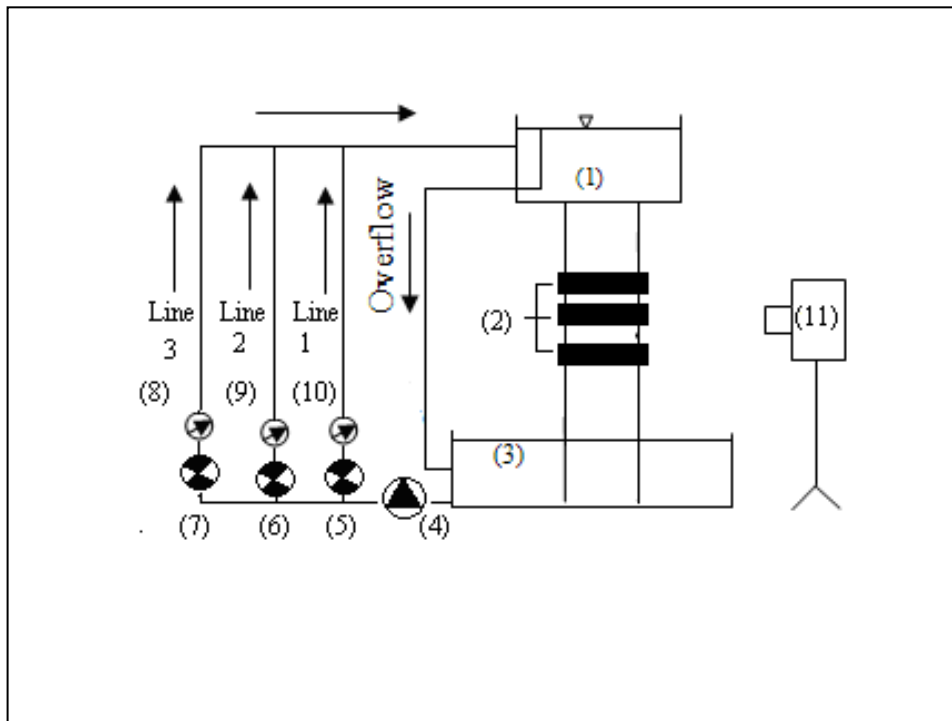


Figure 2.12. Schematic diagram of the flow field experimental setup with components. 1) water tank, 2) test tubes, 3) reservoir, 4) water pump, 5), 6), 7) valves, 8) low flow rate flow meter, 9) high flow rate flow meter, 10) bypass line, 11) digital camera.

2.4.2 Heat Transfer Apparatus Modification

For the heat transfer experiments, modifications had to be made to the flow field apparatus. Aluminium cylinders have been selected according to the results obtained from Section 2.3. Bakelite insulation has been chosen, as the thermal conductivity of Bakelite is close to that of Gypsum. The Aluminium solid cylinders have been drilled at the center to inset the heating element. For the surface thermocouples, twelve grooves at 15-degree intervals circumferentially have been made with the dimensions of 0.005 m width, 0.005 m depth and 0.05 m long, as shown in Figure 2.13. A cartridge or element heater is inserted inside each cylinder to generate heat. Then, an Aluminium tube of diameter of 0.12 m and thickness of 0.002 m is placed on each cylinder to fix the thermocouples in the grooves, as shown in Figure 2.14.

In order to minimize axial heat conduction losses through the two ends of the cylinder, insulation made of Bakelite is used at the ends of heated cylinders (the thermal conductivity of the Bakelite is 0.21 W/m.K for up to 200 °C). Bakelite is machined into two parts of insulation cups, the inner and outer, parts as shown in Figure 2.15. The inner part has twelve rectangular holes to insert the thermocouples to their placement grooves. This part is fixed to the cylinder with screws as shown in Figure 2.16. The outer part of Bakelite covers the inner part as shown in Figure 2.17 for a single cylinder and in Figure 2.18 for three Aluminium cylinders. The thermocouples must be very carefully inserted, and they must be calibrated after installation in the cylinders.

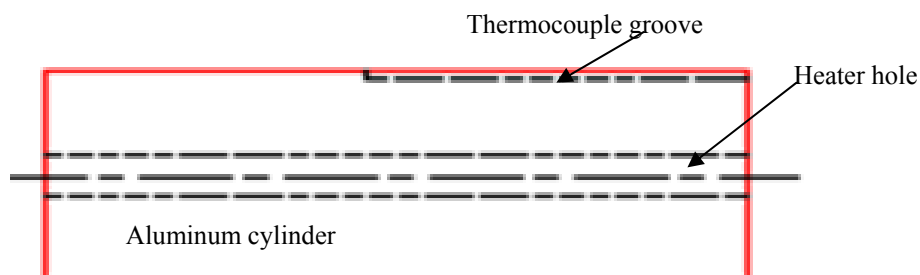


Figure 2.13. Sketch of the thermocouple placements.

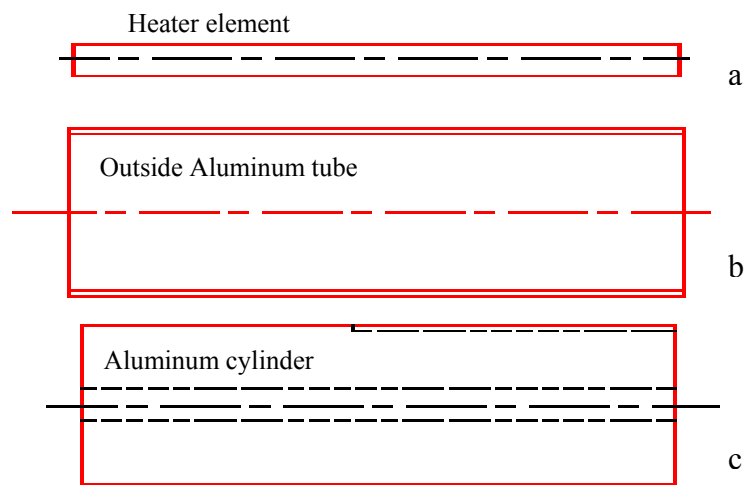


Figure 2.14. Sketch of thermocouple placement and heater. a) heater element, b) Aluminium tube which located outside the cylinder, c) Aluminium cylinder.

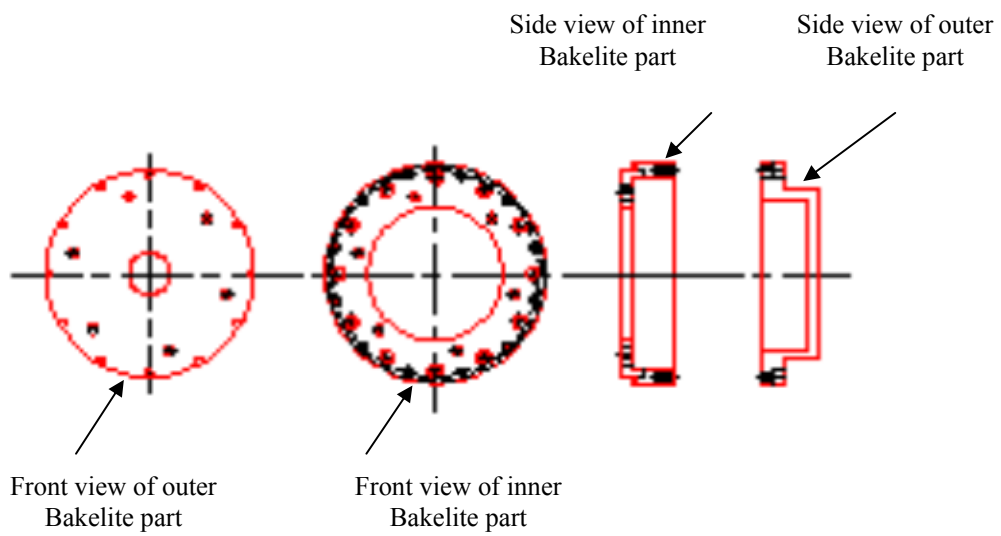


Figure 2.15. Sketch of inner and outer part of Bakelite insulation caps.



Figure 2.16. Photograph of one cylinder with element heater and inner part of the Bakelite insulation cap.

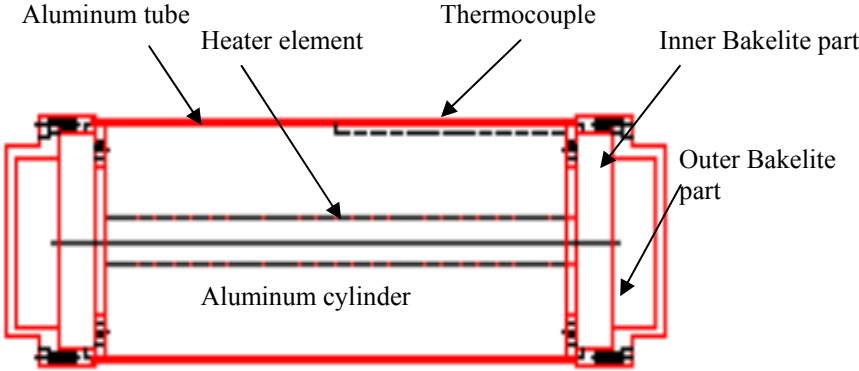


Figure 2.17. Sketch of a cylinder with element heater and two parts of Bakelite cap insulation.



Figure 2.18. Photograph of the three cylinders with element heaters inside and Bakelite at both ends of each cylinder.

A water distributor is manufactured to perform as a water tank as shown in Figures 2.19 and 2.20. The distributor is connected to two water flowmeters with different ranges for better performance and accuracy. The water distributor is a cylinder made of Aluminium. The inner diameter is 0.002 m and the outer diameter is 0.005 m. The top part of the cylinder has been shaped on a milling machine, and then, twenty four vertical holes have been drilled along the length of distributor to connect the outer and the inner diameters. A spherical groove is carved longitudinally across the vertical holes, such that the water flown up through the holes is collected in this reservoir. To guide the water flowing out from the reservoir, multiple horizontal slots have been made along the length of the distributor on the lips at either side. The completed final system of three cylinders and the water distributor is shown in Figure 2.21.

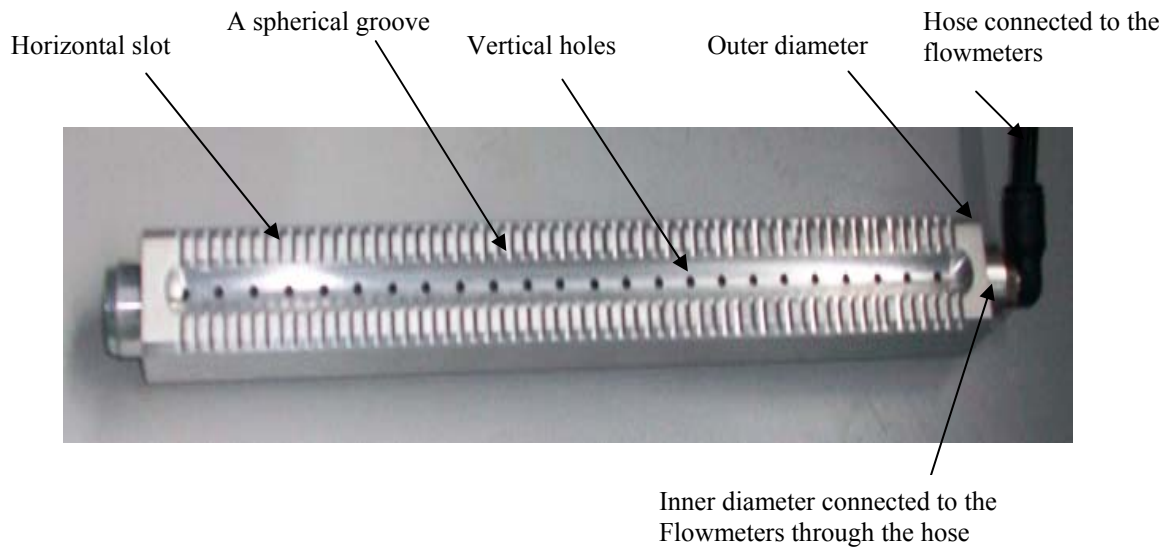


Figure 2.19. Photograph of water distributor. The water flows from the Flowmeters to the inner and then, to the spherical groove through the vertical holes, and then, drops down on to the cylinders through the vertical holes.

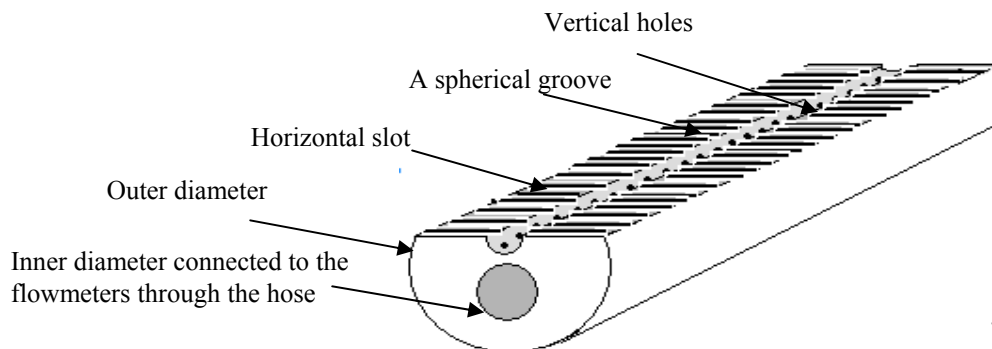


Figure 2.20. Sketch of water distributor where at the inner diameter, it is connected to the outer with twenty four holes.

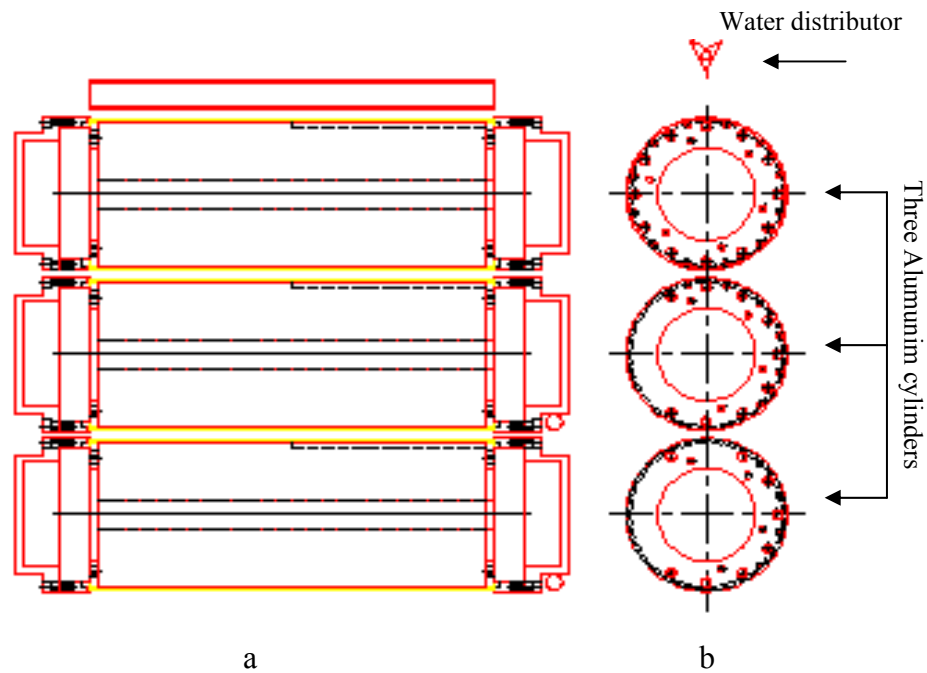


Figure 2.21. Sketch of the heated setup. a) the front view of three Aluminium cylinders and water distributor, b) side view of the set up.

2.5 Flowmeters

Liquid flow rates are measured using two MPS series 1200 variable area Flowmeters with operating ranges of 0.05 to 0.5 l/min to 0.75 to 7.5 l/min and uncertainty of $\pm 5\%$ predicted and $\pm 2\%$ series calibrated.

The two flowmeters have been employed in the final setup for different liquid flow rates. The first one is used to record the liquid flow rates when the flow rate is below 0.06 l/min: Hence, this one is used for droplet and drop-jet mode experimental, as shown in Figure 2.22a. For higher flow rates, the second flowmeter is used for jet, jet-sheet and sheet mode experiments. A bypass line which is controlled manually is designed to be used for the low flow rates. This line is shown in Figure 2.22b.

Type T thermocouples that were used in the experiments are calibrated using a thermostatic bath with NIST traceable thermometers that have uncertainties of ± 0.05 °C. The thermocouples are also calibrated after installation on the cylinders. After calibration, temperature measurements proved to have uncertainties less than ± 0.18 °C. The thermocouples are connected to a computerized system, and the data are loaded automatically onto a computer. To avoid the over heating the cylinders a control voltage has been employed. A photograph and sketch of heat transfer setup are shown in Figures 2.23 and 2.24, respectively.

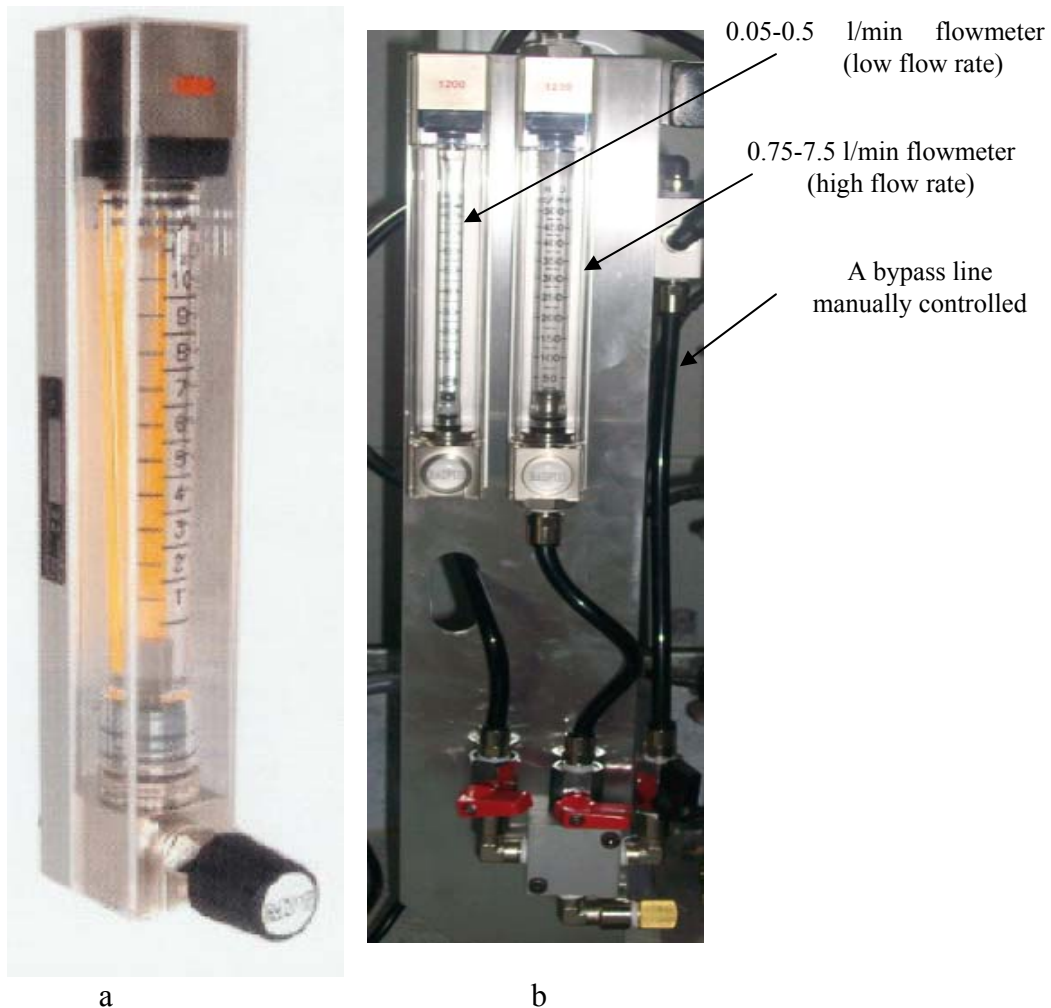


Figure 2.22. Flowmeter. a) MPB Series 1200B flowmeter, b) a photograph of the two Flowmeters used in the apparatus.

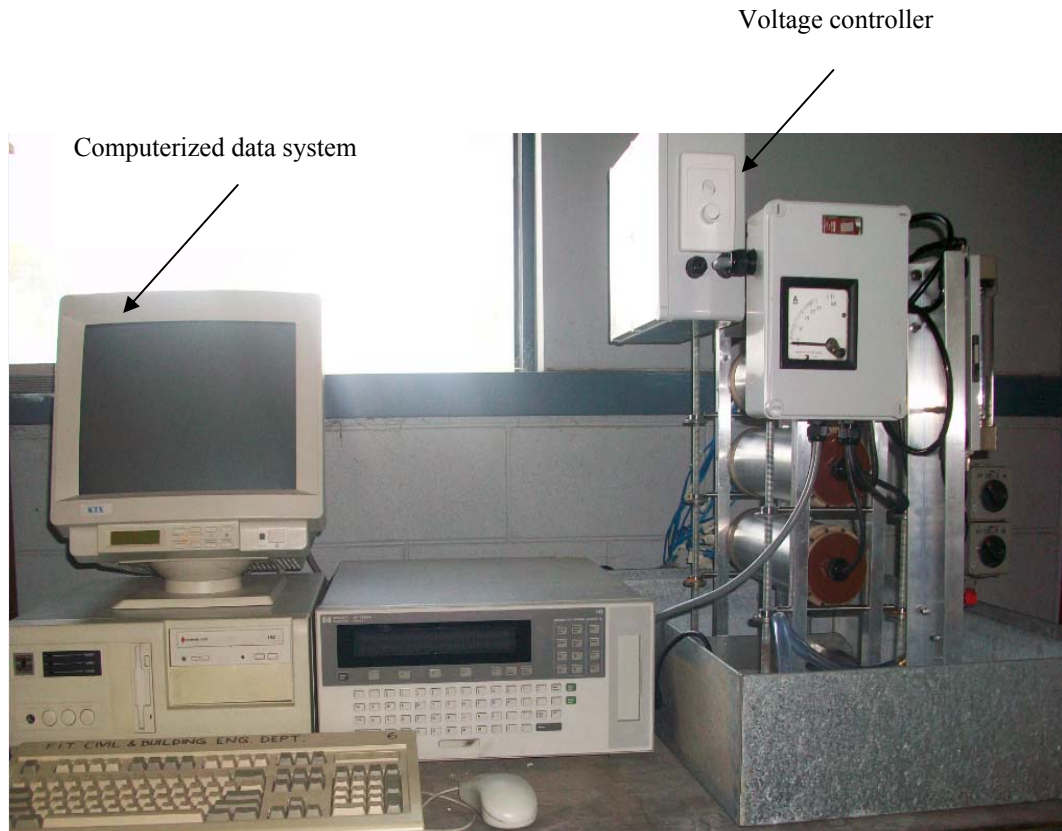


Figure 2.23. The completed setup on the right connected to the computerized data acquisition system.

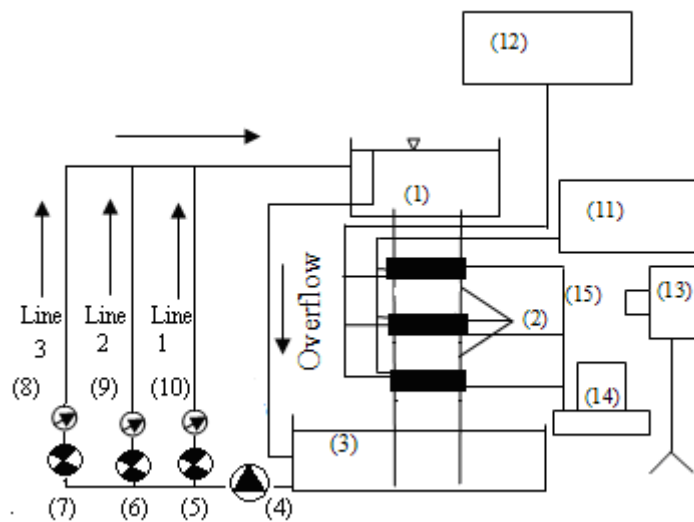


Figure 2.24. Schematic diagram of heat transfer setup. 1) water tank, 2) cylinders, 3) reservoir, 4) water pump, 5), 6), 7) valves, 8) low flow rate flow meter, 9) high flow rate flow meter, 10) bypass line, 11) digital voltmeter, 12) electric power meter, 13) digital camera, 14) computerize collected data, 15) thermocouples.

2.6 Data Reduction Procedure and Uncertainty Analysis

The governing parameter for the flow field experiments is the Reynolds number, Re . For heat transfer experiments, in addition to the Reynolds number, the Nusselt number is also calculated. The definitions of these parameters are listed in Table 2.5. Calculations of these parameters are straight forward, although the calculation of the local or average Nusselt numbers, it is necessary to first determine the local heat transfer coefficient using

$$h = \frac{q''}{(T_s - T_i)} \quad (2.1)$$

Where h is the heat transfer coefficient, q'' is the heat flux, T_s is the surface temperature and T_i is the liquid inlet temperature. Due the variation of the local heat transfer coefficient and the high conductivity, the heat flux at the outer surface of the cylinder may not be uniform but the design of the apparatus as mentioned before helps to ensure that the imposed flux is uniform.

Applying the method of Moffat (1988) to each of the parameters in Table 2.5 results in expressions for the uncertainties for each of the parameters

Film Reynolds number

$$\left(\frac{\delta(Re)}{Re} \right)^2 = \left(\frac{\delta\Gamma}{\Gamma} \right)^2 + \left(\frac{\delta\mu}{\mu} \right)^2 \quad (2.2)$$

Nusselt number

$$\left(\frac{\delta(Nu)}{Nu} \right)^2 = \left(\frac{\delta h}{h} \right)^2 + \left(\frac{\delta k}{k} \right)^2 + \frac{4}{9} \left(\frac{\delta\mu}{\mu} \right)^2 + \frac{4}{9} \left(\frac{\delta\rho}{\rho} \right)^2 \quad (2.3)$$

Where δ is water film thickness, Re is Reynolds number, Γ is liquid mass flow rate per unit length of cylinder, μ is dynamic viscosity, Nu is Nusselt number, k is thermal conductivity and ρ is density

The laminar film thickness, δ at any position is given by Rogers (1981)

$$\delta = \left(\frac{3\Gamma\mu}{g\rho^2 \sin \phi} \right)^{1/3} \quad (2.4)$$

where δ is the liquid film thickness, Γ is film mass flow rate on one side per unit length of cylinder, μ is viscosity of liquid film, g is acceleration due to gravity, ρ is density of liquid film and ϕ is the angular position on a horizontal tube.

The above equations predict the typical uncertainties of the experiments for Reynolds number and Nusselts numbers. The uncertainties are shown in Table 2.5.

Table 2.5. Definition of the Dimensionless physical parameters.

Parameter	<i>Re</i>	<i>Nu</i>
Characterization	$\frac{4\Gamma}{\mu}$	$\frac{h}{k} \left(\frac{v^2}{g} \right)^{\frac{1}{3}}$
Uncertainty	$\pm 1\%$	$\pm 6\%$

2.7 Scope of Experiments

The two basic experimental directions, to investigate the flow field and heat transfer respectively, are described in Table 2.6. The flow field experiments are focused on the flow mode characterization. The heat transfer experiments are focused on the heat transfer behavior under different liquid falling film modes.

The variables controlled and measured are, the liquid flow rate, cartridge heater power output, liquid inlet and outlet temperatures and cylinder surface temperatures

Table 2.6. Experimental Scope.

Flow Field Experiment	Heat Transfer Experiment
Control Liquid Film Flow Rate	Control Liquid Film Flow Rate Heater Power
Measure Mode Characteristics (Flow Mode)	Measure Flow Mode Cylinder Surface Temperature Liquid Inlet and Outlet Temperature

2.8 Conclusion

The objective of this chapter is to describe the design of the apparatus used to generate experimental verification cases.

A cylinder that had a constant heat flux in its central region was cooled using water at ambient temperature.

The numerical results indicate that the dominant scenario can be simulated by using Aluminium cylinders as center wall region with Bakelit as the insulation substance for the right and left ends.

CHAPTER THREE

FLOW FIELD OF LIQUID JET IMPINGING SURFACE WITHOUT AND WITH HEAT TRANSFER

Hydrocooling systems used to cool horticultural produce may be examined as three phase porous media. The macroscopic flow field and heat transfer processes that occur in hydrocooling systems can be analysed using empirical correlations established for designing chemical reactors.

The work in this chapter represents a first step towards the goal of using the power of computational fluid dynamics (CFD) to better understand the heat transfer processes that occur in beds of irrigated horticultural produce. Here, flow field simulations are presented involving three phases (gas, liquid and solid) to study heat transfer associated with jet impingement. A single slot liquid jet is used on flat and curved surfaces using a CFD code (FLUENT) for 2D configurations to study the effects of Reynolds number, nozzle to plate spacing, nozzle width and the surface configuration on the flow and heat transfer characteristics.

The Reynolds number range is 100 – 1900, the liquid medium is water. Here, the Reynolds number is defined in terms of the hydraulic nozzle diameter, inlet jet velocity and fluid kinematic viscosity.

3.1 Introduction

Jet impingement is used in many industrial operations to achieve high rates of heat transfer. A liquid jet can be used for industrial cooling and heating purposes. Cooling jet impingement is used to cool turbine blades, walls of combustion chambers and electronic components.

The parameters which possibly govern jet impingement are nozzle to plate surface distance S , nozzle hydraulic diameter, D , target surface geometry and the flow rate of the liquid or its Reynolds number, Re . The flow field of an impinging jet can be divided into three zones or regions as shown in Figures 3.1 and 3.2 for flat and curved surfaces, respectively, where a liquid jet is typically discharged from a slot nozzle. These regions are:

- (1) The free jet region prior to impingement. This region comprises a potential core in the central region where the velocity profile is uniform, and the velocity decreases in the outer region of the jet.
- (2) The impingement region.
- (3) The wall jet (parallel flow) region.

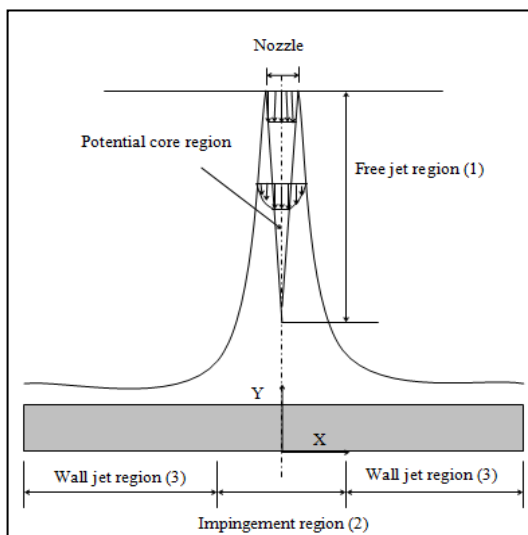


Figure 3.1. A schematic of liquid jet impinging on a flat surface.

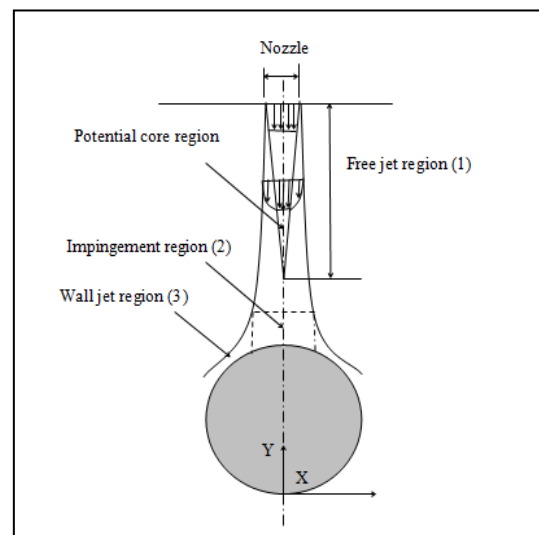


Figure 3.2. A schematic of liquid jet impinging on a curved surface.

The flow field and heat transfer characteristics of jet impingement on a flat surface have received considerable attention in the literature. To avoid high hydrodynamic pressure caused by the impingement on the surface, low Reynolds number are often desirable as reported by Chung and Sandharm (2002). The theory of film flows is widely described in the precursor works of Watson (1964). He developed expressions for the velocity field in different regions using the boundary layer theory. Martin (1977) has reviewed flow and heat transfer of a jet impinging on a

flat surface. He found that the length of the potential core varies between 5 and 6 slot widths from the jet exit.

The study of impingement cooling with a jet from a round nozzle over a heated surface has been reported by Hrycak (1983). He conducted experiments of heat transfer between a round jet and flat plate, employing a variety of methods of surface temperature measurement.

Jets impinging on a smooth surface have been studied by Jambunathan *et al.* (1992). They presented literature surveys of jet impingement that reported enhanced rates of heat transfer, with non uniform radial distribution of the local and surface average Nusselt numbers. Hansen and Webb (1993) have studied the effect of the surface fins on the average heat transfer between an impinging circular jet and a flat plate. They found that there is an increase in the average Nusselt number value by 12-23% by using a square fins and reduction in the value of the average Nusselt number by 4-38% for the other types of fins.

Huang and El-Genk (1994) have investigated the heat transfer between a uniformly heated flat plate and a circular impinging jet. They employed different Re along with different nozzle to plate distances. They found that the maximum Nusselt number occurred at the stagnation point where $X = 0$. Lytle and Webb (1994) studied the effect of very low nozzle to plate spacing ($S/D < 1$) on the local heat transfer distribution on a flat plate.

Siba *et al.* (2003) have investigated the relationship between the heat transfer to the jet flow and the fluctuations of the free stream velocity. Lee *et al.* (2004) have studied the effect of nozzle diameter (1.36, 2.16, and 3.40 cm) on impinging jet heat transfer and fluid flow. They reported that local Nusselt numbers in the stagnation point region corresponding to $0 \leq X/D \leq 0.5$ increases with increasing nozzle diameter, where X is the distance of the flat plate from the stagnation point. This is attributed to the increase in the jet momentum with the larger nozzle diameter, which results in increased the heat transfer at the stagnation point. Narayanan *et al.* (2004) have studied the fluid mechanics and heat transfer in an impinging slot jet within two non-dimensional nozzle-to-surface distances of 3.5

and 0.5. They found that variations the location of the high streamwise fluctuating velocity occur in the wall jet flow for both distances.

Two-dimensional impinging jets and heat transfer at the stagnation point, the stagnation region and wall jet region have been investigated by Beitelmal *et al.* (2006). They found that the theoretical solutions in the wall jet region fit better than at large distances from the stagnation point.

Correlations for local and average heat transfer coefficients are reported by Hoffman *et al.* (2007). They conducted an experimental investigation on flow structure and heat transfer from a single jet impinging on a flat plate. The influences of nozzle to plate spacing and Reynolds number on local heat transfer coefficient are investigated.

The food industry has utilized the technology of jets impinging on surfaces. Dirita *et al.* (2007) reported that the temperature distribution within the processed food and related local heat transfer are important in the cold treatment of foods. Their results include the temperature distributions within the food and at its surface, along with the flow field details. They stated that the temperature distribution within the processed food and associated local heat transfer are significant in the cold treatment of foods in order to achieve the best food preservation.

An experimental investigation of jet impingement is performed by Katti and Prabhu (2008). They studied the local distribution of heat transfer coefficients between a nozzle and flat plate at different jet to plate spacing of 0.5 to 8.0 nozzle diameters. They reported the three regions of the jet impingement on a flat surface. These regions are, the stagnation region where $X/D = 0$, transition region where $1.0 < X/D < 2.5$ and wall jet region where $X/D > 2.5$.

Liquid and gas jet studies of flow field and heat transfer are summarized in Table 3.1.

Table 3.1: Summary of relevant studies of jet impingement

Investigation	Impingement surface	Investigation	Comments
Current study	Flat and curved	Flow field and heat transfer	Experimental and numerical – liquid jet
Watson (1964)	Flat	Flow field and hydraulic jump	Experimental – liquid jet
Gardon and Akfirat (1965) (1966)	Flat	Flow field and heat transfer	Experimental – air jet
Yokobori <i>et al.</i> (1978)	Flat	Flow field and heat transfer	Experimental – liquid jet
Looney and Walsh (1984)	Flat	Governing equation for Laminar free jet, turbulent free and impinging jets	Numerical – air jet
Slayzak <i>et al.</i> (1994)	Flat	Heat transfer	Experimental – liquid jet
McDaniel and Webb (2000)	Circular cylinder	Heat transfer	Experimental – air jet
Chan <i>et al.</i> (2002)	Semi-circular convex	Flow field and heat transfer	Experimental – liquid jet
Wen and Jang (2003)	Flat plate	Flow field and heat transfer	Experimental - air jet
Olsson <i>et al.</i> (2004)	Circular cylinder	Flow field and heat transfer	Numerical – air jet
Goppert <i>et al.</i> (2004)	Flat	Flow field and heat transfer	Experimental – air jet
Fenot <i>et al.</i> (2005)	Flat	Heat transfer	Experimental – air jet
Dirita <i>et al.</i> (2007)	Cylindrical foods	Flow field and heat transfer	Numerical – air jet
Robinson and Schnitzler (2007)	Flat	Heat transfer	Experimental – liquid jet
Sung and Mudawar (2008)	Flat	Heat transfer	Experimental and numerical - gas jet (HFE 7100)
Kanna and Das (2008)	Flat	Flow field and heat transfer	Numerical – gas jet
Zhang <i>et al.</i> (2008)	SMA actuator	Flow field and heat transfer	Experimental and numerical – liquid Jet

In the present study, simulations of three phases (gas, liquid and solid) using FLUENT[®] code are carried out to investigate the flow field and heat transfer characteristics of a slot liquid jet impingement. The objective is to determine the distribution of the local Nusselt numbers on the surface of the target surface for different Re , jet to plate distance, nozzle width, and the surface configuration (flat and curved surfaces)

In this chapter the problem geometries for a flat and curved surface are shown in Figure 3.3 and 3.4 respectively. A two-dimensional jet with velocity V_j enters from a nozzle of width W to a surface of high of S .

In this chapter, the study is focused on a liquid jet impinging a flat and curved surface. This investigation comprises a study of the flow field and heat transfer within the liquid film. This study presents the numerical results of a laminar flow for four cases as shown in Table 3.2. The four cases are;

- Effect of Reynolds number.
- Effect of nozzle to plate spacing.
- Effect of jet nozzle width.
- Effect of target surface configuration.

The jet Reynolds number, based on a hydraulic diameter of $2W$ is varied from 100 to 1900. The Prandtl number is 6.587 for water as the cooling fluid medium. The inlet water jet temperature is 25 °C and the heat flux = 1000 W/m².

The flow is assumed to be two dimensional, unsteady, incompressible and laminar. The fluid density, viscosity and the thermal conductivity are assumed to be constant.

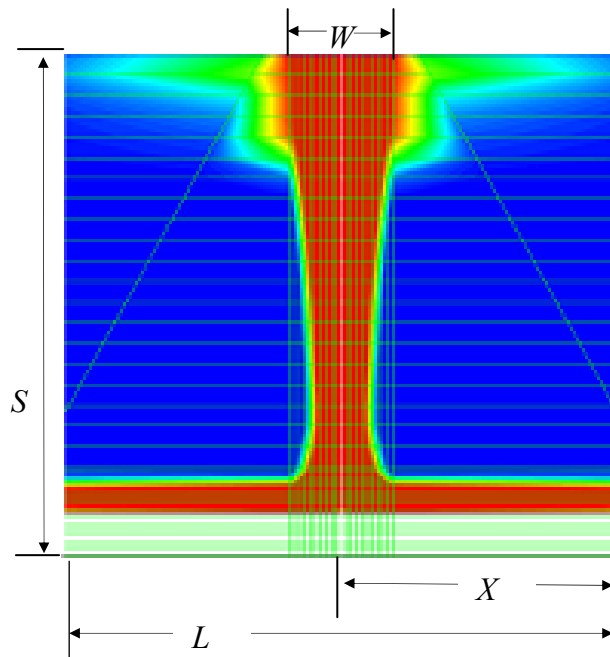


Figure 3.3. 2D impinging jet flat surface where water is indicated by red, air by blue and the target surface is green.

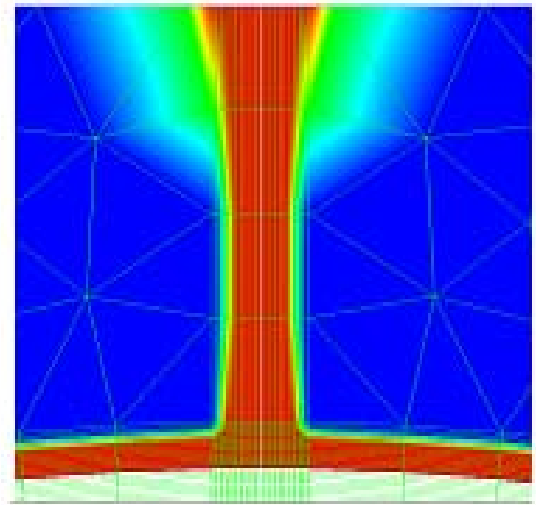


Figure 3.4. 2D impinging jet curved surface where water is indicated red, air by blue and the target surface is green.

Table 3.2. The parameters used in this study

Case study	S , mm	W , mm	D , mm	S/D	X , mm	L , mm	X/D	Re	Surf.
1	20	4	8	2.5	25	50	3.12 5	1900 700 500 100	Flat
2	100 40 20 10	4	8	12.5 5 2.5 1.25	25	50	3.12 5	1900	Flat
3	100	4 2	8 4	12.5	25	50	3.12 5 6.25	1800	Flat
4	40	4	8	5	25	50	3.12 5	250	Flat Cur.

3.2 Mathematical Analysis

Heat transfer in the cylinder, water and air are governed by the fundamental conservation equations of continuum mechanics listed below.

- Continuity equation:

$$\frac{\partial u}{\partial x} + \frac{\partial v}{\partial y} = 0 \quad (3.1)$$

- Horizontal momentum equation (x-direction)

$$\frac{\partial u}{\partial t} + u \frac{\partial u}{\partial x} + v \frac{\partial u}{\partial y} = -\frac{1}{\rho} \frac{\partial p}{\partial x} + \nu \left(\frac{\partial^2 u}{\partial x^2} + \frac{\partial^2 u}{\partial y^2} \right) \quad (3.2)$$

- Vertical momentum equation (y-direction)

$$\frac{\partial v}{\partial t} + u \frac{\partial v}{\partial x} + v \frac{\partial v}{\partial y} = -\frac{1}{\rho} \frac{\partial p}{\partial y} + g + \nu \left(\frac{\partial^2 v}{\partial x^2} + \frac{\partial^2 v}{\partial y^2} \right) \quad (3.3)$$

- The fluid energy equation:

$$\frac{\partial T_L}{\partial t} + u \frac{\partial T_L}{\partial x} + v \frac{\partial T_L}{\partial y} = \left[\alpha_L \frac{\partial^2 T_L}{\partial x^2} \right] + \left[\alpha_L \frac{\partial^2 T_L}{\partial y^2} \right] \quad (3.4)$$

where ρ is the density, T_L is the liquid temperature, u is the x-component of the water velocity, v its y-component velocity, α_L is the thermal diffusivity and g is the gravitational acceleration in the y-direction.

The boundary conditions are:

- At the jet exit

$$v = v_{in}; \quad u = 0$$

- At the pressure outlet

$$P = P_0$$

- At the solid wall

$$u = v = 0$$

The governing equation for VOF as follows,

$$\frac{DF}{Dt} = \frac{\partial \overline{F(x,t)}}{\partial t} + \overline{V \cdot \Delta F(x,t)} = 0 \quad (3.5)$$

where F is defined as the volume fraction of fluid whose value is equal to 1.0 in the liquid and 0.0 outside. Averaged over a control volume, the value of F will be within the segment $[0.0, 1.0]$, as shown early in Figure 2.1. A cell with F values between zero and one contains a free surface.

Surface tension is defined as follows,

$$P_s - P_A = \sigma \left(\frac{1}{R_1} + \frac{1}{R_2} \right) \quad (3.6)$$

where P_s and P_A are the surface and atmospheric pressures, respectively. R_1 and R_2 are the principal radii of curvature at a point on a free surface, and σ is the surface tension coefficient between air and water.

3.3 Computational Details

As mentioned previously in Section 2.1 a commercial finite-volume CFD code, FLUENT[®] is used. 2D simulations have been implemented with similar characteristics of mesh generation and solver setup with laminar flow for the two types of target surfaces. In Figures 3.5 and 3.6, the modelled grid is shown for flat and curved surface respectively. In these two figures, a liquid jet of velocity V_j issues from a nozzle of width W flows down on the flat or curved surfaces. The two sides of the geometry represent pressure outlet at atmospheric pressure. The top left and right side of the geometry are air pressure inlets. The bottom boundary represents walls of the flat and curved surfaces.

Two continuum fluids have been modelled to represent the water and air. The solid face represents either a flat or curved surface. The boundary layer technique has been employed on the velocity inlet region, and on top of the solid face. This technique has been found to accurately capture phenomena that occur in the liquid adjacent to the flat and curved walls.

A size function technique has been employed to smoothly control the growth in the mesh size distribution within the fluid and solid regions. It is also used to produce a smooth transition from the fine mesh needed to resolve the flow physics. The grid has been generated in GAMBIT[®] and then used in FLUENT[®] to implement a transient, segregated and implicit solution procedure. The size function chosen here is 0.003 m with growth rate of 1.1 to a size limit of 1.

The VOF (volume of fluid method) method described in Section 2.1, is used to define the water-air interface.

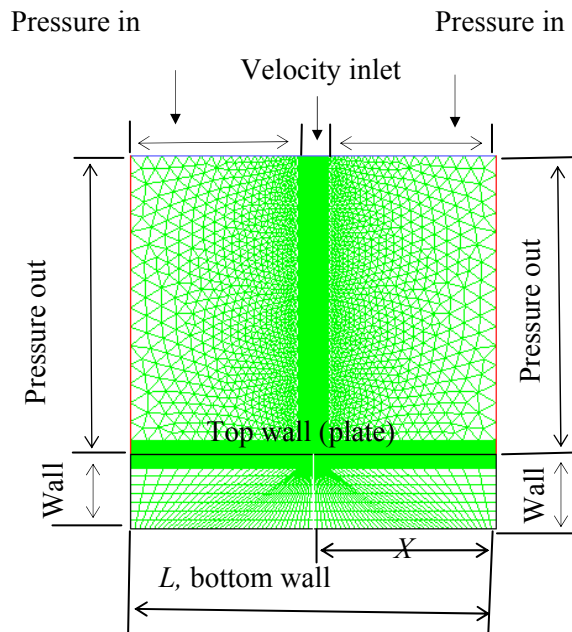


Figure 3.5. Grid for the flat surface.

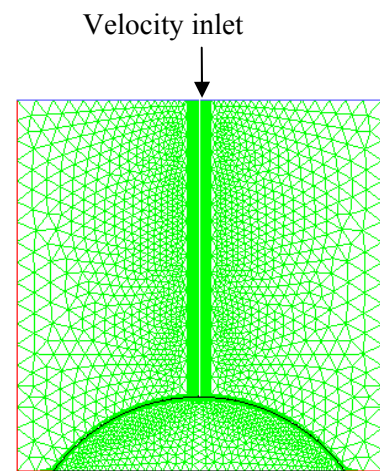


Figure 3.6. Grid for the curved surface.

3.4 Flow Field Analysis

In the following, four cases are presented to study the flow field.

3.4.1 Effect of Reynolds Number, Re (Case study 1)

Numerical simulations have been conducted with a slot jet falling vertically on a heated horizontal surface to study the effect of Reynolds number. A non-dimensional nozzle to plate spacing of $S/D = 2.5$ is studied when Re is between 100 and 1900. The inlet liquid jet temperature is 25 °C, and the nozzle hydraulic diameter is 0.008 m.

When a liquid jet impinges on a flat or curved surface, three different regions are identified as shown in Figure 3.7. As expected from Figure 3.1, the first zone is the free jet region where the flow accelerates due to gravity. The second is the impingement region where the interaction between the jet and the surface produces

a strong deceleration of the flow, and then the liquid flows in a direction parallel to the surface called the wall jet region.

The Reynolds number is calculated based on the inner hydraulic diameter of the nozzle, $D = 2W$, where W is the nozzle width, as follows:

$$\text{Re} = \frac{\rho_l V_j D}{\mu_l} \quad (3.7)$$

where ρ_l is the liquid density, V_j is the inlet velocity of the jet of water with values of 0.23, 0.22, 0.087, 0.062, 0.03, and 0.012 m/s corresponding to Reynolds numbers of 1900, 1800, 700, 500, 250, and 100, respectively. D , the hydraulic diameter of the nozzle, is equal to 0.008 m, and μ_l is the Newtonian dynamic viscosity for water is equal to 0.001 kg/ms.

As further seen in Figure 3.7, with decreasing Reynolds number, the jet diameter along the falling flow decreases, attaining a minimum value near the surface for S less than 1 mm. For $\text{Re} = 500$, water thickness increases after this minimum, because of the interaction between the jet and the surface which forms a stagnation point. After the stagnation zone, the liquid flows parallel to the surface where the water film thickness remains fairly uniform as seen in Figure 3.8.

In Figures 3.9 and 3.10, the velocity profile is shown for impinging and wall jet regions, respectively, at different Reynolds numbers.

Along the falling jet zone and wall region, no evaporation has been produced, and the mass flow rate is conserved. Thus, the amount of the liquid mass flow rate for the free jet region is equal to the amount of the wall jet region and equals to 1.49 kg/ms for $\text{Re} = 1900$. The corresponding mass conservation can be expressed as follows:

$$m^{\bullet} = \rho_L V_j W b \quad (\text{For y-axis}) \quad (3.8)$$

$$m^{\bullet} = \rho_L U \delta b \quad (\text{For x-axis}) \quad (3.9)$$

where m^{\bullet} is the mass flow rate, ρ_L is the liquid density, V_j is the inlet velocity, W and b is the nozzle width and depth respectively. U is the liquid velocity at the wall jet rejoin and δ is the liquid film thickness at wall jet rejoin.

The velocity profile along the x and y axis is different because of the effect of the wall pressure and wall friction. The corresponding coefficients are presented in Figures 3.11 and 3.12, respectively. The wall pressure and friction coefficient are calculated from the following equations;

$$C_p = \frac{P - P_{\infty}}{0.5 \rho V_j^2} \quad (3.10)$$

$$C_f = \frac{\tau_w}{0.5 \rho V_j^2} \quad (3.11)$$

where P is the pressure at the point for which pressure coefficient is being evaluated, P_{∞} is the pressure in the freestream, ρ is density and V_j is jet inlet velocity, and τ_w is wall shear stress,. From an inspection of the pressure coefficient, C_p , in Figure. 3.11, it can be seen that that $C_p = 1.0$ for $Re = 1900$. This result indicates that, the jet core with velocity V_j impinges on the plate, and a recovery of nearly 100% of the total jet pressure is achieved at the stagnation point. The wall static pressure drops rapidly as the flow change direction and accelerates. At all Reynolds numbers, the wall shear stress τ_w rapidly increases away from the stagnation point, as the stagnation point flow evolves to a parallel wall jet, as shown in Figure. 3.12.

The velocity V in free jet region increases because the gravitational force is significant. Whereas in the impinging region, the velocity decreases quickly because of the wall friction that retains the liquid on the wall surface. It can be

seen from Figure 3.13 that near the stagnation region, the x-velocity U increases continually in the x direction.

Hydraulic jump is studied for two Reynolds numbers of 250 and 100. The hydraulic jump can be defined being where the liquid layer depth attains a high value in a parallel flow region. A hydraulic jump radius increases with the Reynolds number, because the parallel flow is accelerated in the x direction and the hydraulic jump is moved far from the stagnation region.

In Figure 3.14 the influence of the flow rate on the hydraulic jump radius is shown. These results are in agreement with those of Stevens and Webb (1989).

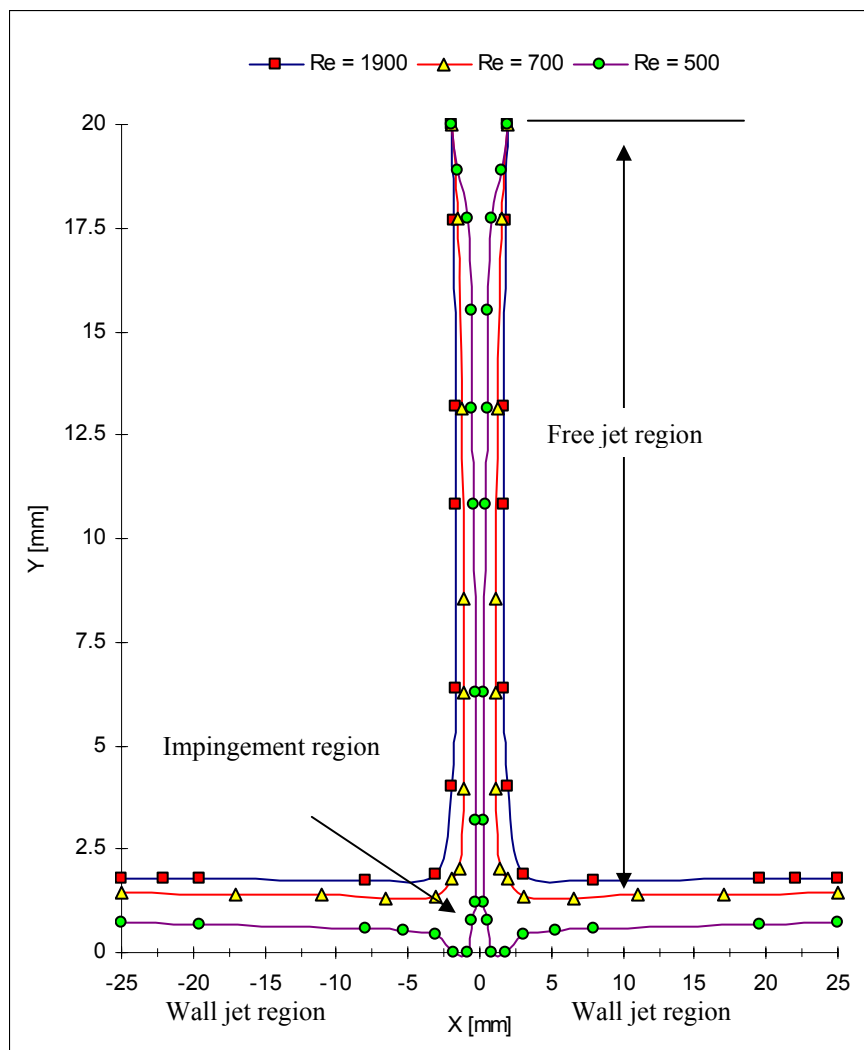


Figure 3.7. Flow field developing from a nozzle to a plate for a range of Reynolds numbers.

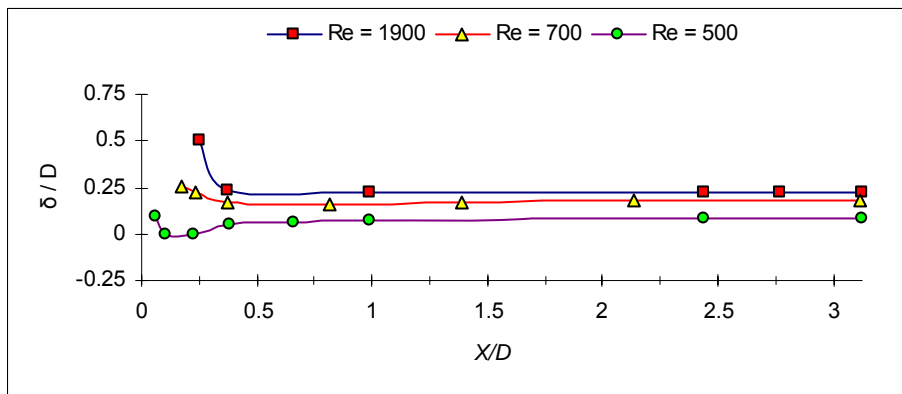


Figure 3.8. Non-dimensional water film thickness in the horizontal direction at different Reynolds numbers for $S/D = 2.5$.

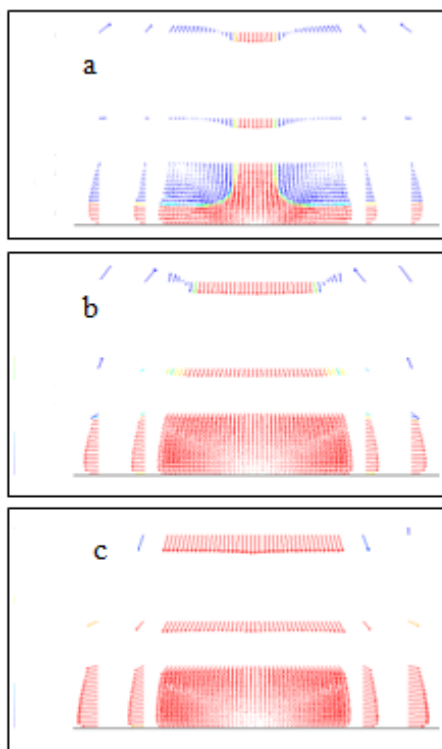


Figure 3.9. Flow field for impinging zone. (a) $Re = 500$, (b) $Re = 700$, and (c) $Re = 1900$.

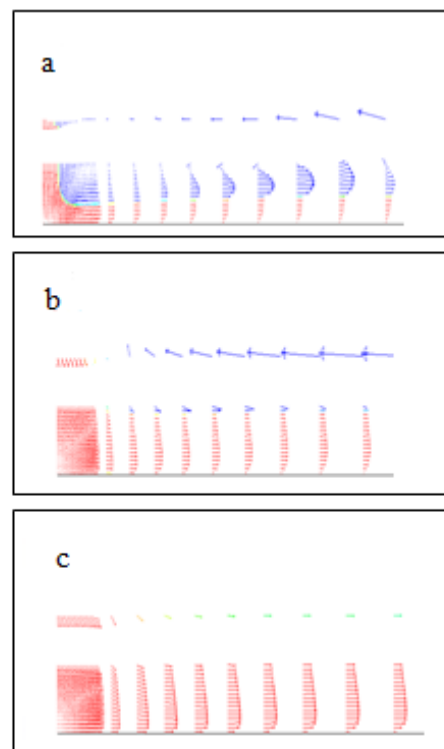


Figure 3.10. Flow field for wall jet zone. (a) $Re = 500$, (b) $Re = 700$, and (c) $Re = 1900$.

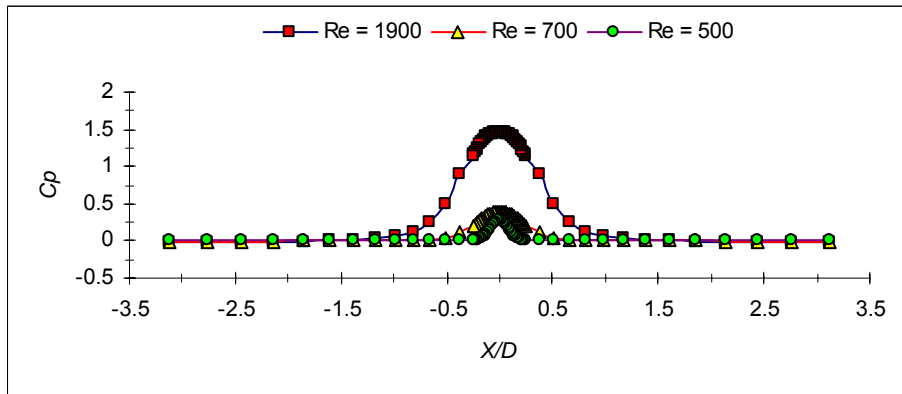


Figure 3.11. Wall pressure coefficient for different Reynolds number.

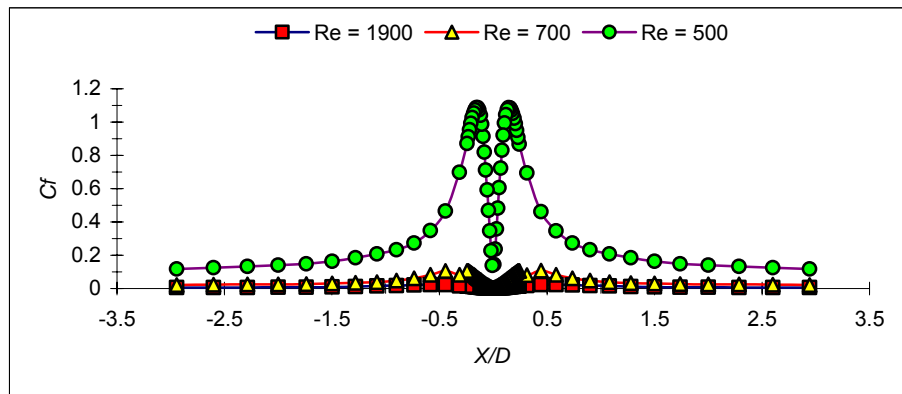


Figure 3.12. Wall friction coefficients for different Reynolds number.

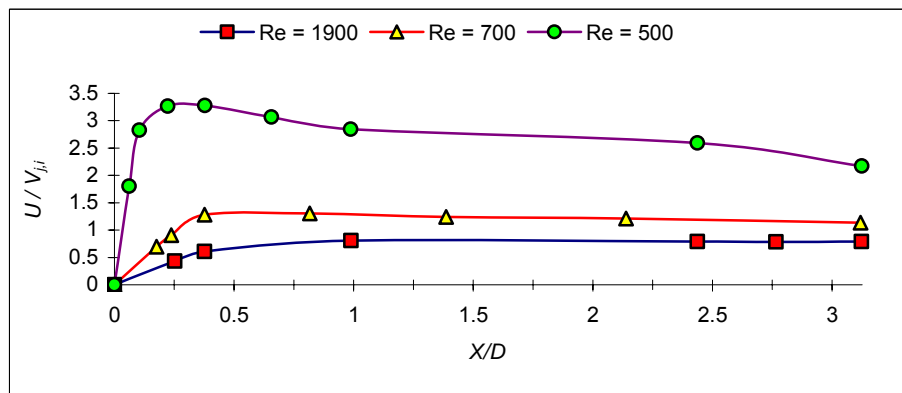


Figure 3.13. Non-dimensional U velocity for different Reynolds number.

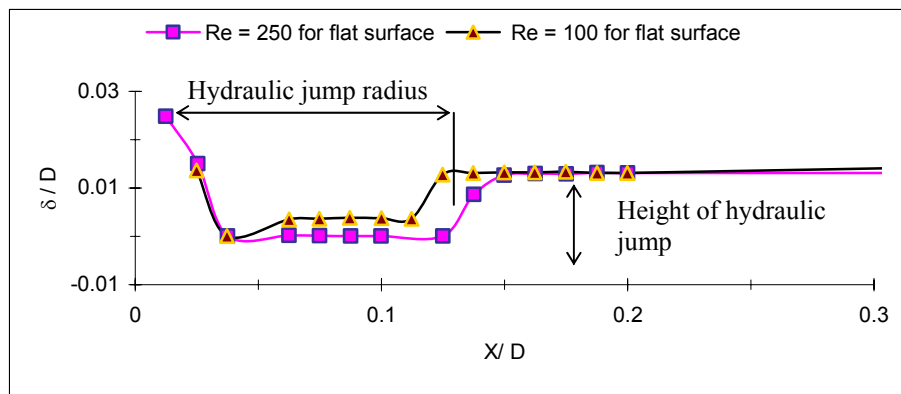


Figure 3.14. Hydraulic jumps at different Reynolds numbers of 250 and 100.

3.4.2 Effect of Nozzle to Plate Spacing, S (Case study 2)

In Figures 3.15 and 3.16, the free jet impingement and the wall jet regions are shown for non-dimensional nozzle to plate spacing of $S/D = 1.25, 2.5, 5$ and 12.5 for $Re = 1900$ for the grid geometry and velocity field, respectively. In Figure 3.17, the non-dimensional velocity parallel to the impingement surface at different nozzle to plate spacing is given. For $S/D = 12.5$, the velocity after passing the impingement region reaches a maximum value at of $U/V_j = 1.0$ at $X/D = 0.8$. After $X/D = 0.8$, the velocity ratio shows fluctuations at this S/D , but not for other S/D values. For S/D of $5, 2.5$ and 1.25 , the effect of S/D on the non-dimensional horizontal velocity is small.

The flow transition from the stagnation region to the wall jet region occurs starting from the edge of the stagnation region where $X/D = 0.25$. This transition region extends up to $X/D = 0.5$. The wall jet region as shown in Figure 3.17 occurs after the transition region where X/D is more than 0.5 . The transition and wall jet regions are sensitive to the jet to plate spacing due to the shear stress along the wall in the horizontal direction.

In Figure 3.18, the non-dimensional velocity in the y direction is shown within the free jet. It can be seen from this figure that the maximum non-dimensional

velocity of 1.5 occurred at $S/D = 12.5$. Past impingement, the non-dimensional y velocity is high, where a large streamwise flow velocity gradient exists.

In Figure 3.19, the distribution of the wall shear stress is shown at different S/D . It can be seen that the shear stress sharply increases with S/D . It attains a peak at around $X = 0.05$ m and then drops rapidly.

The free jet approaching the impingement region and wall jet regions are shown in Figure 3.20 at different jet nozzle to plate spacing. In Figure 3.21, the velocity field within the wall jet region is illustrated further at $Re = 1900$ for $S/D = 1.25$ to 12.5. The flow visualization for jet nozzle plate to spacing S/D of 5 and 1.25 at jet impingement and wall jet regions are shown respectively in Figures 3.22 and 3.23. The free jet region extends after 0.02s when $S/D = 12.5$, although this region extend after 0.01s when $S/D = 2.5$. The simulations indicate that for $S/D = 12.5$, the impingement occurs after 0.045s, and 0.018s for $S/D = 2$.

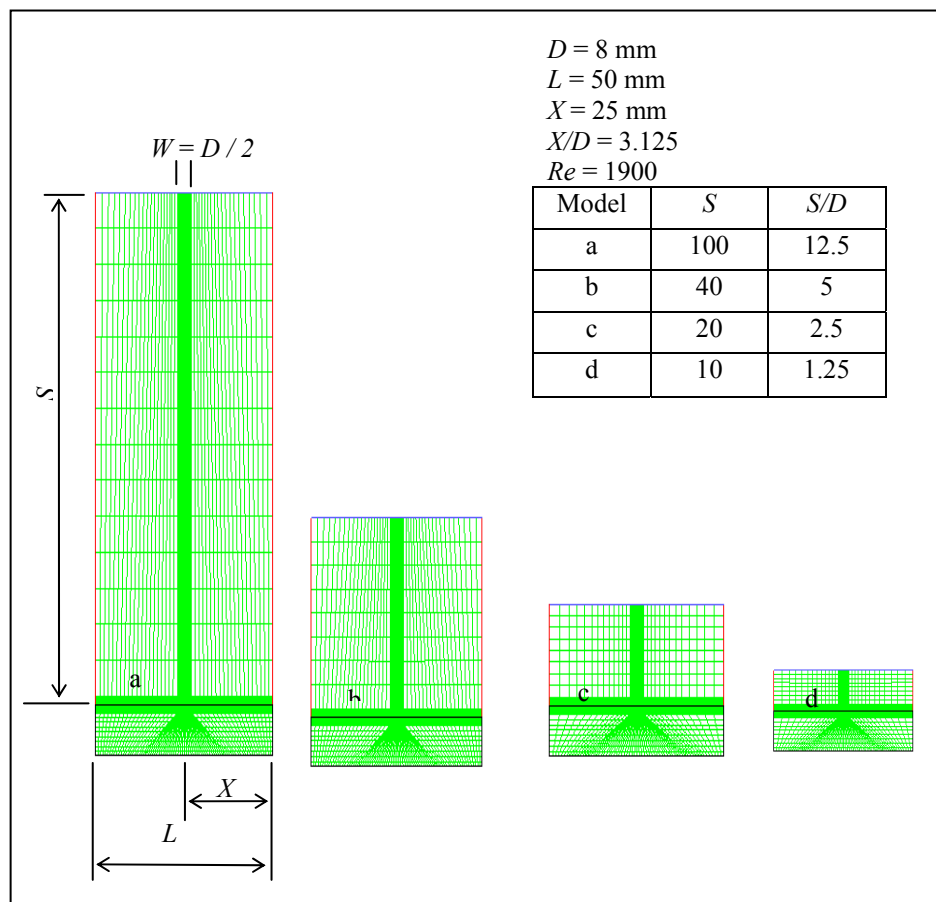


Figure 3.15. Geometry of impinging jet at different nozzle plate spacing.

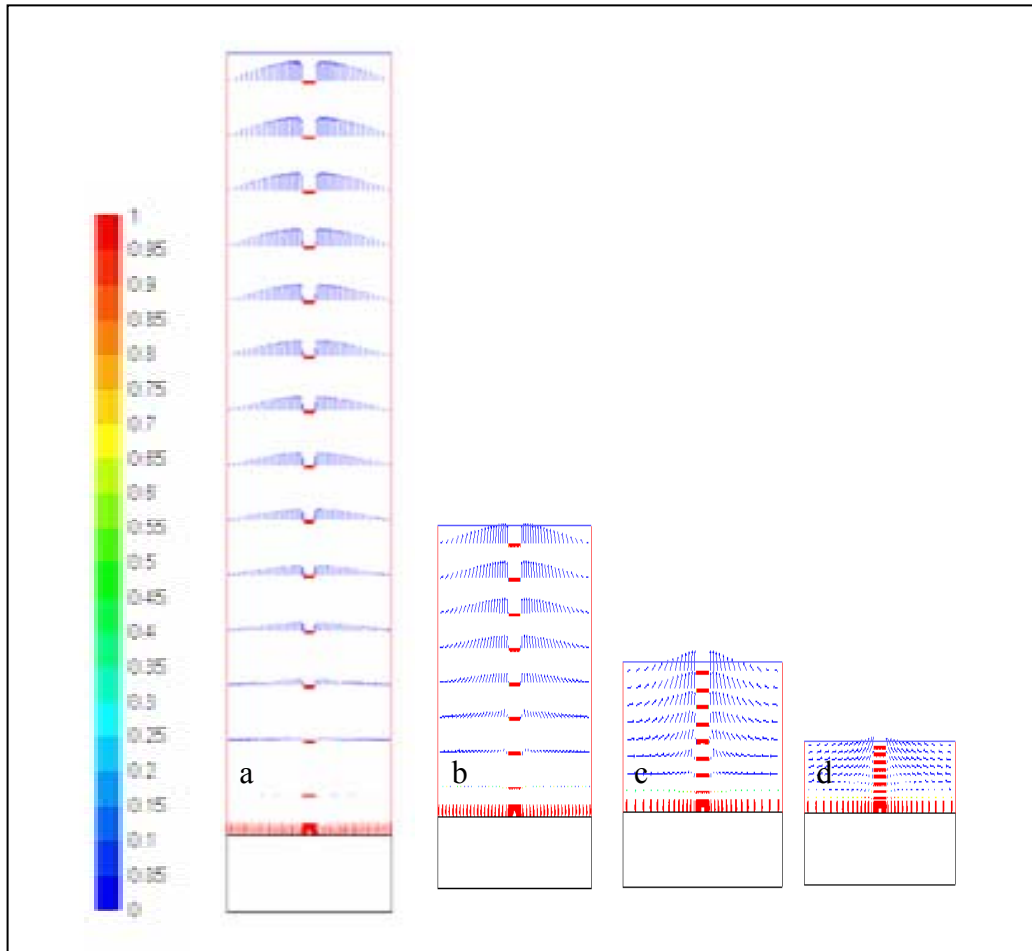


Figure 3.16. Velocity field for the three flow regions coloured by volume fraction (red is water and blue is air) for a Reynolds number of 1900, for S/D , a) = 12.5, b) = 5, c) = 2.5, and d) = 1.25. Mass flow rate for liquid is equal to 1.49 and for air is 0.15 kg /ms.

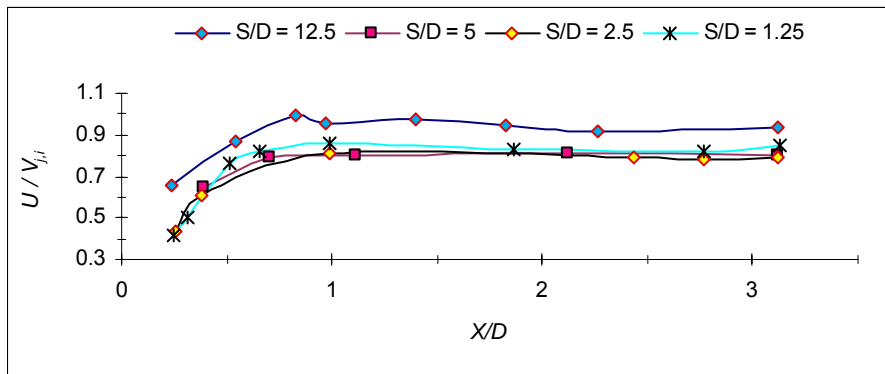


Figure 3.17. Non-dimensional horizontal velocity U at $Re = 1900$, with different jet nozzle to plate spacing.

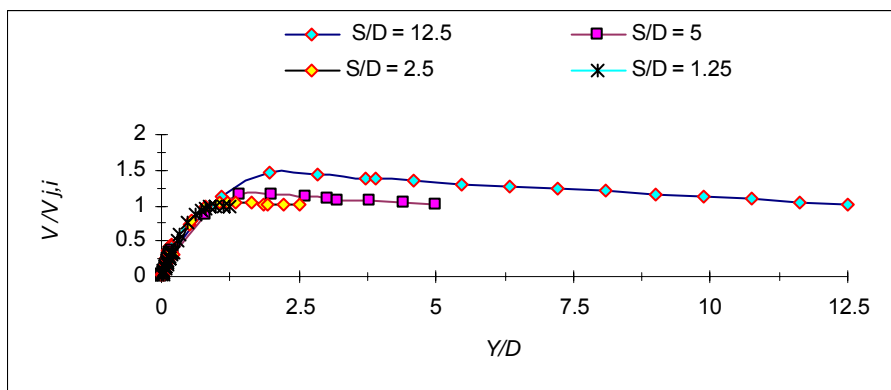


Figure 3.18. Non-dimensional y-direction velocity V at same Reynolds number of 1900, with different jet nozzle to plate spacing.

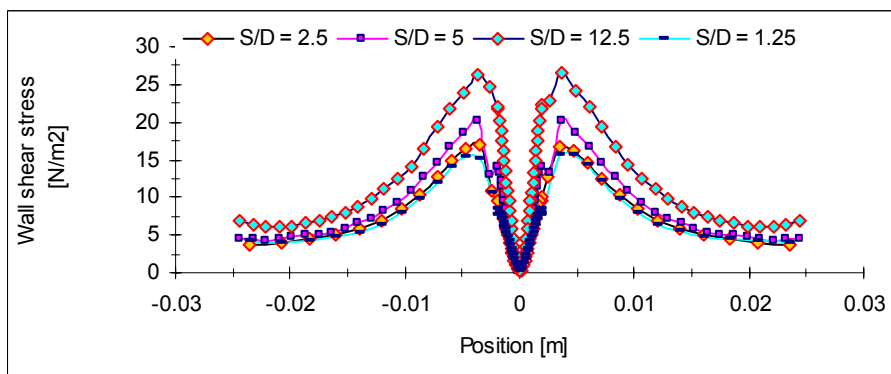


Figure 3.19. Distribution of wall shear stress at different nozzle to plate spacing S/D at $Re = 1900$.

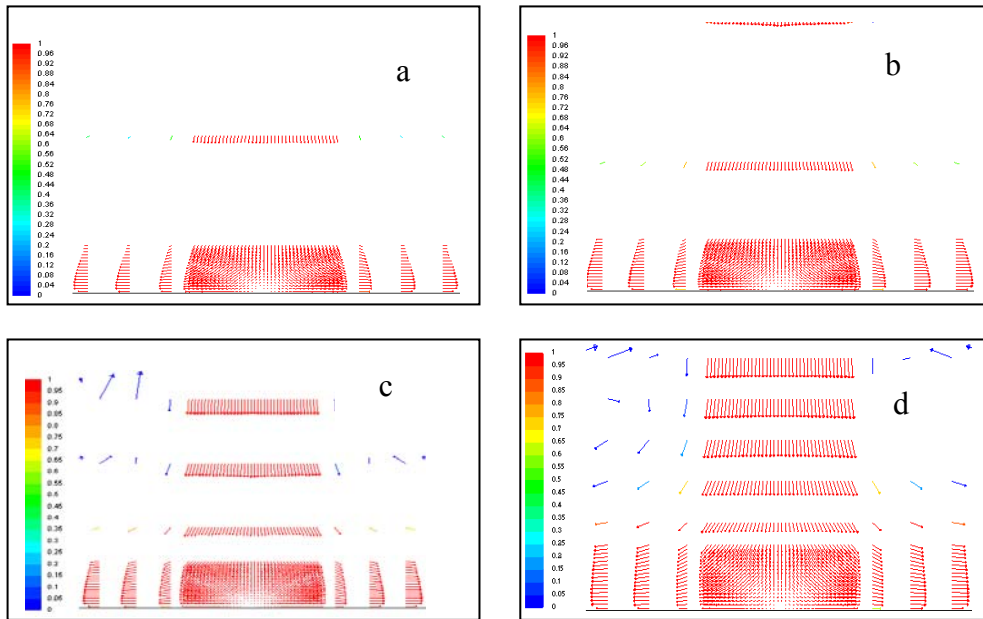


Figure 3.20. Velocity profile for impingement region for $Re = 1900$, slot jet $W = 4$ mm, $D = 8$ mm at different jet nozzle plate spacing, S/D . (a) $S/D = 12.5$, (b) $S/D = 5$, (c) $S/D = 2.5$, and (d) $S/D = 1$.

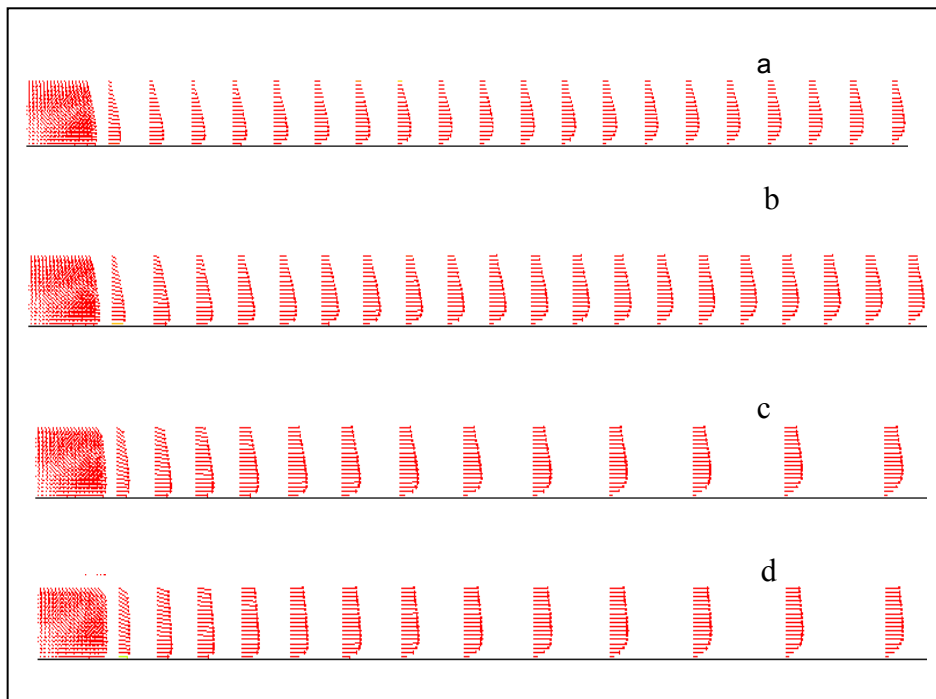


Figure 3.21. Velocity field in stagnation and wall flow regions for same Reynolds number of 1900, slot jet $W = 4$ mm, $D = 8$ mm and $S/D = 12.5, 5, 2.5$ and 1.25 for (a), (b), (c), and for (d) respectively.

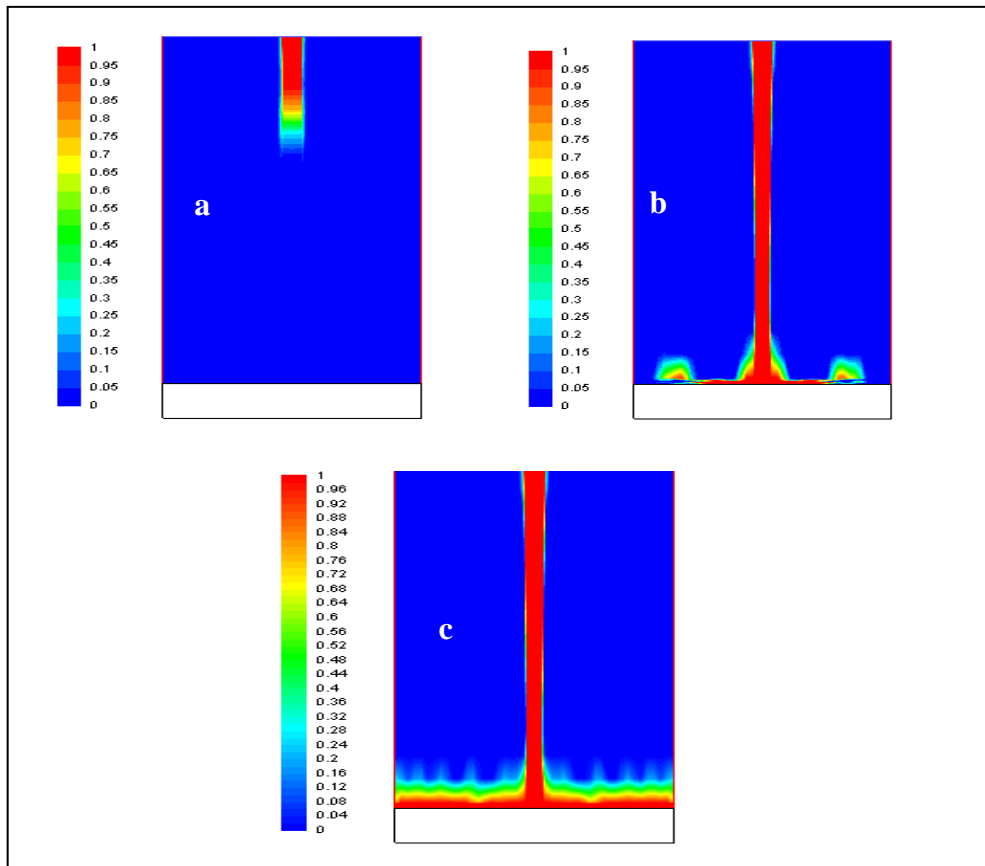


Figure 3.22. Flow visualization of 1900 Re, $S/D = 5$. (a) Free jet region at 0.02 s, (b) impingement region at 0.045 s and (c) wall jet region at quasi steady state.

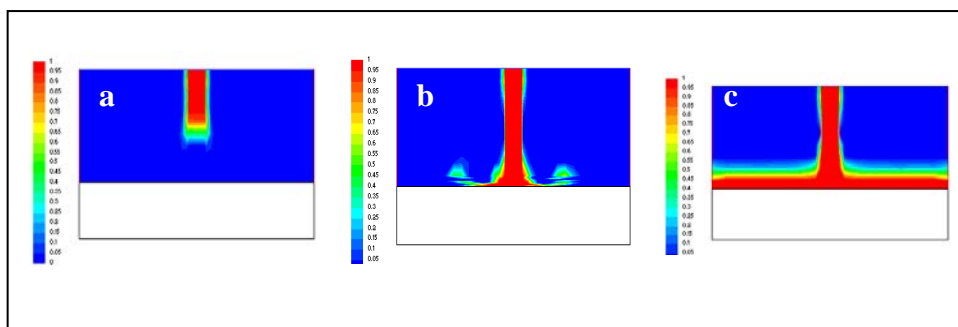


Figure 3.23. Flow visualization of 1900 Re and $S/D = 1.25$. (a) Free jet region at 0.01 s, (b) impingement region at 0.018 s and (c) wall jet region at quasi steady state.

3.4.3 Effect of Nozzle Width, W (Case study 3)

The effect of different jet nozzle width is investigated in this section. In Figure 3.24, the different nozzle widths are shown. At $Re = 1800$, nozzle to plate spacing $S = 100$ mm, plate length $L = 50$ mm, two nozzle widths of $W = 4$ mm and 2 mm are studied

The velocity vectors of the impingement and the wall jet regions are shown in Figure 3.25. It can be seen from this figure that the stagnation region at nozzle width of 4 mm is larger than in 2 mm, as expected.

In Figures 3.26 and 3.27, the flow visualization for all regions is shown for nozzle widths of 4 mm and 2 mm, respectively. Decreasing the jet width increases the flow velocities at the free, impinging and the wall jet regions as shown in Figures 3.28 and 3.29, again as expected. As shown in Figure 3.30, the liquid film thickness at the wall region for the wider jet nozzle has been found to exceed that with the smaller jet nozzle. This result agrees with Watson (1964) and Baonga *et al.* (2006).

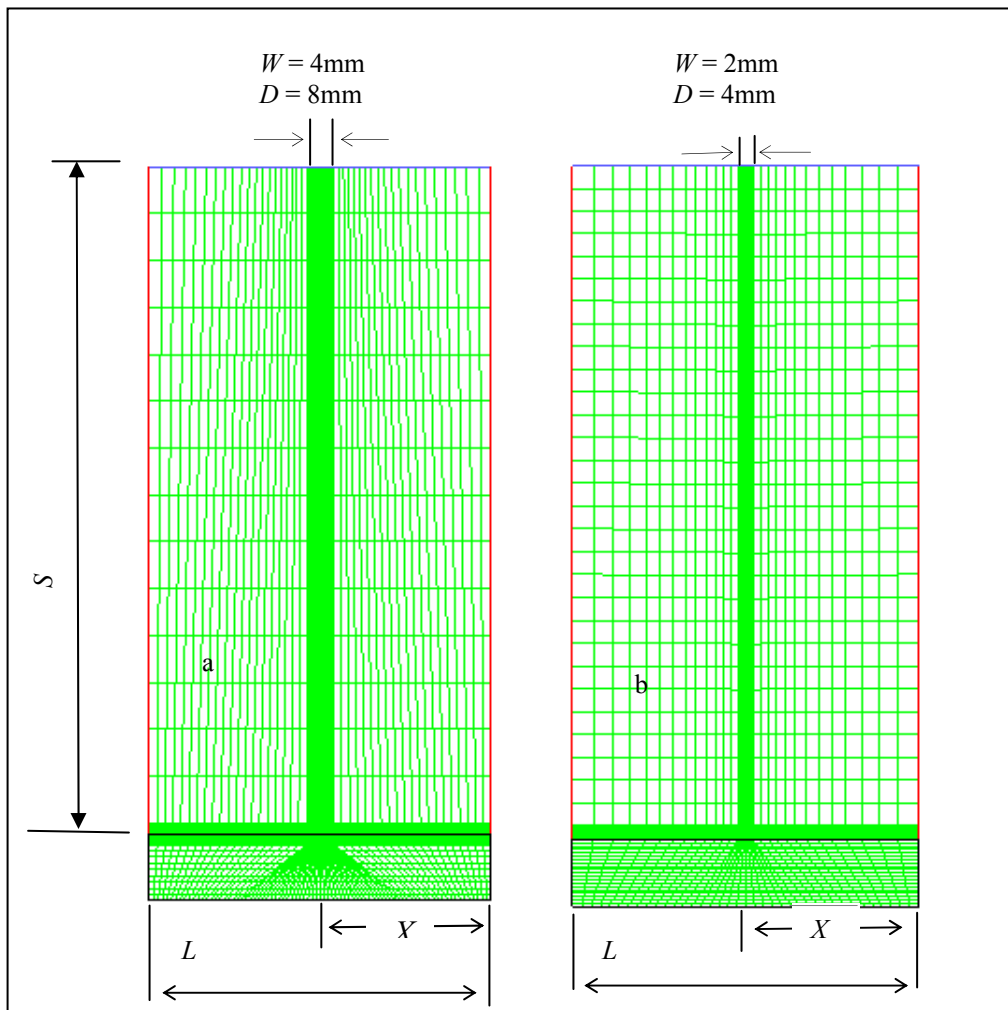


Figure 3.24. Case study 3: Effect of jet nozzle width with the same $S = 100$ mm, plate length $L = 50$ mm and $Re = 1800$. (a) jet nozzle width $W = 4$ mm and (b) $W = 2$ mm.

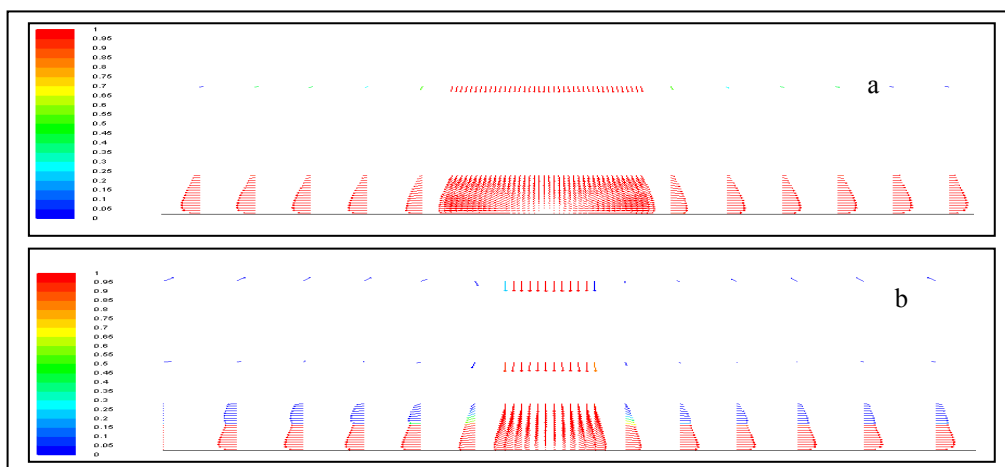


Figure 3.25. Velocity profile colored by volume fraction (red is liquid) at 1800 Re. (a) $W = 4$ mm and (b) $W = 2$ mm.

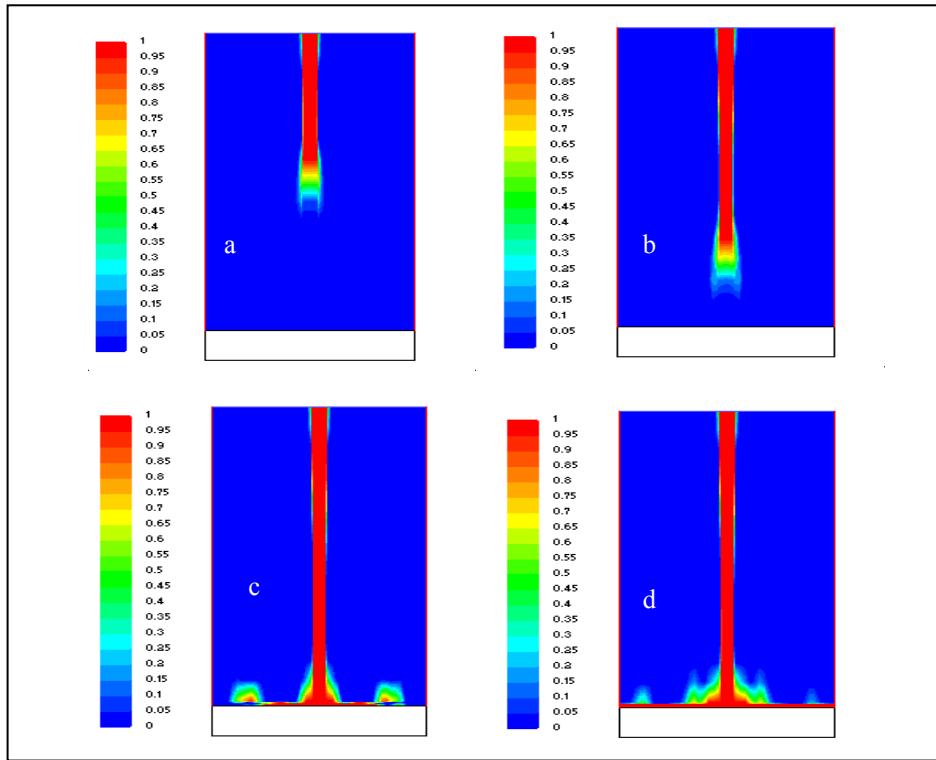


Figure 3.26. Flow visualization of 1800 Re, $S = 100$ mm and $W = 4$ mm. (a Free jet region at time of 0.04 s, (b at 0.06 s, (c Impingement region at 0.09 s and (d wall jet region at quasi steady state.

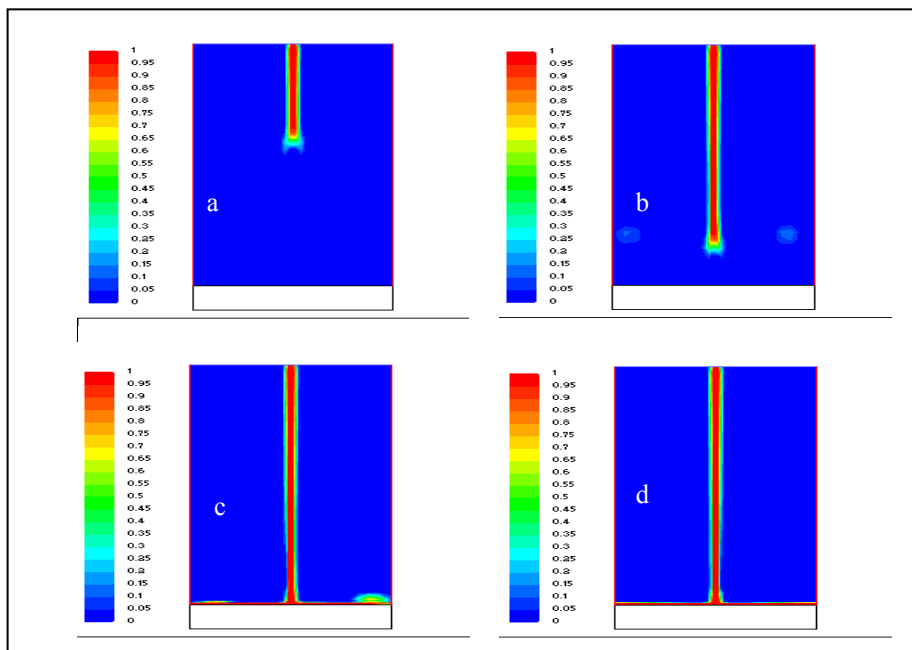


Figure 3.27. Flow visualization of $Re = 1800$, $S = 100$ mm and $W = 2$ mm. (a Free jet region at time of 0.02 s, (b at 0.04 s, (c after impingement region at 0.06s and (d wall jet region at quasi steady state.

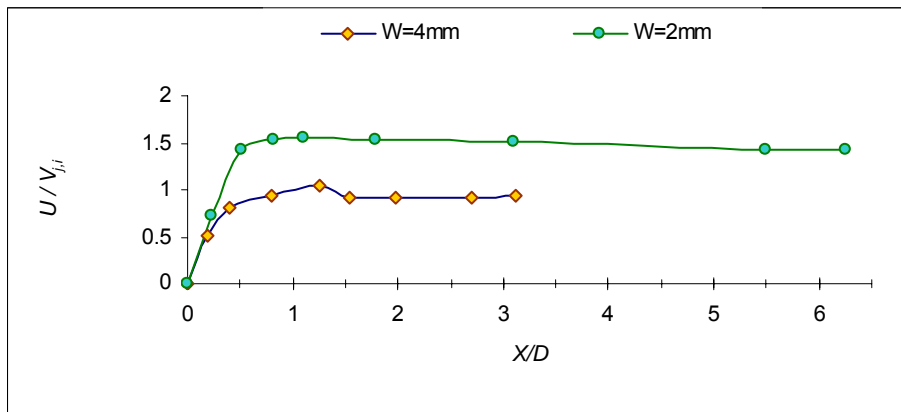


Figure 3.28. Non-dimensional velocity in the x-direction at the impinging and wall jet regions.

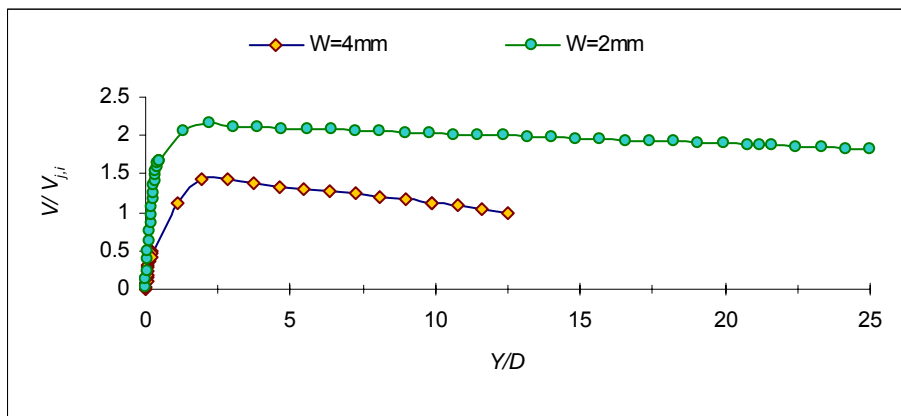


Figure 3.29. Non-dimensional velocity in the y-direction at the free and impinging regions.

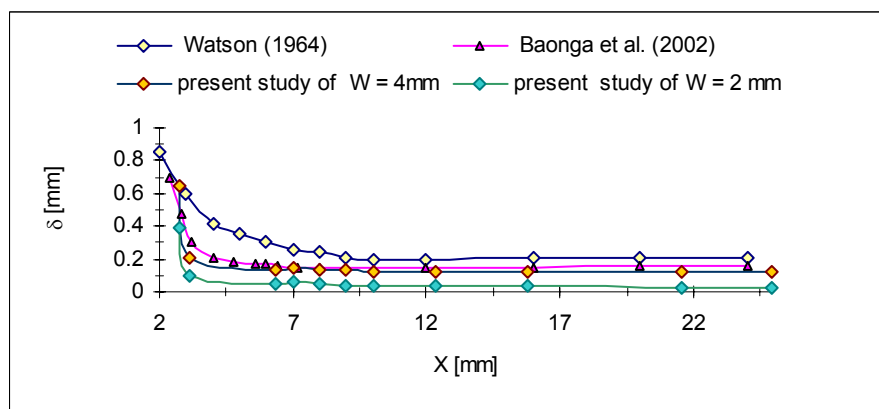


Figure 3.30. Water film thickness at the wall jet region for different nozzle widths compared with literatures values at Re = 1800.

3.4.4 Effect of Surface Configuration (Case study 4)

As mentioned previously, the flow field results presented in this chapter form the base of the flow visualization and heat transfer results presented in Chapter 4 and 5 respectively. The configuration of the target surface is a significant factor in this respect.

A flat and curved surfaces have been studied using the same nozzle width of $W = 4\text{mm}$, nozzle to plate spacing $S/D = 5$ and Reynolds number of 250. Three curved arc surfaces have been examined for 0.1 m, 0.05 m and 0.01 m diameters.

It can be seen in Figure 3.31 that water film thicknesses are similar for the three arcs and the flat surfaces at the impinging area. This result is because of the same fluid velocity for both cases, so the impact of the flow on the stagnation area is similar.

In Figure 3.32 and 3.33 the flow visualization at the free and impinging regions for flat and curved surfaces are shown, respectively. It can be seen from these two figures that the flow field at all regions is similar. This result can be explained because of the nozzle to plate spacing, and the width of the nozzle, Reynolds number and the effect of the gravity all being the same in both cases. Thus, the flow behaves in an identical manner for both cases.

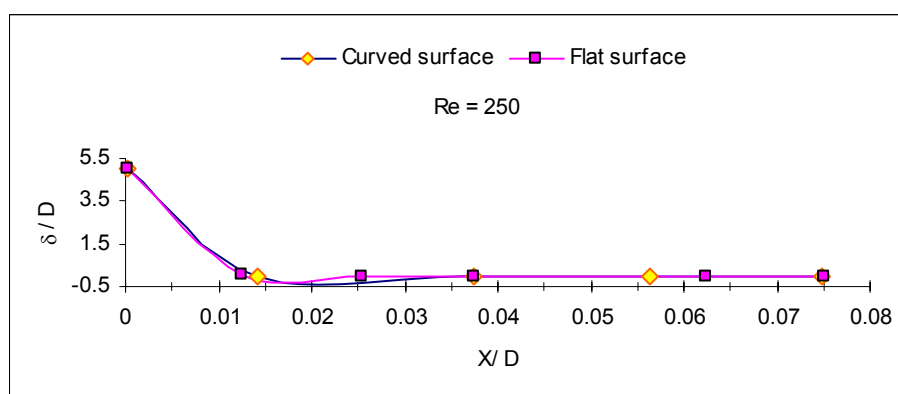


Figure 3.31. Non-dimensional water film thickness at the impinging region for the flat and curved surfaces at $Re = 250$.

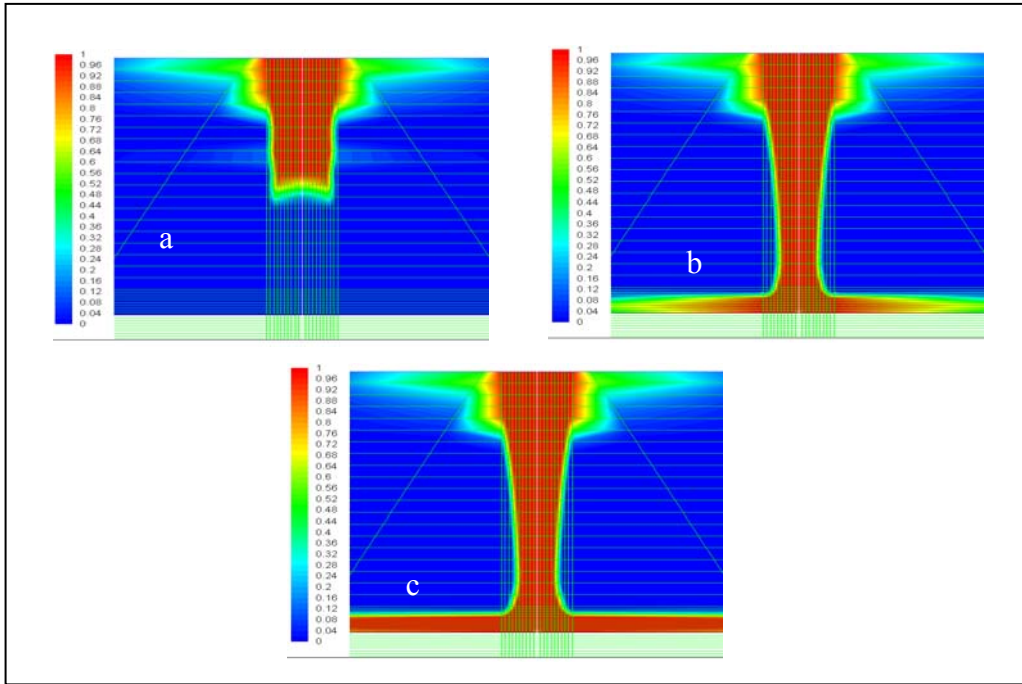


Figure 3.32. Flow visualization (water is red and air is blue) over a flat surface. (a) for jet approaching the surface at 0.15 s, (b) Impinging flow at 0.3 s and (c) at quasi-steady.

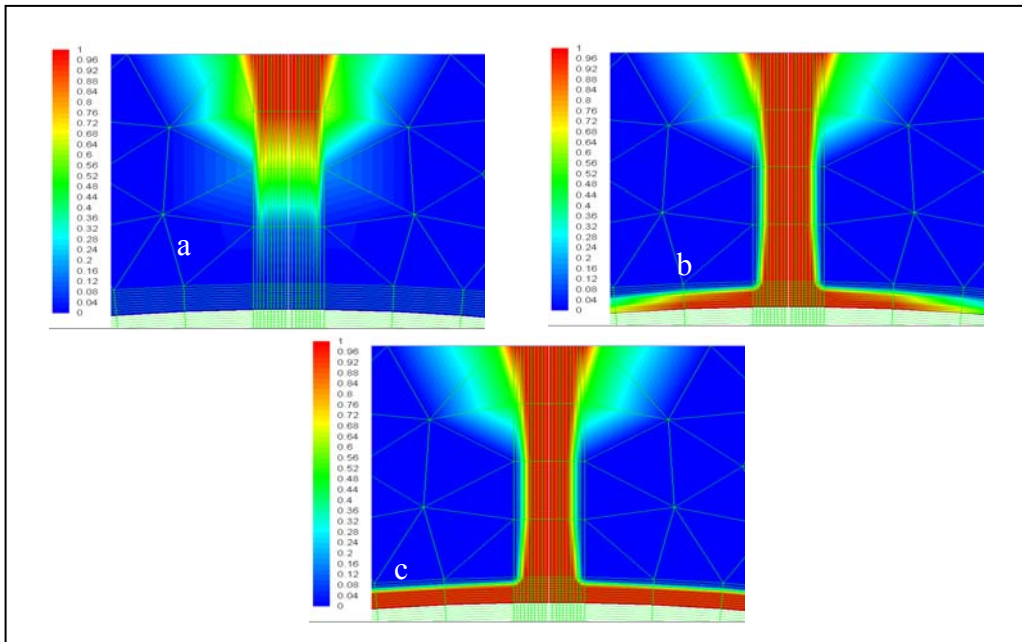


Figure 3.33. Flow visualization (water is red and air is blue) over a curved surface. (a) for jet approaching the surface at 0.15 s, (b) Impinging flow at 0.3 s and (c) at quasi-steady.

3.5 Heat Transfer Characterization of Liquid Jets

The Nusselt number is a dimensionless heat transfer coefficient. The heat transfer coefficient is a relationship between the heat flux and the temperature difference between the target surface and the liquid. The heat transfer coefficient has a complex dependence on many variables, such as the fluid properties and the flow velocity. For a single nozzle, the corresponding heat transfer correlations are expected to be of the form

$$\overline{Nu} = f(Re, Pr, X/D_h, S/D_h) \quad (3.12)$$

where \overline{Nu} is the average Nusselt number, Re is the Reynolds number, Pr is Prandtl number, X is the radial distance, D_h is the hydraulic diameter of the nozzle and S is the height of the nozzle.

$$D_h = D \quad (\text{Round nozzle})$$

$$D_h = 2W \quad (\text{Slot nozzle})$$

For laminar flow, Incropera and DeWitt (1990) used the following expression for the local Nusselt number, Nu_x and the average Nusselt number, \overline{Nu} .

$$Nu_x = 0.332 Re^{-1/2} Pr^{1/3} \quad (3.13)$$

$$\overline{Nu} = 0.664 Re^{-1/2} Pr^{1/3} \quad (3.14)$$

Martin (1977) recommends the following correlation for a single round nozzle:

$$\frac{\overline{Nu}}{Pr^{0.42}} = G\left(\frac{X}{D}, \frac{S}{D}\right) F_a(Re) \quad (3.15)$$

where

$$F_a = 2 Re^{1/2} (1 + 0.005 Re^{0.55})^{1/2} \quad (3.16)$$

and

$$G = \frac{D}{x} \frac{1 - 1.1(D/x)}{1 + 0.1(S/D - 6)D/x} \quad (3.17)$$

or, replacing D/x by $2 Ara^{1/2}$

where Ara is the nozzle area ratio

$$G = 2Ara^{1/2} \frac{1 - 2.2Ara^{1/2}}{1 + 0.2(S/D - 6)Ara^{1/2}} \quad (3.18)$$

Martin (1977) has also provided correlations for a single slot nozzle. These equations are,

$$\frac{\overline{Nu}}{Pr^{0.42}} = \frac{3.06}{x/W + S/W + 2.78} Re^m \quad (3.19)$$

where

$$m = 0.695 - \left[\left(\frac{x}{2W} \right) + \left(\frac{S}{2W} \right)^{1.33} + 3.06 \right]^{-1} \quad (3.20)$$

The numerical analysis of heat transfer is performed in order to study the influence of various Reynolds numbers. Nusselt number on the stagnation point (Nu_0) is determined from the local heat flux q , the average water temperature at the local surface (T_s) and the inlet jet water temperature (T_i):

$$Nu = \frac{hD}{k_l} = \frac{h2W}{k_l} \quad \text{for the present study} \quad (3.21)$$

where h is the local heat transfer coefficient, D is the hydraulic diameter and k_l is the thermal conductivity of the water. h is given as

$$h = \frac{q''}{(T_s - T_i)} \quad (3.22)$$

Various correlations of Nu have been summarized in Table 3.3 including that of the present numerical study, Chung *et al.* (2002) and Olsson (2004) and other previous experimental studies.

3.5.1 Effect of Reynolds Number, Re on Heat Transfer

In Figure 3.34 the variation is presented in the Nusselt number at the impinging and wall jet regions at Reynolds numbers of 700, and 1900 and S/D of 12.5. It is observed that with the increase in Re , the heat transfer at the impinging and wall jet regions increases. The increase is higher at the stagnation point compared to within the wall jet region at a given Re . For example, as the Reynolds number changes from 700 to 1900, the stagnation Nusselt number increases from 134 to 533 (increasing by 297%) as shown in Figure 3.34. Whereas at different horizontal locations corresponding to X/D (wall jet region), the increase in Nusselt number is from 33 to 60 (increasing by 81%) at $X/D = 3$ as shown in Figure 3.35, in this figure, the same data as in Figure 3.34 has been used but zoomed in. This result suggests that the stagnation point heat transfer is a stronger function of Reynolds number than that within the wall jet region. The reason is because the liquid flow velocity in the wall jet region decreases and the thin liquid layer becomes relatively uniform on the wetted surface.

Table 3.3. Analytical results of heat transfer for jet impingement.

Correspondence equations	Geometry	Flow type	References
$Nu = \frac{h D}{k_L} = \frac{h2W}{k_L}$	Impinging jet on flat and convex surfaces	Laminar	Present study, Chung <i>et al.</i> (2002) and Olsson (2004)
$Nu = 0.797 Re^{1/2} Pr^{0.4}$	Impinging jet (circular liquid jet)	Laminar, $Pr > 3$	Liu <i>et al.</i> (1991)
$Nu_x = 0.332 Re^{-1/2} Pr^{1/3}$	Flow on a flat plate	Laminar, local, $0.6 \leq Pr \leq 50$	Incropera and DeWitt (1990)
$\overline{Nu} = 0.664 Re^{-1/2} Pr^{1/3}$	Flow on a flat plate	Laminar, average, $0.6 \leq Pr \leq 50$	Incropera and DeWitt (1990)
$\overline{Nu} = C Re^m Pr^{1/3}$	Flow on a cylinder	Average, $0.4 < Re < 4 \times 10^5$, $Pr \geq 0.7$	Incropera and DeWitt (1990)
$\frac{\overline{Nu}}{Pr^{0.42}} = G\left(\frac{X}{D}, \frac{S}{D}\right) F_a(Re)$	Impinging jet (round nozzle)	Average, $2000 < Re < 4 \times 10^5$	Incropera and DeWitt (1990)
$\frac{\overline{Nu}}{Pr^{0.42}} = \frac{3.06}{X/W + S/W + 2.78} Re^m$	Impinging jet (slot nozzle)	Average, $3000 < 9 \times 10^4$	Incropera and DeWitt (1990)
$\overline{ejH} = \overline{ejm} = 2.06 Re^{-0.575}$	Packed bed of spheres	Average, $90 \leq Re \leq 4000$, $Pr \approx 0.7$	Incropera and DeWitt (1990)

\overline{ejH} is the turbulent diffusivity for heat transfer in m^2/s . \overline{ejm} is the turbulent diffusivity for momentum transfer in m^2/s .

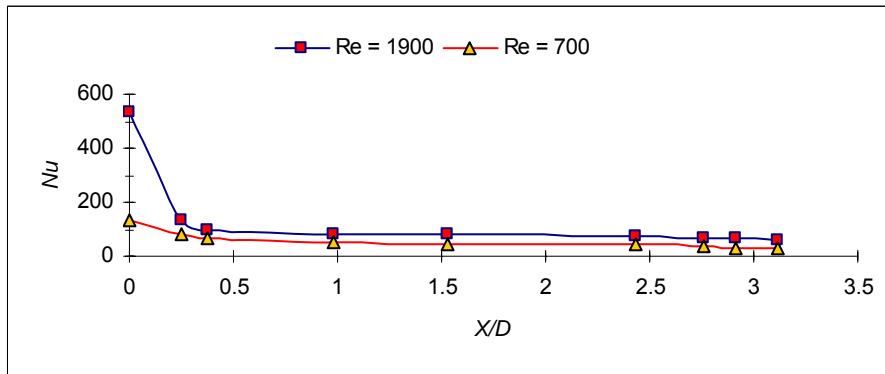


Figure 3.34. Local Nusselt number at free jet, impinging and wall jet regions for different Reynolds numbers at $S/D = 12.5$.

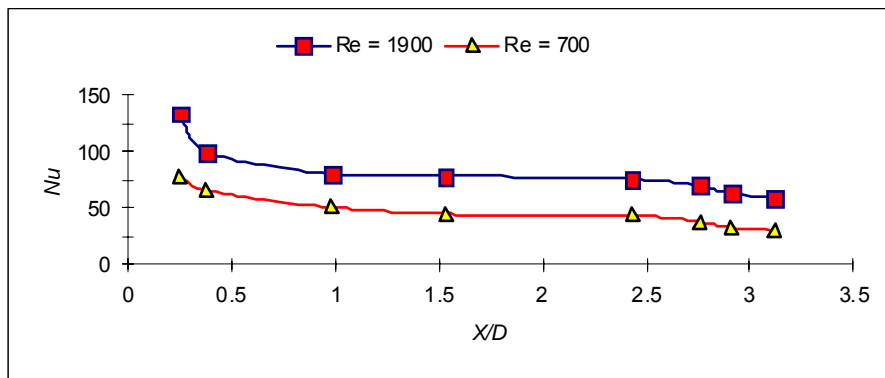


Figure 3.35. Local Nusselt number at wall jet region for different Reynolds numbers at $S/D = 12.5$. The same data as in Figure 3.34 but zoomed in.

In Figure 3.36, the stagnation Nusselt number is plotted at different Reynolds numbers at a nozzle to plate spacing of 12.5 and compared with that of Wheeler and Neti (1999) at $Re = 500$. In Figure 3.37, this comparison of the stagnation Nusselt number at $Re = 500$ is repeated to emphasize the agreement. It is observed that with the increase in Re , the heat transfer at the stagnation region increases at a given nozzle to plate spacing. This result is due to the cooling stagnation area's being larger at higher Reynolds number as shown in Figures 3.38 and 3.39.

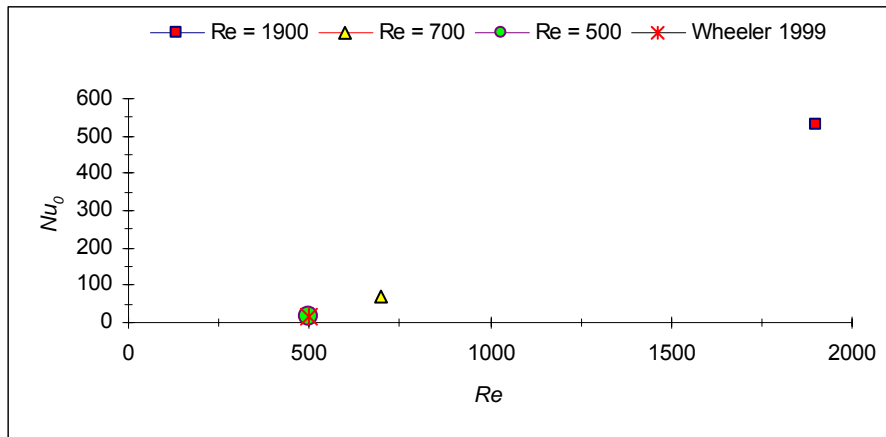


Figure 3.36. Stagnation Nusselt number for different Reynolds numbers at nozzle plate spacing S/D of 12.5.

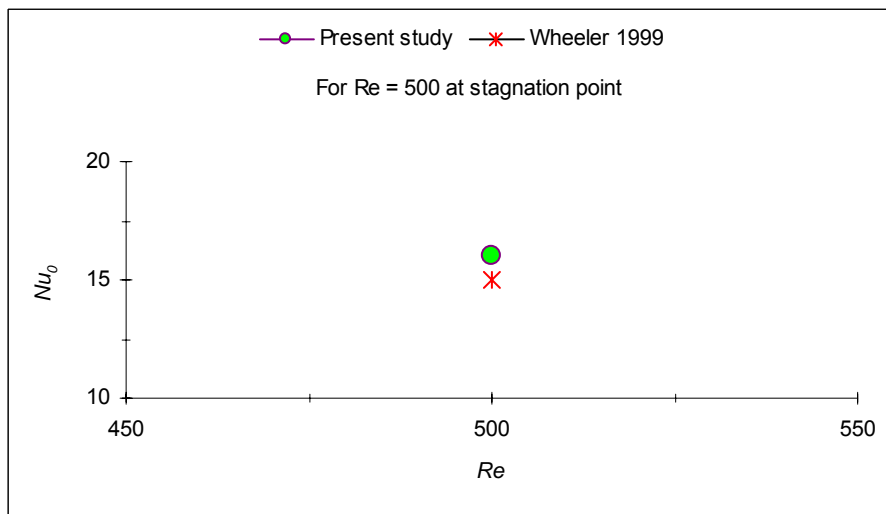


Figure 3.37. Stagnation Nusselt number for Re of 500 compared with literature at S/D of 12.5.

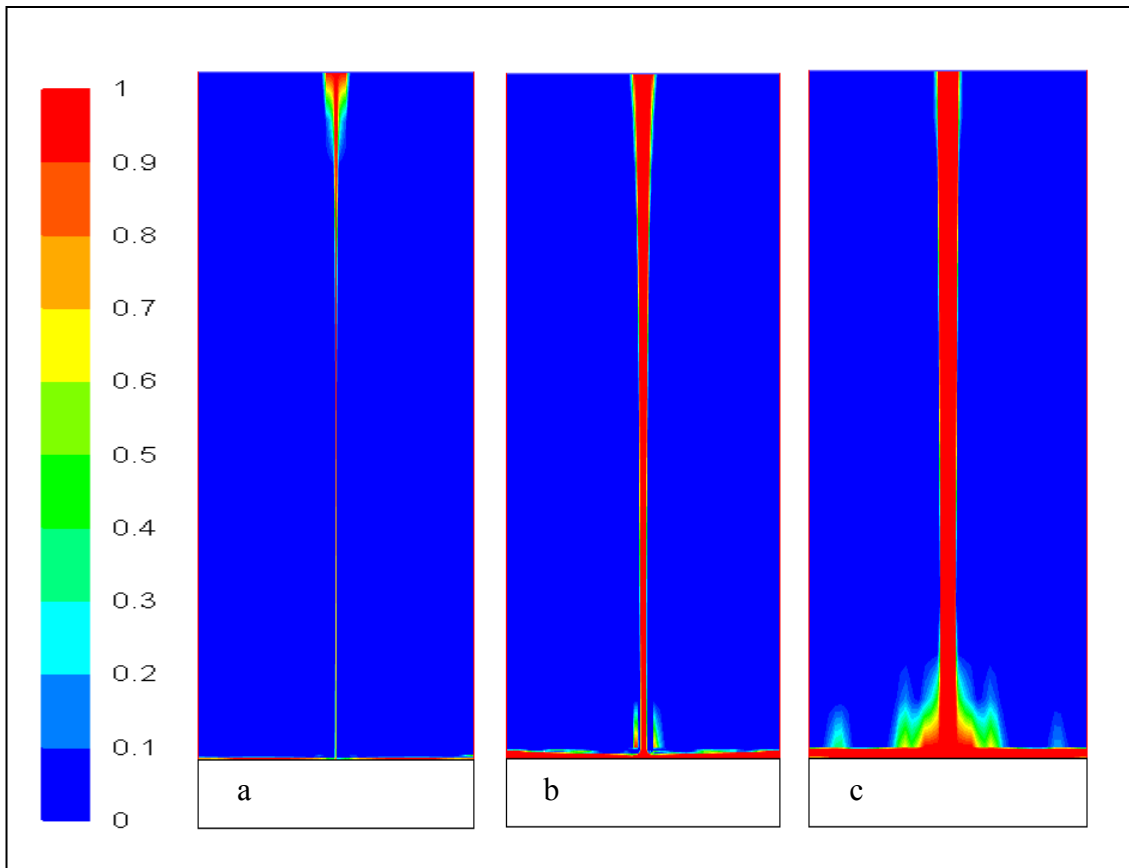


Figure 3.38. Flow field of liquid jet over heated surface for free, stagnation and wall jet regions coloured by volume fraction (red signifies water and blue signifies air) at $S/D = 12.5$ and Re of a) = 500, b) = 700, c) = 1900.

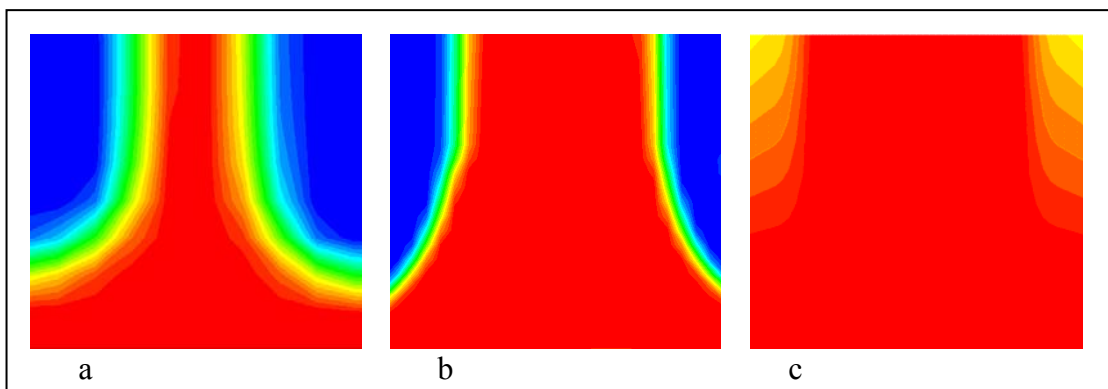


Figure 3.39. Zooming in the stagnation area coloured by volume fraction at $S/D = 12.5$ and Re of a) = 500, b) = 700, c) = 1900.

3.5.2 Effect of Nozzle to Plate Spacing S/D on Heat Transfer

In Figure 3.40, the variation of the stagnation Nusselt number, Nu_0 is shown at $Re = 1900$ with different nozzle to plate distances of $S = 10, 20, 40,$ and 100 mm, corresponding to $S/D = 1.25, 2.5, 5,$ and $12.5,$ respectively. As mentioned previously the maximum heat transfer is observed at the stagnation point, and heat transfer decreases in the horizontal direction for all nozzles to plate spacing values. The highest Nu_0 is for $S/D = 1.25$ and it decreases with increasing S/D . The reason for this variation with S/D is that the acceleration of the fluid through the small distance between the target plate and nozzle exit is more effective than with a longer distance. These results agree with those of Nakod *et al.* (2008). The present results disagree with those of Gardon and Akfirat (1965) who found that higher heat transfer occurs with higher nozzle to plate spacing. Their explanation is that the jet shear layer at the centre of the high nozzle to plate spacing gave higher heat transfer coefficient. The present results suggest that the Nusselt number decreases in the wall jet region in a similar manner for all S/D . The drop in the value of the Nusselt number in this region is attributed to the decrease in fluid velocity over the plate because of the horizontal flow and excessive exchange of momentum of the wall jet with the surrounding air. The flow in the wall jet region can be divided into two parts. The first part is the inner layer where the effect of the wall surface is present, and the outer layer of interacting fluid. The maximum local horizontal velocity is between these two layers

In Figure 3.41, the variation of the stagnation Nusselt number with different nozzle to plate distances of $S/D = 1.25, 2.5, 5,$ and 12.5 at different Re of 1900, 1500, 1000, 700, 500, 375 and 250 is shown. The maximum heat transfer is observed at the highest Reynolds number and the lowest nozzle to plate spacing. It can be seen that the highest stagnation Nu is for $S/D = 1.25$ and it decreases with increasing S/D . Also, the highest stagnation Nu is for $Re = 1900$ and it decreases with decreasing Reynolds number.

The variation of stagnation Nusselt number with different Reynolds numbers and at different nozzle to plate spacing is presented further in Figure 3.42. The highest

stagnation Nusselt number is observed at the highest Reynolds number and at the lowest nozzle to plate spacing. As stated before the stagnation Nusselt number is maximum at the lowest nozzle to plate spacing, because the impinging cooling area at a lower nozzle to plate spacing is larger than in higher nozzle to plate spacing, as shown in Figures 3.43 and 3.44.

These results indicate that the heat transfer coefficient decreases monotonically with increasing distance from the jet nozzle. This conclusion is in agreement with Narayanan *et al.*(2004). The result also agrees with Bula *et al.*(2000) who indicate that increasing S/D decreases the heat transfer coefficient.

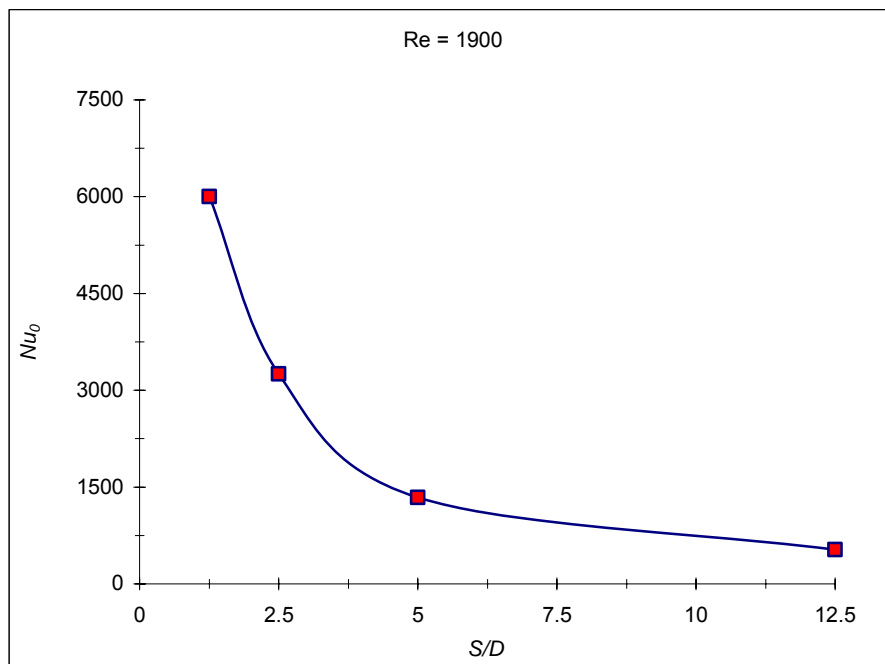


Figure 3.40. The stagnation Nusselt number for different jet nozzle to plate distances at $Re = 1900$.

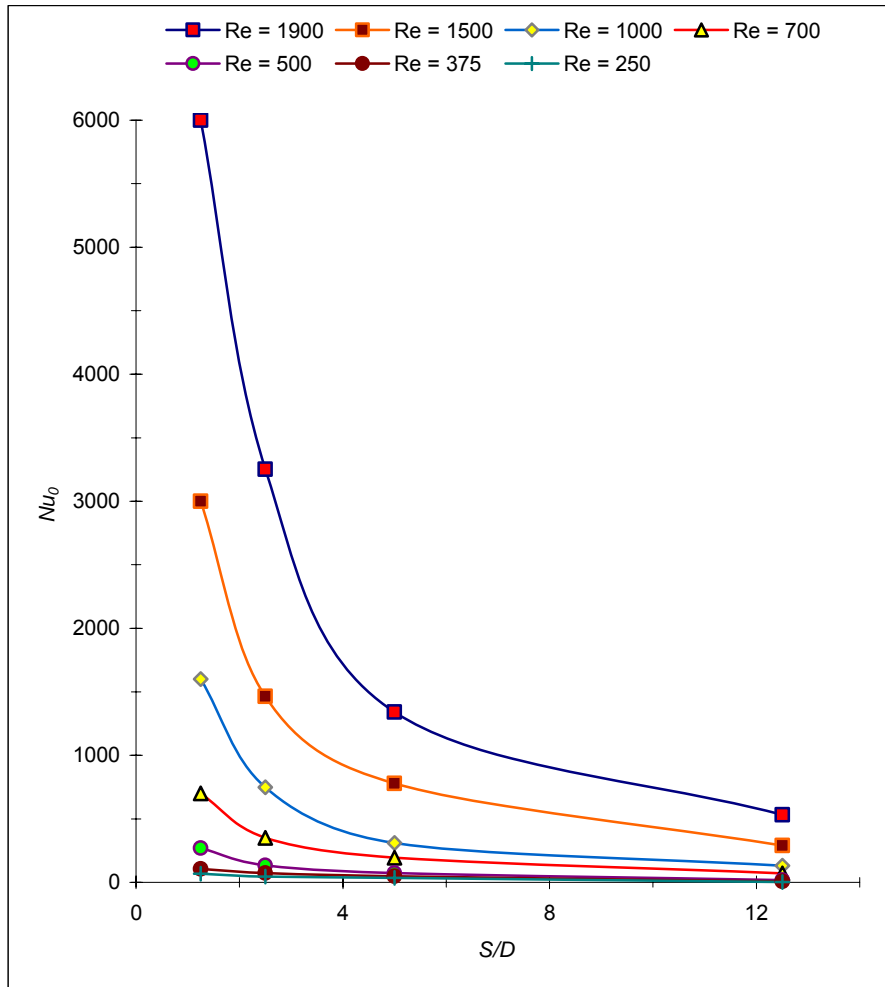


Figure 3.41. The stagnation Nusselt number for different jet nozzle to plate distances at different Re.

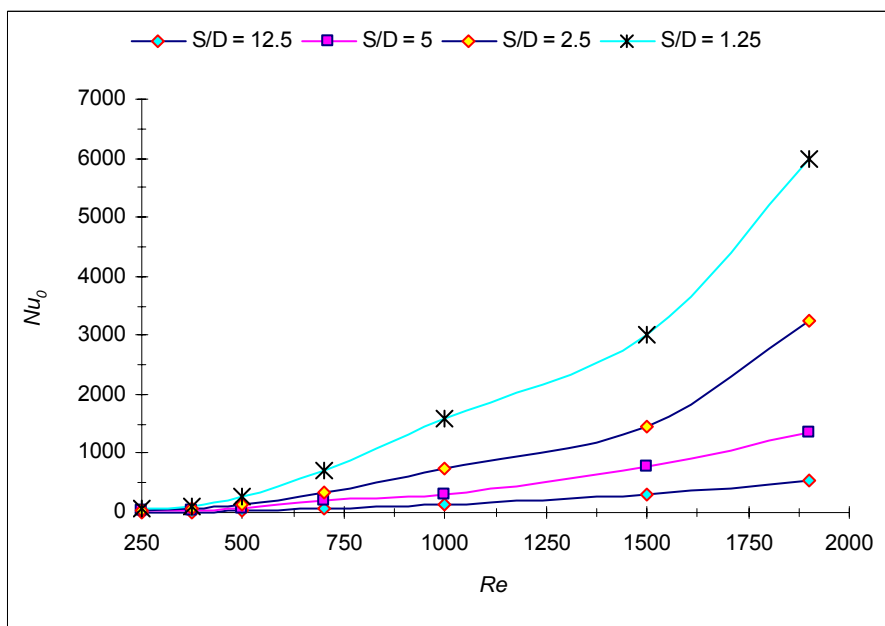


Figure 3.42. The stagnation Nusselt number variation with Reynolds number with different jet nozzle to plate spacing.

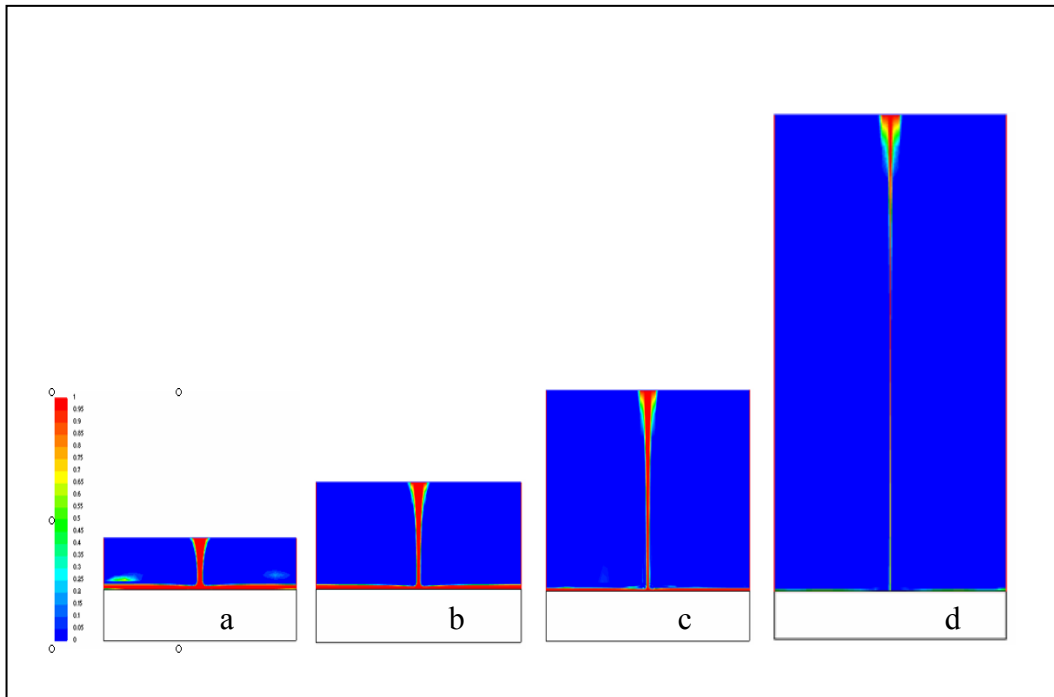


Figure 3.43. Effect of different nozzle to plate spacing on the stagnation cooling area at 1900 Reynolds number. a) $S/D= 1.25$, b) $S/D=2.5$, c) $S/D= 5$ and d) $S/D= 12.5$.

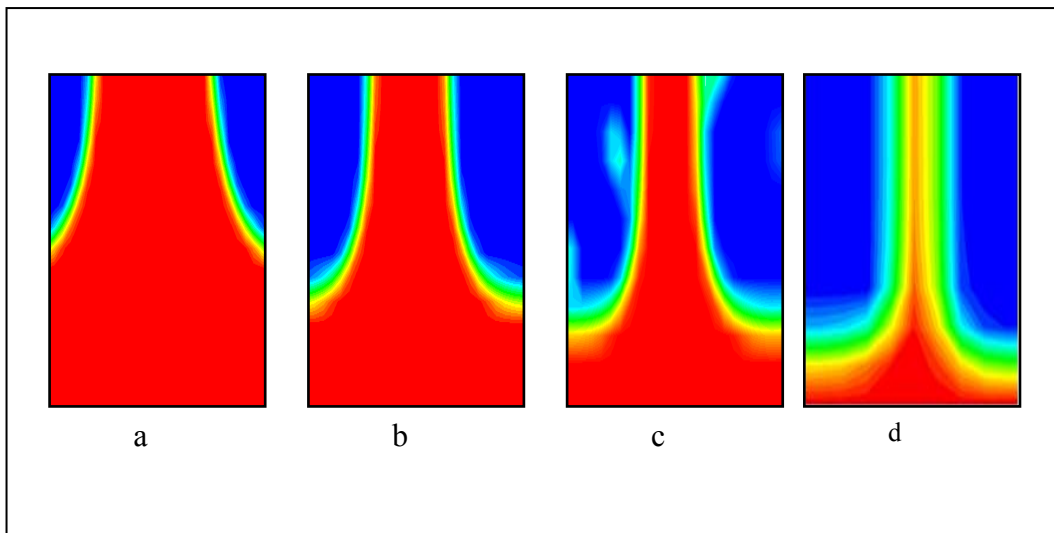


Figure 3.44. Zooming in on the stagnation cooling area at 1900 Reynolds number and different nozzle to plate spacing a) $S/D= 1.25$, b) $S/D=2.5$, c) $S/D= 5$ and d) $S/D= 12.5$.

3.5.3 Effect of Nozzle Width on Heat Transfer at Impinging and Wall Jet Regions

Results shown in Figure 3.45 confirm that for the same Reynolds number, Nusselt numbers with $W = 4$ mm are higher than those obtained with $W = 2$ mm. This result is due to the liquid film thickness increasing or the liquid layer depth becoming thicker with the larger nozzle width. The stagnation point with a larger nozzle width is longer than that with a smaller one. This increase leads to an increased heat transfer coefficient, because the heated surface is cooled more due to the increased liquid contact area. The dependence of the stagnation point Nusselt number on the nozzle diameter have been studied by different authors in the literature such as Stevens and Webb (1989), (1993), and Siba *et al.* (2003).

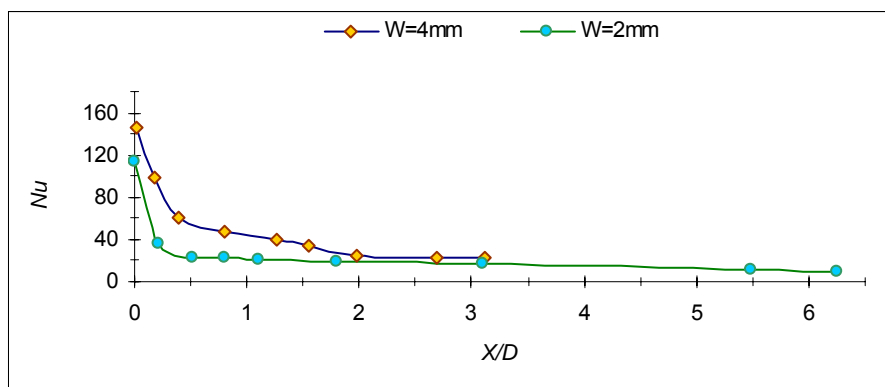


Figure 3.45. The influence of nozzle width on Nusselt number.

3.5.4 Effect of Surface Configuration on Heat Transfer

It can be seen from Figure 3.46, that the Nusselt number is higher in the impingement zone. The Nusselt number is same for the flat and curved surfaces. This result is because of the equal velocity and film thickness on both surfaces. Hence, it can be seen further from Figure 3.46 that there is no impact of the configuration of the target surface on heat transfer for the surfaces chosen here.

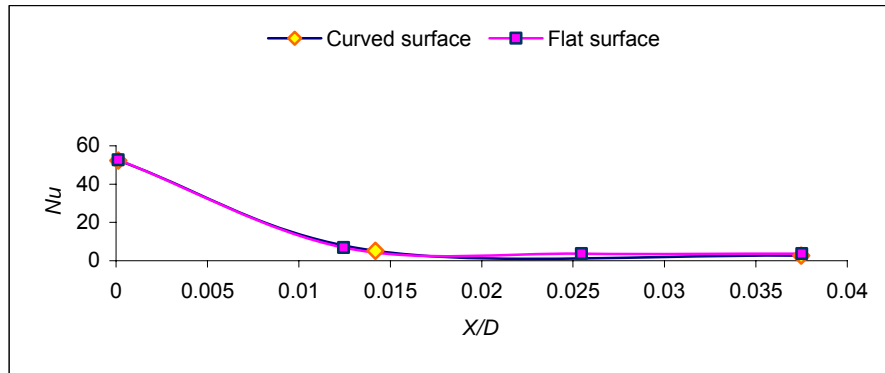


Figure 3.46. Local thermal boundary condition on the stagnation and wall regions for flat and curved surfaces at $Re = 250$.

3.6 Analysis of Heat Transfers Characteristics.

3.6.1 Heat Transfer at Stagnation Point ($X/D = 0$)

Heat transfer rates at the stagnation point can be analysed based on wall static pressure distribution. The previous results show that the stagnation point Nusselt number increases with decrease in S/D . This result may be due to the flow acceleration at lower S/D .

3.6.2 Heat Transfer in Stagnation Region ($0 < X/D < 0.25$)

The Nusselt numbers depend on the distance from the stagnation point in the stagnation region. The heat transfer coefficient decreases from the stagnation point till the edge of the stagnation region. This result may be because of the small increase in the boundary layer thickness in the radial direction.

3.6.3 Heat Transfer in Transition Region ($0.25 < X/D < 0.5$)

The flow from the impingement region to the wall jet region occurs from the edge of the stagnation region where $X/D = 0.3$. The transition region can be considered to extend up to $X/D = 1$ as shown previously in Figure 3.17. This region is sensitive to jet to plate spacing due to the shear stress along the wall in the radial direction. The shear stress increases sharply from lower S/D and it attains a peak

at around X/D of about 0.5 and then drops. The thickness of transition jet region is thicker for lower S/D , and hence, the heat transfer coefficients in this region are higher.

3.6.4 Heat Transfer in Wall Jet Region ($X/D > 1$)

The Nusselt number decreases in the wall jet region in as almost similar fashion for all S/D . Drops in the value of the Nusselt number in this region is attributed to the decrease in the velocities of the fluid over the plate because of radial flow and excessive exchange of momentum of the wall jet with the surrounding air. The flow in the wall jet region can be divided into two parts as mentioned previously.

3.7 Conclusion

In this chapter, the results of a numerical investigation are presented on the effect of the Reynolds number, nozzle to plate spacing, nozzle width and configuration of the heated target surface on the flow field and thermal characteristics of a liquid jet impinging on a heated surface. The liquid layer depth and velocity have been studied to evaluate the heat transfer coefficient.

The results indicate that Re has a significant effect on the flow field and heat transfer. The heat transfer rate in the stagnation and wall jet regions is enhanced with an increase in Re . Increasing the Reynolds number increases the diameter of the cooling zone around the stagnation point significantly and causes a decrease in temperature at the stagnation point. When the Reynolds number increases, the consequence is an increase in the velocity of the flow and an increase in the convective heat transfer which results in better surface cooling.

The following are the brief conclusions of this chapter:

- Three regions of free jet impingement surface are identified. These regions are:
 1. Stagnation region, where ($0 \leq X/D \leq 0.25$),
 2. Transition region, where ($0.25 < X/D < 0.5$),

3. Wall jet region, where ($X/D > 0.5$).

- The stagnation Nusselt numbers increase with a decrease in S/D . This result may be due to flow acceleration at lower S/D .
- The transition and wall jet regions are sensitive to jet to plate spacing due to the shear stress along the wall in the horizontal direction. The shear stress increases sharply from lower S/D . At all S/D , it attains a peak at around $X = 0.05$ mm and then drops.
- The heat transfer coefficient with a larger nozzle width is greater than that with a smaller nozzle. This result is because the heated surface is cooled more by the increased cooling area with a larger nozzle.
- There is no significant effect due to the configuration of the heated target surface on the flow field and heat transfer. This result is because the film thickness and the velocity are same for the two cases chosen here.

CHAPTER FOUR

FLOW VISUALIZATION AND FALLING FILM MODES

The objective of this chapter is to report experimental and numerical studies of the nature of the liquid film flowing over three cylinders, the axes of which are perpendicular to the flow direction. The flow field and heat transfer processes that occur under such conditions are generally calculated by means of empirical relationships amongst dimensionless groups.

This work forms part of an experimental and numerical framework in which to study the flow field using the power of computational fluid dynamics. A CFD code, FLUENT[®] has been used for 2D and 3D configurations. The primary objective of the present study is to use experimental and numerical predictions for developing better designs of systems that involve three-phase porous media such as hydrocoolers used to cool horticultural produce. Better hydrocooler designs will involve reduced amounts of energy and cooling water treating horticultural produce.

In this chapter, the behaviour of water falling over horizontal cylinders and the characterization of the flow patterns are reported. The effects of Reynolds number, cylinder diameters, the spatial placement and the vertical separation between the cylinders have been studied. Reynolds number is defined in terms of the liquid mass flow rate per unit length of cylinder divided by the dynamic viscosity. The Reynolds number range studied in this chapter is, 20 to 2000. The cylinder diameters are 0.1m, 0.05m, and 0.02m. The liquid medium is water. The use of a numerical tool has resulted in a detailed investigation of these variables, which has not been available in the literature previously.

In the following, an introduction is given first to flow patterns with the definitions of flow modes. Next, observations of the flow modes are described and the points of transition between flow modes are compared with those reported in the

literature. The last part of the chapter is on the effect of cylinder separation on the flow mode characteristics. Falling film over random, rectangular-pitch arrangements and ten horizontal cylinders are presented in detail in Appendix B. An overview of the experimental and numerical scope is outlined in Table 4.1

Table 4.1. Overview of the experimental and numerical scope.

Experiment	Numerical
Geometry	Geometry
Cylinder diameter 0.1 m, 0.05 m, and 0.02m.	Cylinder diameter 0.1 m, 0.05m, and 0.02 m.
Cylinder separation	Cylinder separation
0.03 m, 0.01m and 0.001 m.	0.05 m, 0.03 m, 0.01 m and 0.001 m for 2D.
Measure	Determine
Mode characteristics of principal modes of droplet, jet, and sheet mode in addition to the intermediate modes. Frequency of droplet detachment for middle cylinder Effect of direction of film flow rate on frequency of small droplet detachment for middle cylinder. Dimensionless wavelength.	Mode characteristics of principal modes droplet, jet, and sheet mode for 2D and 3D.

4.1 Introduction

In general, a high rate of heat transfer exists between falling films and horizontal cylinders. For this reason, falling film heat transfer is widely used in the chemical and food process industries and in refrigeration equipment where high rates of heat transfer are important.

Three flow modes can be observed when liquid films flow over horizontal cylinders, namely:

1. Droplet mode,
2. Jet or column mode and
3. Sheet mode.

The flow patterns observed in falling films described by Mitrovic (1986) are illustrated in Figure 4.1. Armbruster and Mitrovic (1994) predicted transitions between flow modes. Additional work on the flow mode is given by Hu and Jacobi (1996) for the flow characteristics and mode transitions for wide ranges of flow rate and fluid properties. They proposed a flow mode transition map of film Reynolds number against the Galileo number (Ga).

$$Re = a(Ga)^b \quad (4.1)$$

where a and b are empirical constants and Galileo number is a dimensionless number named after Italian scientist Galileo Galilei (1564 – 1642), it defined as proportional to gravity forces divided by viscous forces. Galileo number is used in viscous flow and thermal expansion calculations (Wikipedia® 2009).

Hu and Jacobi (1996) defined the transitions between the three modes of droplet, jet and sheet with two mixed mode zones, namely, droplet–jet and jet–sheet. Their corresponding four flow transition expressions between these five zones are given below for plain tubes. The symbol \Leftrightarrow means the transition is valid in either direction.

$$\text{Droplet} \Leftrightarrow \text{Droplet–Jet: } Re = 0.074 Ga^{0.302} \quad (4.2)$$

$$\text{Droplet–Jet} \Leftrightarrow \text{Jet: } Re = 0.096 Ga^{0.301} \quad (4.3)$$

$$\text{Jet} \Leftrightarrow \text{Jet-Sheet}: \quad Re = 1.414 Ga^{0.233} \quad (4.4)$$

$$\text{Jet-Sheet} \Leftrightarrow \text{Sheet}: \quad Re = 1.448 Ga^{0.236} \quad (4.5)$$

The modified Galileo number of the liquid is the ratio between the gravitational and viscous forces based on the capillary length scale, and it is defined as

$$Ga^* = \frac{\rho_L \sigma^3}{\mu_L^4 g} = \left(\frac{\text{Gravity}}{\text{Viscosity}} \right)^4 \quad (4.6)$$

and the liquid film Reynolds number is

$$Re = \frac{4\Gamma}{\mu_L} \quad (4.7)$$

where Γ is the mass flow rate of film per unit length, ρ_L is the density of the liquid, μ_L is the liquid dynamic viscosity, σ is the surface tension, and g is the acceleration due to gravity.

Studies of flow transition of the falling film modes have attracted the attention of many researchers. Yung *et al* (1980) have investigated the jet-droplet transition. Their correlation can be written as,

$$\Gamma = 0.81 \frac{\rho_l}{\lambda} \frac{\pi d_p^3}{6} \left(\frac{2\pi\sigma}{\rho_l \lambda^3} \right)^{0.5} \quad (4.8)$$

where Γ is the mass flow rate per unit length at the jet-droplet transition, λ is the stability wavelength on horizontal tubes and d_p is the diameter of primary drops which can be written as,

$$d_p = C_l \sqrt{\frac{\sigma}{\rho_l g}} \quad (4.9)$$

where C_l is an empirical constant equal to 3 for water.

To define the transition between different flow modes Honda *et al.* (1987) have developed the following correlation.

$$K = \frac{\Gamma}{\sigma^{3/4}} \left(\frac{g}{\rho_l} \right)^{1/4} \quad (4.10)$$

where Γ is the liquid flow rate per unit length, σ is the surface tension, g is the acceleration due to gravity, and ρ_l is the density of the liquid. The K values for different modes are listed in Table 4.2 from Honda *et al.* (1987) compared with those of the present study. Close agreement is shown between the present experimental and numerically determined values, as well as with those of Honda *et al.* (1987).

Table 4.2. Values of the transition constant, K , reported by Honda *et al.*(1987) compared with those from the present study.

Mode Transition	K Value by Honda <i>et al.</i> (1987)	Present numerical K	Present experimental K
Droplet-Jet	0.06 – 0.13	0.08	0.08
Jet-Jet/Sheet	0.32	0.32	0.32
Jet/ Sheet – Sheet	0.37 – 0.47	0.40	0.45

In the droplet and jet modes, the liquid falls from one cylinder to the cylinder below at a fixed distance. The horizontal distance between two neighbouring drops or jets is defined as the wavelength λ of the falling film, as shown in Figures 4.1 and 4.2. To calculate λ , the results are analysed for the development of waves at the boundary between two fluids, air and water, with different

densities. The growth rate of the instability and the rate of mixing between the two fluids depend on the effective viscosity of the two fluids.

In this study, the two fluids are water and air. If both fluids are considered to be inviscid and incompressible, the critical wavelength, λ_c , which is the shortest disturbance that could be unstable is as given by Bellman and Pennington (1954):

$$\lambda_c = 2\pi \sqrt{\left(\frac{\sigma}{g(\rho_l - \rho_a)} \right)} \quad (4.11)$$

where σ is the surface tension, ρ_l is the density of the water, ρ_a is the density of the air and g is the acceleration due to gravity.

Lienhard and Wong (1964) calculated the critical wavelength according to the following equation:

$$\lambda_c = 2\pi \sqrt{\left(\frac{g(\rho_l - \rho_a)}{\sigma} + \frac{2}{D^2} \right)^{-1}} \quad (4.12)$$

where D is the tube diameter.

The wavelength at which disturbance grows most rapidly is called the most dangerous wavelength, λ_d , and it is given by Bellman and Pennington (1954) and Lienhard and Wong (1964) as:

$$\lambda_d = \lambda_c \sqrt{3} \quad (4.13)$$

Yung *et al.*(1980) calculated the wavelength by developing an equation for low viscosity liquids like water, ammonia and ethyl alcohol. Their instability wavelength is given by

$$\lambda = 2\pi \sqrt{\frac{n\sigma}{\rho_l g}} \quad (4.15)$$

where $n = 2$ for a thin liquid layer (such as what would form with water) and $n = 3$ for thick a layer (as with glycerine).

The value of the wavelength λ is found to be set between the critical and dangerous values, $\lambda_c \leq \lambda \leq \lambda_d$, by Mitrovic (1986).

Armbruster and Mitrovic (1994) calculated the wavelength of jet spacing of the water and isopropyl alcohol, and their correlation can be written as,

$$\lambda = \frac{2\pi\sqrt{2}}{\sqrt{\frac{g(\rho_l - \rho_a)}{\sigma} \left(1 + \left(\frac{\text{Re}/2}{\text{Ga}^{1/4}}\right)^{0.8}\right) + \sqrt{\frac{2}{D^2}}}} \quad (4.16)$$

The wavelength of the falling film is considered to be one of the most important fluid characteristics in the falling film flow behaviour. Mohamed (2007) defined the dimensionless wavelength λ^* as the spacing between neighbouring jets or droplets, divided by the capillary constant ξ .

$$\lambda^* = \frac{\lambda}{\xi} \quad (4.17)$$

where ξ is the capillary constant defined by

$$\xi = \sqrt{\frac{\sigma}{g\rho}} \quad (4.18)$$

Equations 4.16 to 4.18 are used in the present study. All variables in these three equations are as defined previously.

Mohamed (2007) concluded that the wavelength of the falling film depends on the Reynolds number and the fluid properties.

Liquid film thickness is another important parameter used in studies of the behavior of liquid film falling on horizontal tubes. The laminar film thickness, δ at any position is given by Rogers (1981) :

$$\delta = \left(\frac{3\Gamma\mu}{g\rho^2 \sin \phi} \right)^{1/3} \quad (4.19)$$

where δ is the liquid film thickness, Γ is film mass flow rate on one side per unit length of cylinder, μ is viscosity of liquid film, g is acceleration due to gravity, ρ is density of liquid film and ϕ is the angular position on a horizontal tube.

The evolution of the liquid film thickness has been examined by Ouldhadda and Idrissi (2002). Their analysis is performed to study the laminar flow of non-Newtonian liquid film falling on a horizontal tube. Particularly, the effects of the liquid flow rate on the film thickness profiles are examined. They found that liquid film thickness increases significantly with liquid flow rate.

The present work involves an experimental and numerical study of the falling film behaviour. This study includes experimental and numerical investigation of the flow mode, flow mode transitions, wavelength, λ , the effect of cylinder placement and also the vertical separation distance between the horizontal cylinders, \bar{S} . The numerical predictions are validated with the present experimental results, as well as those from the literature. Some of the present results have been presented by Jafar *et al.* (2007) and Jafar *et al.* (2009).

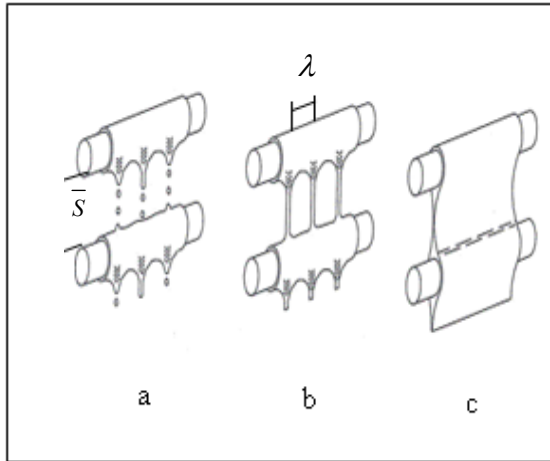


Figure 4.1. Schematic of the three main flow modes: (a) Droplet, (b) jet, and (c) sheet mode after Mitrovic (1986).

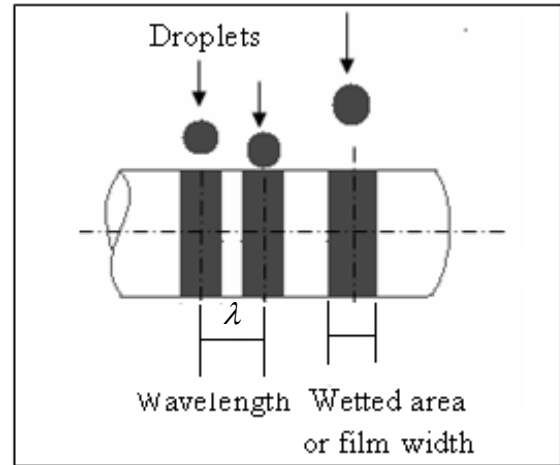


Figure 4.2. Schematic of droplet flow for the present study.

4.2 Experimental Setup

An apparatus to study the flow characteristics and heat transfer phenomenon of liquids flowing over cylinders has been constructed. A photograph and a schematic diagram of the apparatus have been previously presented in Chapter 2 in Figures 2.11 and 2.12 respectively. The apparatus consists of three aluminium cylinders item (2) over which water falls from a tank (1) via a distributor. Water falling from the cylinders is collected in a reservoir (3) from which it is returned by a pump (4) to the holding tank (1). The flow rate of the water is measured by one of two MPB series 1200B variable area flow meters (8) and (9). The ranges for these flow meters are 0 to 0.00375 liters/second and 0.00375 to 0.225 liters/second. Item (10) represents a bypass line. It is possible to choose the appropriate flow meter by using one of three valves (5), (6), and (7). The line size is 10 mm. The type of end fitting is $\frac{1}{4}$ BSP or 8 mm. The frequency and size of the droplets are measured by (11) a Kodak video camera with a resolution of 12.3 mega pixels. Each experiment was carried out three times. A detailed description of the experimental setup is given in Section 2.4.

4.3 Numerical Model

The system investigated in this chapter consists of a column of cylinders, the axes of which are parallel and located directly above each other as indicated in Figure 4.3 and 4.4, for 2D and 3D configurations respectively.

Water, deemed to have a uniform velocity, is introduced onto the array of cylinders through a slot nozzle located above the top cylinder.

Numerical simulations have been performed at liquid mass flow rates per unit length of 0.005, 0.0125, 0.025, 0.0375, 0.0625, 0.125, 0.2, 0.325, and 0.5 kg/ms, to achieve Reynolds numbers of 20, 50, 100, 150, 250, 500, 800, 1300, and 2000, respectively. A finite-volume CFD code, FLUENT[®] was used for the simulations. The VOF (volume of fluid) technique has been employed to mark a point occupied by fluid as unity, and zero if occupied by air. Some finite volumes may be partially filled with water, and FLUENT[®] indicates this situation with number between 0 and 1. The volume of fluid method was established by Hirt and Nicholas (1981), when they traced the fluid regions through an Eulerian mesh of stationary cells. Three phases, liquid (water), gas (air) and solid (the cylinders) are modelled numerically.

The 2D and 3D simulations were implemented with similar characteristics of mesh generation and the solver setup for laminar flow. The upper and lower surfaces are modelled as pressure boundaries that operate at zero gauge pressure.

For the three cylinder geometries, the topmost and middle cylinder diameters were kept at 0.1 m. Three diameters are used for the bottom cylinder, namely, 0.02, 0.05 and 0.1 m. In each case, the outlet of the water jet was 0.03 m above the top cylinder. The geometry and the grid have been generated in GAMBIT[®]. A symmetrical domain has been used for faster FLUENT[®] simulations. The details of grid and time step independence studies are described in Section 2.2.1 and 2.2.2.

A tri-pave mesh is implemented in the 2D case. A hex/wedge with a Cooper type for the 3D geometries as shown in Figure 4.5. The total number of elements and

the worst grid elements for the three 3D geometries considered are listed in Table 4.2. In the grid, if the skew of the element exceeds 0.97, it will not be acceptable for a solution.

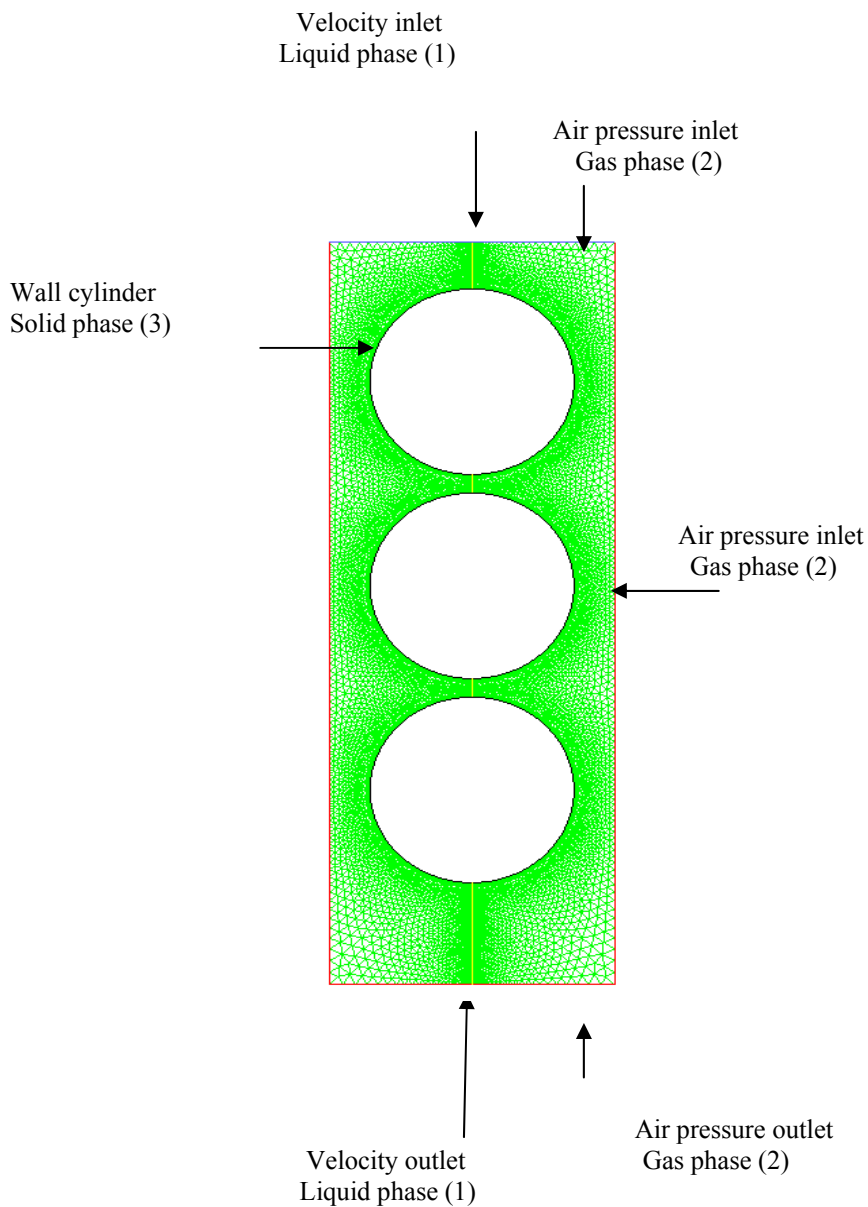


Figure 4.3. 2D geometry used to model the three phases of (1 liquid, (2 gas and (3 solid).

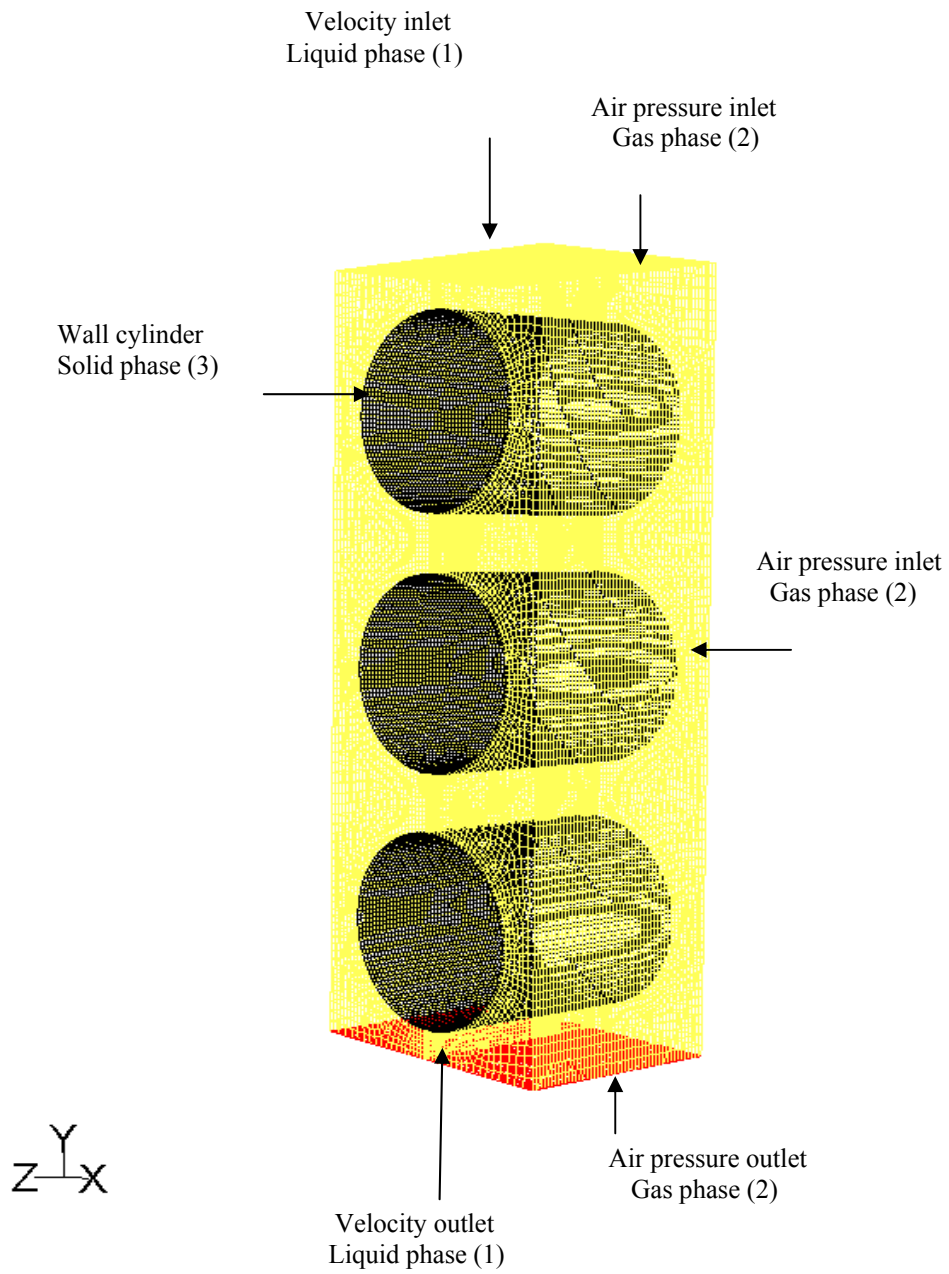


Figure 4.4. 3D geometry used to model the three phases of (1 liquid, (2 gas, and (3 solid).

Table 4.3. Total grid elements of the three 3D geometries.

3D configurations	Total grid elements	Skew or the worst element
0.1 m bottom cylinder	105,250	0.44813 m
0.05 m bottom cylinder	109,1750	0.48712 m
0.02 m bottom cylinder	110,300	0.41431 m

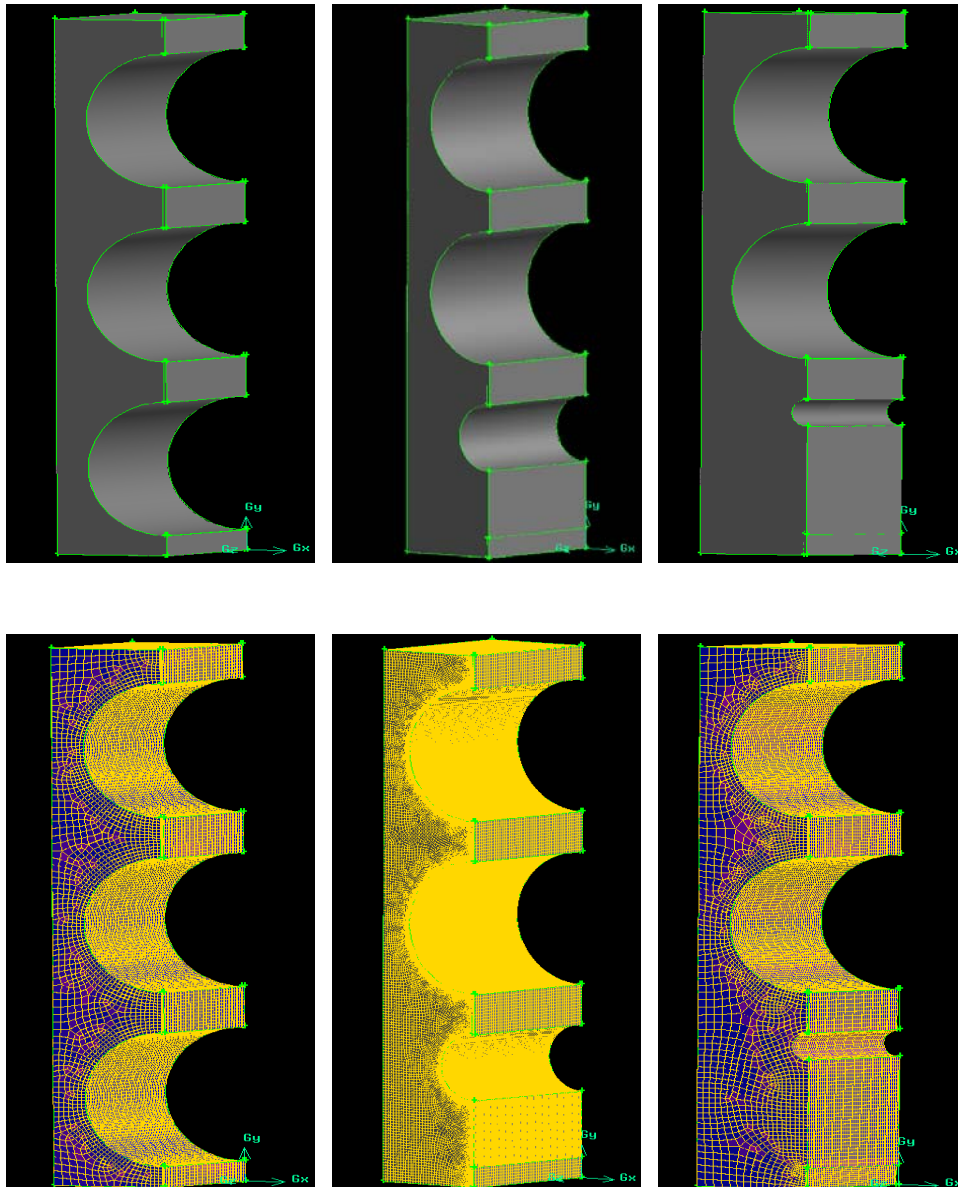


Figure 4.5. Three 3D geometries for the three lowest cylinder diameters. The two upper cylinders have diameters of 0.1 m, and the lowest cylinder diameters are 0.1 m, 0.05 m and 0.02 m. The lower row of figures indicate the finite volume mesh used in each case.

4.4 Flow Mode Visualization

To understand the falling film modes and transitions, a horizontal cylinder can be considered with a smooth thin liquid film around it. The hanging or suspended drops separate from the lowest cylinder position. Some drops might break away from the film and fall under the effect of gravity prior to this position. This is the beginning of the droplet mode from a falling liquid film. The axial distance between the neighbouring droplets is determined primarily by the wavelength of the most unstable free surface.

At low liquid flow rates, liquid droplets fall with a low frequency from the bottom of the top horizontal cylinder to the one below. The droplet formation frequency increases with an increasing liquid flow rate. With a further increase of the liquid flow rate, the liquid leaves the cylinder at the same location in a continuous column. This event is the transition from the droplet to droplet-jet mode. With a further increase of the liquid flow rate, a transition from the droplet-jet to the jet mode occurs.

With a further increase of the flow rate, the liquid leaves the surface in a continuous column in jet mode, where the diameter of the liquid jet increases with the flow rate. When the flow rate increases further, the jet becomes unstable and an additional column appears, resulting in the jet-sheet to sheet mode transition. The liquid jets are unsteady in location for a short time. Then, the sheet thickness becomes thin and the sheet becomes stable at a closer spacing to produce a full sheet mode.

Below is a summary of the three principal and two intermediate flow modes.

4.4.1 Droplet Mode

The flow is in droplet mode when the liquid flows only between the cylinders in the form of distinct droplets. There are no continuous liquid links between the bottom of the upper cylinder and the top of the one below. The frequency of these

droplets increases with flow rate, while the distance between the droplets remains the same.

4.4.2 Droplet-Jet Mode

This intermediate mode is manifest when at least one stable column exists between the cylinders in addition to falling droplets. A jet is a continuous liquid linking cylinders. The jet can move horizontally alongside the cylinders but must be continuous to define this mode.

4.4.3 Jet Mode

This mode occurs when there is liquid flow only in jets between cylinders. At lower flow rates, the jets tend to be in line while at higher flow rates they are staggered from one cylinder to the next.

4.4.4 Jet-Sheet Mode

In this intermediate mode, both jets and sheets exist between the cylinders at different locations along the cylinders. This mode occurs when at least one small sheet is observable. A small sheet is created by the merging of two nearby jets, and normally, it has a triangular shape.

4.4.5 Sheet Mode

At higher flow rates, the diameters of the jets increase. The liquid jets extend sideways to form a liquid sheet. At the beginning, this mode is not continuous, but several unstable triangular small sheets can be observed. With increasing flow rate, the unstable triangular sheets merge together and form a complete sheet along the entire cylinder length. Sheet mode occurs when there is one single wide sheet between the two cylinders.

These modes are illustrated in Figure 4.6 within water falling on three horizontal cylinders. In Figures 4.6a to 4.6f, droplets, droplet-jet, in line jet, staggered jet, jet-

sheet and then sheet modes are seen with increasing flow rates. In Figure 4.7, the falling film modes predicted from the numerical simulations in the 2D configuration are shown. The principle modes predicted with the 3D configurations are shown in Figure 4.8.

In Figure 4.9, the three main flow modes are illustrated as a function of Reynolds number, Re . In addition to the present experimental and numerical results, results of Roques and Thome (2007) are shown. Close agreement is observed amongst all three sets of results.

In Figure 4.10, the intermediate modes are illustrated as a function of Galileo number, Ga . Present experimental results compare favourably with those of Roques and Thome (2007).

4.5 Measuring the Flow Behaviour

4.5.1 Effect of Flow Rate on Droplet Mode

The experiments were carried out with Reynolds numbers in the range 20 to 150. As seen in Figure 4.11, the number of large drops increased relatively slowly as the Reynolds number was increased to about 80, and the frequency of the large drops remained about constant as the Reynolds number increased further. In contrast, the frequency of the small droplets increased sharply by a factor of about 4 as the Reynolds number increased from 20 to about 50. The average diameter of large droplets is about 5 mm while the average size of the small droplet is about 1 mm.

The droplets and jets are characterized by the departure of fluid from regularly spaced sites along the bottom of the cylinder. As defined earlier, the spacing between the sites for the droplet and jet mode is referred to as the droplet or jet spacing or the wavelength. The flow rate has a large effect for the droplet and jet spacing. Increasing the flow rate causes a decrease in droplet and jet spacing and decreasing in the flow rate causes an increase in the droplet and jet spacing. This result is in agreement with Yung *et al.* (1980).

The results presented in Figure 4.11 are obtained with increasing flow rate. The experiment is started when the flow rate was low, and it is then increased gradually. When the flow rate was subsequently progressively decreased from its high value, it was observed that the general relationship between the droplet frequency and Reynolds number is very similar to that obtained when the flow rate is increased. However, the frequency at which the droplets detach decreases somewhat more rapidly when the flow rate decreases. The system apparently stabilizes at different frequencies and sites at the same flow rate, depending on whether the desired flow rates are reached by positive or negative increments, as shown in Figure 4.12. For instance, in the Reynolds number range of 80–150, the frequency of the small drops is 15.5/s for positive and 14.3/s for negative changes in the flow rate, and the corresponding dimensionless wavelengths are 4.8 and 4.1, as illustrated in Figure 4.13.

In Figure 4.13, the dependence of the distance between the active sites (the wavelength) on the Reynolds number is presented. For Reynolds numbers less than 80, the horizontal spacing between two streams of droplets remains constant. The distance between simultaneously active sites is larger at lower Reynolds numbers. As the film flow rate increases, more sites become simultaneously active, and complete wettability of the cylinder is obtained at $100 < Re < 150$.

4.5.2 Effect of Spatial Placement of Cylinder on Droplet Mode

In many practical applications, the cylinders that may form part of a heat transfer system are axially aligned one above the other. One might assume that the flow mode of water around a lower cylinder will be influenced by the flow around the cylinder immediately above it. To examine the resulting flow field, the data are taken from each horizontal cylinder in the vertical column. It has been observed that the horizontal distance between the active sites decreases, with a corresponding change in the frequency of the drops, as the vertical distance of the cylinder from the feeder increases. The large drops decrease in size and fall at lower frequencies. The drop producing sites are distributed closer at the bottom of

the cylinder and drop size becomes more uniform as the water falls down, as shown in Figure 4.14.

In Figure 4.15, the dependence is presented of the wavelength on the Reynolds number for the top, middle and the bottom cylinders. The wavelength is large for the top cylinder, and then, it decreases for the middle and further for the bottom cylinder. As the film flow rate increases, more sites become simultaneously active and the distance between active sites seem to be large at low Reynolds numbers for the top, middle and the bottom cylinders. Experimental results of Hu and Jacobi (1998) are also plotted in Figure 4.15.

4.5.3 Effect of Cylinder Diameter

The effect of cylinder diameter on the frequency of droplet detachment was studied by changing the diameter of the bottom cylinder. Diameters of 0.02, 0.05 and 0.1 m are studied. Drop detachment from smaller cylinders stabilizes at lower frequencies, as shown in Figure 4.16.

The wavelength decreases with increasing cylinder diameter, as shown in Figure 4.17. In this figure, the dimensionless wavelength, λ^* defined by $\frac{\lambda}{\xi}$ which is previously mentioned in equation 4.17, is plotted against Reynolds number. These results agree with those of Lee (1963) who calculated the wavelength for water at a very low flow rate. He found that the wavelength decreases with increasing the tube size.

4.5.4 Effect of Vertical Spacing Distance between Cylinders, Separation

The effects of the separation distance between cylinders, \bar{s} , is represented in Figures 4.18. Cylinder separations of 0.001 m, 0.01 m, 0.03 m, and 0.05 m have been investigated. In Figure 4.19, the different separation distances between the top and the bottom cylinders are shown at $Re = 250$. Zooming in on the separation distance between the bottom top and the top bottom cylinders at the same Reynolds number of 250 is shown in Figure 4.20. As seen in this figure, the flow

modes are different at different separation, \bar{S} , the flow mode tends to be the droplet mode at larger separations, and the jet and sheet modes at smaller separations.

In Figure 4.21, the three non dimensional separation distances between the cylinders, \bar{S}/d of 0.1, 0.3 and 0.5 are illustrated as function of Reynolds number. The three principle modes of droplet, jet and sheet mode in addition to the two transition mode of droplet-jet and jet-sheet modes are presented in this figure. As shown in Figure 4.21a, b, c, and d, the flow modes are droplet, droplet-jet, jet and jet-sheet at large separation distance where $\bar{S}/d = 0.3$ and 0.5 respectively. The flow mode tends to change to droplet-jet, jet, jet-sheet, and sheet modes at smaller separation distance, where $\bar{S}/d = 0.1$ as shown in Figure 4.21a, b, c and d respectively.

4.6 Hysteresis of Falling Film Transition

Hysteresis refers to memory effects in the flow. It is reported in the literature that hysteresis results in flow transitions occurring at different Reynolds numbers as the flow rate increases or decreases.

There are four transition points when considering the hysteresis. These points are the transitions for increasing or decreasing Reynolds number between the sheet and sheet-jet, sheet-jet and jet, jet and jet-droplet, and jet-droplet and droplet modes. It has been observed in the present experiments that Reynolds number to reach a mode with increasing liquid flow rate is higher than that required for a decreasing liquid flow rate. For the range of low Reynolds number, the effect of hysteresis has been found to be small. This point is discussed earlier in Section 4.5.1. Some hysteresis effects are presented in Figures 4.12 and 4.13.

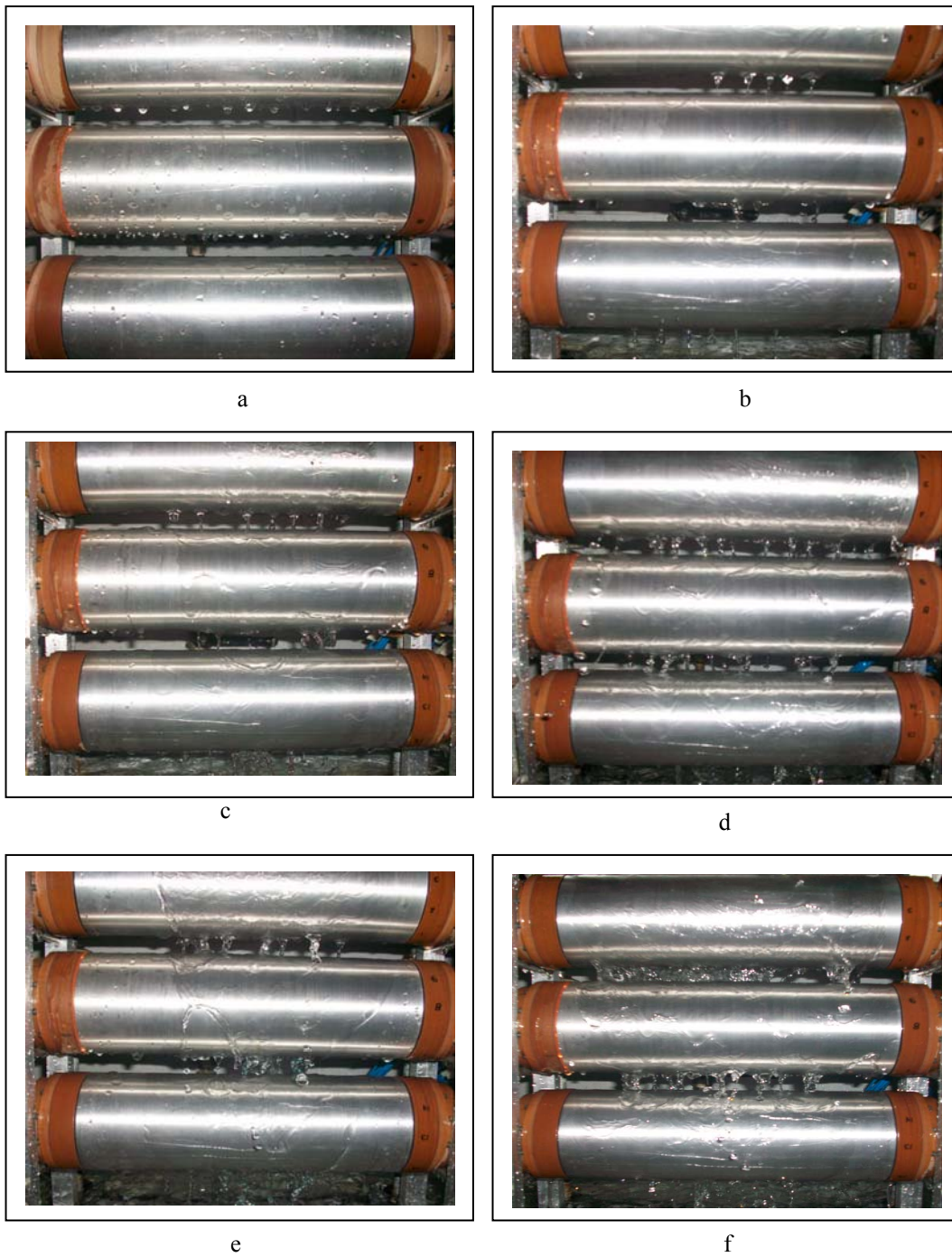


Figure 4.6. Experimental visualization of flow modes. a) droplet, b) droplet-jet, c) inline jet, d) staggered jet, e) jet-sheet, f) sheet mode.

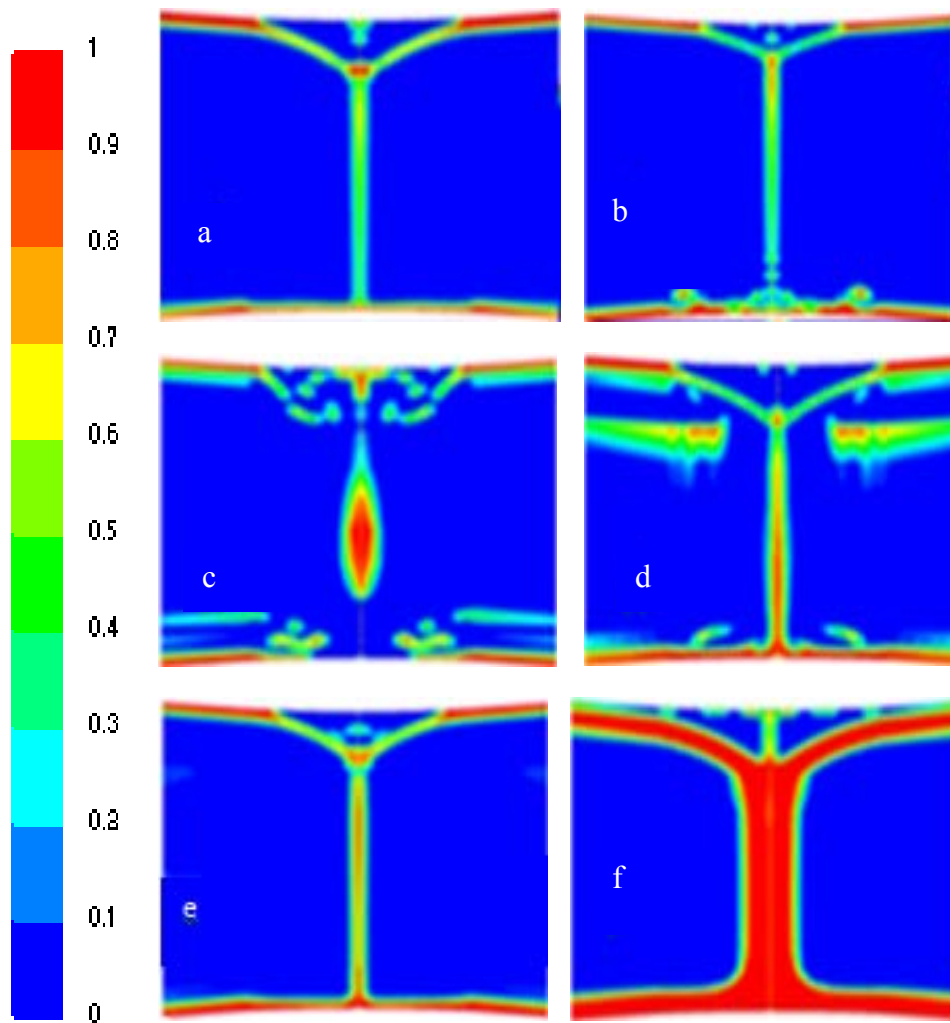


Figure 4.7. Contours of volume fraction (phase water) the flow visualization of 2D falling liquid film between two cylinders a) droplet mode, b) droplet-droplet jet mode, c) jet mode, d) jet-jet sheet mode, e) jet sheet-sheet mode, f) sheet mode. Red colour indicates water which is equal to 1 and blue is air which is equal to 0.

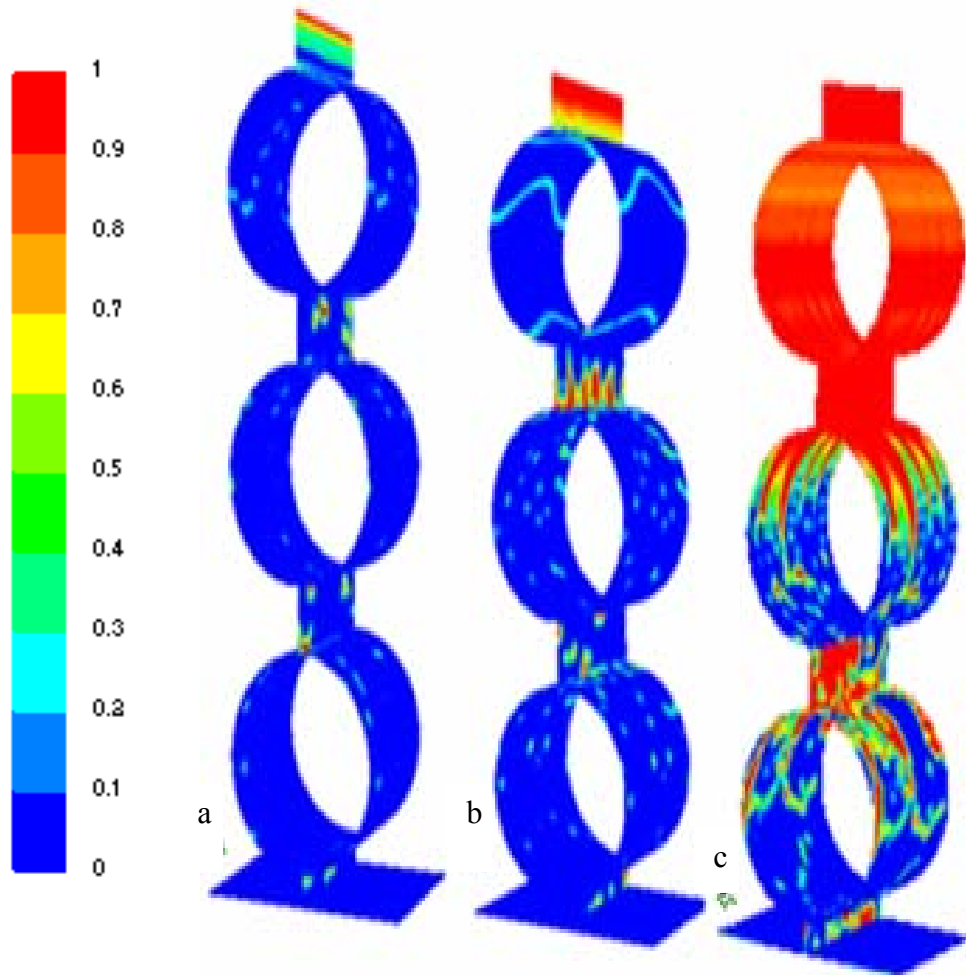


Figure 4.8. Contours of volume fraction (phase water) for flow visualization of 3D falling liquid film. a) droplet mode, b) jet mode and, c) sheet mode. Red indicates water which is equal to 1 and blue is air which is equal to 0.

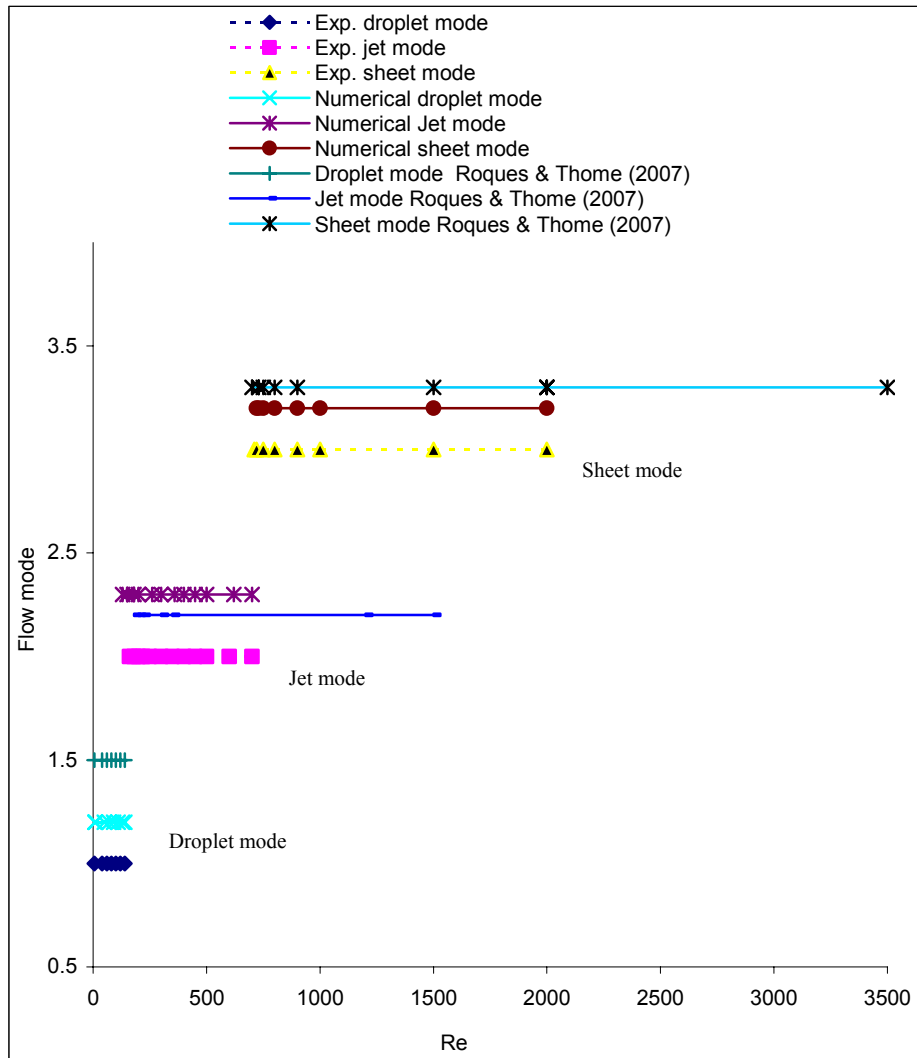


Figure 4.9. The experimental and numerical principal flow modes compared with the literature.

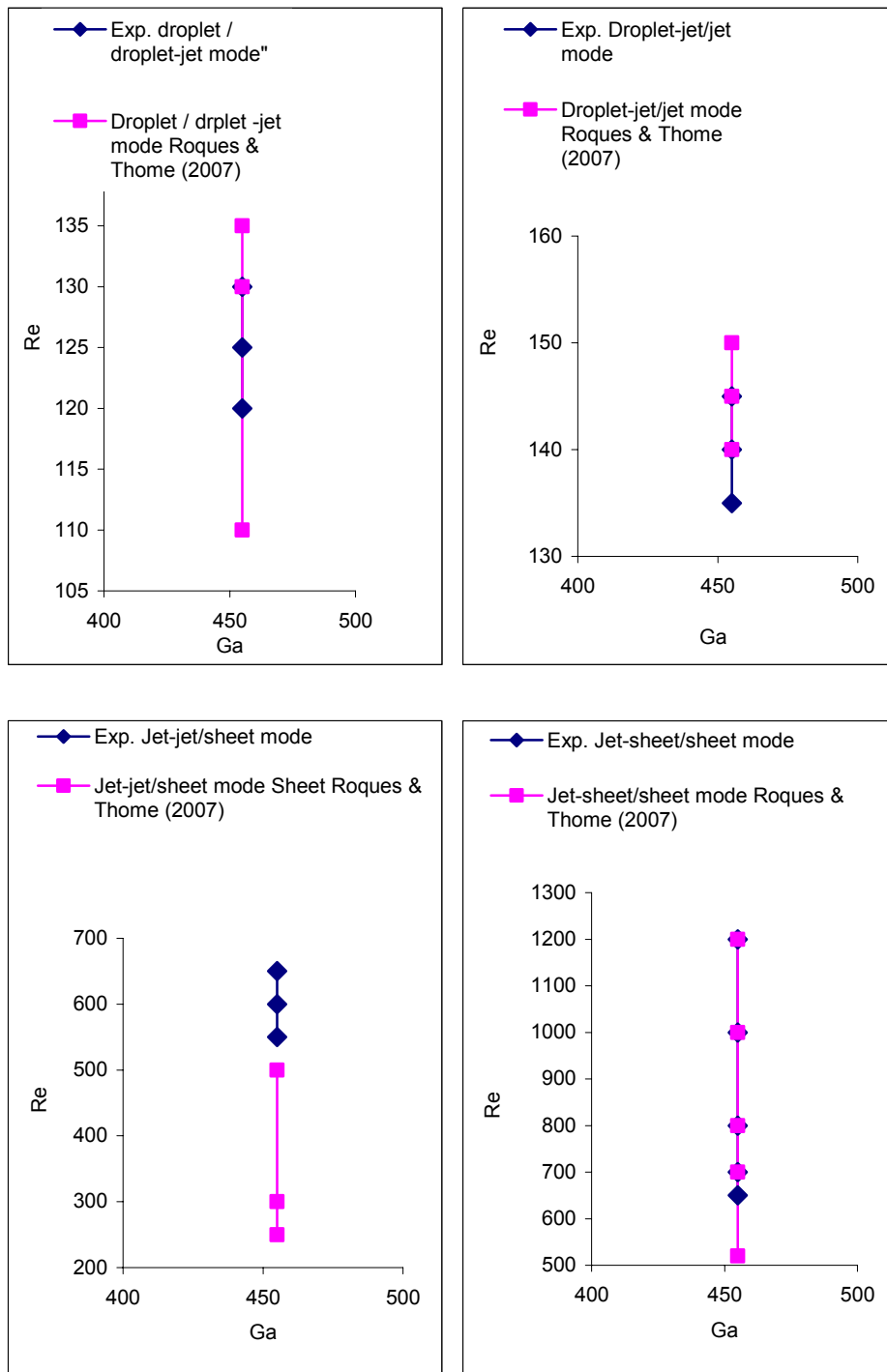


Figure 4.10. The experimental transition modes compared to Roques and Thome (2007).

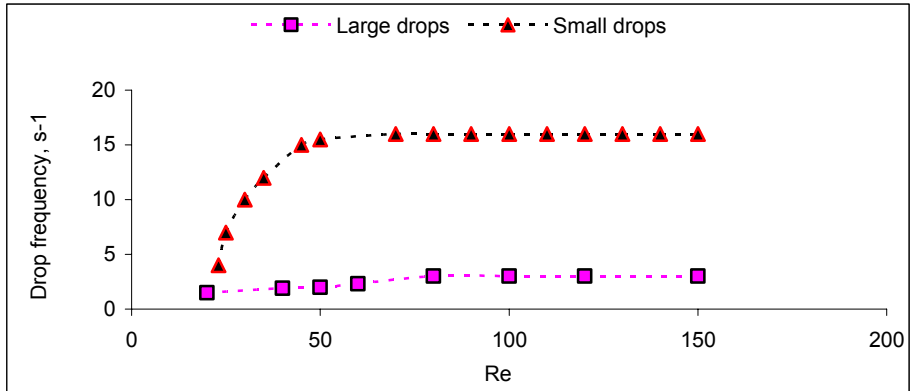


Figure 4.11. Effect of film Reynolds number on the frequency of droplet detachment for the middle cylinder.

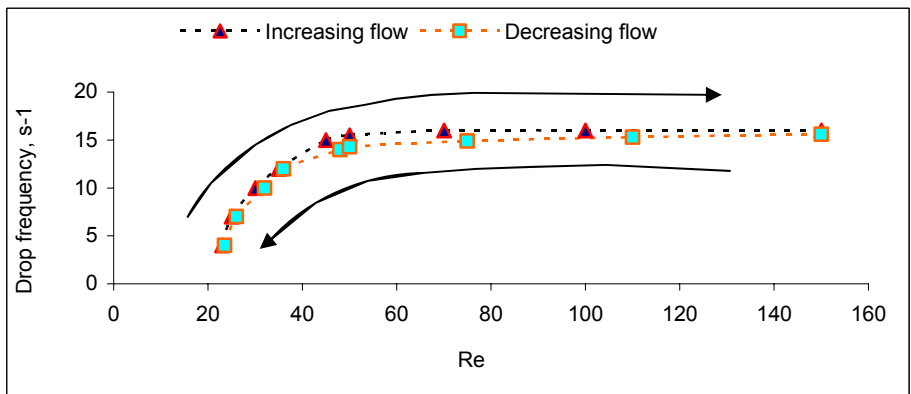


Figure 4.12. Effect of increasing and decreasing film flow rate on the frequency of small droplet detachment for the middle cylinder.

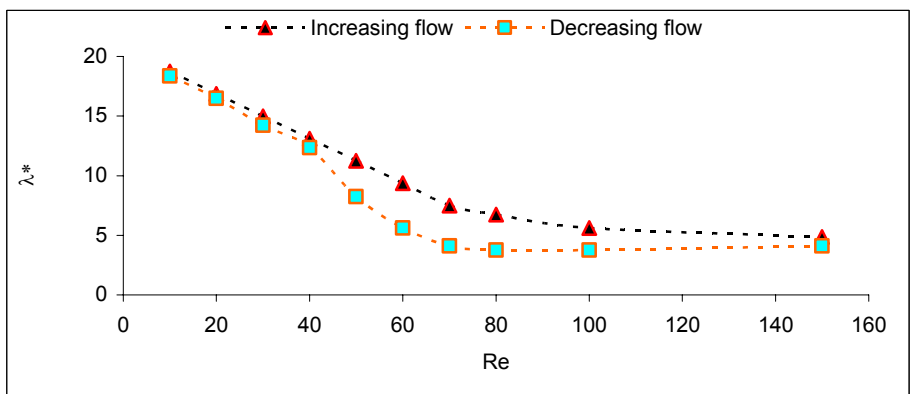


Figure 4.13. Effect of increasing and decreasing film flow rate on the distance between small droplet producing sites for the middle cylinder.

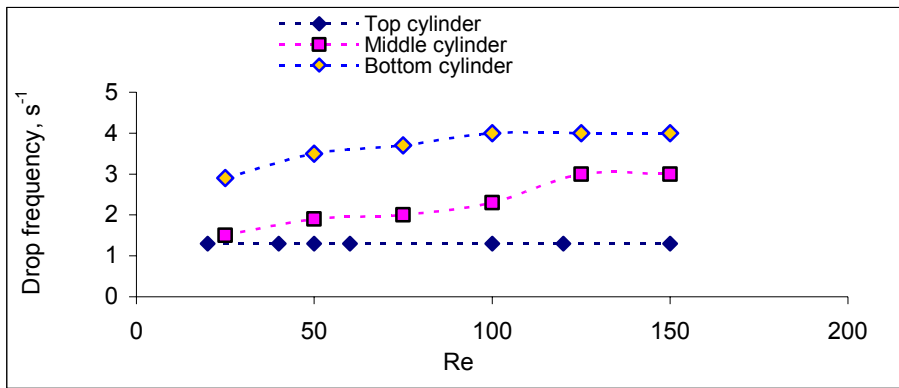


Figure 4.14. Effect of spatial placement of a cylinder in the column on the frequency of large droplet detachment.

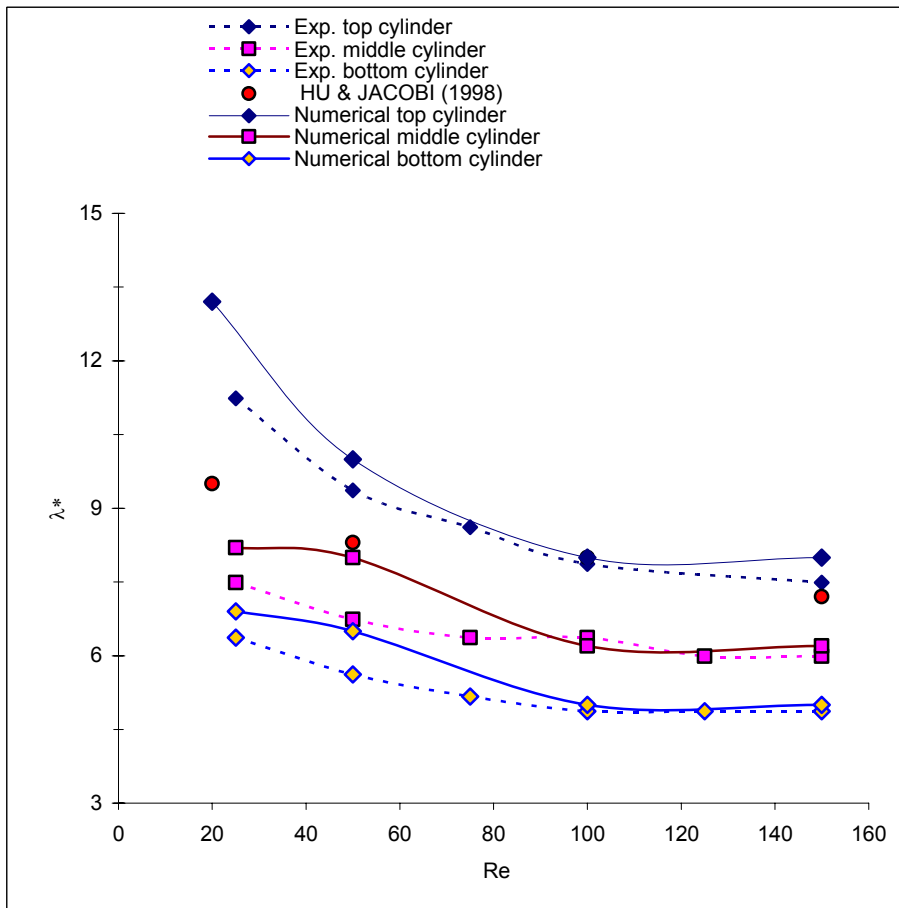


Figure 4.15. Effect of spatial placement of cylinders in the column on the distance between drop producing sites, the present results and those of Hu and Jacobi (1998).

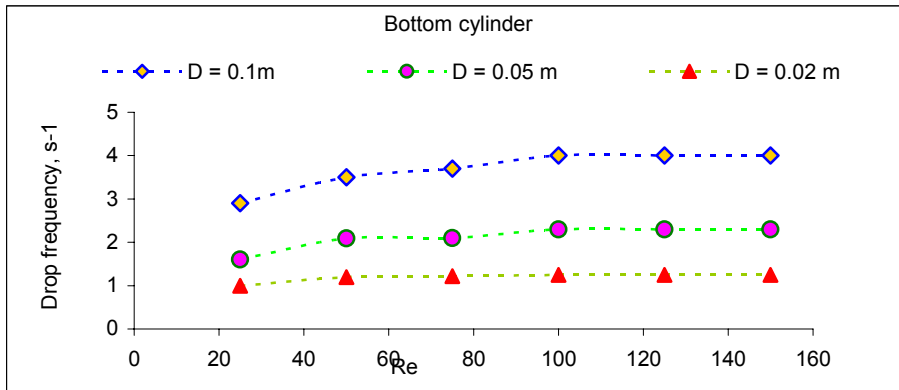


Figure 4.16. Effect of bottom cylinder diameter on the frequency of drop detachment.

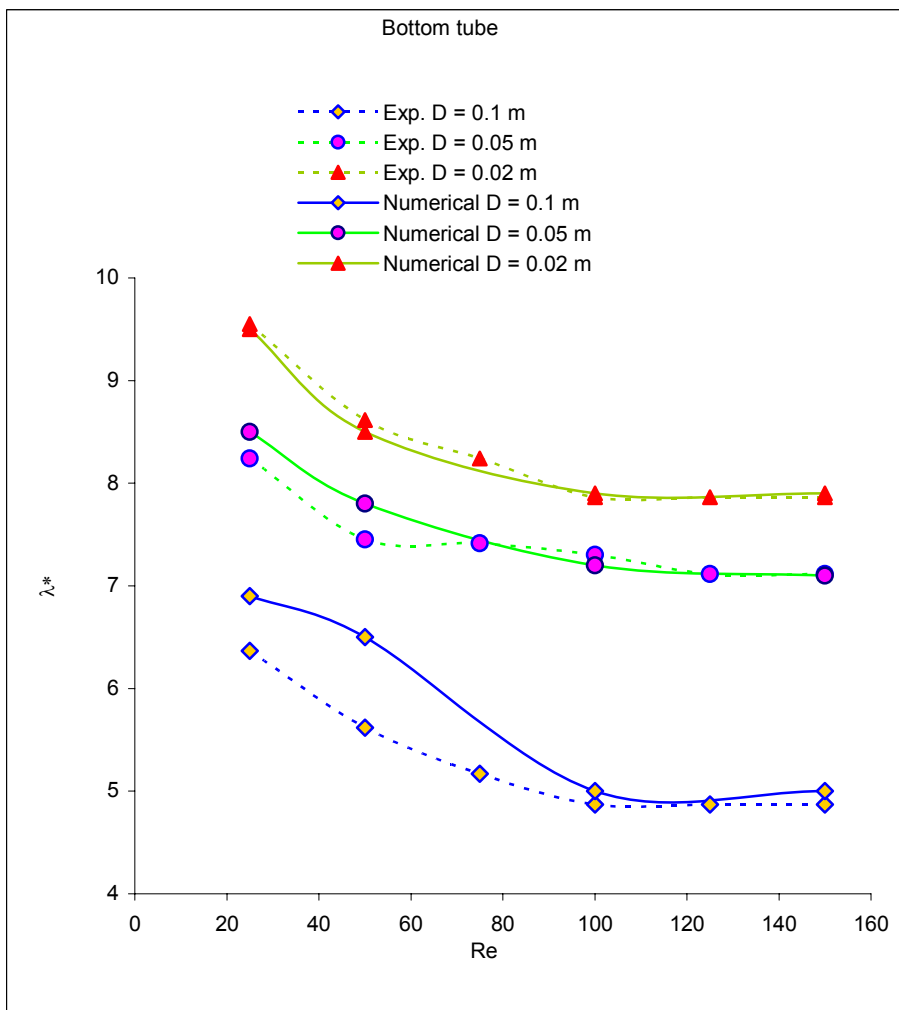


Figure 4.17. Effect of bottom cylinder diameter on the distance between drop producing sites.

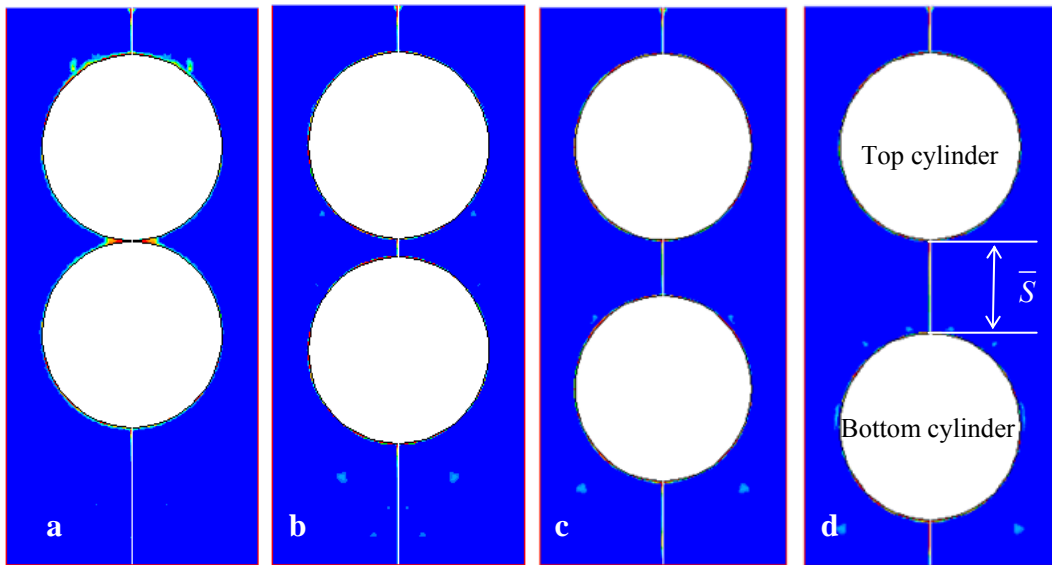


Figure 4.18. Four geometries of two cylinders with different separation distance, \bar{S}
 a) $\bar{S} = 0.001$ m, b) $\bar{S} = 0.01$ m, c) $\bar{S} = 0.03$ m and d) $\bar{S} = 0.05$ m.

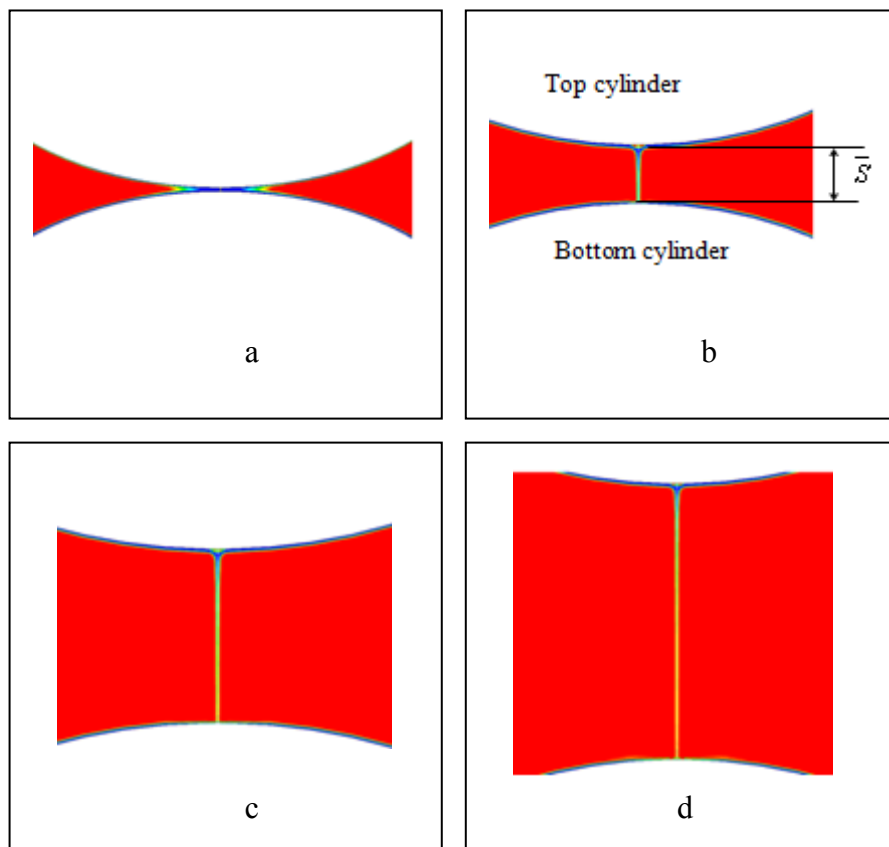


Figure 4.19. Separation distance between two cylinders; a) $\bar{S} = 0.001$ m, b) $\bar{S} = 0.01$ m,
 c) $\bar{S} = 0.03$ m and d) $\bar{S} = 0.05$ m.

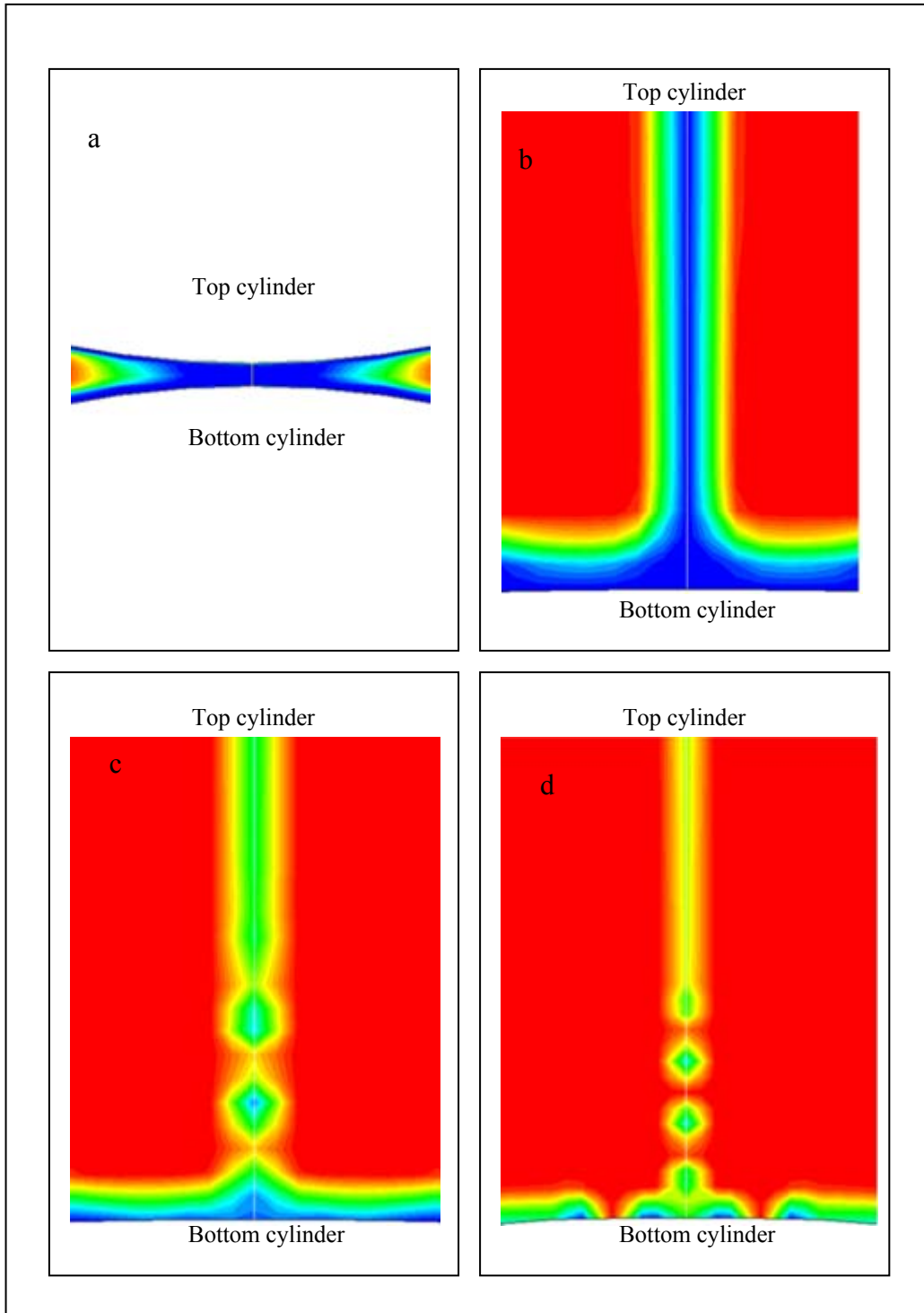


Figure 4.20. Zooming in between the top and bottom cylinders. a) sheet mode, b) Sheet mode, c) droplet-jet mode and d) droplet at $\bar{s} = 0.001$ m, 0.01 m, 0.03 m and 0.05 m respectively.

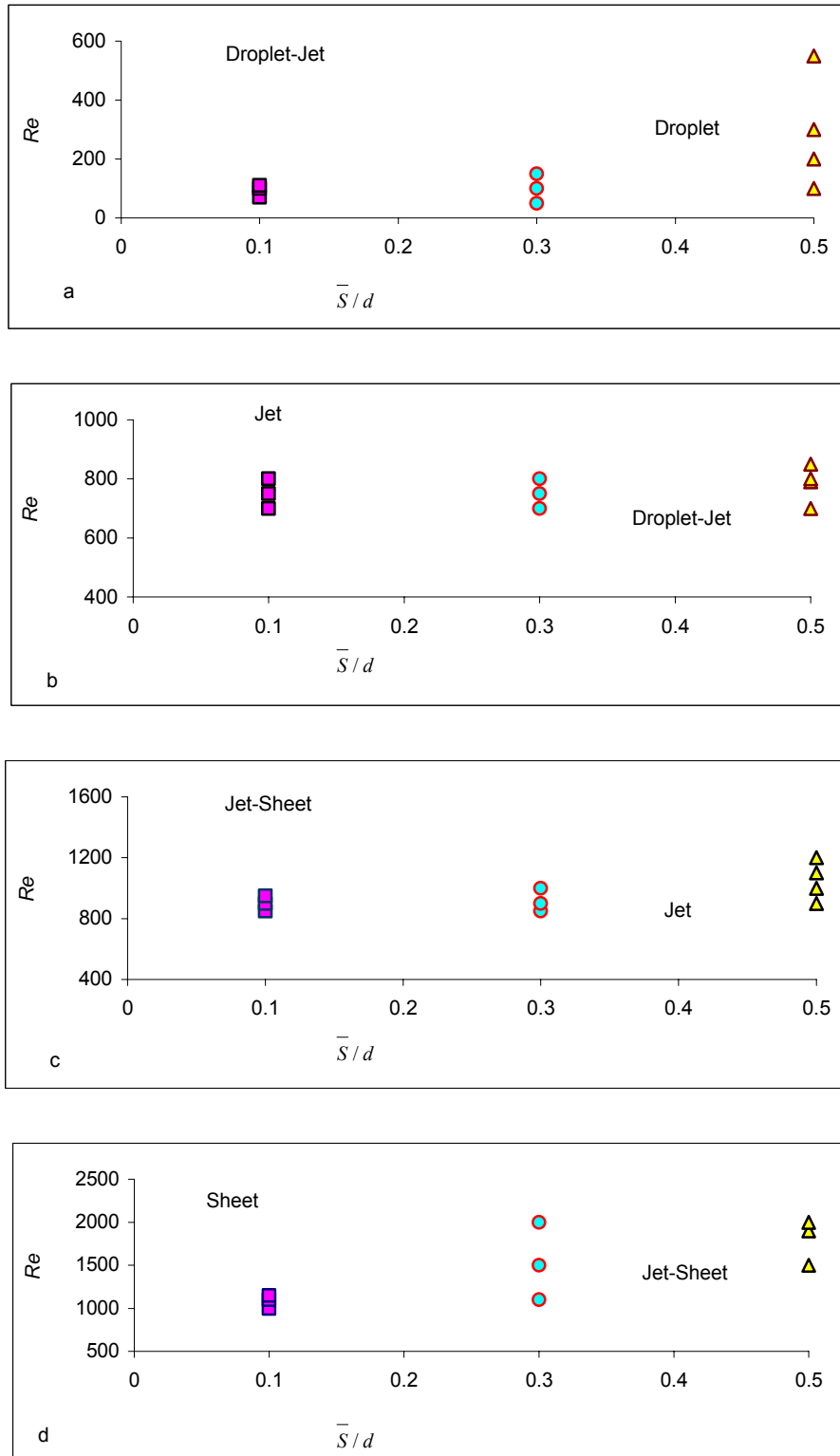


Figure 4.21. Transition as a function of relative spacing. (a) droplet and droplet-jet modes, (b) jet and droplet-jet modes, (c) jet-sheet and jet modes, (d) sheet and jet-sheet modes.

In Figure 4.22, flow visualization is presented as a sample result of liquid water falling over three cylinders, where red indicates water and blue indicates air at $Re = 1200$.

These geometries are designed towards the simulation of more realistic experiments in a hydrocooler system. As indicated in Figures 4.22 for this Reynolds number, the flow field is as expected. Showing falling liquid film fall on the top, middle and bottom cylinders at 0.75 s, 1.27 s and 1.8 s respectively.

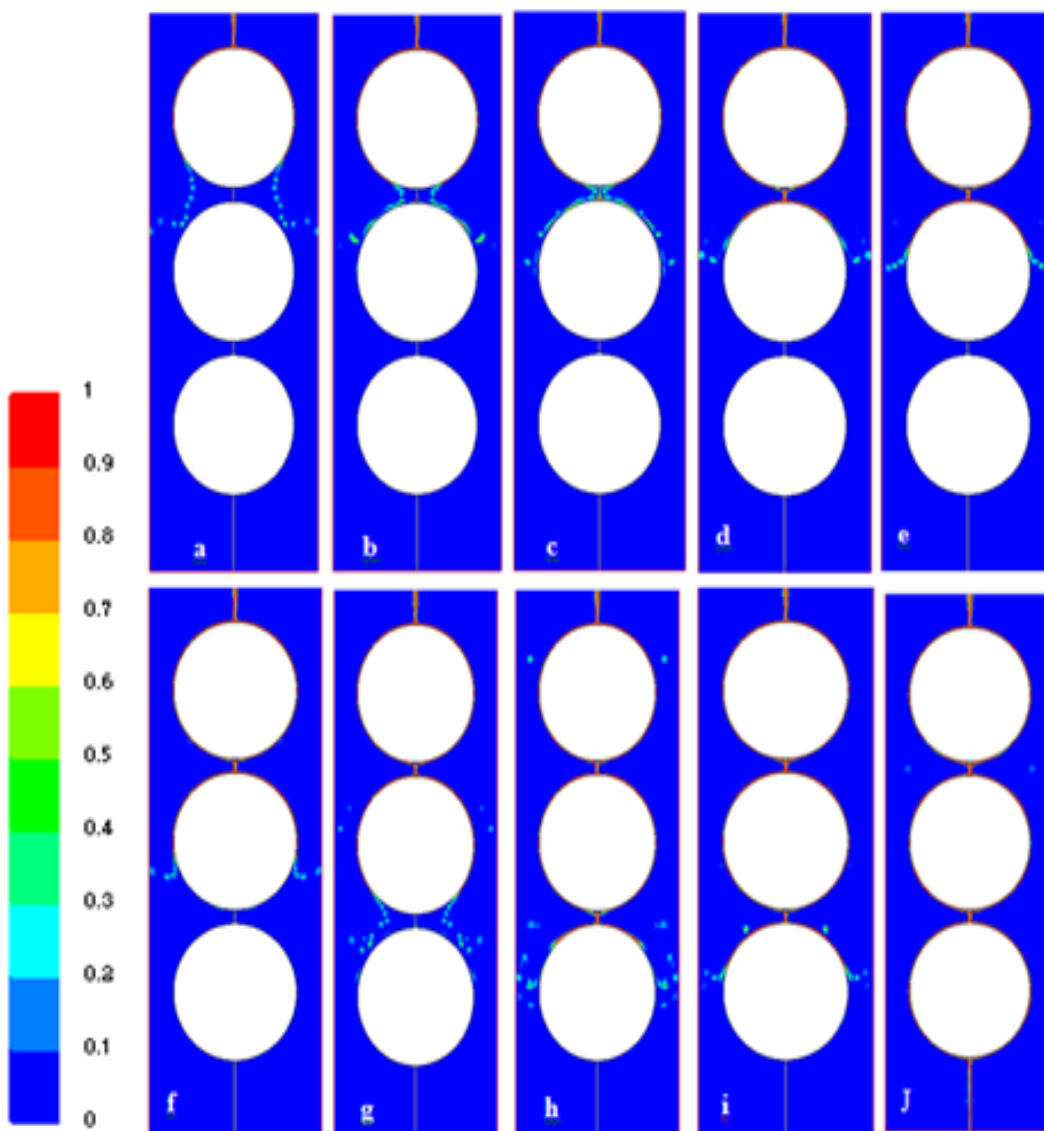


Figure 4.22. Flow visualization of falling liquid over three cylinders at different times. a) at time of 0.45 s, b) at 0.6 s, and c) at 0.675 s, d) at time of 0.75 s, e) at 0.825 s, and f) at 0.9 s, g) at time of 0.975 s, h) at 1.2 s, and i) at 1.275 s and j) at (quasi-steady state) after 1.8 s at $Re = 1200$.

4.7 Conclusion

The liquid film falling between horizontal cylinders exhibits the following flow patterns:

- Droplet mode,
- Droplet-jet mode,
- Jet mode (inline jets and staggered jets),
- Jet-sheet mode and
- Sheet mode, depending on the flow Reynolds number.

The streams of droplets between vertically adjacent horizontal cylinders have been studied as a function of the flow rate, cylinder diameter and location. The following major points have been observed:

- The number of the large drops increases relatively slowly as Reynolds number increases; whereas the frequency of the small droplets increases sharply with increases in Reynolds number.
- There is no significant impact of hysteresis when the flow regime is laminar.
- The drop frequency decreases as the distance of the cylinder from the feeder increases.
- The wavelength decreases with increasing Reynolds number, increasing distance between the feeder and cylinder, and increasing cylinder diameter.

The flow mode is also related to the separation distance between the horizontal cylinders. The flow mode tends to be the droplet mode at large separation; whereas it tends to be the jet and sheet modes at small separation.

CHAPTER FIVE

HEAT TRANSFER IN FALLING LIQUID FILM

In this chapter, results from experiments and numerical studies are used to investigate heat transfer to falling liquid films.

Trickle bed chemical reactors and equipment used to cool horticultural produce usually involve three phase porous media. The fluid dynamics and heat transfer processes that occur in such equipment are generally quantified by means of empirical relationships amongst dimensionless groups. The results reported in this chapter are motivated by the possibility of using detailed numerical simulations of the phenomena that occur in beds of irrigated porous media to obviate the need for empirical correlations.

5.1 Introduction

Beds of irrigated porous media possess several desirable attributes, one of which is a high rate of heat transfer between the trickling fluid and the solids within the bed. High heat transfer coefficients exist between the liquid and the solids - typically $1000 \text{ W}/(\text{m}^2 \text{ K})$. The specific surface, m^2/m^3 , of the solids within the bed is high, on the order of $1/d_p$, where d_p is a linear dimension that characterizes the size of the particles that constitute the bed.

The process of heat transfer associated with liquid films flowing over particles in beds of porous media has many technological and industrial applications. The majority of these are in chemical engineering operations, in the polymer and food industries and also in distillation columns, evaporators and cooling systems.

The work presented in this chapter is relatively generic in nature, but it was prompted by a technological need to cool horticultural produce such as broccoli, sweet corn, peas, beans and carrots. The ultimate aim of this research is to reassess

the empirical correlations that govern the performance of trickle bed reactors and other porous media that involve two fluid phases with more detailed computer simulations.

A step towards being able to model heat transfer in beds of porous media that contain three phases, namely a flowing liquid, a gas and the solid phase, is to consider arrangements of cylinders over which the liquid flows. In this study, a commercial computational fluid dynamics code has been used to study temperature distributions and heat transfer, as the code enables changes to the geometry to be made rapidly.

Many researchers have studied the parameters which affect heat transfer between liquids and horizontal tubes. Parken (1975) reported that the heat transfer coefficient increases with the liquid flow rate, and also that the liquid temperature is related to the decrease of viscosity, which causes a decrease in film thickness. Fletcher *et al.*(1975) reported that the Nusselt number increases with flow rate and heat flux. Ganic and Roppo (1980) have studied experimentally the effect of liquid flow rate over heated horizontal tubes on the flow regimes. They found that there are two types of flow modes associated with liquid films. The first is the droplet mode, which is associated with lower flow rates, and the second is the jet mode which manifests at higher flow rates. They have also found that the heat transfer coefficient increases with liquid flow rate and tube spacing. Furthermore, the effects of the liquid flow rate and heat transfer coefficient have been studied by Fujita and Tsutsui (1995b). They found that when the flow rate increases, the heat transfer coefficient initially decreases and then increases as the flow rate increases.

Sensible heat transfer under different film modes has been investigated intensively. Hu and Jacobi (1996) have found that the heat transfer coefficient in the sheet mode shows large circumferential variations related to flow. They also found that the average Nusselt number depends on Reynolds, Archimedes and Prandtl numbers, as well as tube spacing. They reported that average Nusselt number increases with Reynolds number and decreases with tube diameter.

Studies of heat transfer have been reported not just for simply aligned horizontal tubes but also for horizontal tube bundles. Zeng *et al.*(2001) have experimentally studied the heat transfer by using spray nozzles distributing liquid ammonia downward onto a horizontal, 3–2–3 triangular-pitch plain-tube bundle. Heat transfer performance of individual tubes in the tube bundle was studied by changing heat flux, spray flow rate, nozzle height, and nozzle type. They found that the tube bundle effect is less significant at a lower spray flow rate, a smaller nozzle height, and with standard-angle compared with wide-angle nozzles.

In the field of heat and mass transfer in three phase porous media, Larachi *et al.* (2003) have presented a single correlation for the heat and mass transfer in trickle beds and validated it using 1259 data points. Thorpe (2006) noted that beds of horticultural produce are similar to trickle bed chemical reactors, and it is possible to apply established correlations for the heat and mass transfer coefficients, degree of wetting and volume fractions of the various phases to describe the phenomena that occur in beds of horticultural produce.

Such studies of heat transfer have also been utilized to design evaporators and cooling systems. Roques and Thome (2007) have investigated the effect of falling films on arrays of horizontal tubes and found that it is possible to design falling film evaporators using a fully incremental approach, where the local heat transfer coefficient depends on the local film Reynolds number of the liquid falling on the top of the tube. Heat transfer depends on film flow rate and Reynolds number, as Yoon *et al.* (2008) have found. They reported that heat transfer coefficient increases as flow rate and cooling liquid velocity increase.

The investigation in this chapter is part of an experimental and numerical exploration of heat transfer and falling film modes. Different parameters such as liquid flow rate or Reynolds number, feeder height, cylinder diameters and heat flux are investigated. The effect of multiple horizontal cylinders and bundles of horizontal cylinders (rectangular and random pitch cylinder arrangements) on the heat transfer coefficient are presented in detail in Appendix C.

The numerical predictions are obtained using a CFD code FLUENT[®] for 2D configurations. Local and average heat transfer coefficients around these non-contacting horizontal cylinders are calculated. The present results compare well with those available in the literature. The numerical results provide an insight into the cooling mechanisms within beds of unsaturated porous media.

5.2 Experimental Setup and Numerical Model

A full description of the experimental setup is given in Chapter 2. However, recapitulating briefly, the system investigated in this chapter consists of a column of cylinders, the axes of which are parallel and located one above the other, as shown in Figures 2.38 and 2.39. Water is introduced on to the array of cylinders through a nozzle located above the top cylinder. Each cylinder is hollow, and a heat flux is imposed on the inner wall of the annulus by means of resistance heaters located axially within the centres of the cylinders.

Numerical simulations have been performed using the liquid mass flow rates per unit length of 0.0125, 0.025, 0.0625, 0.125, 0.2, 0.325, 0.5 and 0.75 kg/(m.s), to achieve Reynolds numbers of 50, 100, 250, 500, 800, 1300, 2000 and 3000, respectively. For the numerical simulations, the water velocity is assumed to be uniform at the velocity inlet as shown in Figure 5.1

The heat transfer model described in this chapter differs from that described in Chapter 2 and Appendix A where a single cylinder was studied made of different materials for heat transfer characteristic with no flow.

In this chapter, it is necessary to model the cylinder as a solid in order to study the temperature distribution inside the cylinder as shown in Figure 5.1. Whereas for flow field cases as described previously in Chapter 4, a solid cylinder is not necessary, due to the study focusing on the outside shell of the cylinder where all cylinders are treated as surfaces. The flow field results of chapter 4 are used in this chapter.

The grid has been generated in GAMBIT[®]. A commercial finite-volume CFD code, FLUENT[®] has been used to implement 2D simulations. Half of the domain has been modelled in order to obtain faster solutions. The boundary conditions have been imposed as indicated in Figure 5.1. The radius of the cylinders is 0.05 m, the radius of the axially located electrical resistance heater is 0.02 m, as shown in Figure 5.2. Three regions have been specified, namely, the air, the liquid flow and the solid cylinder.

A tri-pave mesh has been generated for the fluid and solid domain using a boundary layer technique, where the boundary layer around the cylinder is relatively small. This boundary layer thickness has been found to accurately capture phenomena that occur in the liquid adjacent to the cylinder walls as shown in Figure 5.2.

A size function technique has been employed to smoothly control the growth in the mesh size over a particular region of the geometry starting from a source or origin. It can also be used for smooth transition from a fine mesh needed to resolve flow physics with curved geometries and to model flows in thin gaps. The grid generation, boundary layer and the size function technique are shown in Figure 5.2. The details of grid generation, boundary layer and the size function technique are described in Section in 2.2.

To study the effect of cylinder diameter on heat transfer coefficient, three geometries have been modelled for in an arrangement of three cylinders. The first one is for a cylinder diameter of 0.1 m, the second is for a cylinder diameter of 0.022 m, and the third is for a cylinder diameter of 0.132 m with the same feeder height of 0.003 m. These three models are used for comparisons with the present experimental results, numerical and published values from the literature.

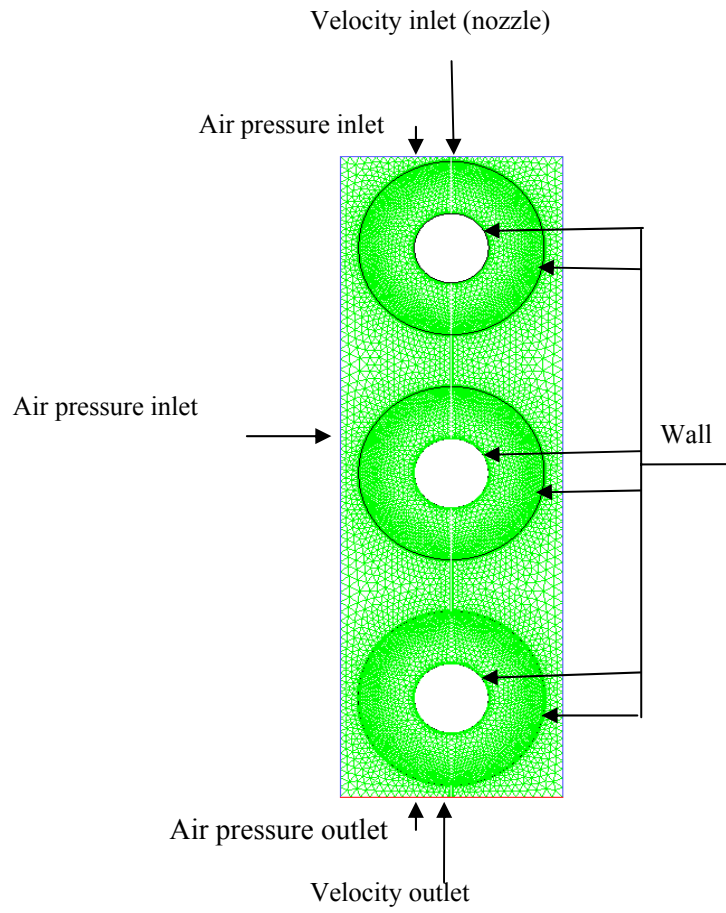


Figure 5.1. The physical configuration of the system.

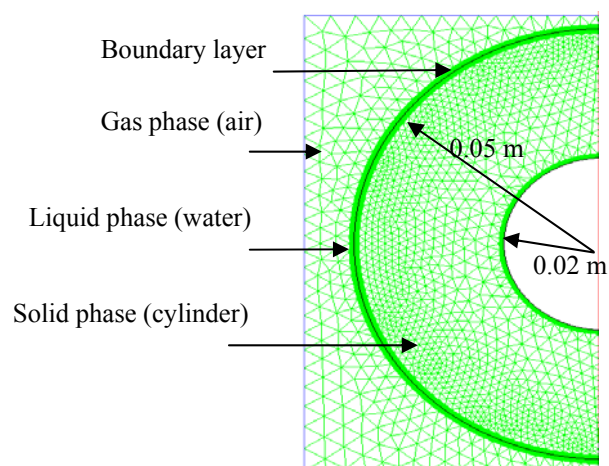


Figure 5.2. Details of the grid in the vicinity of the cylinder surface.

In Table 5.1, the 2D simulation settings in FLUENT[®] are listed. In Table 5.2, the range of numerical conditions is given for velocity, liquid flow rate and Reynolds number. In Table 5.3, the constant parameters employed in FLUENT[®] are listed.

Table 5.1. FLUENT[®] 2D simulation settings for half domain.

Settings	Choice
Simulation	2D
Solver	Segregated implicit
Model	VOF
Material	Air–primary; water–secondary
Gravitational acceleration	-9.81m/s ²
Volume fraction	1 for water and 0 for air
Top right boundary	Velocity inlet
Top left boundary	Air pressure inlet
Left side boundary	Air pressure inlet
Right side boundaries	Symmetry
Bottom left boundary	Air pressure outlet
Bottom right boundary	Velocity outlet
Wall boundary	Cylinder wall and heater wall

Table 5.2. Numerical conditions.

Inlet velocity (m/s)	Liquid flow rate Γ (kg/m.s)	Reynolds number (Re)
0.0025	0.0125	50
0.005	0.025	100
0.01252	0.0625	250
0.025	0.125	500
0.04	0.2	800
0.0651	0.325	1300
0.1	0.5	2000
0.15	0.75	3000

Table 5.3. Constant parameters.

Parameter	Magnitude	Units
Liquid thermal conductivity (k)	0.6	W/(m.K)
Liquid specific heat (C_p)	4180	J/(kg.K)
Liquid dynamic viscosity (μ)	0.001003	kg/(m.s)
Liquid kinematic viscosity (ν)	$9.79e^{-7}$	m^2/s
Liquid density (ρ)	998.2	kg/m^3
Cylinder diameter (d)	0.022, 0.1, 0.132	m
Cylinder separation (\bar{s})	0.01	m
High of feeder (S)	0.05, 0.01, 0.03	m
Heat flux (q'')	50 – 171.368	kW/m^2
Inlet liquid temperature, (T)	5	$^{\circ}C$

5.3 Interpretative Framework

The differential equations that govern heat and momentum transfer have been presented in Chapter 2.

The local heat transfer coefficient, h_{ϕ} varies with the angular position ϕ along the circumference of the heated cylinder. The local heat transfer coefficient is defined as,

$$h_{\phi} = q'' / (T_w - T_m) \quad (5.1)$$

where q'' is the heat flux at the surface of the cylinder which is produced by an internal electric heater in this study, T_w is the local wall temperature on the cylinder, and T_m is the local average temperature of the film of water.

An average heat transfer coefficient, \bar{h} over the entire cylinder is defined as,

$$\bar{h} = 0.5\pi \int_0^{2\pi} h_{\phi} d_{\phi} \quad (5.2)$$

where ϕ is the angle measured anticlockwise from the top of the cylinder. Local calculations were carried out for $\phi = 0, 30, 60, 90, 120, 150$ and 180 . Reynolds number is expressed for the film flow as $Re = 4\Gamma/\mu$ where Γ is the liquid flow rate in the film per unit length and μ is the dynamic viscosity of the liquid film. The total flow rate over the top cylinder is divided by two to obtain the liquid flow rate Γ on one side.

The definitions of the local and average Nusselt numbers, respectively, are

$$Nu = (v^2/g)^{1/3} h_\phi/k \quad (5.3)$$

$$\overline{Nu} = (v^2/g)^{1/3} \overline{h}/k \quad (5.4)$$

where ν is the kinematic viscosity of the liquid, g is the gravitational acceleration, h_ϕ is the local heat transfer coefficient, \overline{h} is the average heat transfer coefficient, and k is the thermal conductivity of liquid.

5.4 Design of Heat Transfer in Liquid Film

In Figure 5.3, the flow regions in falling liquid film on a horizontal cylinder are shown. As the film flows around the cylinder, four regions develop: these are stagnation flow, impingement flow, thermal boundary layer developing and fully developed regions Fujita and Tsutsui (1995a). These regions are investigated next.

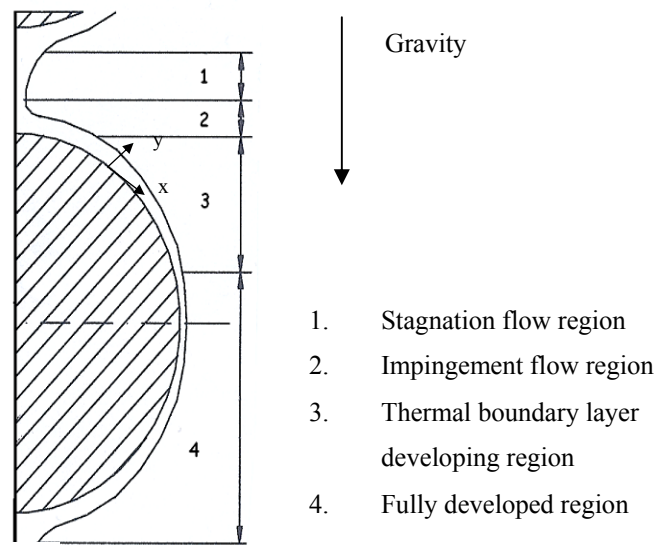


Figure 5.3. Model for falling liquid film on two heated horizontal cylinders. Fujita and Tsutsui (1995a)

5.4.1 Jet Impingement Region

Since the film thickness is much smaller than the cylinder radius and also that the impinging jet flow is expected to be influential only in a short region, the flow at the top of the horizontal cylinder is considered to be similar to a liquid jet flow impinging on a flat plate (as discussed previously in Section 3.4.4).

Heat transfer to a sheet of liquid jet has been studied by a number of authors, McMurray *et al.* (1966), Miyasaka and Inada (1980), Hu and Jacobi (1996), and Roques and Thome (2007) among others. According to Miyasaka and Inada (1980), the flow field can be divided into three zones, namely, the stagnation flow

zone which is characterized by the velocity field just outside the boundary layer, linearly proportional to the distance x from the stagnation point. The local heat transfer coefficient, h , in the stagnation flow zone can be expressed by the following equation:

$$h = 1.03 \text{Pr}^{1/3} k \left[\frac{\partial(V_y/V_j)}{\partial(x/w)} \cdot \frac{V_j}{\nu w} \right]^{0.5} \quad (5.5)$$

where Pr is the Prandtl number, k is the thermal conductivity, V_y is the maximum velocity within the impingement region, V_j is liquid jet velocity, x is the distance along the heating surface, w is the jet width and ν is the kinematic viscosity. As shown in Figure 5.4, the stagnation flow zone of the present numerical work is characterized by the sharp velocity gradient between $x = 0$ and $x = 0.5\text{m}$.

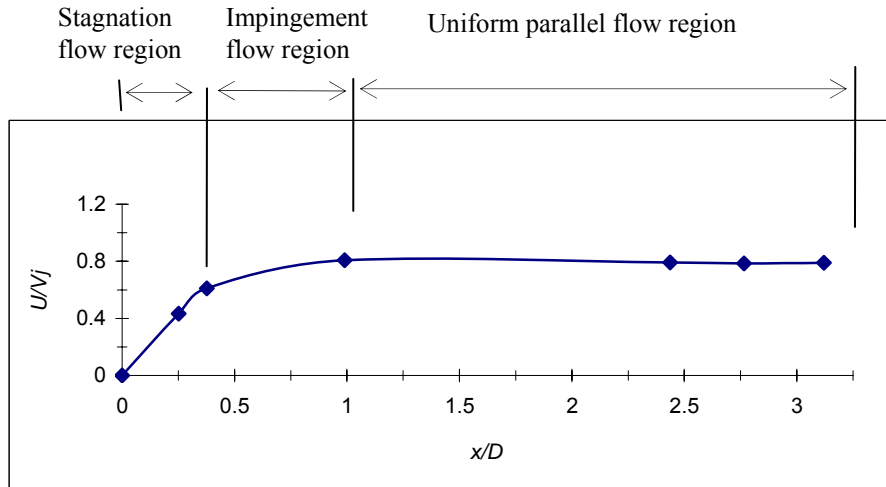


Figure 5.4. Distribution of velocity in the jet impingement region for $\text{Re} = 500$ where U is the main velocity, V_j is the liquid jet velocity, x is the distance along the heated surface and D is the nozzle diameter.

5.4.2 Developing Thermal Boundary Layer Region

The analysis for the thermal boundary layer development region is based on the following assumptions

- The flow is laminar,
- The entire surface of the cylinder is completely wet,
- There is no boiling within the film,
- Heat transfer is only by conduction across the film,
- The fluid properties remain constant, and
- The simulation is unsteady until a quasi steady state solution is attained.

According to the data reported by Chyu and Bergles (1987), the film thickness has been calculated in the thermal developing region, with the following equation:

$$\delta_{\phi} = \left[\frac{3\mu\Gamma_{\phi}}{g\rho_l(\rho_l - \rho_a)\sin\phi} \right]^{1/3} \quad (5.6)$$

where δ_{ϕ} is the film thickness at the angular position, μ is dynamic viscosity, Γ is the mass flow rate of film per unit length on one side of the cylinder, g is the acceleration of gravity, ρ_l is liquid film density and ρ_a is air density.

Rogers and Goindi (1989) measured the film thickness of water falling on a large diameter horizontal tube. The following correlation is given for the film thickness:

$$\frac{\delta}{D} = 1.186 \text{Re}^{1/3} \text{Ar}^{-1/3} \quad (5.7)$$

where δ is film thickness, D is the diameter of the cylinder, Re is Reynolds number and Ar is Archimedes number which is calculated as follows:

$$\text{Ar} = g\rho^2 D^3 / \mu^2 \quad (5.8)$$

Ouldhadda *et al.* (2002) evaluated the thickness of liquid film as a function of the polar angle, ϕ , for different values of mass flow rate per unit length, governed by the following equation:

$$\delta = \left[\frac{(2n+1)\Gamma}{n\rho \left(\frac{\rho g \sin \phi}{K} \right)^{1/n}} \right]^{n/(2n+1)} \quad (5.9)$$

where n is the flow behaviour index which is equal to 1 for water, Γ is mass flow rate, ρ is the liquid density, g is gravity, and \bar{K} is the fluid consistency index which is equal to 1.071×10^{-3} Pa s for water.

At a desired Reynolds number or liquid flow rate, the film thickness approaches infinity toward the top and the bottom of the cylinder, as shown in Figure 5.5. It is observed that as the simulation reaches a quasi steady state, the temperature profile becomes more and more linear within the time. The temperature profile in the thermal developing film is presented in Figure 5.6.

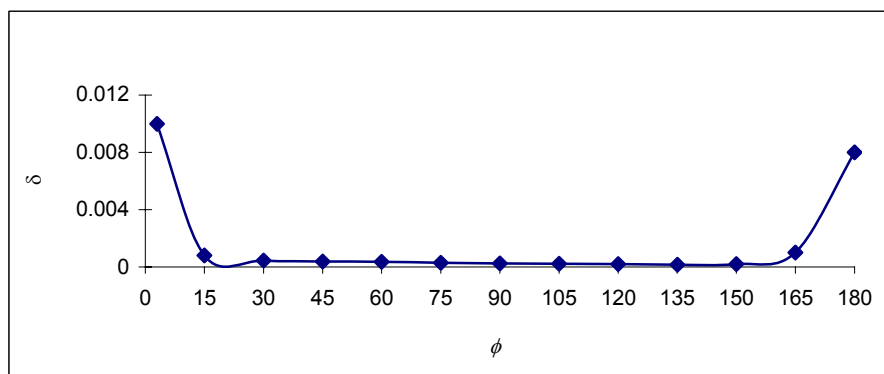


Figure 5.5. Variation of liquid film thickness around the cylinder with respect to angular position at liquid mass flow rate of 0.6 kg/ms.

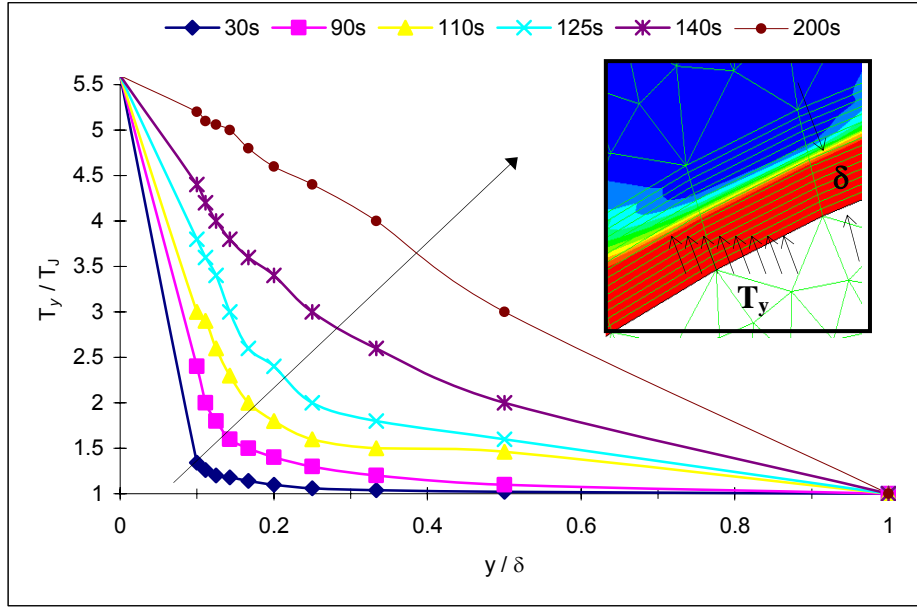


Figure 5.6. Temperature profile development over time of liquid film in thermal boundary layer development region. y is the location in x-axis, δ is the water film thickness, T_y is the local temperature in the water film and T_j is the liquid jet temperature at $Re = 1200$.

5.4.3 Fully Developed Region

The fully developed region is based on the assumption that heat transfer is only by conduction across the liquid film. Chun and Seban (1972) adopted the following correlations which are based on experimental data.

For laminar flow

$$\frac{\bar{h}}{k} \left(\frac{v^2}{g} \right)^{1/3} = 1.10 Re^{-1/3} \quad (5.10)$$

For wavy-laminar flow

$$\frac{\bar{h}}{k} \left(\frac{v^2}{g} \right)^{1/3} = 0.822 Re^{-0.22} \quad (5.11)$$

All variables are as defined earlier in this section.

5.5 Effect of Falling Film Modes on Heat Transfer Characteristics

The flow and heat transfer interactions are essentially different for each of the falling film modes. The flow behavior has been described in detail in Chapter 4, while the heat transfer behavior has been investigated in detail in this chapter.

5.5.1 Heat Transfer Coefficient for the Droplet Mode

At low Reynolds numbers, the liquid falls in the droplet mode and the average heat transfer coefficient and Nusselts number show a strong dependence on the Reynolds number, as shown in Figure 5.7. The Reynolds number dependence in the droplet mode is related to the dripping frequency. According to Maron-Moalem *et al.*(1978), the dripping frequency for water increases almost linearly with Reynolds number. This effect has been observed during the present experiments.

The heat transfer coefficient varies significantly in both the axial and circumferential directions on the cylinder surface. The droplet impingement zone, which is relatively larger than the jet or sheet impingement zones, shows higher Nusselt numbers than over the rest of the cylinder.

The size of the droplet impingement region is related to the size of the droplets. At low Reynolds numbers, the droplet impingement sites are alternatively active and the momentum interaction among neighbouring droplet sites apparently has little heat transfer effect. The effect of heat transfer coefficient on Reynolds number in the droplet mode is due to the increase of droplet frequency with increasing Reynolds number.

5.5.2 Heat Transfer Coefficient for the Jet Mode

At higher Reynolds numbers when approaching a transition from droplet to jet mode or when two neighbouring droplet sites become active, the heat transfer in the jet mode exhibits significant axial and circumferential variation. In this type of mode, the heat transfer is high in the jet impingement regions along the top of the cylinder. The Nusselt number is relatively low elsewhere and decreases with

distance from the impingement sites. The enhanced heat transfer of the impingement region is due to the surface normal velocities and velocity gradients associated with jet stagnation. In the jet mode, the average heat transfer coefficient increases with the Reynolds number, but the dependence is less pronounced than for the droplet mode. The effect of heat transfer coefficient on Reynolds number in the jet mode is due to the increase of heat transfer coefficient in the impingement region more than what occurs in droplet mode. The average Nusselt number for jet region is shown in Figure 5.7.

5.5.3 Heat Transfer Coefficient for the Sheet Mode

For falling film in sheet mode, the Nusselt number still exhibits a Reynolds number dependence as shown in Figure 5.7. In this mode, the heat transfer coefficient in the impingement region is higher than in the jet and droplet modes, due to greater heat removal. In Figure 5.7, the present experimental and numerical results are presented for the variation of the average Nusselt number with Reynolds number. Different liquid film modes are identified based on visual inspection. Numerical results are verified with the experimental ones.

The local Nusselt number depends on its circumferential location at the same liquid flow rate and Reynolds number, as shown in Figure 5.8 for the sheet mode. It is high close the stagnation point at $\phi = 0^\circ$, and decreases downstream due to the development of the thermal boundary layer. The Nusselt number is high in the impinging zone and relatively low elsewhere and decreases with distance from the impingement zone.

In Figure 5.8, variation in the local heat transfer coefficient is presented as a function of the position on each of the three cylinders at a Reynolds number of 3000 corresponding to sheet mode. Again, the experimental and numerical results show similar trends. There were problems associated with controlling the liquid flow rate experimentally. The difference between the experimental and numerical results might come for this difficulty.

Along the bottom of the cylinder, there appears to be a small increase in the heat transfer coefficient. When a sheet falls onto a cylinder, the liquid is rapidly decelerated in the surface normal direction and accelerated in the circumferential direction, downstream of the impingement region, as the flow around the cylinder is accelerated by gravity. The Nusselt number reaches a relatively constant value in the region where the flow is fully developed.

As a result of the flow velocity increasing in the circumferential direction and decelerating rapidly towards the surface, the heat transfer coefficient is the highest in the impingement area. Then, under the effect of the gravity, the liquid film develops over the cylinder. There is some increase in the heat transfer coefficient obtained from numerical simulations at the bottom of the cylinder where $\phi = 180$, when the flow leaves the cylinder to the one below.

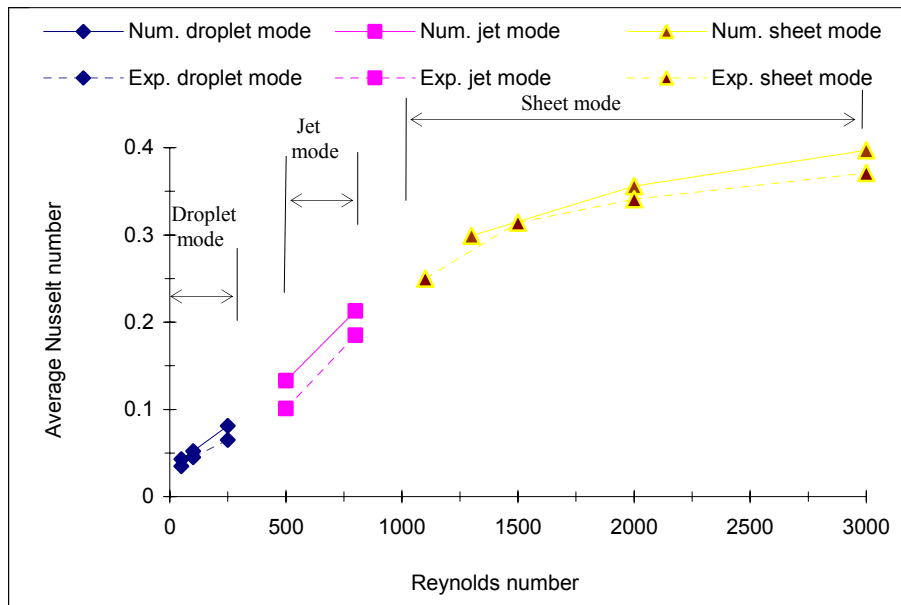


Figure 5.7. Average Nusselt number for droplet, jet and sheet modes at different Reynolds numbers.

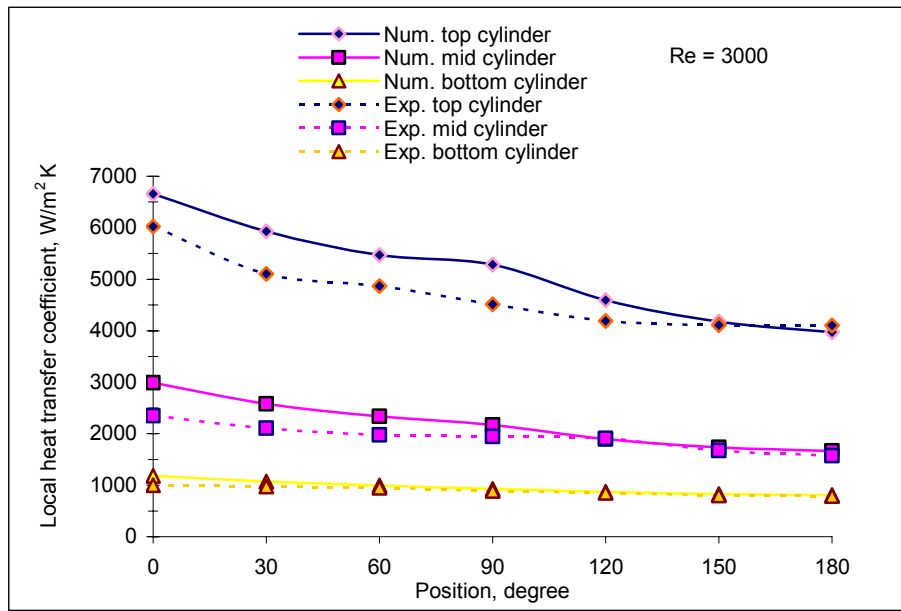


Figure 5.8. The modelled variation of local heat transfer coefficient as a function of the angle ϕ at sheet mode of at Re of 3000.

5.6 The Effects of Operating Conditions and Geometry on the Heat Transfer

5.6.1 Liquid Flow Rate, Γ and Reynolds Number, Re

The heat transfer coefficient is dependent on the flow rate of the liquid film and Reynolds number. When the liquid flow rate increases, the heat transfer coefficient increases. Transition from laminar flow to wavy laminar or to turbulent flow can also occur. According to Brumfield and Theofanous (1976) the film can be fully turbulent for Reynolds numbers higher than 6000. They suggest that the film is controlled by wave structures imposed on the base film flow. Ouldhadda *et al.*(2002) consider laminar flow for Re up to 4000 and transition from laminar to turbulent flow when $Re \cong 4000-6000$.

Increasing the flow rate of the liquid means increasing its velocity which causing a change of the flow mode from drop to jet to sheet modes. As shown in Figure 5.9, increasing the flow velocity for each cylinder has a proportional effect on heat transfer. This effect is most clearly seen in the case of the top cylinder.

When the liquid film is heated over the circumference, the local liquid temperature is always higher than the liquid inlet temperature. The results presented in Figures 5.10, 5.11 and 5.12, for the top, middle and bottom cylinders respectively, confirm that when the liquid flow rate increases (increasing Reynolds number), the heat transfer coefficient increases. The highest heat transfer coefficient is at $\phi = 0^\circ$ and lowest at 150° . At 180° , the heat transfer coefficient is slightly above or equal to that at $\phi = 150^\circ$. As shown in Figure 5.10, as the Reynolds number increases from 500 to 3000, the local heat transfer coefficient at the stagnation point where $\phi = 0^\circ$ increases from $2581 \text{ W/m}^2 \text{ K}$ to $6660 \text{ W/m}^2 \text{ K}$ (an increase of 158%). This is to repeat what has been said before in Section 5.5.3

It can be seen from Figures 5.10, 5.11, and 5.12 that the highest heat transfer rate occurs in the stagnation area where $\phi = 0^\circ$. This is due to the thermal boundary layer being very thin in this region, and its constant replenishment with cold water. As shown in Figure 5.10 for a Reynolds number of 3000, the local heat transfer coefficient at $\phi = 0^\circ$ is 6660 whereas at $\phi = 180^\circ$, it is 4974 (increase by 67.5 %). The stagnation point heat transfer has been found to be a stronger function of Reynolds number than at other locations around the cylinder.

It can also be seen from Figures 5.10, 5.11 and 5.12 for top, middle and bottom cylinders respectively, that the heat transfer coefficient is the highest on the top cylinder followed by on the middle cylinder, and lowest on the bottom cylinder. For example, at a Reynolds number of 2000, the local heat transfer at $\phi = 0^\circ$ for the top cylinder as shown in Figure 5.10 is $6195.5 \text{ W/m}^2 \text{ K}$. At the same Reynolds number of 2000 for the middle cylinder, it can be seen in Figure 5.11 that the heat transfer coefficient is $2072 \text{ W/m}^2 \text{ K}$ at $\phi = 0^\circ$. Hence the heat transfer coefficient for the top cylinder is higher by 119 % compared to that for the middle cylinder. At the bottom cylinder, for the same Reynolds number of 2000 and the same position as shown in Figure 5.12, the heat transfer coefficient is $877.9 \text{ W/m}^2 \text{ K}$, indicating that the heat transfer coefficient for the middle cylinder is higher by 136 % compared to that for the bottom cylinder. For this Reynolds number, the heat transfer coefficient for the top cylinder is 605% of that for the bottom cylinder.

In Figures 5.13 and 5.14, the agreement with the literature is shown for the heat transfer distribution around the circumference of the cylinder. The variation of average Nusselt number is presented in Figure 5.15 with different values of liquid flow rate Γ (different Re) and different positions (top, middle and bottom cylinders). It can be observed that the heat transfer coefficient, which is directly proportional to Nu , is high at the top and decreases for the middle and bottom cylinders. This means that the better temperature distribution occurs at higher Reynolds number.

In Figure 5.16, the wall temperature is given for the three cylinders (top, middle and bottom) at the stagnation point for different liquid flow rates (different Reynolds numbers) in quasi-steady state for a cylinder diameter of 0.1 m. The stagnation point wall temperature falls rapidly with increasing Reynolds number for the three cylinders, due to increasing heat transfer coefficient. The temperature for the top cylinder is equal to 31°C, 26°C, 17°C, 12°C, 9°C, 7.8°C, 6.2°C, 5.3°C for $Re = 50, 100, 250, 500, 800, 1200, 2000,$ and 3000, respectively. The temperature for the middle cylinder is equal to 39°C, 36°C, 31°C, 27°C, 24°C, 17°C, 13°C, 11°C for $Re = 50, 100, 250, 500, 800, 1300, 2000,$ and 3000, respectively. It can be seen from the same figure that the temperature for the bottom cylinder is equal to 42°C, 40°C, 39°C, 34°C, 32°C, 28°C, 22°C, and 19°C for $Re = 50, 100, 250, 500, 800, 1200, 2000,$ and 3000, respectively. These results mean, for example at $Re = 50$, that at the stagnation point, the experimental wall surface temperature decreases from 42°C to 39 °C to 31 °C for the bottom, middle and the top cylinders, respectively. The drop of the wall surface temperature for the top cylinder at $\phi = 0^\circ$ is 35% compared to the bottom cylinder at the same position.

The surface wall temperature for the top, middle and bottom cylinders at different Reynolds numbers is captured with a thermal imaging camera, Neo Thermo, type TVS-700 Radiometric UFPAIR to verify the numerical results. The surface wall temperature for the top, middle and bottom cylinders is illustrated in Figures 5.17 and 5.18 from numerical simulations and thermal photographs, respectively. In these figures, the temperature distribution is presented for the three cylinders at different Reynolds numbers where droplet, jet and sheet modes are represented.

These two figures agree that the cylinder wall temperature decreases significantly with increasing Reynolds numbers, because the flow mode changes from droplet to jet, and then, to sheet mode. Also, when the Reynolds number increases, the average heat transfer coefficient also increases, because the heated surface is cooled more by the increased liquid flow rate. Consequently, the difference between the wall and the liquid temperatures decreases.

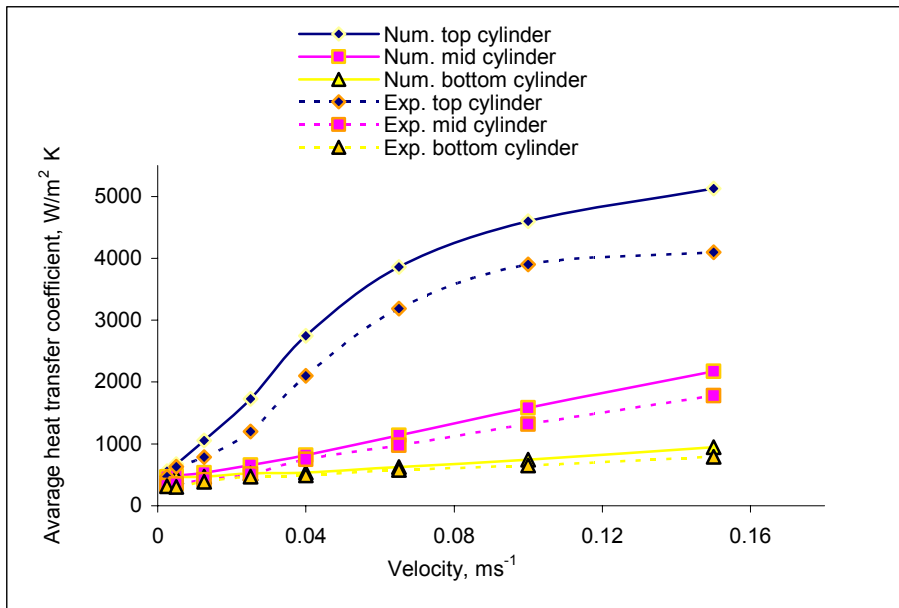


Figure 5.9. Effect of the cooling water velocity on the average heat transfer coefficient.

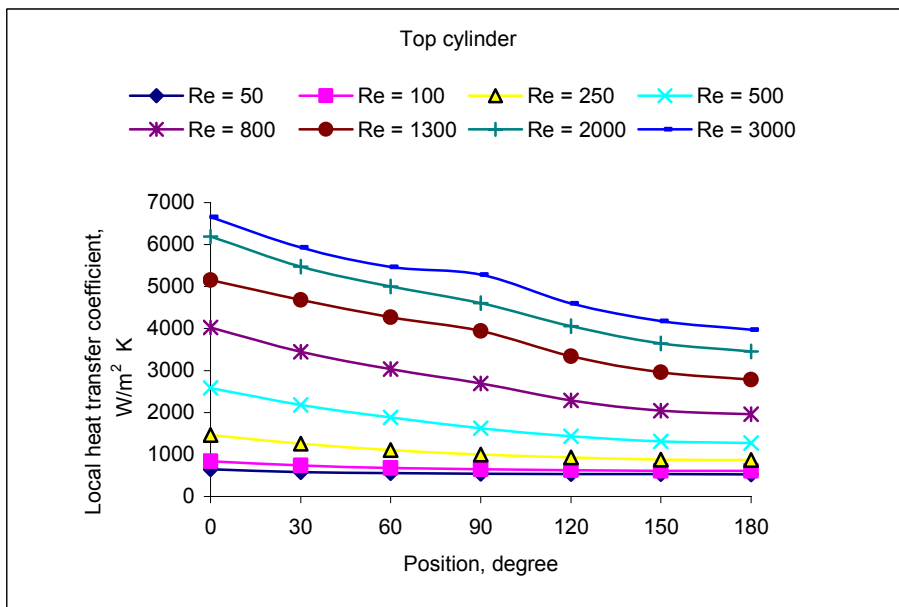


Figure 5.10. Effect of the liquid flow rate and Re on heat transfer coefficient for the top cylinder of 0.1 m diameter.

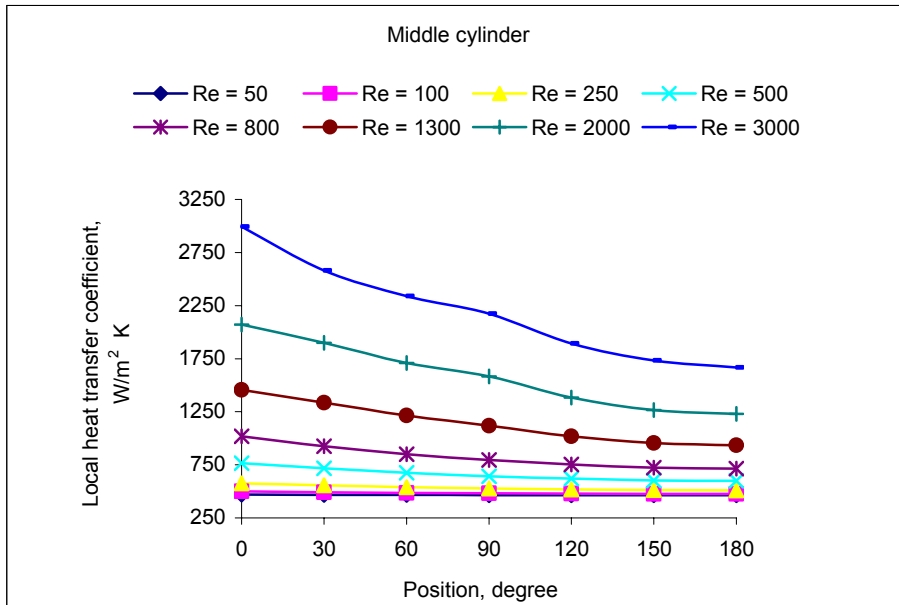


Figure 5.11. The effect of the liquid flow rate and Re on the heat transfer coefficient for the middle cylinder of 0.1 m diameter.

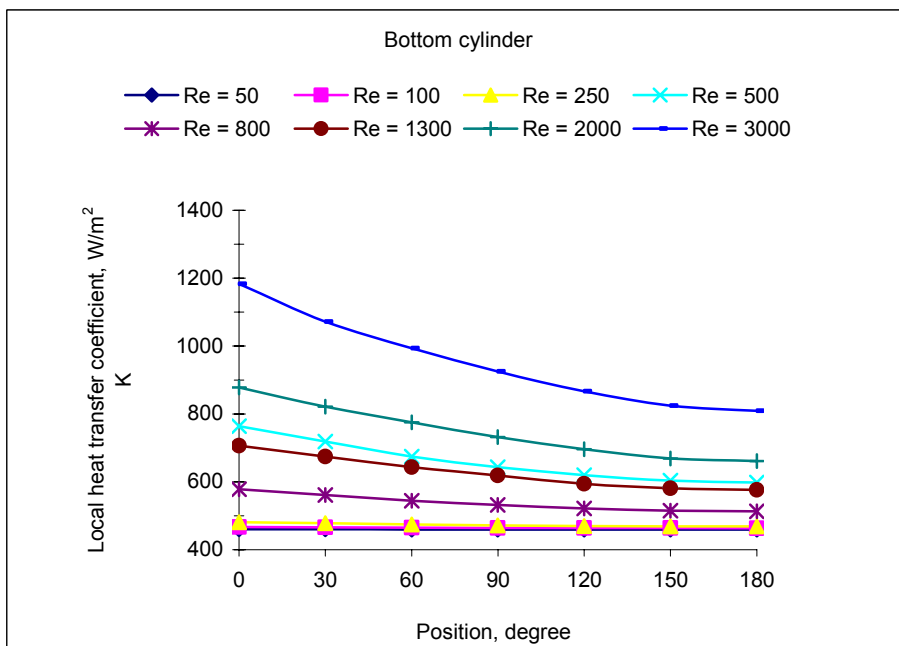


Figure 5.12. The effect of the liquid flow rate and Re on the heat transfer coefficient for the bottom cylinder of 0.1 m diameter.

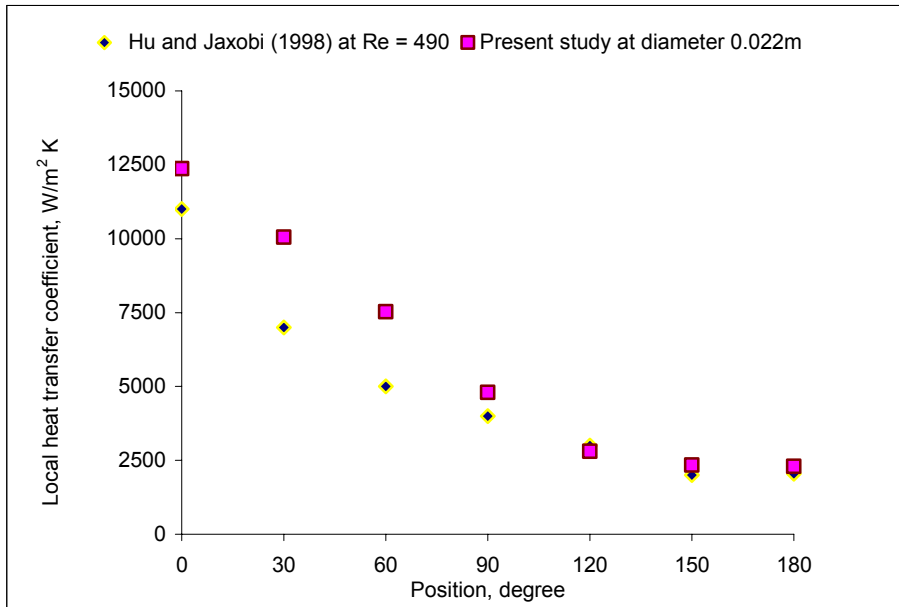


Figure 5.13. The distribution of the local heat transfer coefficient around the circumference of the cylinder at Re = 500, cylinder diameter 0.022 m.

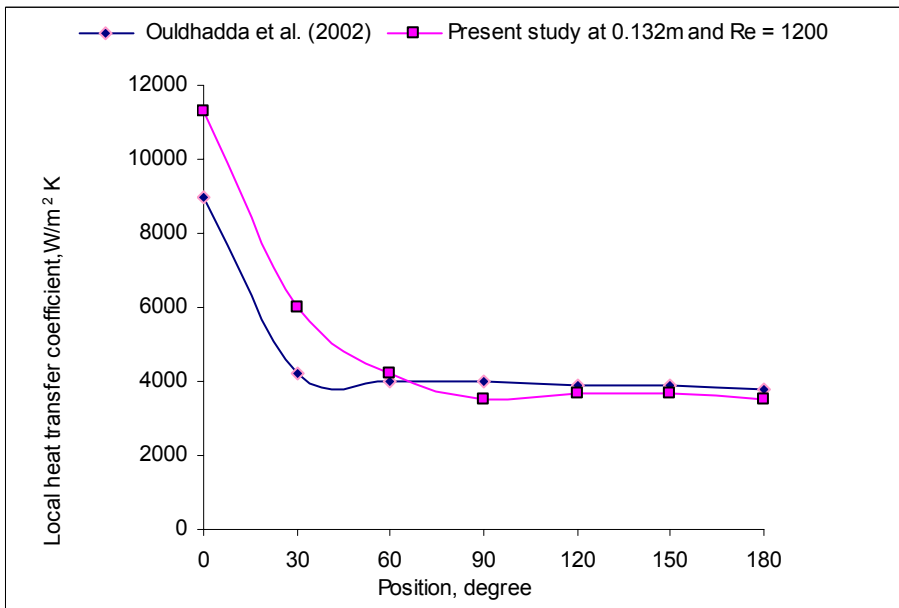


Figure 5.14. The distribution of heat transfer coefficient around the circumference of a cylinder diameter of 0.132 m, Re = 1300, compared with Ouldhadda *et al.* 2002.

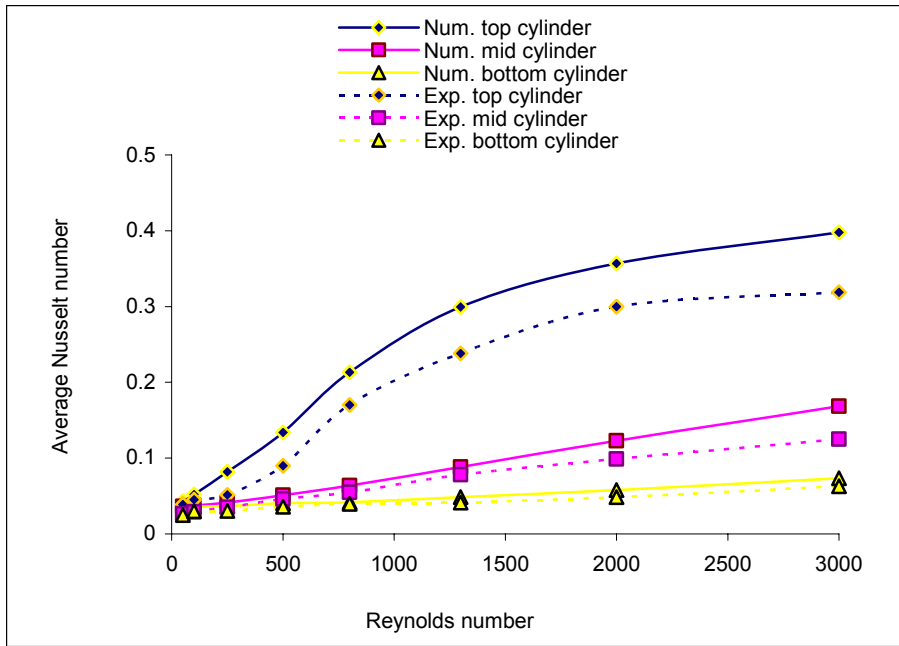


Figure 5.15. The effect of Reynolds number on the average heat transfer coefficient or the average Nusselt number and the position of the cylinder.

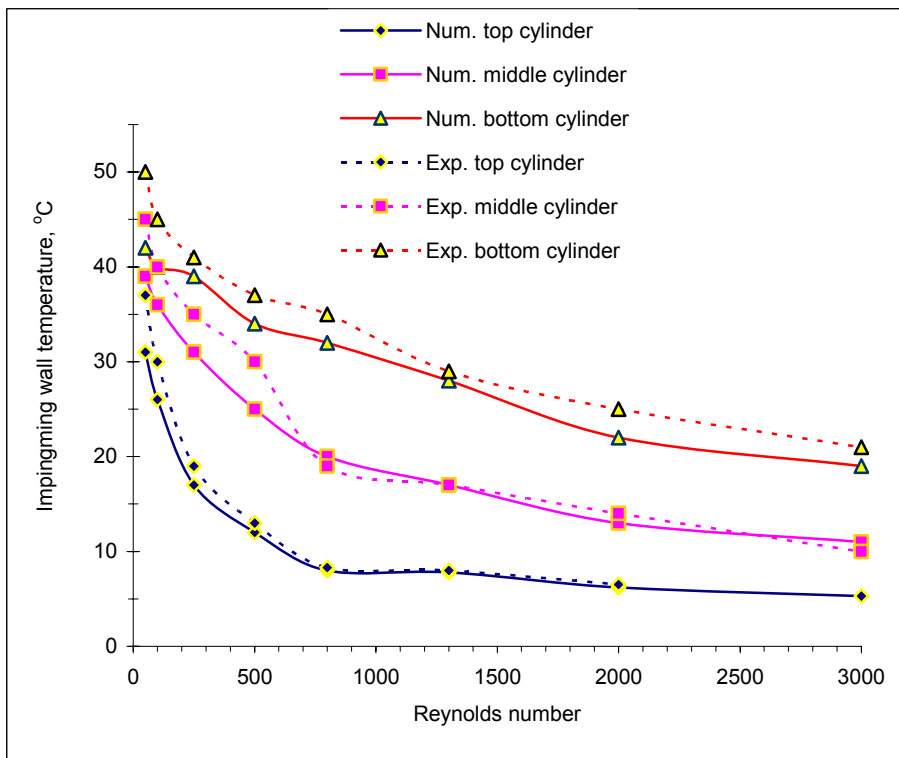


Figure 5.16. Impinging wall temperature for the top, middle and bottom cylinders where $\phi = 0$ at different Reynolds numbers.

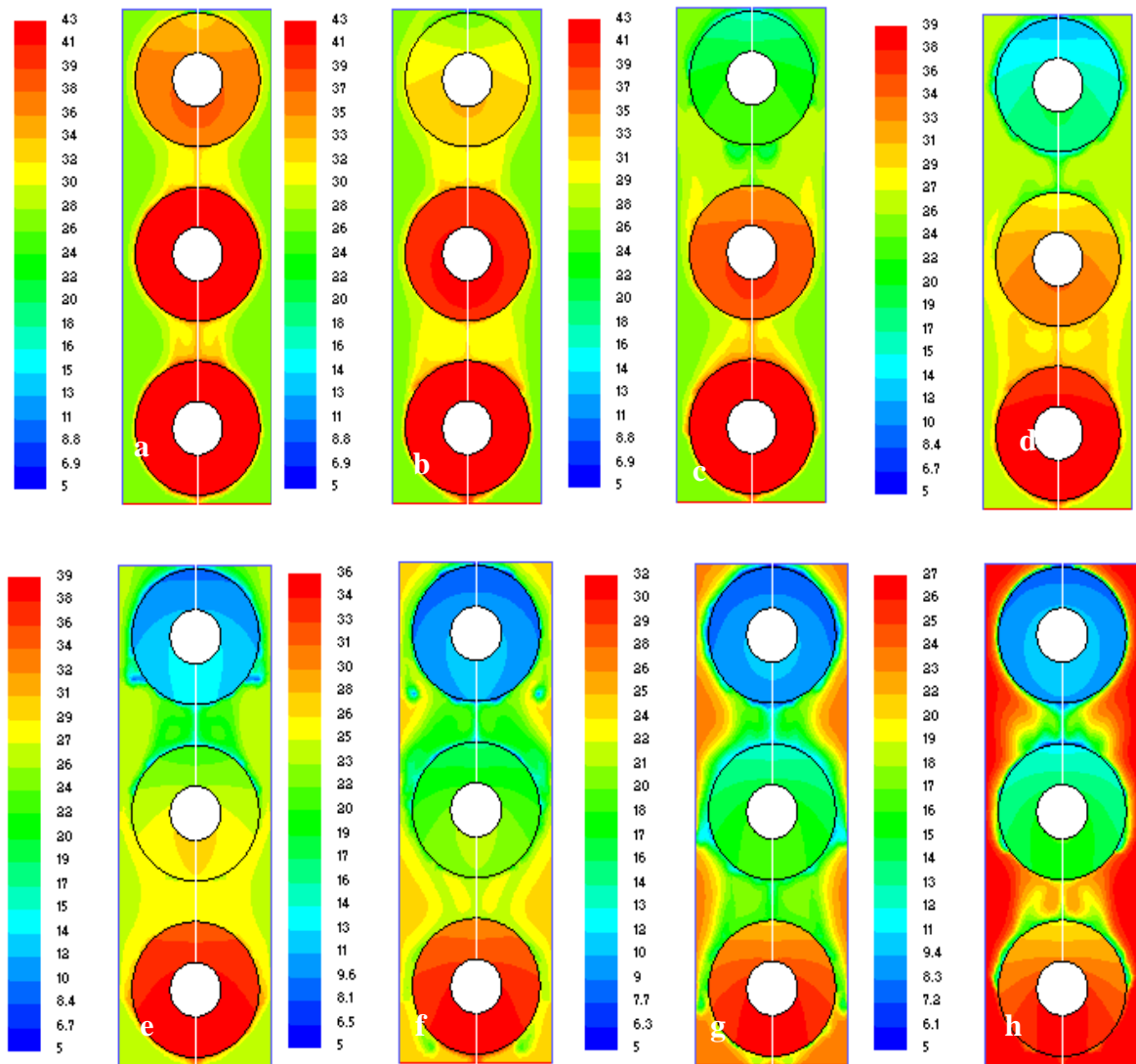


Figure 5.17. Temperature distributions in the top, middle and bottom cylinders at different Reynolds numbers. (a $Re = 50$, (b $Re = 100$, (c $Re = 250$ and (d $Re = 500$, (e $Re = 800$, (f $Re = 1300$, (g $Re = 2000$ and (h $Re = 3000$).

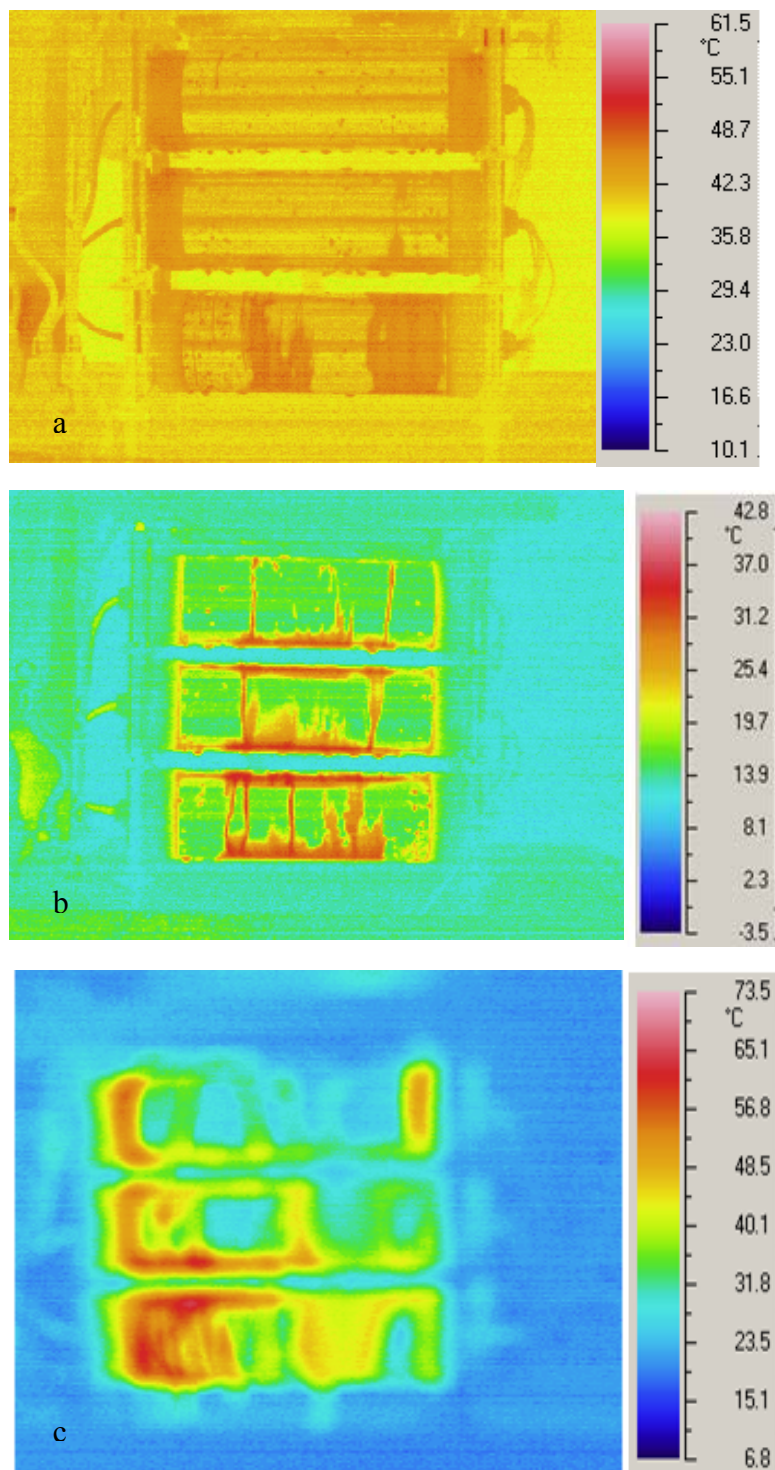


Figure 5.18. Thermal images photographs of temperature distributions in the top, middle and bottom cylinders at different Reynolds numbers. (a) Droplet mode, (b) jet mode, and (c) sheet mode.

5.6.2 Height of Feeder

The effectiveness of the heat exchanger was found to change with the displacement of the heating cylinder from the distributor, S . Three geometries with the same diameter of 0.1 m, the same separation distance of S of 0.01 m and different feeder heights of 0.005 m, 0.01 m and 0.03 m are shown in Figure 5.19. The corresponding temperature distribution for the three different nozzle heights is illustrated in Figure 5.20.

At a low Reynolds number such as 50 when the flow is in the droplet mode, a weak effect of S on heat transfer occurs as shown in Figure 5.21. This result is in agreement with Ganic and Roppo (1980). When the flow rate increases, the sheet mode occurs at a high Reynolds number such as 2000. The local heat transfer is the highest at the feeder height of 0.005 m. It decreases for the feeder height of 0.01 m, and the lowest for the feeder height of 0.03 m, as shown in Figure 5.22.

The change in the heat transfer coefficient with the cylinder displacement from the feeder must be due to the poor liquid coverage of the heated cylinder at a large displacement, resulting in ineffective heat exchange. At the desired Reynolds number, the heated cylinders at a small feeder height are covered with thicker liquid films which help to remove more heat from the heated cylinder, and then, enhance the convective heat transfer. These results disagree with Ribatski and Jacobi (2005) who noted that the heat transfer coefficient increased with increasing of S , as better spray distribution occurred. This disagreement may arise from their small cylinder diameter.

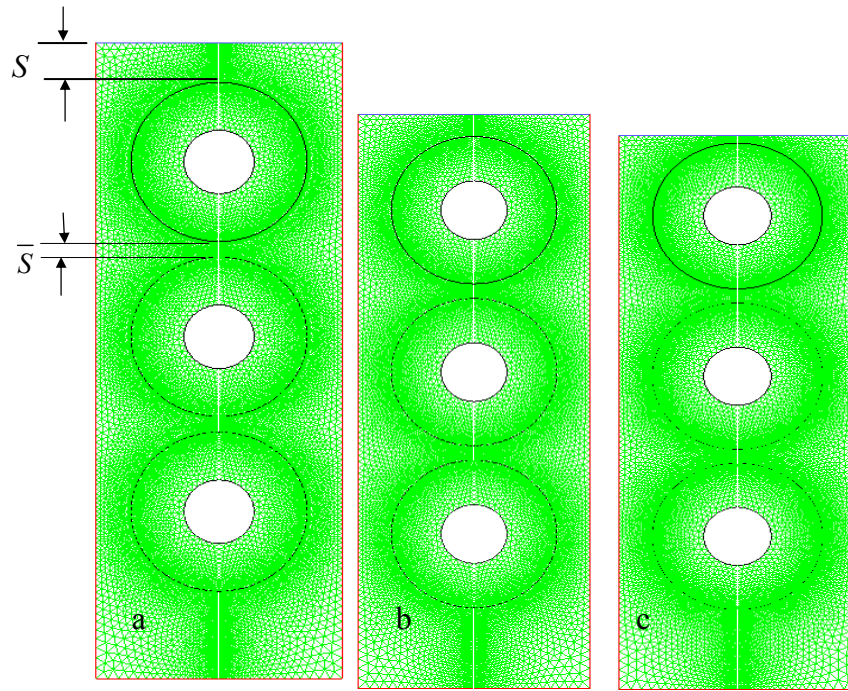


Figure 5.19. Three geometries with different nozzle heights, S : a) $S = 0.03$ m, b) $S = 0.01$ m, and c) $S = 0.005$ m.

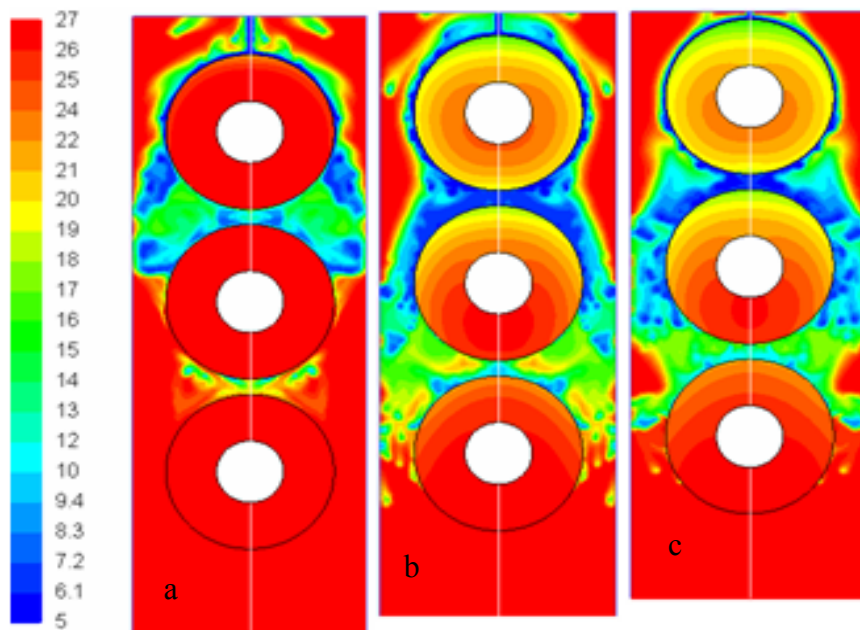


Figure 5.20. Temperature distribution at Re of 3000 for different nozzle heights, S . a) $S = 0.03$ m, b) $S = 0.01$ m, and c) $S = 0.005$ m.

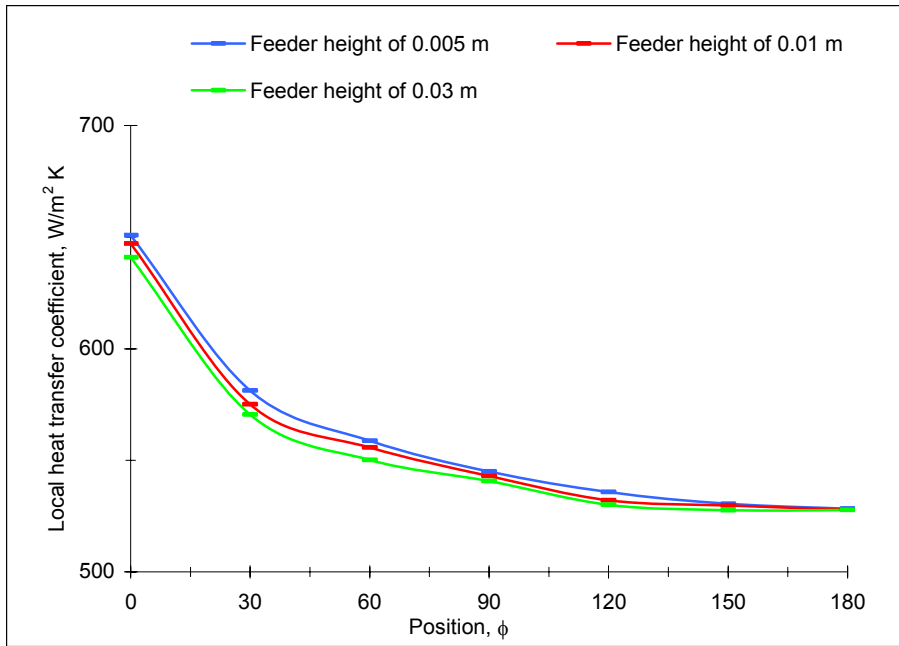


Figure 5.21. Local heat transfer coefficient for the top cylinder at $Re = 50$ for three nozzles heights, S , of 0.005 m, 0.01 m and 0.03 m.

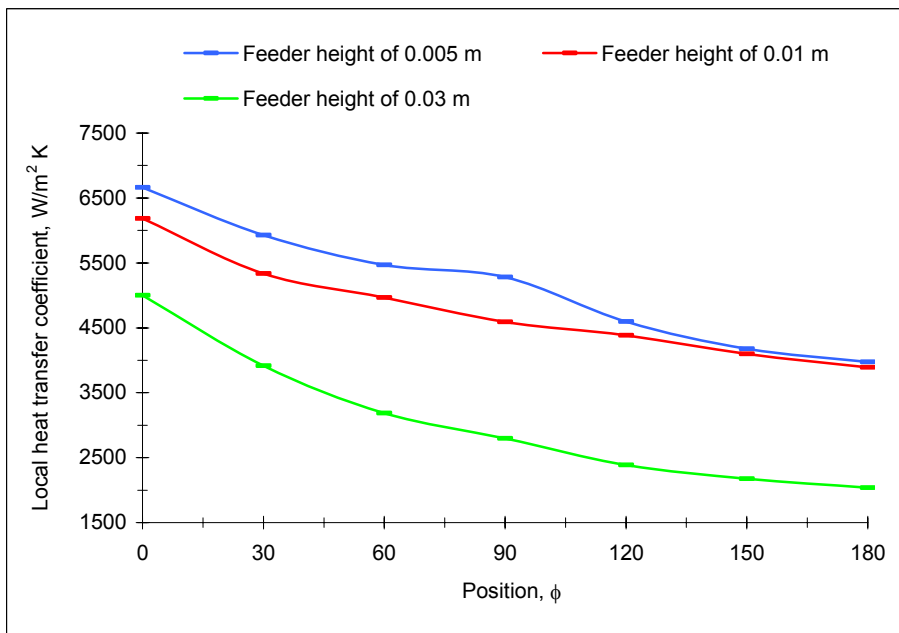


Figure 5.22. Local heat transfer coefficient for the top cylinder at $Re = 3000$ for three nozzles heights, S , of 0.005 m, 0.01 m and 0.03 m.

5.6.3 Cylinder Diameter

Cylinder diameter has a significant effect on the heat transfer coefficient as demonstrated by the results shown in Figure 5.23. The heat transfer coefficient is larger for the smaller diameter cylinder over the whole range of liquid flow rates or Reynolds numbers covering the droplet, jet and sheet modes. The effect of tube diameter on the heat transfer coefficient can be explained in terms of the boundary layer development. The film thickness is larger on a smaller diameter cylinder, keeping all other parameters constant, due to its smaller surface area. Therefore, the average heat transfer coefficient is also greater for a smaller diameter cylinder. It is expected, based on the results presented so far, that the largest contribution to the high average heat transfer coefficient on a smaller diameter cylinder must come from its impingement region.

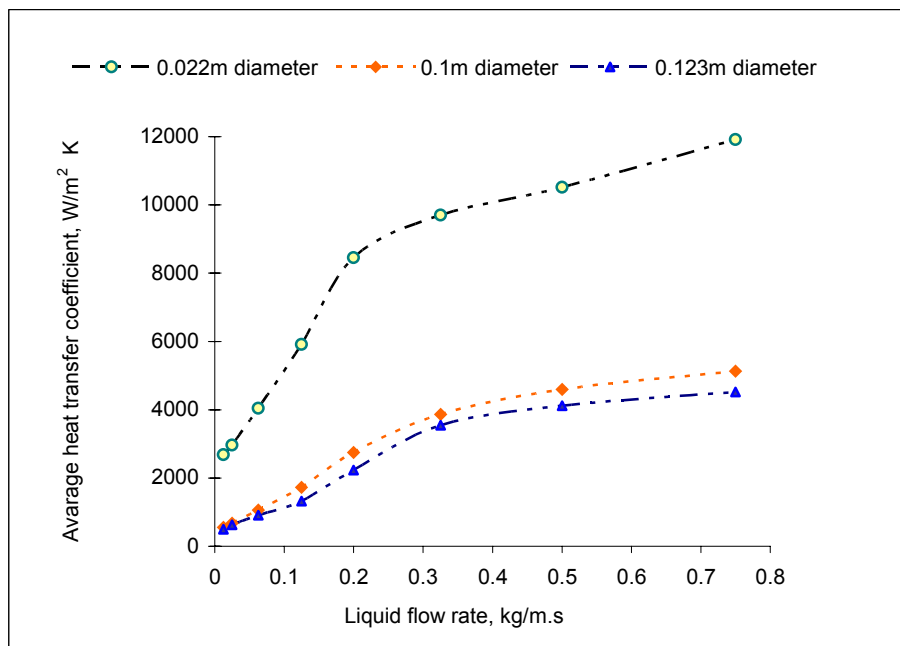


Figure 5.23. Effect of cylinder diameter on average heat transfer coefficient.

5.6.4 Heat Flux

The experimental and numerical results indicate that for completely wetted surfaces, the heat flux has no significant impact on the heat transfer coefficient as shown in Figure 5.24. In Figure 5.4, the variation of the average Nusselt number is presented with heat flux. Both experimental and numerical results are given, and the numerical results are verified with the experimental ones.

In the experiments and the numerical simulations, the cylinder diameter is 0.1 m, and the Reynolds number is 800. The heat flux on the cylinder surface is the range 50 - 171.368 kW/m². While the surface temperatures varied significantly, there is no significant change in the heat transfer coefficient.

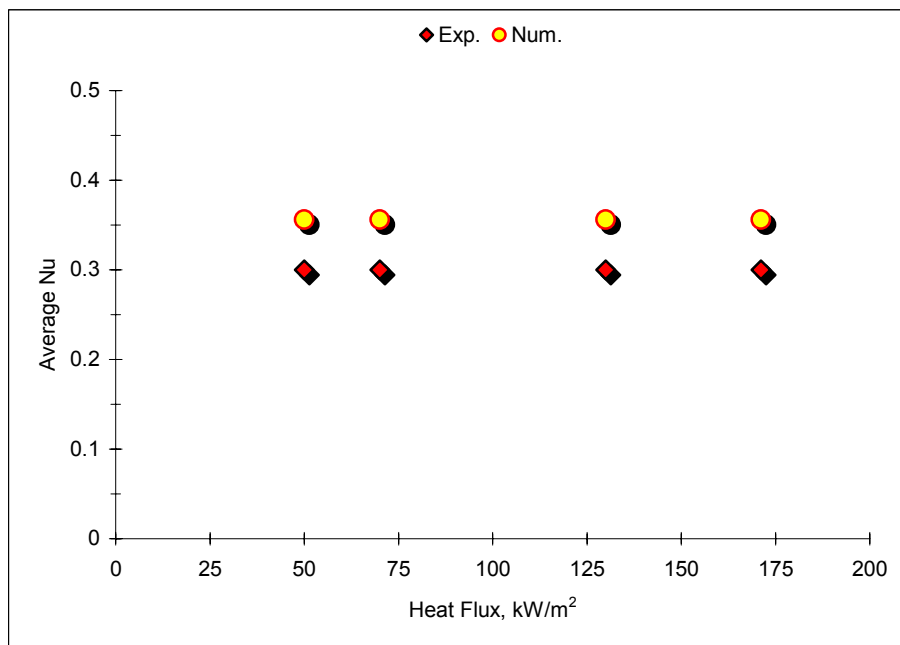


Figure 5.24. Effect of heat flux on average heat transfer coefficient.

5.7 Conclusions

Experimental work and numerical simulations with a commercial finite volume CFD code, FLUENT[®] have been used to study heat transfer to falling liquid film and the effect of different parameters such as liquid flow rate or Reynolds number, the height of the feeder, cylinder diameter and the heat flux on the heat transfer.

From the experimental and numerical results, the following can be concluded:

- Increasing the liquid flow rate and Reynolds number results in an increase in the heat transfer coefficient.
- The local heat transfer coefficients have been found to decrease gradually from a large value near the stagnation point where $\phi = 0^\circ$ due to the development of a thermal boundary layer.
- Decreasing the cylinder diameter results in an increase in the heat transfer coefficient.
- Decreasing the height of the nozzle results in an increase in the heat transfer coefficient.
- For the completely wetted surfaces, the heat flux has no significant impact on the heat transfer coefficient.

CHAPTER SIX

PERFORMANCE OF HYDROCOOLER SYSTEMS

Most fresh vegetables and fruits require cooling immediately after harvest to deliver the best quality product to the consumer. When warm produce is cooled directly by spraying it with chilled water, the process is known as hydrocooling, and the cooling device is known as a hydrocooler. From an engineering perspective, hydrocoolers contain three phase porous media.

Hydrocooling is an effective way to cool produce, such as asparagus, broccoli, sweet corn, green beans, carrots, celery, cherries, nectarines, parsley, peaches and more (Boyette *et al.* (1992) . In this chapter, the performance, design, construction and operation of hydrocoolers are described in detail.

6.1 Introduction

When horticultural products are harvested, it is highly recommended that they be cooled as soon as possible to reduce deterioration and to keep the product fresh to meet market requirements. Cooling allows the produce to maintain its flavour, texture and nutritional qualities.

Hydrocooling is a procedure in which fruits and vegetables are sprayed with cold water to reduce their temperature. The useful effects of hydrocooling include cleaning horticultural products and delaying fruit decay, ensuring that the surface of produce will not lose water. Instead, water will be absorbed, to keep fruits and vegetables looking fresh and clean. Cooling the horticultural produce immediately after harvest is a determining factor for their quality and durability in storage (Tonini *et al.* (1979).

Thorpe (2006) developed a mathematical model of a hydrocooler system. He noted that the heat transfer coefficient between the water and the produce increased with

the increasing of the flow rate. His results showed that the rate of cooling of horticultural produce also increased with the flow rate

Postharvest technologists need to calculate the temperature distribution along the bed of produce to ensure that all of the produce is adequately cooled. Therefore, the primary point of designing any cooling system is to calculate the rate of heat transfer between the cooling medium and the produce.

Hydrocooling involves three phases, namely, solid (the produce), liquid (the water) and gas (the air). In this chapter, types of hydrocoolers are investigated. The design and operation of a type of hydrocooler smart water are, studied in detail. The results of experiments with this in hydrocooler system to cool broccoli are presented. These results are interpreted, where possible, in the light of the experimental and numerical work presented in the earlier chapters.

6.2 Types of Hydrocoolers

Hydrocooling methods differ in their cooling rates and efficiencies. In addition, hydrocoolers vary in their method of cooling and the placement of the products. The various kinds of hydrocoolers are described below.

6.2.1 Continuous Flow Hydrocooler

A continuous hydrocooler allows the produce in bulk bins or in cartons to pass on a conveyor under a shower of chilled water. The produce harvested from the field is placed in one end of the conveyor, and cooled produce is removed at the other end. Most continuous flow hydrocoolers are high-production units with large refrigeration systems and heavy-duty components. This type of a hydrocooler needs to be used by more than one grower to be cost effective, as the initial and running costs are high. A continuous flow hydrocooler is shown in Figure 6.1.

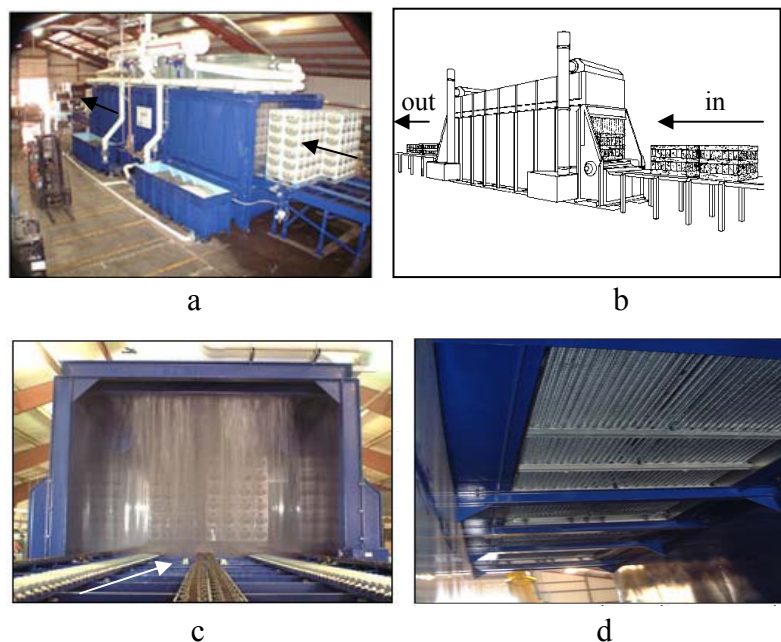


Figure 6.1. Continuous flow hydrocooler system: a) and b) a photograph and a diagram, respectively, of a continuous flow hydrocooler showing the cartons of the produce being loaded to enter the cooling bay where the produce is cooled by chilled water, and then removed from other end. c) The cartons of produce enter the shower room. d) the heavy duty cooling coils are suspended above the produce (Boyette *et al.* (1992) and Anon (2007)).

6.2.2 Immersion Hydrocooler

Immersion hydrocoolers are usually large in size, and they have a rectangular tank that holds chilled shallow water. Boxes of warm product are loaded in one end of the hydrocooler and moved by a submerged conveyor to the other end where they are removed. Crushed ice or a vapor-compression refrigeration system keeps the water cold. The length of time that the produce remains in the water varies with the initial conditions and desired ending temperature. (Boyette *et al.* (1992))

Immersion hydrocooling reduces the temperature more rapidly than in the continuous flow type, because the chilled water completely surrounds the external surface of the produce. An immersion hydrocooler is shown in Figure 6.2.

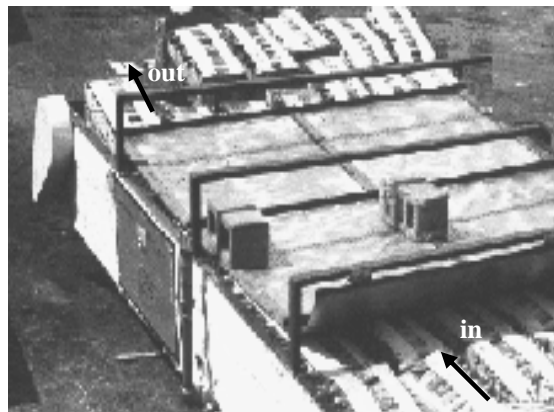


Figure 6.2. Immersion hydrocooler system where the boxes of the product are loaded in one end and moved by a submerged conveyor. The products are floated in a tank of chilled water and then removed from the other end (Boyette *et al.* (1992)).

6.2.3 Truck Hydrocooler

In truck hydrocoolers, the cooled water is delivered to the products by a simple system consisting of a tank holding several thousand liters of water, a pump, associated pipes and valves, and an ice crusher. Boxes of produce are loaded from the field into a trailer. Pipes are inserted into the trailer to deliver a shower of chilled water from a stationary cooling system. The water flowing out of the trailer is collected, re-cooled, and then recycled. After an hour or more of hydrocooling, the pipes are disconnected, and crushed ice is added to cover the top of the boxes of produce, and the boxes are immediately dispatched.

Truck hydrocoolers can be built by the grower at their farm for a low cost. The cooling rate is poor, because most of the water flows through the spaces between boxes, decreasing the total heat transfer. A truck hydrocooler is shown in Figure 6.3.

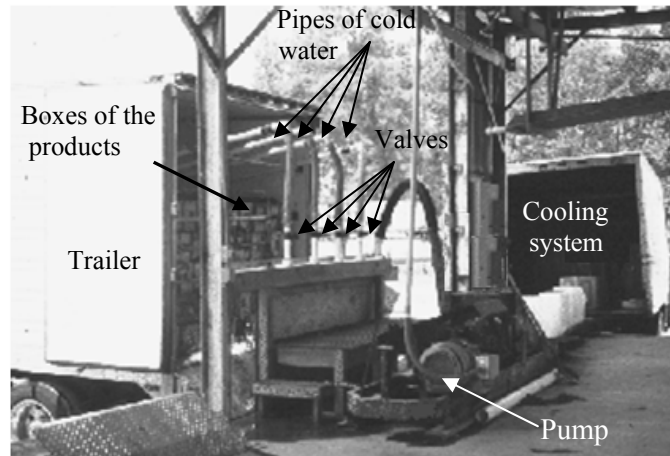


Figure 6.3. Truck hydrocooler system which has a tank holding water, pump, valves and pipes that deliver chilled water sprays to the product (Boyette *et al.* (1992).

6.2.4 Batch Hydrocooler

Batch hydrocoolers are systems without conveyors. Palletized cartons or bulk bins of product are loaded by a fork lift to be cool by a large amount of falling chilled water. The falling water is collected from the bottom to cool again, and then recycled.

Some batch hydrocoolers are small in capacity which can cool only one pallet of produce at a time, but some are larger to cool many pallets at once. These hydrocoolers generally have a smaller capacity than continuous flow hydrocoolers, and therefore, they are less expensive to operate. This type of hydrocooler is better suited to growers with a limited amount of produce that could not economically justify a larger unit. A batch hydrocooler is shown in Figure 6.4.

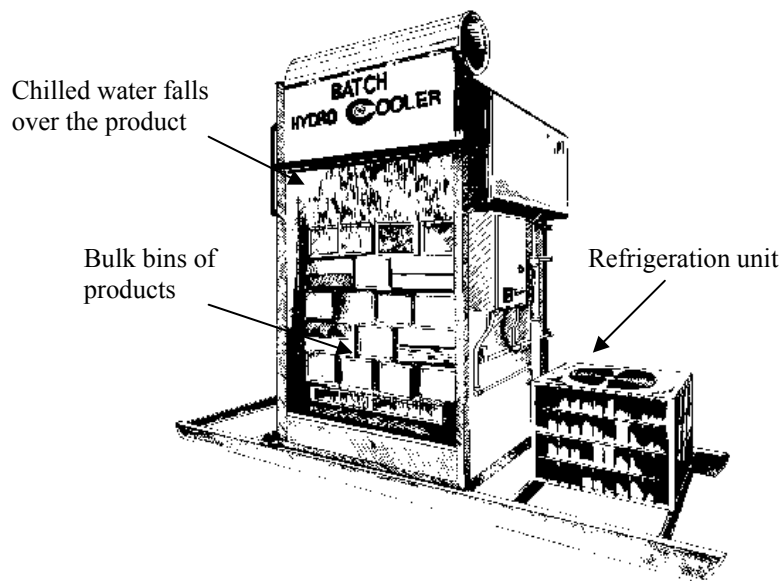


Figure 6.4. Batch hydrocooler system with a small refrigeration unit to cool the water after it falls over the bulk product bins (Boyette(1992).

The performance of a batch hydrocooler system, named the Smart Water hydrocooler, has been studied further next.

6.3 Design and Operation a Smart Water Hydrocooler

The primary specifications of the particular Smart Water hydrocooler studied here are to cool 6 tonnes per hour of horticultural produce from 29°C to 12°C, or 4 tonnes per hour from 29°C to 6°C. It should also be transportable from one horticultural growing region to another, and it should have a low water and energy consumption. It is desirable that the produce can be loaded into the cooling bays using a fork lift track

6.3.1 Realization of a Practical Commercial Hydrocooler

To ensure that the system is transportable and that it can hold ten boxes of produce at the same time, the hydrocooler is based on a refrigerated shipping container. The dimensions of the shipping container are given in Table 6.1.

Table 6.1. Principal dimensions of the Smart Water hydrocooler

	Length, mm	Width, mm	Height, mm
External	6050	2420	2590
Internal	5600	2200	2200

The Smart Water hydrocooler has two main units. The first unit is the portable container, and the second is the transportable chilling unit. A photograph of the portable container is shown in Figure 6.5. The container is fitted with three cooling bays in which the produce to be cooled is loaded with a forklift. Seven tanks that act as reservoirs for the chilled water are located at the rear of the container. On the left side of these seven tanks, there is a small tank which holds clean water, a backwash tank. This tank holds water used to backwash a sand filter when it is blocked with debris. In Figure 6.6, the chemical treatment room is shown which contains the water treatment system, and it is located on the left hand side of the hydrocooler. A pump room is located between cooling bays 2 and 3, and space is left on the right-hand side of the hydrocooler in which a water chilling unit may be placed.

A transportable chilling unit supplies the hydrocooler with chilled water. This water-chilling unit consists of a vapour-compression refrigerator. The transportable chilling unit is shown in Figure 6.7

There are essentially seven separate sub-systems that operate in conjunction with each other, namely:

- The supply of chilled water to the system and its return to the water-chilling unit.
- The distribution of chilled water used to irrigate the produce being chilled.
- A chemical treatment system that doses the re-circulated water with disinfectant to maintain it biocidal.
- A filtration system to remove both large pieces and fine debris to ensure that the water has low turbidity.
- A backwashing process to remove debris from the sand filter.
- Circuits that aim to ensure that the disinfectant and chilled water are distributed uniformly around the system.
- A supply of fresh water to the system to compensate for water loss on the produce.

The process flow diagram is shown in Figure 6.8. The details of these sub-systems are described individually next.

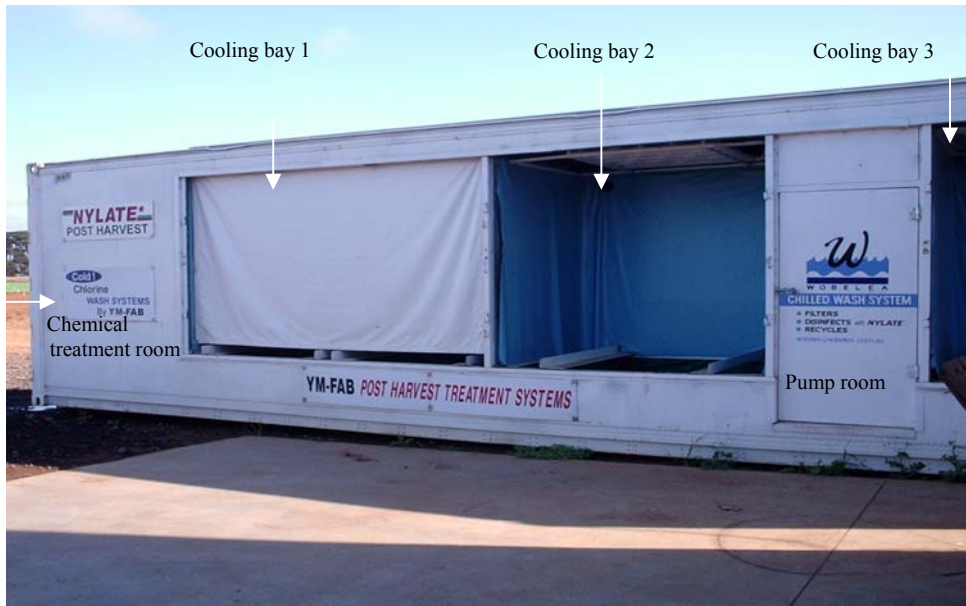


Figure 6.5. The hydrocooler system has three cooling bays, a pump room and the chemical treatment room. Cooling bay 1 is covered with a blind to reduce the water lost as a result of splashing.

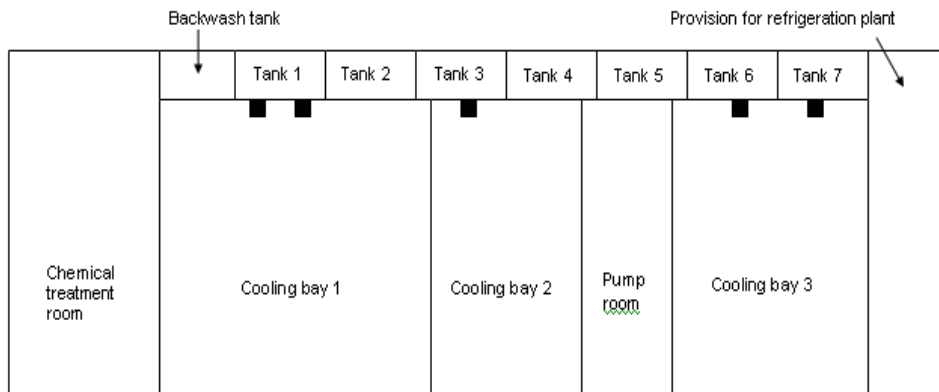
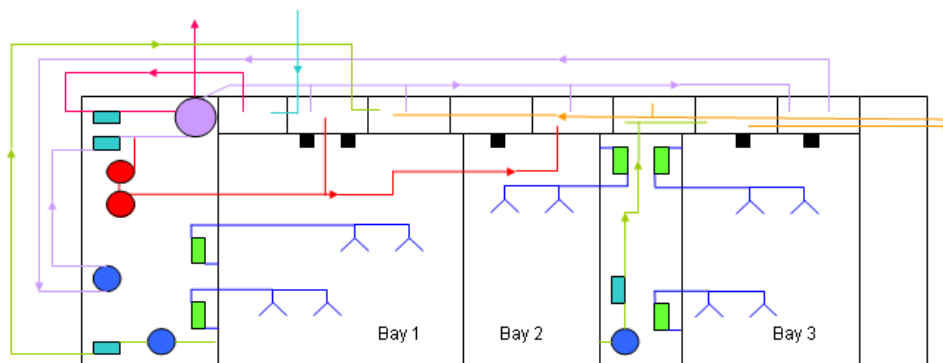


Figure 6.6. A general diagram of the hydrocooler, showing the three cooling bays, pump room, chemical treatment room, seven tanks, backwash tank and the provision for the refrigeration plant.



Figure 6.7. Water chilling unit supplies the hydrocooler with chilled water, and it is transported separately from the hydrocooler.



Legend to process flow diagrams:

Filter system	Sand filter		Ebara pumps	
Backwash system	Chemical feeders		Onga pumps	
Chemical system	Pre-strainers		Overflows	
Mixing systems				
Spray systems				
Chilled water system				
Mains system				

Figure 6.8. A process diagram of the hydrocooler showing the three cooling bays and seven principal circuits.

- **Chilled Water Supply, Storage and Removal System**

The chilled water from the water refrigeration unit is stored in seven tanks located at the rear the system and it is withdrawn from tank 6, as shown in Figure 6.8a.

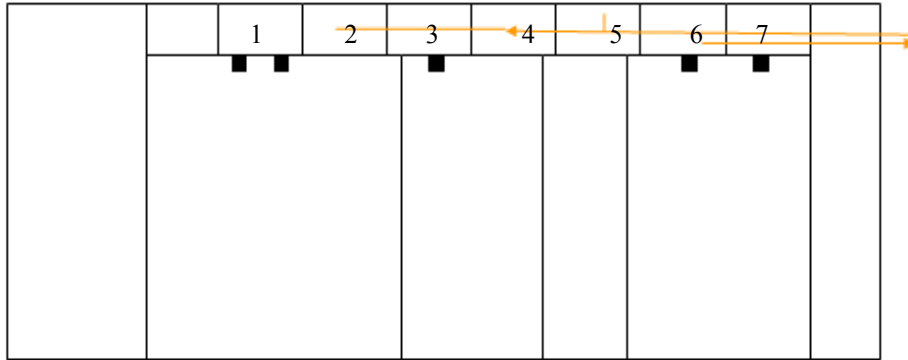


Figure 6.8a. Cold water from the hilling unit flows into tanks and returns to the chiller from tank 6 (Thorpe (2008)).

- **Distribution of Chilled Water Used to Irrigate the Produce**

The horticultural products to be cooled are placed in the three cooling bays. Water is contained in the bases of each of the bays, and it is pumped from these sumps into the water distribution system, as shown in Figure 6.8b. The internal distance between the front and rear of each cooling bay is 1.6 m, and the depth of the water is 0.3 m. Bays 1 and 3 are 2.95 m long, and bay 2 is 1.95 m long. The total volume of water that accumulates in the cooling bases is 3770 liters, and the volume of water in the seven chilled water tanks totals 9660 liters. It can be seen that bays 1 and 3 are each served by two *Ebara* DWO 400 pumps that re-circulate water from the reservoirs at the bottom of the bays up to the water distribution system. The smaller bay 2 is supplied with only one *Ebara* DWO 400 pump. The pumps consume about 3kW of power when they are pumping 18 liters per second of water (their maximum flow rate) through a head of about 6.5 m.

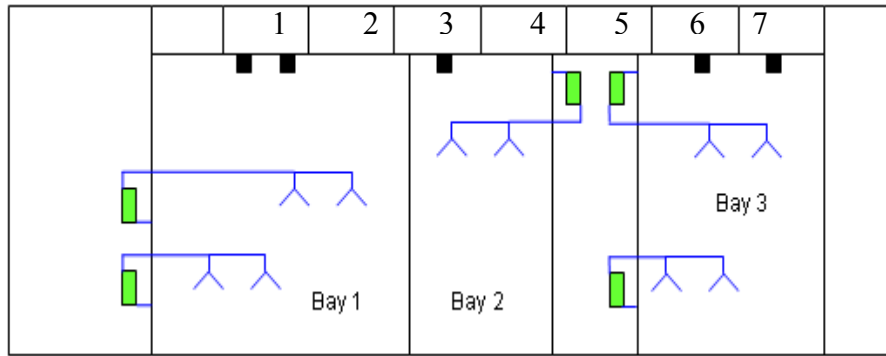


Figure 6.8b. The water distribution circuits in the Smart Water hydrocooler. Bays 1 and 3 are each supplied by two pumps, whereas the sprays in the smaller bay 2 are supplied using only one pump (Thorpe (2008)).

- **Chemical Treatment System**

Water in the hydrocooler is disinfected with bromo-chloro-dimethylhydantoin (BCDMH). BCDMH is a sparingly soluble white solid, and in the hydrocooler, it is retained in two column feeders. In Figure 6.8c, the process diagram of the chemical treatment system is shown.

As shown in Figure 6.8d, the valve opens when the Oxidation Reduction Potential sensors (ORP) indicate that the level is below the set point, typically 450 mV. pH and ORP sensors are located in a small diameter pipe in parallel with the line that returns water from the sand filter to tanks 1, 2, 4 and 7. A temperature sensor is integrated with the electrical conductivity sensor, and it is used in the calibration of the ORP and pH sensors.

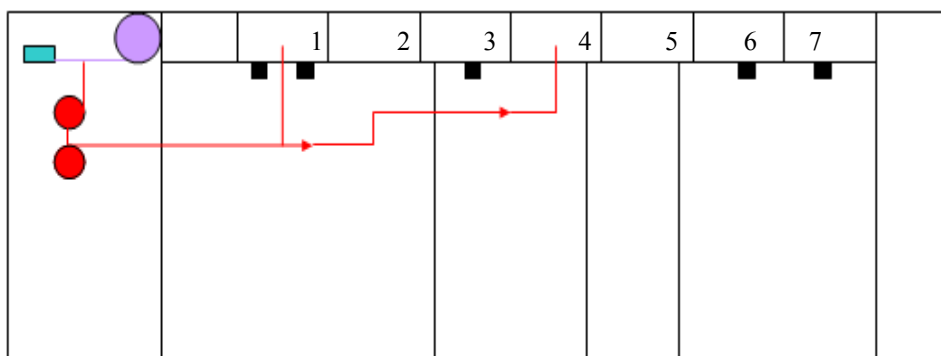


Figure 6.8c. The chemical dosing system in which solid bromo-chloro-dimethylhydantoin (BCDMH) is dissolved in water that has been recycled within the hydrocooler. The treated water is returned to tanks 1 and 4.

- **Filtration System**

In Figure 6.8d, the filtration circuit is shown. Water is drawn by means of an *Onga* pump from tank 7 through a stainless steel strainer. After it has been strained, it is pumped through a sand filter before being returned to tanks 2, 3, 5 and 7. After the water has been filtered, its pH and ORP are sensed by sensors placed in the water line leading to the tanks.

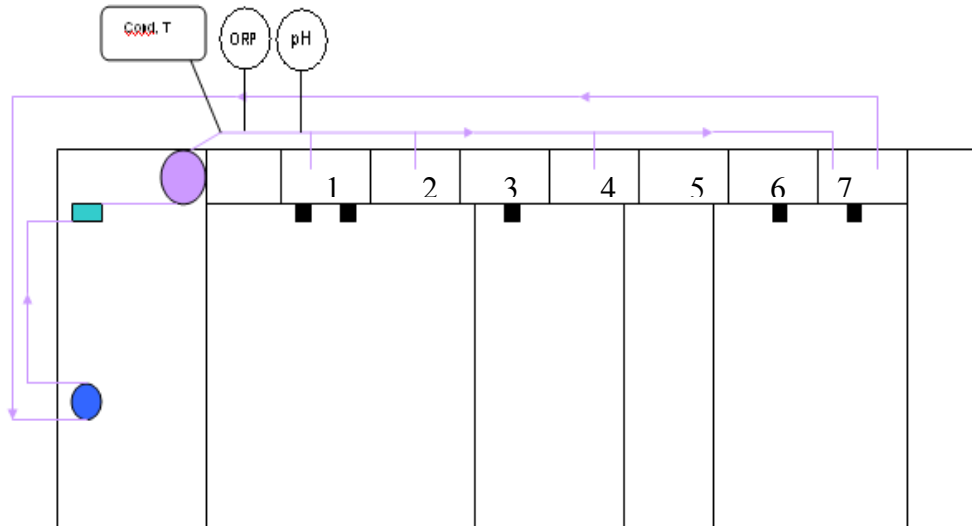


Figure 6.8d. Water is removed from tank 7 on the right of the hydrocooler before passing through a stainless steel strainer. It is then pumped through a sand filter before being returned to tanks 1, 2, 4 and 7. The ORP, temperature and electrical conductivity, and pH of the re-circulated water are measured in the line that leaves the sand filter and leads to the water tanks.

- **Backwash Circuit**

When the pressure drop across the sand filter exceeds 120 kPa, the downwards flow of the water is terminated. Water then flows up through the sand – fluidising it, and it entrains large or low density detritus which is then discharged from the cooler. As illustrated in Figure 6.8e that the water used to backwash the sand filter is contained in a smaller water tank located towards the left hand side and at the rear of the hydrocooler. This tank has a volume of 1,000 litres, and it contains fresh water. The backwash piping circuit is quite straightforward. Fresh water enters the backwash tank from which it is pumped by an *Onga* 932 pump that has a nominal flow rate of 7 litres per second against a head of 3 m through the sand. The water from the filter is subsequently discharged from the hydrocooler.

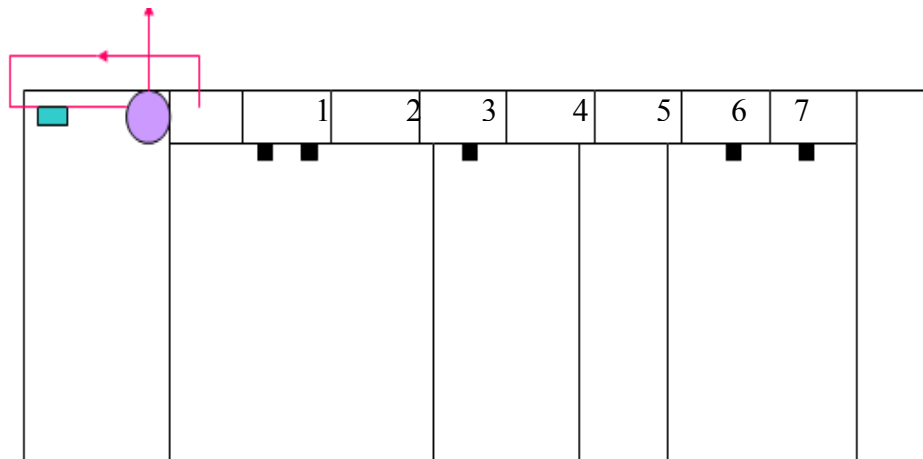


Figure 6.8e. The backwash circuit in which fresh the water from the tank adjacent to the filter is pumped vertically upward through the sand filter. As a result, large pieces of debris that are not removed by the pre-strainers are removed from the filter and discharged from the hydrocooler.

- **Mixing Circuits**

It is essential that the disinfectant is distributed uniformly throughout the hydrocooler. It is important that the levels of the water in the tanks and cooling bays are also maintained constant. Otherwise, the water will gather in one location, and it will overflow. The mixing circuits are shown in Figure 6.8f. This procedure enables for mixing and maintaining the water levels to be combined. The seven tanks that contain chilled water are interconnected by means of two 50 mm diameter holes drilled near their bases. Hence, when the hydrocooler is filled via tank 1, the water levels in all of the seven tanks at the rear of the hydrocooler remain more or less equal. Eventually, the water levels rise in the tanks until they begin to overflow into bays 1, 2 and 3 through 50 mm holes located near the top of the tanks. Two overflows are located in tank 1 which services bay 1. Bay 2 is serviced by an overflow in tank 3, and water flows into bay 3 from tanks 6 and 7. The cooling bays are also interconnected, and the overall effect of the interconnections between the water tanks and the cooling bays is to ensure that the water levels are more or less constant throughout the hydrocooler. If the water level in one tank rises above that of one of its neighbours, water flows from the higher level to the lower level.

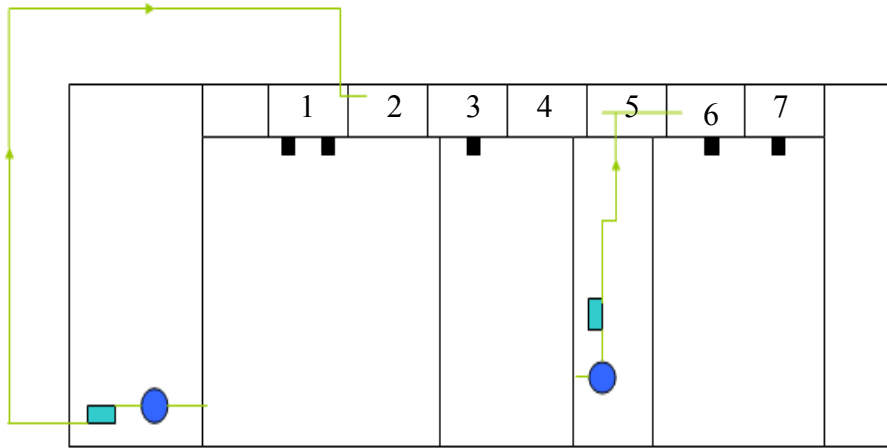


Figure 6.8f. The chilled disinfected water is mixed by ensuring it flows by gravity into tanks that have overflows, thus making sure the treated water flows into the bases of the cooling bays. The water is returned from the cooling bays to the tanks.

- **Mains Supply of Water**

Some water is lost from the hydrocooler on the cooled produce and as a result of backwashing the sand filter. Make-up water is supplied to the hydrocooler through one external water connection as shown in Figure 6.8g. Two ballcocks independently control the water levels in the backwash tanks and the cooling water tanks.

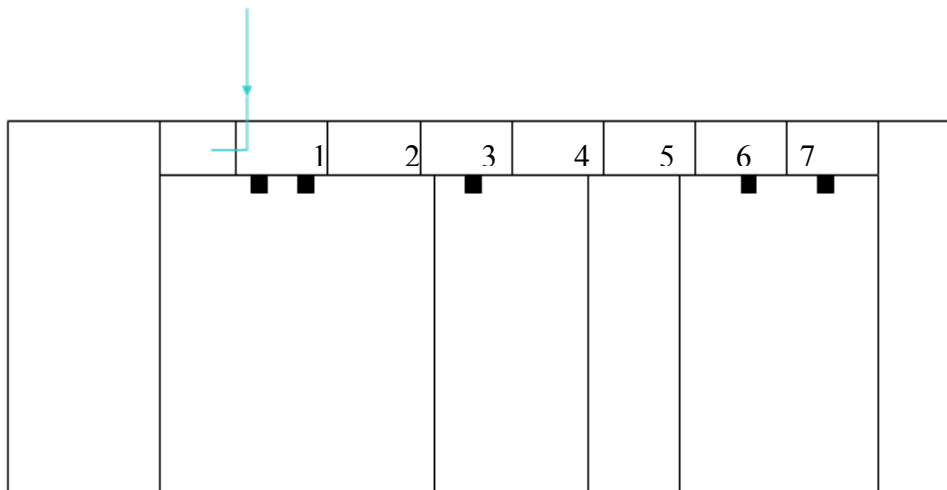


Figure 6.8g. Fresh water is supplied on demand to the backwash tank and tank 1 by means of two independent ballcocks.

6.4 Water Distribution and Treatment in the Hydrocooler

The physical realisation of the hydrocooler is presented below. The cooling water distribution system is fabricated from polypropylene pipe, and water sprays are allowed from T junctions that face vertically upwards as shown in Figures 6.9, 6.10. Also, it can be observed from Figure 6.11 that the shower of water consisting of large droplets leaves the water distribution system and then, large droplets land at the base of the cooling bay as shown in Figure 6.12.

In Figure 6.13, the general layout of the chemical treatment and filter room is shown. There are two pumps, the blue pump, *Ebara DW 400*, is used to pump the water from bay 1 to one of the water distribution arrays. The green pump *Onga* draws the water from bay 1 to tank 2. In these figures, red is the chemical dosing units. The cylinders that contain the disinfectant, bromo-chloro-dimethylhydantoin, are red, too. Water leaving the strainer is pumped by an *Onga* pump to the sand filter as shown in Figure 6.14.



Figure 6.9. Water distribution system in the roof of the shipping container. Water goes out of the inverted tee-pieces and the pipe elbows.



Figure 6.10. A view of the water distribution system from below. It is supported by a light metal frame.



Figure 6.11. Water leaving the distribution system at a rate of about 18 litres per second.



Figure 6.12. Water landing in the base of cooling bay of the hydrocooler.



Figure 6.13. Chemical treatment system.



Figure 6.14. The sand filter

6.5 Determining Hydrocooling Rates

To operate a hydrocooler effectively and efficiently, it is necessary to understand how water removes heat from the produce and the factors that affect the rate of cooling for various types of produce. The next section provides a fundamental description of these points and how to calculate approximate hydrocooling rates.

6.5.1 Cooling Rate of Product (Broccoli)

Horticultural produce with the dimensions of broccoli approach the temperature of the cooling water after about 30 minutes of being cooled. As a component of this research, experiments were carried out to investigate the cooling of broccoli. A bin containing about 40 kg of broccoli was placed in cooling bay 2 of the hydrocooler. Thermocouples were inserted into the stalks of pieces of broccoli and carefully placed in the bin. Two pieces of thermocouple-containing produce were located in each of six locations of the bin, namely the bottom left, centre and right of the bin, and top left, centre and right of the bin

Placing two pieces of produce in the same location helped to make the results more reliable. Two thermocouples were also placed in the water in bay 2 and this water was re-circulated around the system. The thermocouples leaving the box of produce are shown in Figure 6.16 and the instrumented broccoli is shown in Figure 6.17.



Figure 6.16. The box in which the instrumented pieces of broccoli were placed to measure their rate of cooling.



Figure 6.17. The instrumented broccoli in the hydrocooler.

The results are shown in Figure 6.18. The data indicate that the broccoli undergoes 80% of its cooling in about 35 minutes.

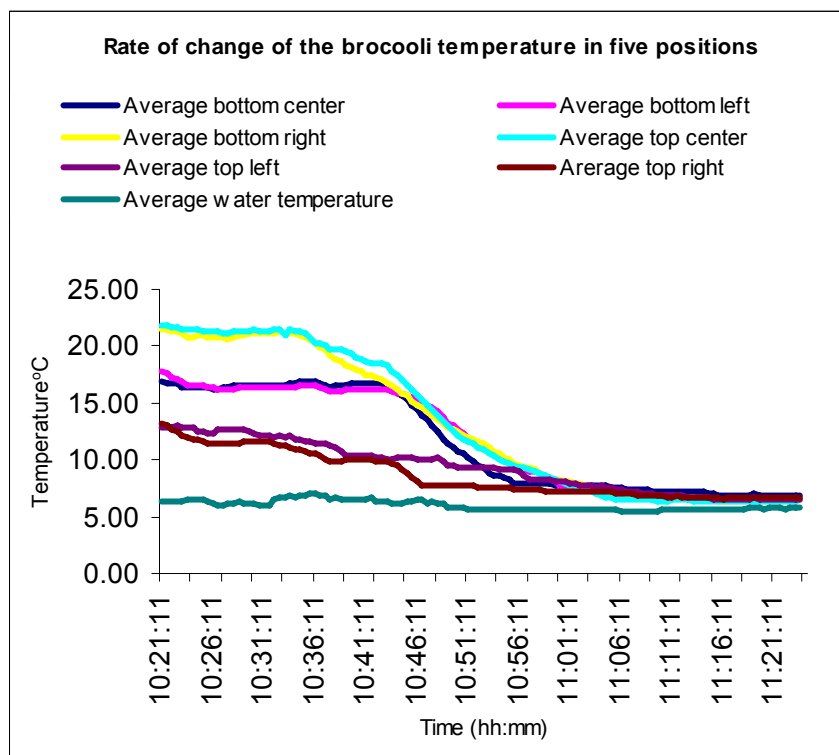


Figure 6.18. The rate at which broccoli cools in the Smart Water hydrocooler.

6.6 Water and Electricity Consumption

When broccoli is cooled in a hydrocooler, it retains about 45 litres of water per tonne of produce after it has been drained for about one minute. The amount of water that is retained by round fruit, such as apples is about 2 litres per tonne. In addition, the sand filter is likely to be cleaned on a daily basis with 1,500 litres of water. If the hydrocooler cools 6 tonnes per hour of broccoli for eight hours per day the amount of water consumed is about 75 litres per tonne. The water consumption in the case of apples is about 35 litres per tonne.

The energy required to cool one tonne of horticultural produce from 30°C to 6°C is 100,000 kJ which is equivalent to 28 kWh. Given a coefficient of performance of two the electrical energy required is 14 kWh per tonne. It follows that for a cooling rate of four tonnes per hour the power consumption of the chilling unit would be 56 kW. If the produce were to be cooled to 12°C at a rate of 6 tonnes per hour the power consumption would be 80 kW. Note that this is not 1.5 times the power consumption when the cooling rate is 4 tonnes per hour because a lower degree of cooling can be achieved at the higher throughput of produce.

The power consumption of the electrical pumps is determined from the manufacturers' literature to be 3.75 and 2.5 kWh per tonne when the cooling rates are 4 and 6 tonnes per hour, respectively. The total power consumption is therefore about 20 kWh per tonne and 16kWh per tonne when the cooling rates are respectively four and six tonnes per hour. If the water were not re-circulated the electricity consumption would be about 300kWh per tonne.

6.7 Modifications to the Hydrocooler

Several points have been learned regarding the materials of construction, process design, modifications to the shipping container and the design of the pipe layout in large scale hydrocoolers. As a result of carrying out the experiments it is possible to help growers specify and optimize hydrocoolers to suit their needs.

6.7.1 Simplify the Design of the Hydrocooler

The design of the hydrocooler seems over complicated. There is a limit to the simplifications that can be made to the system. For example, there have to be circuits to feed the water sprays, there need to be systems for filtering the re-circulated water and dosing it with disinfectant and so on. However, as a result of the experience gained, there appear to be areas in which the design could be simplified. One straightforward simplification is to replace the seven water storage tanks located toward the rear of the container with one large tank, or at least conceive of the tanks as being one large tank. In this case, the chilled, filtered and chemically treated water would enter the tank at one end of the hydrocooler as shown in Figure 6.19. Water would exit the tank at the opposite end. This arrangement would reduce the mixing circuits to one because water would be pumped from between cooling bays 2 and 3 to the region near the exit of the one large tank.

Installing a system of valves on the tank overflows may reduce heat ingress into the system. As a result, it would be possible to shut off water flowing into the cooling bays not being used to cool produce. For example, if bay 1 were not being used, the water in the base of the bay would be almost stagnant, and it would take little part in the process.

The modifications suggested above are aimed at reducing the complexity of the pipe work and to reduce heat ingress into the system. However, the modifications are somewhat speculative, and it is recommended that they be thoroughly investigated by mathematically modelling a range of alternatives.

6.7.2 Materials of Construction

The water storage tanks are made from plywood that is waterproofed by means of food grade high density polyethylene sheet. The problems with this are that the polyethylene sheet may be torn, and during the manufacture of the hydrocooler it is difficult to seal the sheet when holes have to be made in it. This latter situation occurs when pipes joining the cooling bays must be fitted.

A solution to the problem emerged after the hydrocooler had been built – namely rectangular plastic tanks are now available. It would appear that the use of these would mitigate the problems with plywood.

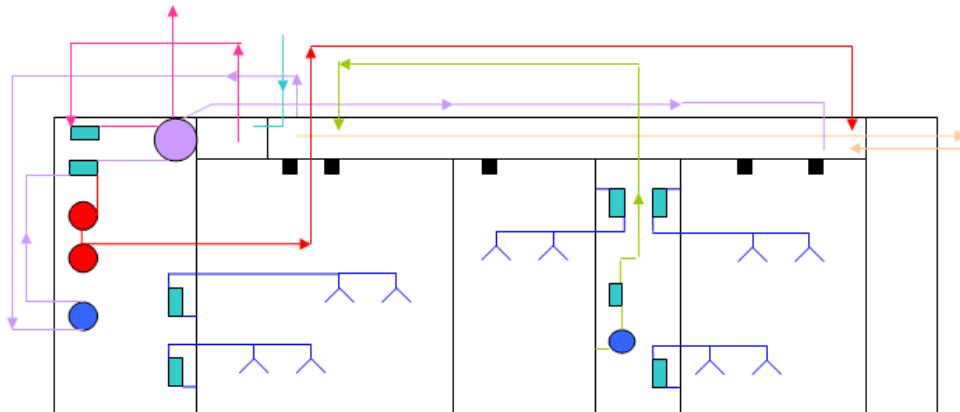


Figure 6.19. A simplified flow diagram that illustrates that there is only one storage tank for chilled water, a mixing circuit has been eliminated and the amount of piping has been reduced. Thorpe (2008).

6.8 Conclusion

A large scale, transportable hydrocooler has been studied. It is designed to cool 6 tonnes per hour of horticultural produce from 30°C to 12°C.

The water in the hydrocooler is re-circulated. It is found that the water consumption is about to be 75 litres per tonne of broccoli. If the water were not re-circulated, the water consumption would be 60,000 litres per tonne of produce cooled.

The electrical running cost is estimated to be 20 kWh and 16 kWh per tonne of produce when the throughput is 4 tonnes per hour and 6 tonnes per hour respectively. If the water were not re-circulated the running cost would be about 300 kW per tonne.

CHAPTER SEVEN

SUMMARY AND CONCLUSIONS

In this research, the prediction and description of flow visualisation and heat transfer between horticultural produce and cooling water in hydrocooler systems are studied. This is achieved following experiments and numerical analysis of falling liquid film over horizontal cylinders. The mathematical approach for this research is based on the Volume of Fluid Method, (VOF). The software packages “GAMBIT[®] and FLUENT[®] are employed to calculate and illustrate the flow modes and the rate of heat transfer in porous media.

Hydrocooling is a procedure in which, fruits and vegetables are sprayed with cold water to reduce their temperature. Hydrocooling involves three phases, which are, solid (produce), liquid (water) and a gas (air).

Several important parameters are addressed in this research for better understanding of hydrocooler systems. These parameters are, the total mass flow rate of water, the size of the nozzle and the distance between the nozzle and the horticultural produce. To establish these parameters within an intellectual framework, the results of this study are expressed in terms of dimensionless quantities such as Reynolds number, Re , Nusselt number, Nu , dimensionless distance between the nozzle and the surface, S/D or S/W where S is the distance between the nozzle and the surface and D and W are the diameter and the width of the nozzle, respectively.

In this research the computational fluid dynamic CFD codes are validated against experimental data such as temperature distribution, flow modes and heat transfer characteristic. The research reported in this thesis contributes to the validation of a commercial CFD package against a significant range of phenomena associated with three phase flow. These include, the flow modes of liquid film, namely, the droplet, jet and sheet modes.

The scope of this study which includes liquid flow field and heat transfer is fundamentally extensive. The computational domain, mesh generation, model validation and the experiment setup are studied.

Numerical investigations of liquid jet impinging on flat and curved surfaces are presented and extended to account for heat transfer. It is found that there is no significant effect due to the surface configuration of the flat and curved surfaces on the flow field and heat transfer. The flow field of the impinging jet is found to be divided into three regions. These regions are, the free jet region, impingement region, and the wall jet region. The heat transfer coefficient in the impinging and wall jet regions is enhanced with increase in Reynolds number. Reynolds numbers between 100 - 1900 are employed to study the effects of liquid flow rate on flow field and heat transfer. It has been found that the Reynolds number has a significant effect on the flow field and heat transfer with the increase of the cooling area at impinging zone significantly and causes a decrease in temperature at this zone.

The effect of the dimensionless nozzle to plate spacing S/D , nozzle width W , on the flow field and heat transfer are also studied. It has been found that the stagnation Nusselt numbers increase with decrease in S/D this is due to flow acceleration at lower S/D . It is also found that the heat transfer coefficient with a larger nozzle width is greater than with a smaller nozzle. This is because the heated surface is cooled more by increased liquid flow from the larger nozzle.

The flow visualization and falling film modes are represented experimentally and numerically in 2D and 3D. The behavior of water falling over horizontal cylinders and the definition of the flow patterns are reported. The effects of Reynolds number Re , hysteresis, cylinder diameters d , placement of the cylinders (top, middle and bottom) and the vertical separation \bar{s} between the cylinders are studied. The Reynolds number range studied in this investigation is 50 to 3000. The cylinder diameters are 0.1m, 0.05m, and 0.02m. The frequency and the wave length of the droplet mode are studied too. It has been found that, the number of large drops increases relatively slowly as the Reynolds number increases to about

80 and the frequency of the large drops remain about constant as the Reynolds number increases further. For the small droplet, Reynolds number has a large impact where the frequency increases sharply by a factor of about 4 as the Reynolds number increases from 20 to about 50. This finding leads to the result of not needing to use a high liquid flow rate or Reynolds number above 80, which facilitated to consume water and energy.

It is also found that at the same Reynolds number the flow modes are different at different separation distance between the cylinders, \bar{S} . The flow mode is droplet at larger separations where it is jet and sheet mode at smaller separations.

For the effect of the cylinders diameter, it is found that the drops from smaller cylinders become stable at lower frequencies and the wavelength decreases with increasing the cylinder diameter.

Numerical simulations of flow field for 2D are studied for random, rectangular pitch-arrangement and ten horizontal cylinders. It is found that better water distribution occurs in the case of rectangular arrangement. Top cylinder has a better irrigation than the second and the third for the ten horizontal cylinders.

The heat transfer for falling liquid film are investigated in this research. Temperature profile of liquid film is studied and the local and average heat transfer coefficients around the horizontal cylinders are calculated. It is found that the flow and heat transfer interactions are essentially different for each of the falling film modes. The heat transfer coefficient enhances at sheet mode, decreases for jet and further decreases for droplet mode.

Increasing the flow rate of the liquid means increasing its velocity which causing in change a of the flow mode from drop to jet to sheet mode. At the desired Reynolds number, the heated cylinders at the small height of the feeder distance are covered with thicker liquid films which help to remove more heat form the heated cylinder and then enhance the heat transfer. It is found that the effect of the cylinder diameter on the heat transfer coefficient is larger for the small cylinder

over the whole range of liquid flow rate or Reynolds numbers covering the droplet, jet and sheet modes. Since the impingement region occupies a larger portion of the cylinder area, the average heat transfer coefficients are also higher for small cylinder. For small cylinder diameters, the surface area is smaller than the large cylinder and the impinging zone is larger than in large diameter.

The numerical studies of heat transfer coefficient for random and rectangular pitch-arrangements heated cylinders and also ten horizontal heated cylinders. It has been found that the temperature distribution in rectangle cylinders arrangement is more uniform than in random arrangement due to the consistent liquid distribution. Also for completely wetted surfaces, it is found that the heat flux has no significant impact on the heat transfer coefficient.

The results from the experiments and numerical studies are used to explore the effect of heat transfer on the behaviour of falling films. The results reported are motivated by the possibility of using detailed numerical simulations of the phenomena that occur in beds of irrigated porous media to obviate the need for empirical correlations.

This research has addressed in detail the design, construction and the operation of hydrocoolers. The types of the hydrocooler, performance, design and operation of the hydrocooler, are also reported.

APPENDIX A

The objective in this appendix is to summarize the selection of cylinder material used in the laboratory experiments, and the different irrigation temperatures.

Aluminium and Steel have been chosen to represent the centre region. Aluminium, Steel and Gypsum have been selected for the left and right side regions as the two ends for the cylinders to avoid heat loss. In reality, the best material to represent packed horticultural produce as a porous medium is wood, due to its thermal conductivity. However, having to use heat in the laboratory experiments made that selection impossible.

Fifteen simulations have been designed to examine the effect of different materials for the cylinder and the two ends of the cylinders for isolation. The numerical simulations are presented in five groups. These simulations are:

- Group 1 is for cases 1 to 3 to study the effect of water (irrigation) temperature when the center, left and right regions are all made of Aluminium. The cylinder diameter is 0.1 m and the two sides regions have the same temperature of 25 °C.
- Group 2 is for cases 4 to 6 to study the effect of water (irrigation) temperature when the center region is made of Aluminium, left and right regions (end regions) are made of Gypsum. The cylinder diameter is 0.1 m and the two sides regions have the same temperature of 25 °C.
- Group 3 is for cases 7 to 9 to study the effect of water (irrigation) temperature when all regions are made of steel. The cylinder diameter is 0.1 m and the two sides regions have the same temperature of 25 °C.
- Group 4 is for cases 10 to 12 to study the effect of water (irrigation) temperature when the center region is made of steel, left and right regions are made of Gypsum. The cylinder diameter is 0.1 m and the two sides regions have the same temperature of 25 °C.

- Group 5 is for cases 13 to 15 to study the effect of the cylinder diameter where all regions are at 25 °C. The center region is made of Aluminium, left and right regions are made of Gypsum. The cylinder diameters are 0.04 m, 0.06 m and 0.08 m for cases 13, 14, and 15 respectively.

The results of these simulations helped for a better apparatus design by selecting the right material of the cylinder and the two ends, and also to distinguish the irrigation liquid temperature. In Table A.1 these simulations are listed.

Table A.1. Simulations used for the design of the experimental setup.

Group 1			
Case 1 for Diameter of 0.1m	Center region (cylinder)	Right end (right plug)	Left end (right plug)
Temperature °C	5	25	25
Material	Aluminium	Aluminium	Aluminium
Case 2 for Diameter of 0.1m	Center region	Right end	Left end
Temperature °C	25	25	25
Material	Aluminium	Aluminium	Aluminium
Case 3 for Diameter of 0.1m	Center region	Right end	Left end
Temperature °C	30	25	25
Material	Aluminium	Aluminium	Aluminium

In all simulations, after fixing the temperature at the center region or the mid plane of the center cylinder, the two ends, steady state conduction transfer has been calculated.

Group 2

Case 4 for Diameter of 0.1m	Center region (cylinder)	Right end (right plug)	Left end (left plug)
Temperature ° C	5	25	25
Material	Aluminium	Gypsum	Gypsum

Case 5 for Diameter of 0.1m	Center region	Right end	Left end
Temperature ° C	25	25	25
Material	Aluminium	Gypsum	Gypsum

Case 6 for Diameter of 0.1m	Center region	Right end	Left end
Temperature ° C	30	25	25
Material	Aluminium	Gypsum	Gypsum

Group 3

Case 7 for Diameter of 0.1m	Center region (cylinder)	Right end (right plug)	Left end (left plug)
Temperature ° C	5	25	25
Material	Steel	Steel	Steel

Case 8 for Diameter of 0.1m	Center region	Right end	Left end
Temperature ° C	25	25	25
Material	Steel	Steel	Steel

Case 9 for Diameter of 0.1m	Center region	Right end	Left end
Temperature ° C	30	25	25
Material	Steel	Steel	Steel

Group 4

Case 10 for Diameter of 0.1m	Center region (cylinder)	Right end (right plug)	Left end (left plug)
Temperature ° C	5	25	25
Material	Steel	Gypsum	Gypsum

Case 11 for Diameter of 0.1m	Center region	Right end	Left end
Temperature ° C	25	25	25
Material	Steel	Gypsum	Gypsum

Case 12 for Diameter of 0.1m	Center region	Right end	Left end
Temperature ° C	30	25	25
Material	Steel	Gypsum	Gypsum

Group 5

Case 13 0.04m diameter	Center region (cylinder)	Right end (right plug)	Left end (left plug)
Temperature ° C	25	25	25
Material	Aluminium	Gypsum	Gypsum

Case 14 0.06m diameter	Center region	Right end	Left end
Temperature ° C	25	25	25
Material	Aluminium	Gypsum	Gypsum

Case 15 0.08m diameter	Center region	Right end	Left end
Temperature ° C	25	25	25
Material	Aluminium	Gypsum	Gypsum

A.1 Discussion of Design Consideration

In Figures A.1, A.2 and A.3, the temperature distributions are presented within the three regions of a 0.1 m cylinder whose center wall, left and right ends are made of Aluminium. The mid-plane temperature which represents the irrigation temperature is 5 °C, 25 °C and 30 °C, respectively while the two side regions are at a constant temperature of 25 °C. The temperature contours of the three Aluminium regions are shown in Figures A.1a, A.2a and A.3a. The temperature distribution along the cylinder is given in Figures A.1b, A.2b and A.3b, while the heat flux along the surface is shown in Figures A.1c, A.2c and A.3c. In Figure A.1c, the heat flux is not uniform, because heat flows in the center section of the cylinder. The heat leaving the central section is augmented by heat entering from the atmosphere. This is a problem which can be solved by irrigating the cylinder with water at temperature close to the ambient, as shown in Figure A.2c when the temperature of the water (center wall region) is the same as that of the air (right and left side wall regions). The heat flux through the surface of the central region of the cylinder is uniform and close to the expected value.

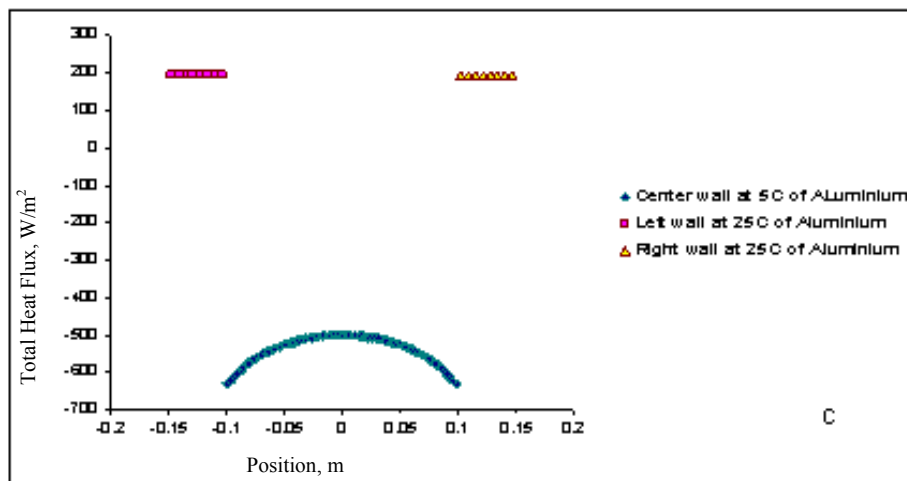
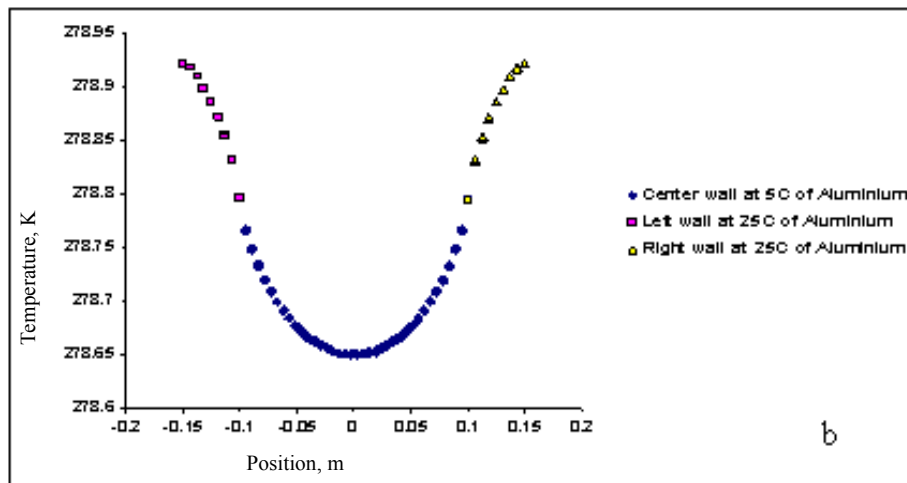
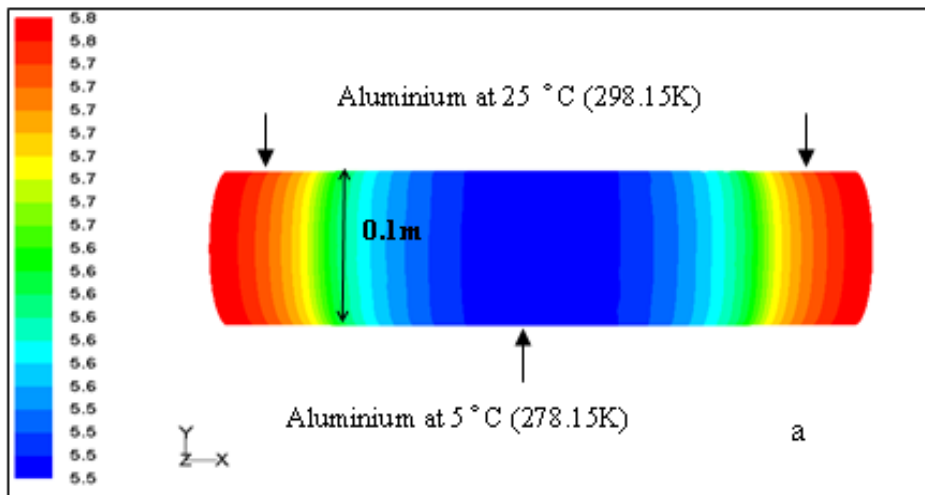


Figure A.1. Case 1 from Table A.1. Center wall and two side regions are made of Aluminium at 5 °C of center wall region (irrigation temperature) and 25 °C two side regions; a) temperature contours for the three regions; b) temperature distribution along the cylinder; c) heat flux along the surface.

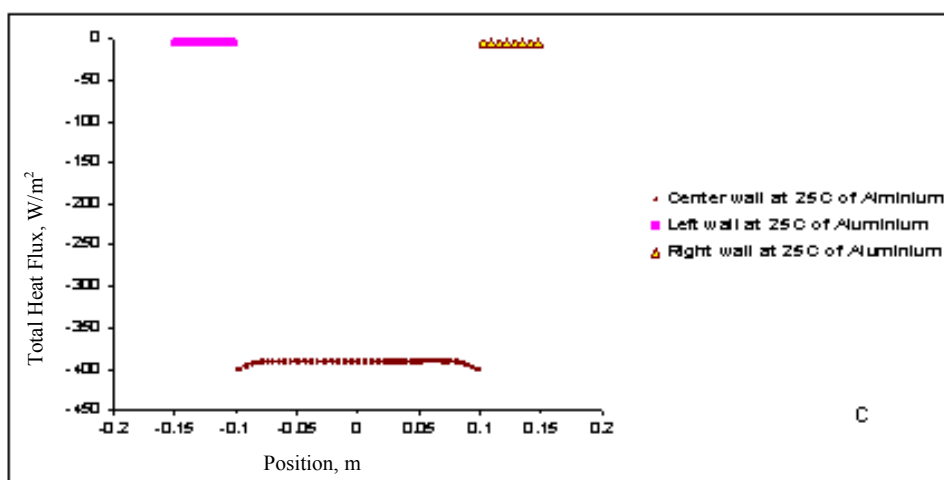
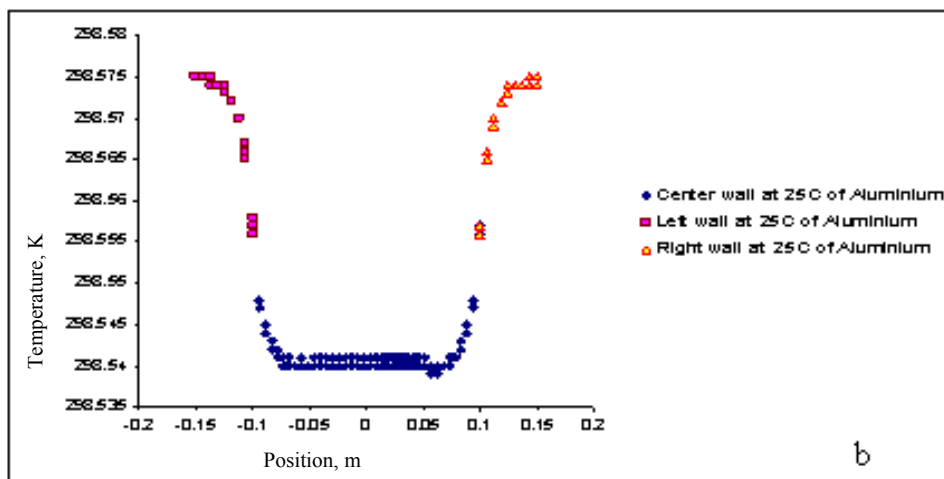
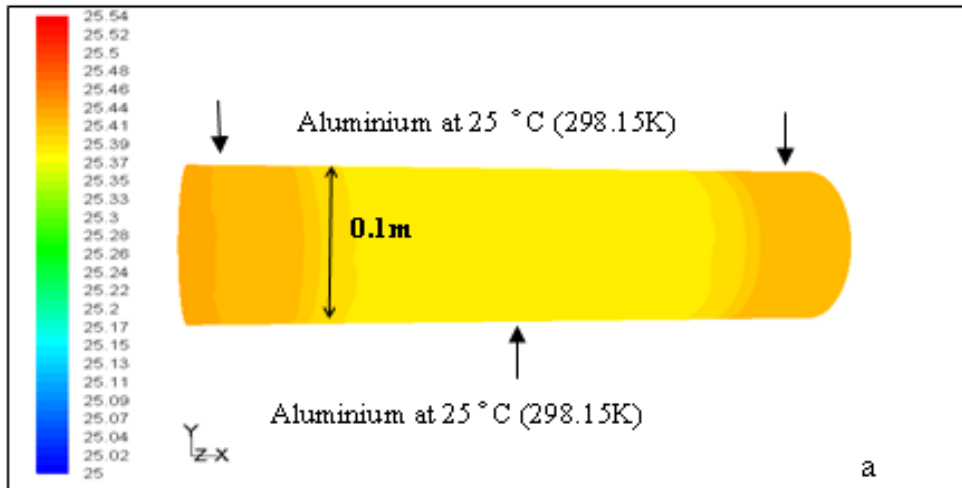


Figure A.2. Case 2 in Table A.1. Center wall and two side regions are made of Aluminium at 25 °C of center wall region (irrigation temperature) and 25 °C two side regions; a) temperature contours for the three regions; b) temperature distribution along the cylinder; c) heat flux along the surface.

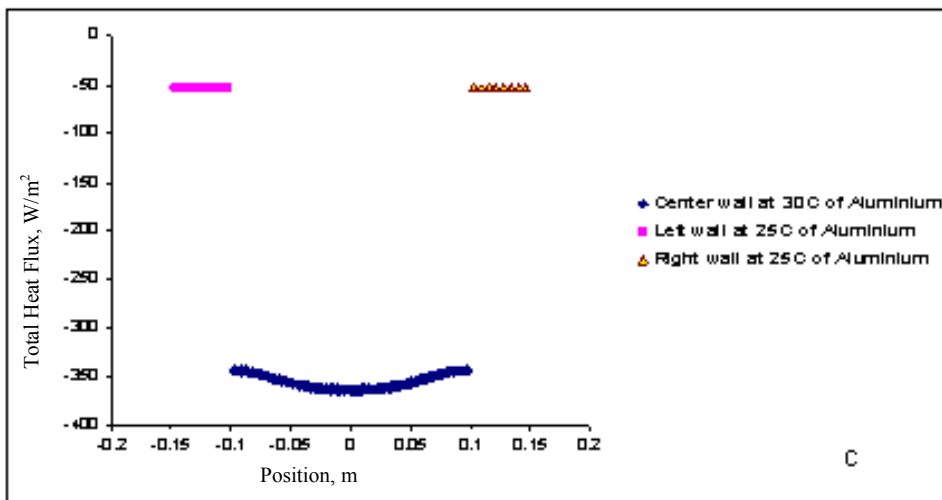
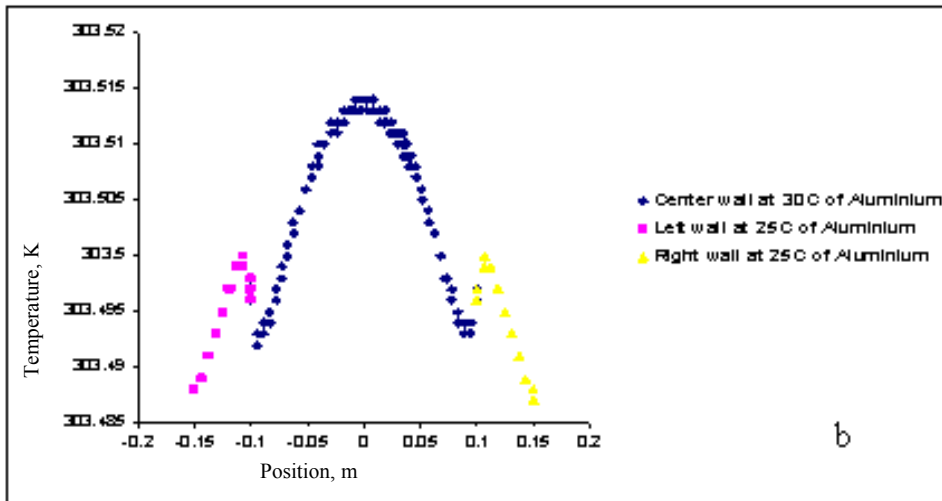
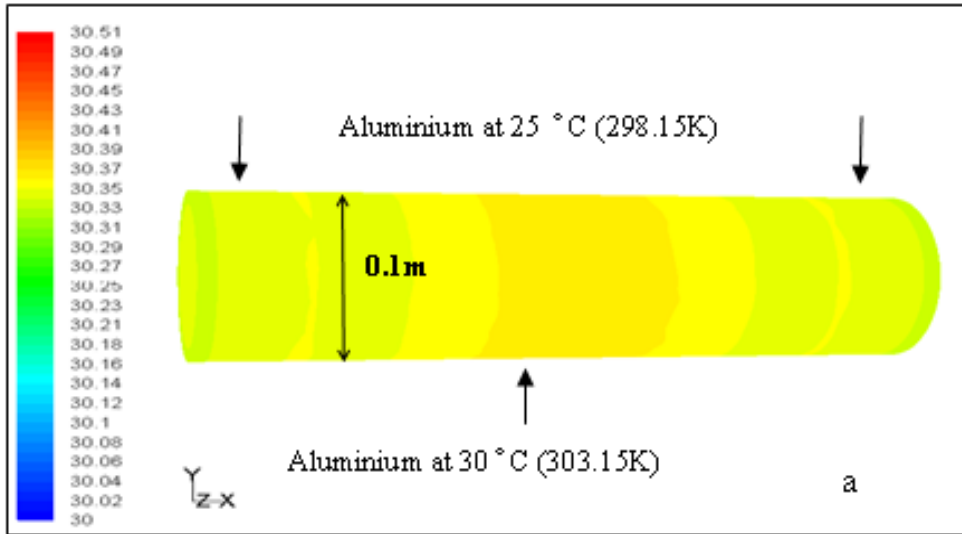


Figure A.3. Case 3 in Table A.1. Center wall and two side regions are made of Aluminium at 30 °C of center wall region (irrigation temperature) and 25 °C two side regions; a) temperature contours for the three regions; b) temperature distribution along the cylinder; c) heat flux along the surface.

Heating the irrigation water to 30 °C has also been studied; heating water to 30 °C has a pronounced effect on the distribution of heat flux. The heat flux from the irrigated region of the cylinder is clearly influenced by conditions of the non irrigated region. These effects are exacerbated by the high thermal conductivity of the Aluminium. It may be that the end effects can be reduced by replacing the Aluminium in the non-irrigated regions with a thermally insulating material. This was investigated by using Gypsum at the two ends, which has a low thermal conductivity similar to Bakelit, thermal conductivity of Gypsum is 0.5 W/m°C, and that of Bakelit is 0.21 W/m°C. These results are given in Figures A.4, A.5, and A.6.

In Figures A.4a, A.5a and A.6a, the contours temperature for three regions of the center wall, right and left side regions are shown when the irrigation temperature is 5 °C, 25 °C and 30 °C, respectively. The temperature distribution for the Aluminum center wall region and Gypsum two side regions are shown in Figure A.4b, A.5b and A.6b. In Figures A.4c, A.5c and A.6c, heat flux is shown. The heat flux at 5 and 30°C are far from uniform, but at 25°C, the heat flux through the surface of the central region of the cylinder is quite uniform and equal to a value of 400 W/m².

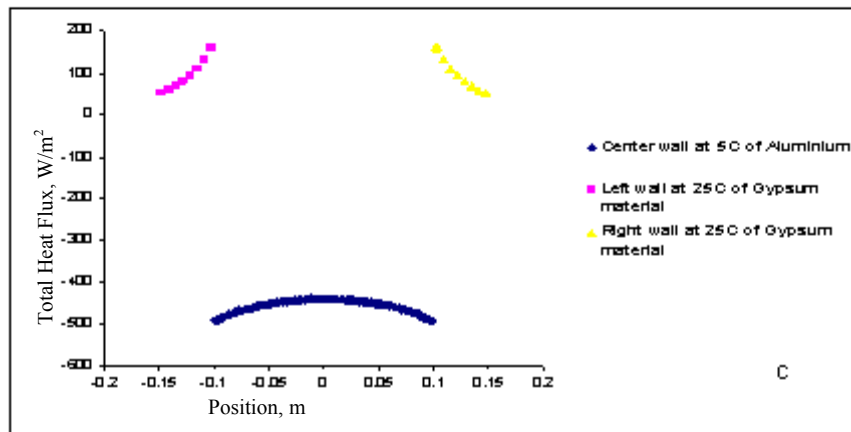
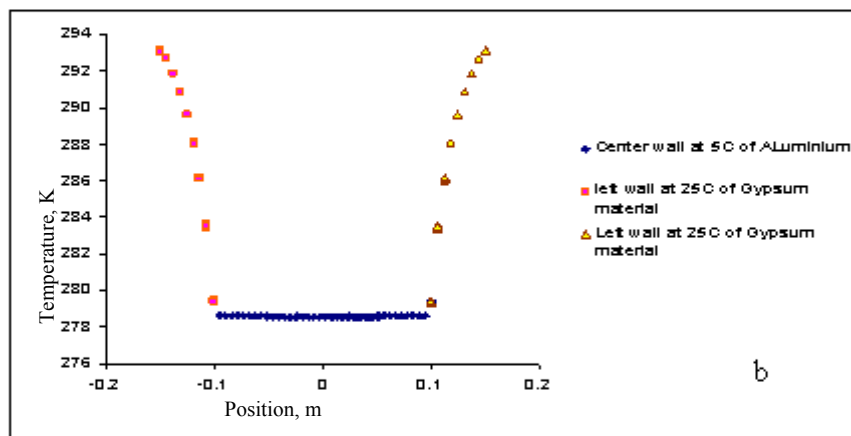
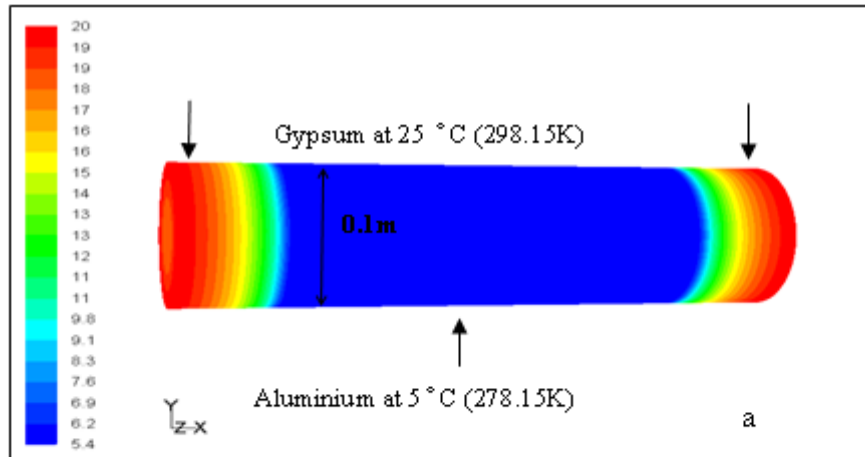


Figure A.4. Case 4 in Table A.1. Aluminium center wall region (irrigation) at 5 °C and Gypsum two side regions at 25 °C; a) temperature contours for the three regions; b) temperature distribution along the cylinder; c) heat flux along the surface.

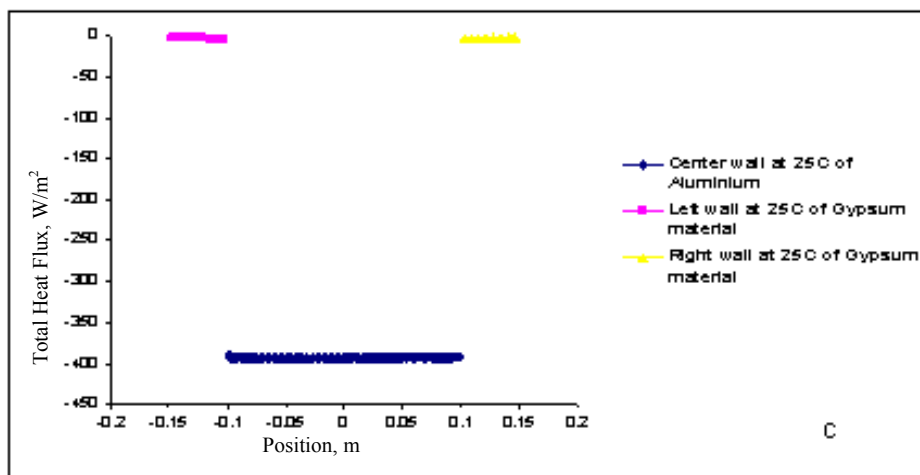
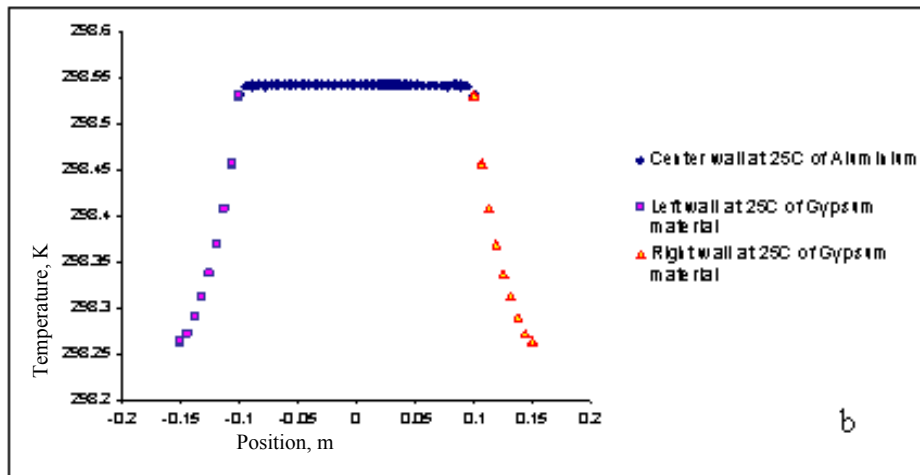
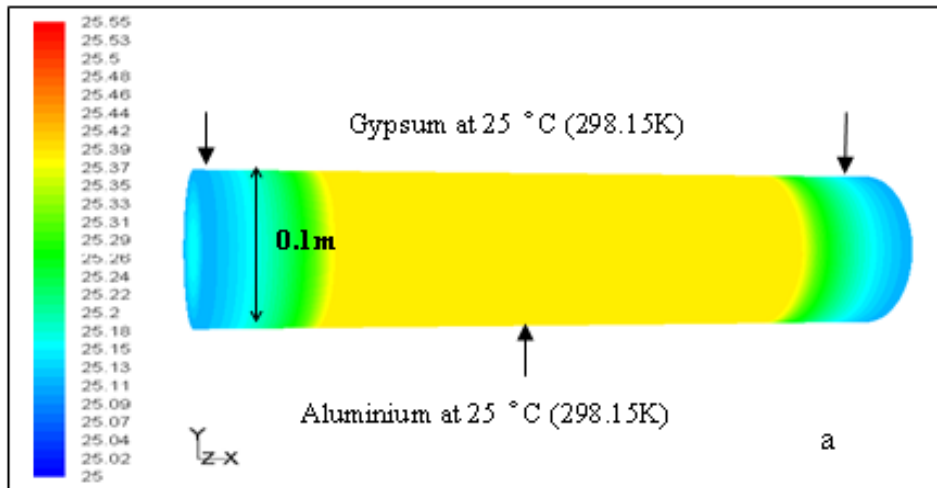


Figure A.5. Case 5 in Table A.1. Aluminium center wall region (irrigation) at 25 °C and Gypsum two side regions at 25 °C; a) temperature contours for the three regions; b) temperature distribution along the cylinder; c) heat flux along the surface.

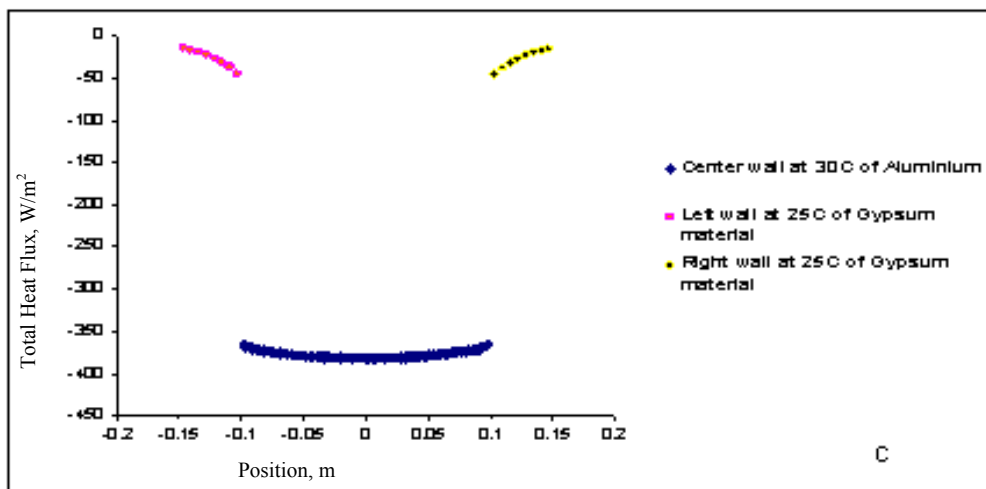
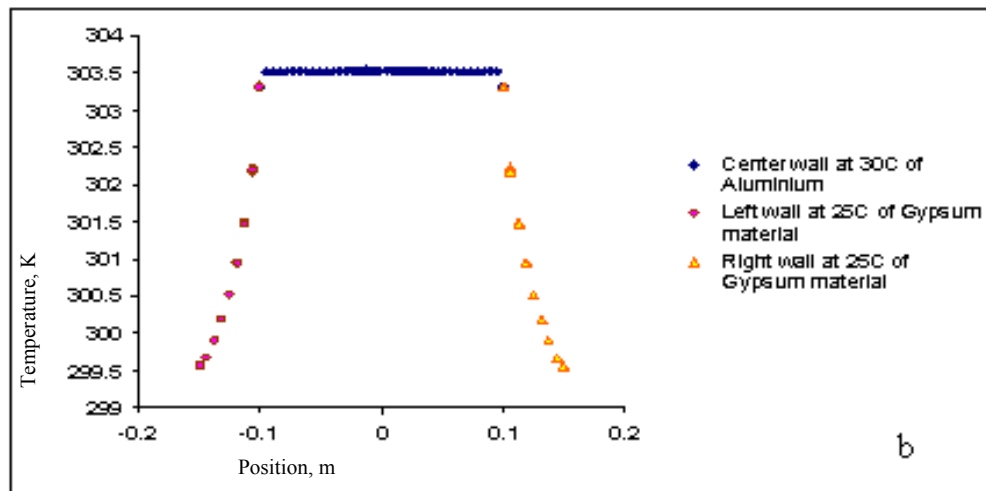
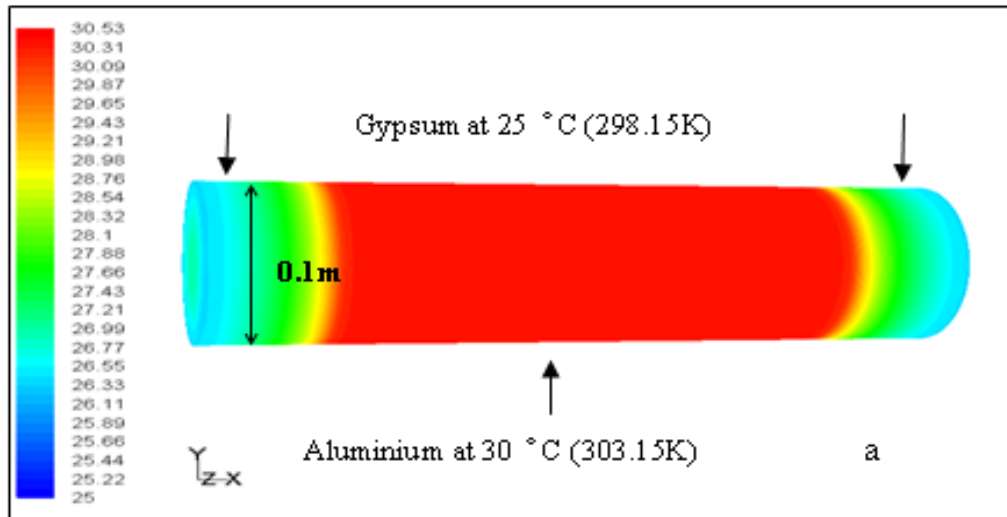


Figure A.6. Case 6 in Table A.1. Aluminium center wall region (irrigation) at 30 °C and Gypsum two side regions at 25 °C; a) temperature contours for the three regions; b) temperature distribution along the cylinder; c) heat flux along the surface.

For the cases in Figures A.7, A.8 and A.9, the center wall and the two side regions are made of Steel where the irrigation temperature is modelled to be 5 °C, 25 °C and 30 °C respectively. The temperature contours are shown in Figures A.7a, A.8a and A.9a. The temperature distribution is shown in Figures A.7b, A.8b and A.9b, while the heat flux along the surface is shown in Figure A.7c, A.8c and A.9c. It can be seen from these figures that the best scenario for these three simulations is the one for Figure A.8, where the irrigation temperature is 25 and the heat flux along the surface is reasonable.

For the cases in Figures A.10, A.11 and A.12, the center wall region is made of Steel at irrigation temperatures of 5 °C, 25 °C and 30 °C respectively. The two side regions are made of Gypsum at a temperature of 25 °C. In Figures A.10a, A.11a and A.12a, the temperature contours are illustrated. The temperature distribution is shown in Figures A.10b, A.11b and A.12b, and heat flux distribution is shown in Figure A.10c, A.11c and A.12c. It can be seen that the best result is the one in Figure A.11 where the irrigation temperature is 25°C and the heat flux distribution is quite uniform and close to the value of 400 W/ m².

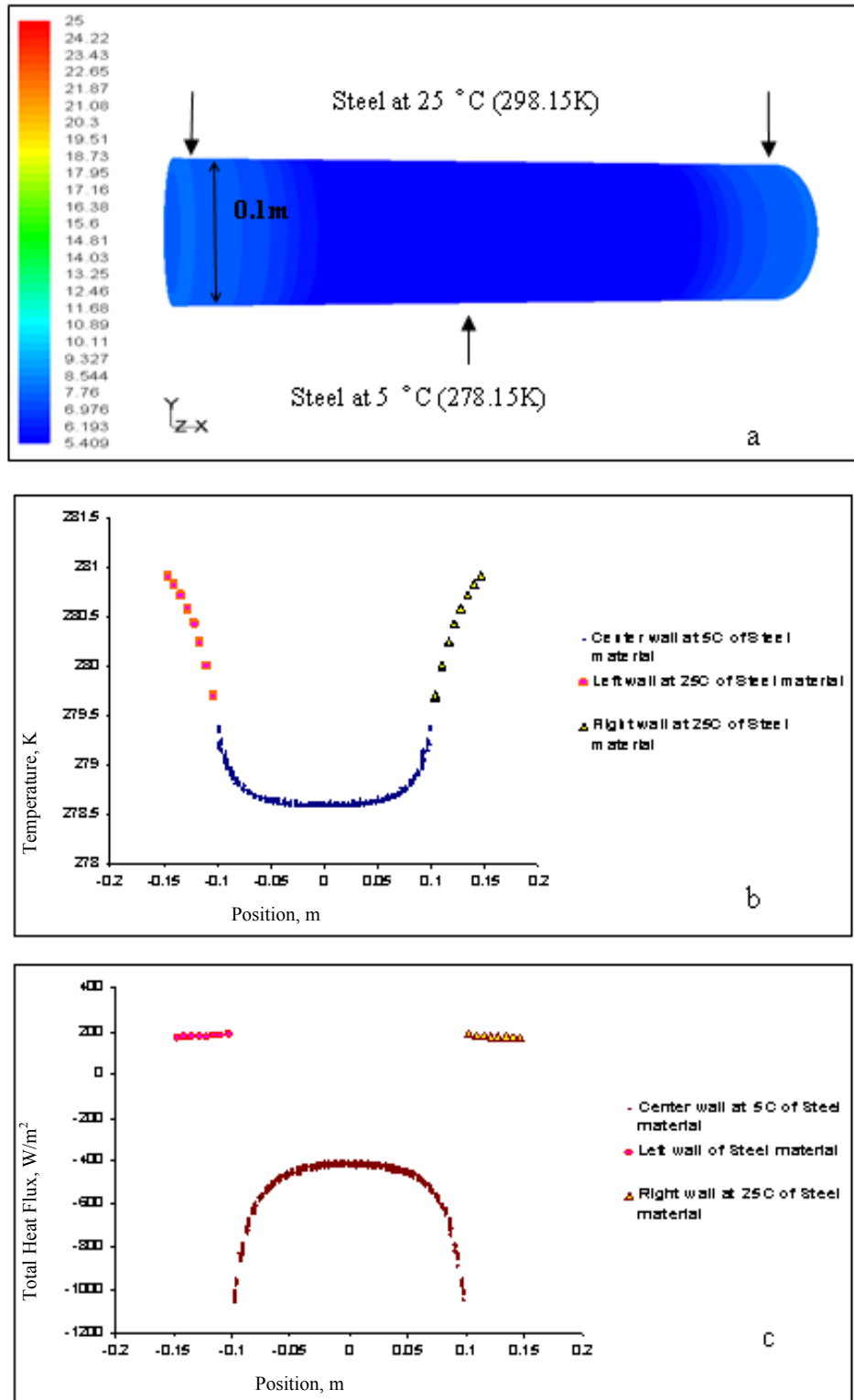


Figure A.7. Case 7 in Table A.1. Three regions of center wall and tow side are made of Steel, at 5 °C of center wall region (irrigation) and 25 °C of the two side region; a) temperature contours for the three regions; b) temperature distribution along the cylinder; c) heat flux along the surface.

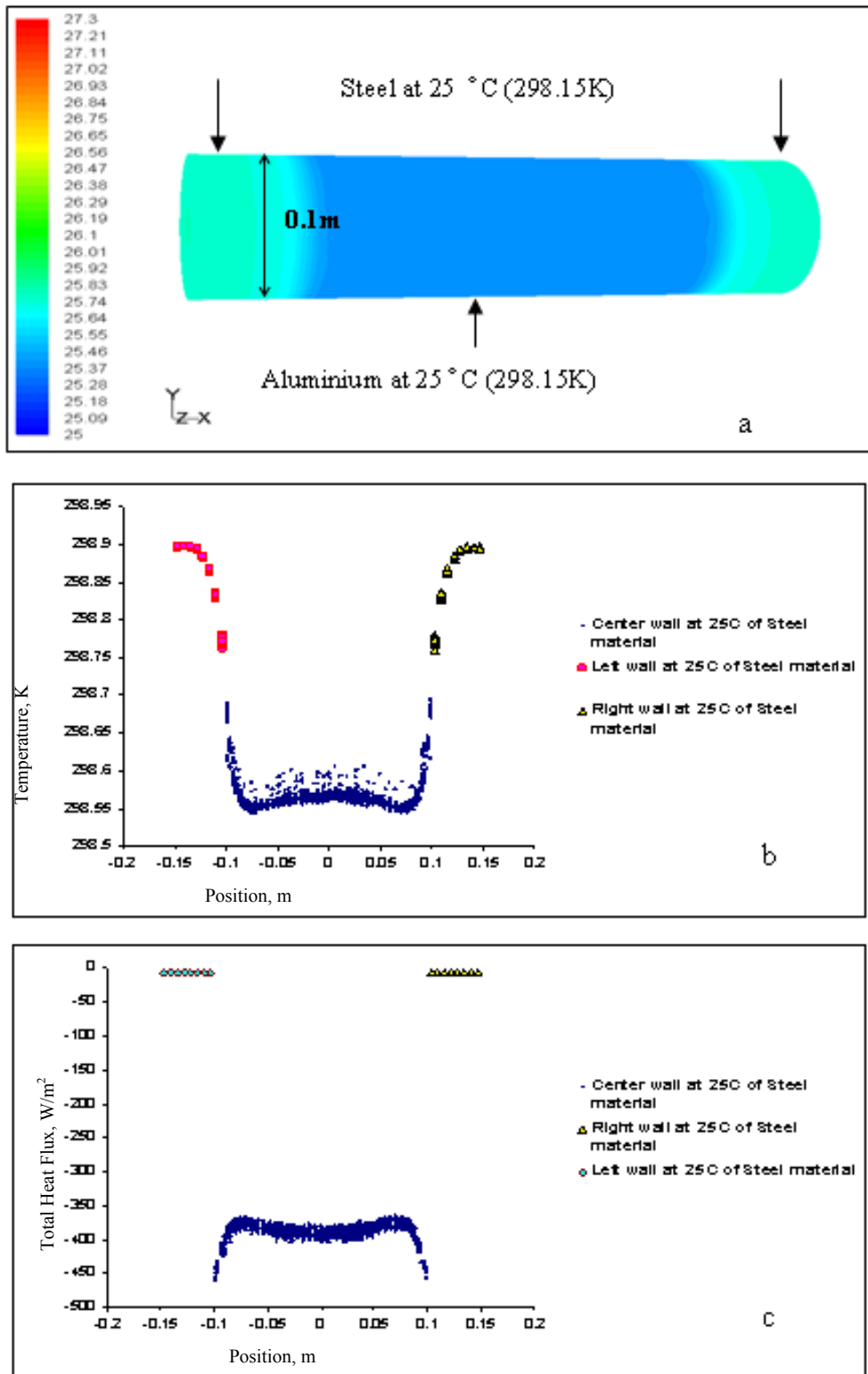


Figure A.8. Case 8 in Table A.1. Three regions of center wall and tow side are made of Steel, at 25 °C of center wall region (irrigation) and 25 °C of the two side region; a) temperature contours for the three regions; b) temperature distribution along the cylinder; c) heat flux along the surface.

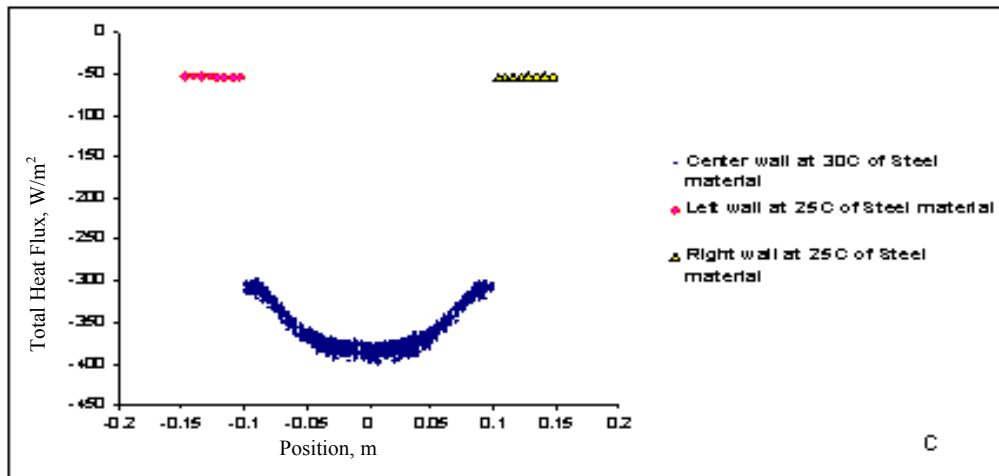
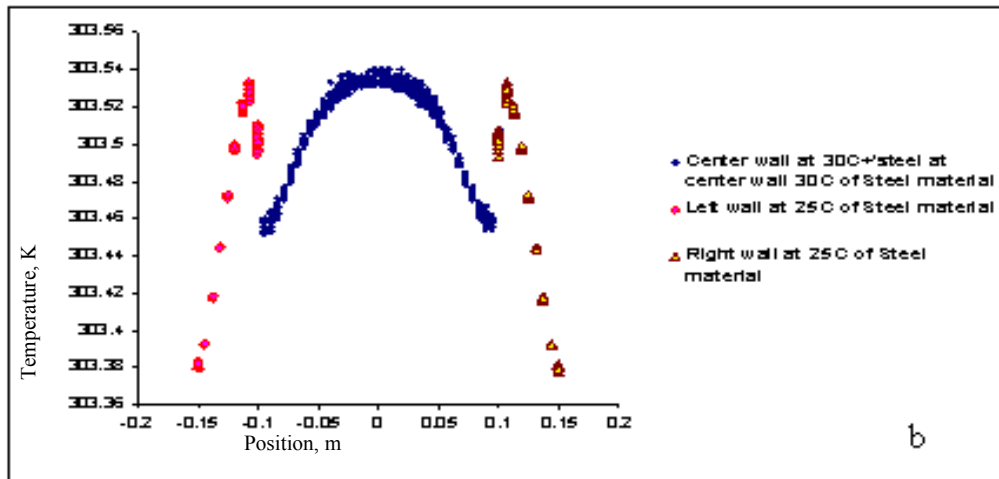
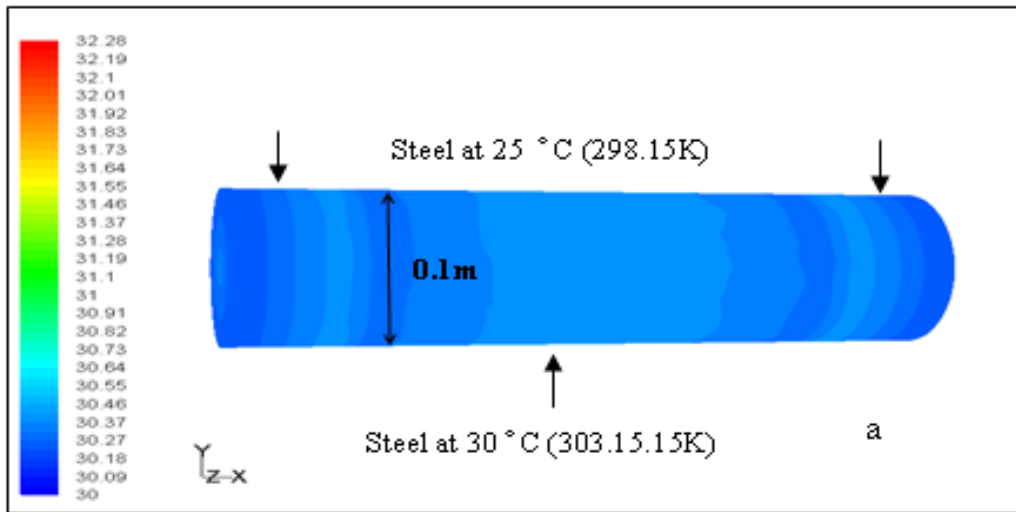


Figure A.9. Case 9 in Table A.1. Three regions of center wall and tow side are made of Steel, at 30°C of center wall region (irrigation) and 25°C of the two side region; a) temperature contours for the three regions; b) temperature distribution along the cylinder; c) heat flux along the surface.

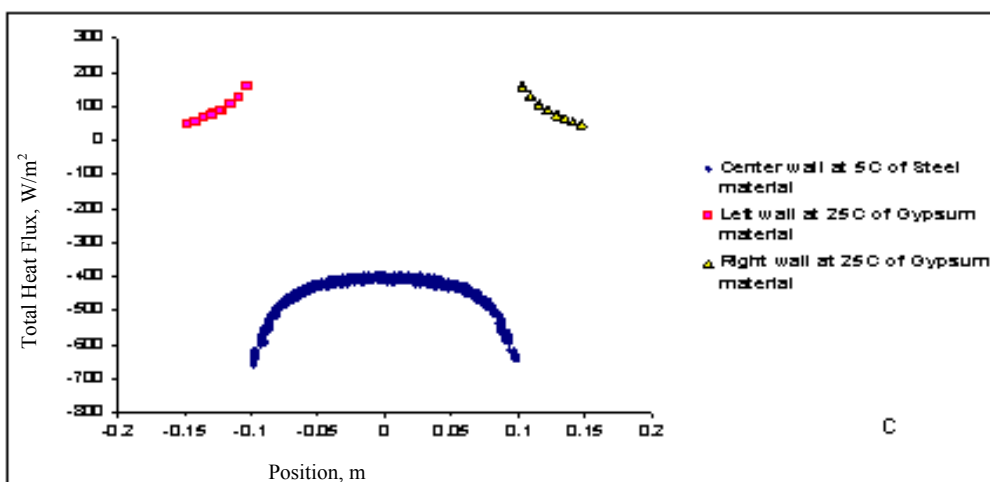
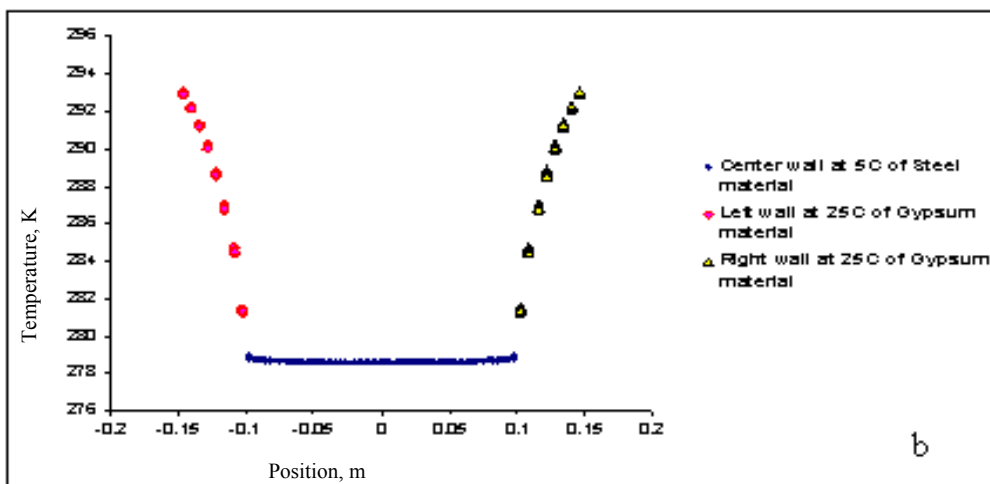
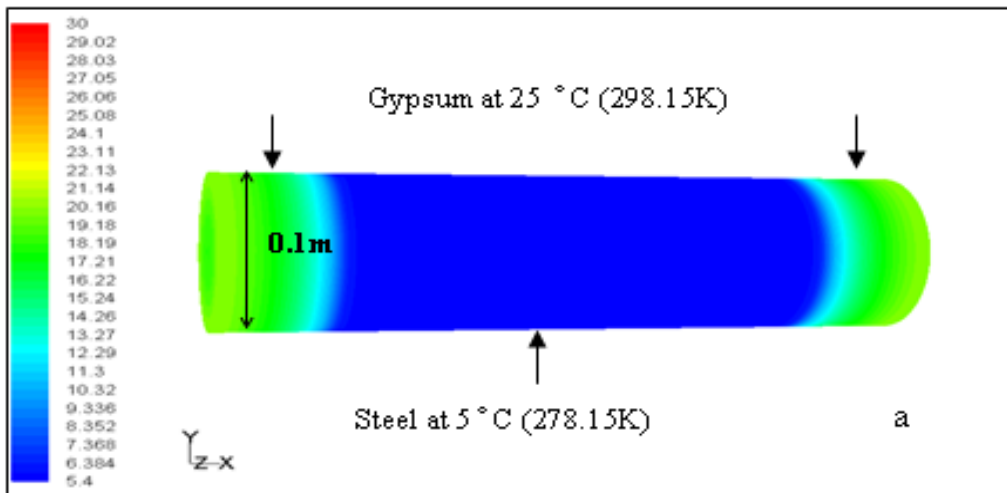


Figure A.10. Center wall region (irrigation) is made of Steel at 5 °C. Two side regions are made of Gypsum at 25 °C; a) temperature contours for the three regions; b) temperature distribution along the cylinder; c) heat flux along the surface.

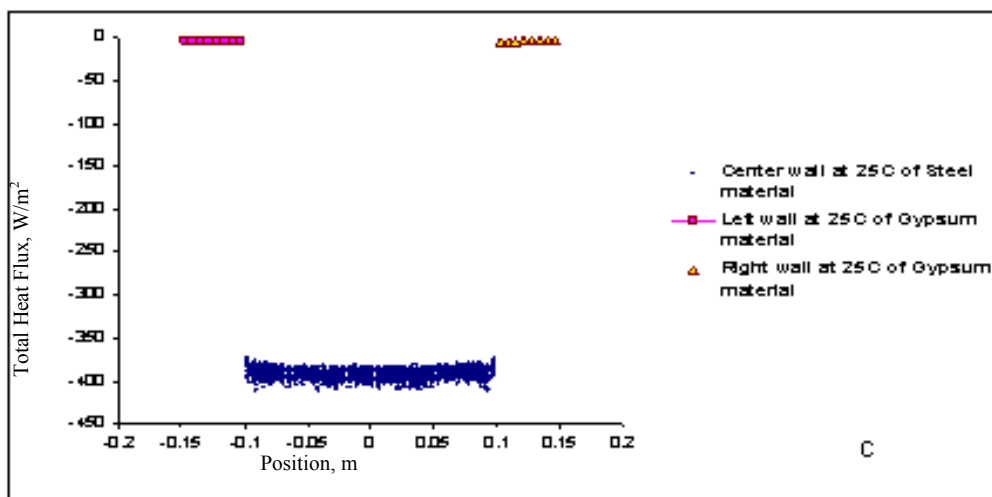
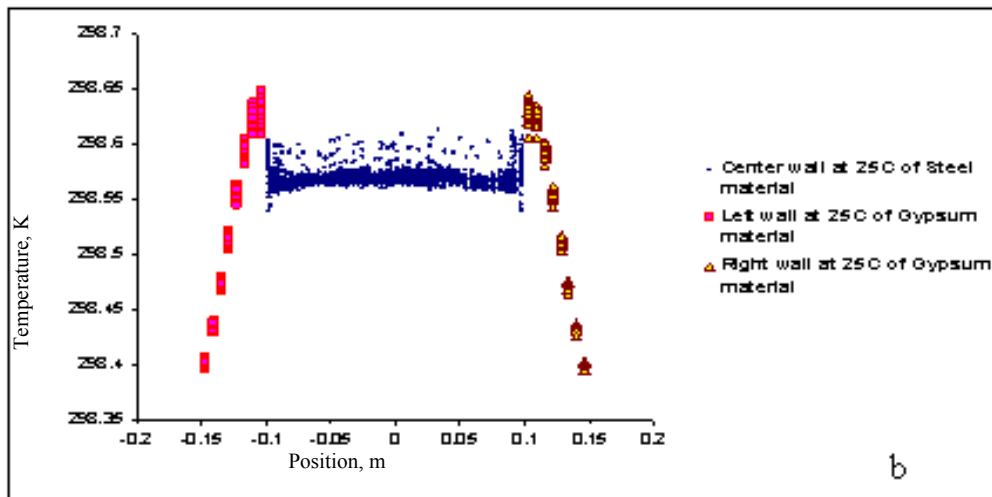
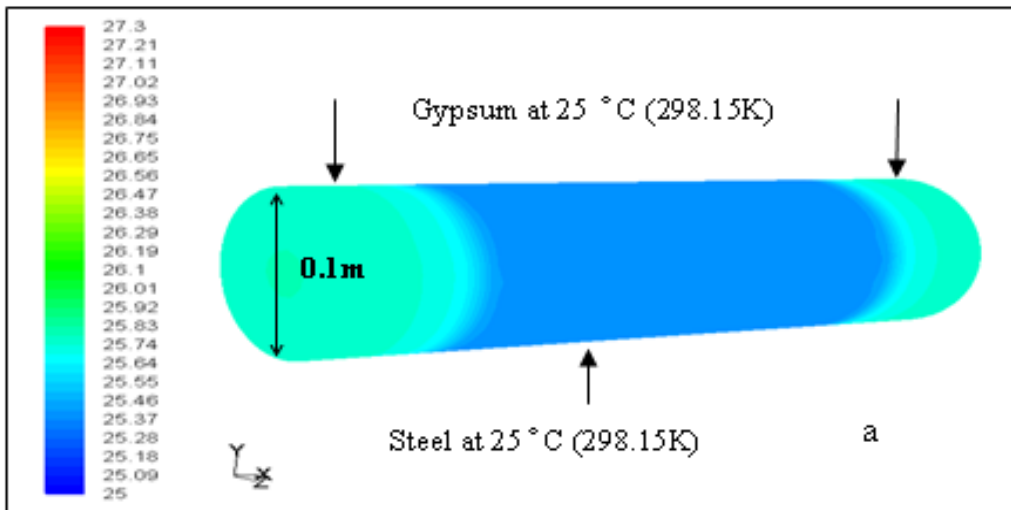


Figure A.11. Case 11 in Table A.1. Center wall region (irrigation) is made of Steel at 25 °C. Two side regions are made of Gypsum at 25 °C; a) temperature contours for the three regions; b) temperature distribution along the cylinder; c) heat flux along the surface.

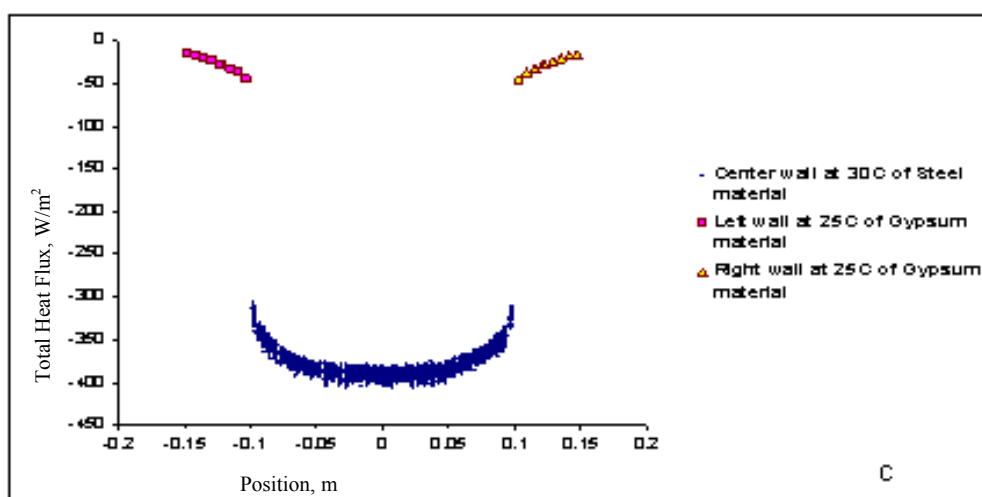
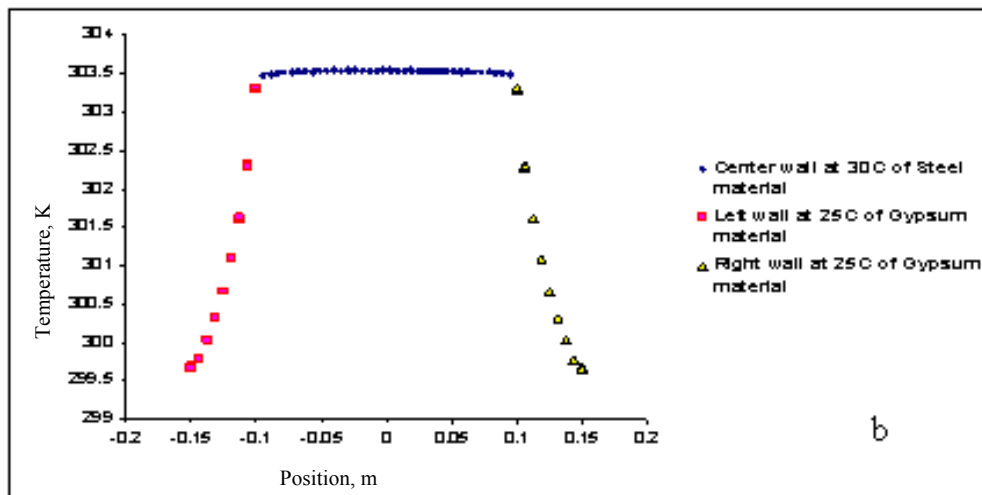
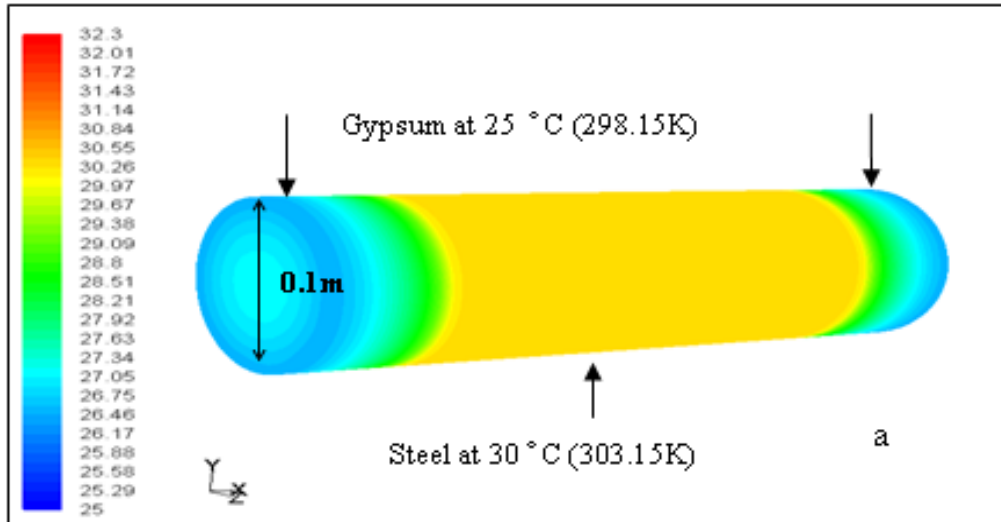


Figure A.12. Case 12 in Table A.1. Center wall region (irrigation) is made of Steel at 30 °C. Two side regions are made of Gypsum at 25 °C; a) temperature contours for the three regions; b) temperature distribution along the cylinder; c) heat flux along the surface.

The effect of the tube diameter has been investigated as shown in Figures A.13, A.14 and A.15 for the diameters of 0.04 m, 0.06 m and 0.08 m respectively. In these figures, the center wall region is made of Aluminium and the two side regions are made of Gypsum. The center wall temperature and the two side temperature are at 25°C.

In Figures A.13a, A.14a and A.15, the temperature contours and distribution are shown for cylinder diameters of 0.04 m, 0.06 m and 0.08 m respectively. The temperature distribution is shown in Figure A.13b, A.14b and A.15b, and the heat flux distribution is shown in Figures A.13c, A.14c and A.15c. The results of these simulations indicate that the best scenario is for a small diameter. This is due to change in the thermal boundary layer development length and the length of liquid impingement region.

As a summary of these results, the heat flux for a Steel cylinder without an insulation region (all three regions are made of Steel) at water temperatures of 5, 25, and 30°C are not dependable as shown in Figures A.7, A.8 and A.9. Replacing the two ends with Gypsum, it is found that irrigation at 5 and 30°C is not promising as shown in Figure A.10 and A.12, whereas the heat flux is adequate when the irrigation is at 25°C as shown in Figure A.11.

It can be seen that the best scenario is the one in Figure A.5 where on Aluminium cylinder is the center region and Gypsum at the ambient temperature of 25°C as the right and left side wall regions, with water irrigation at 25°C.

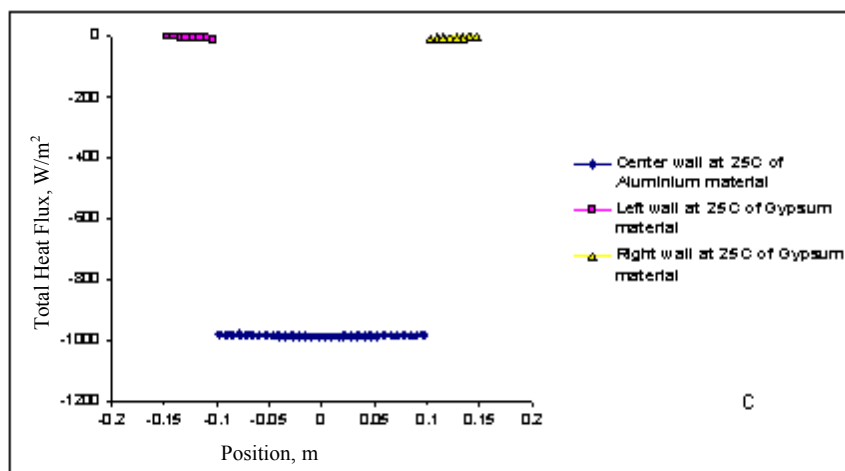
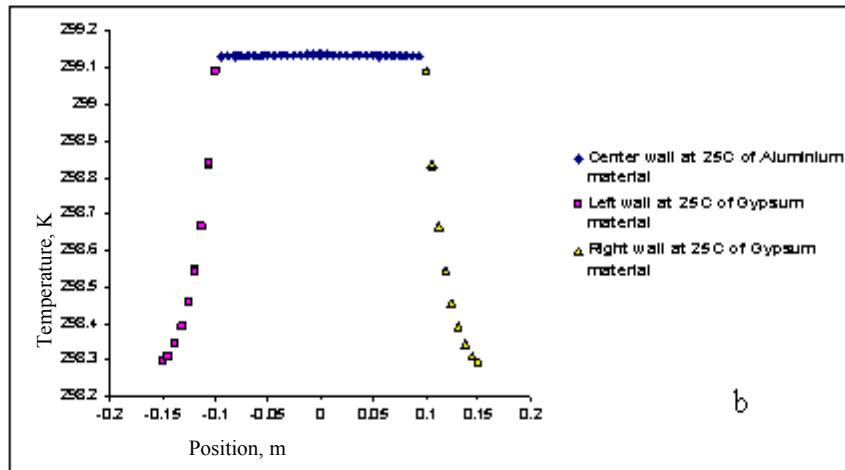
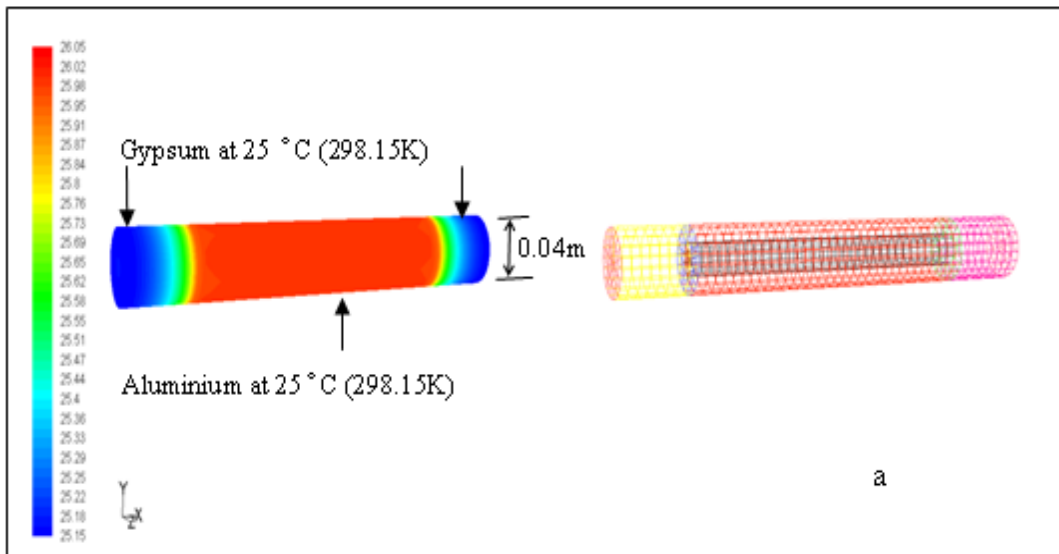


Figure A.13. Center wall region (irrigation) is made of Aluminium of 0.04m diameter at 25 °C. Two side regions are made of Gypsum at 25 °C; a) temperature contours for the three regions; b) temperature distribution along the cylinder; c) heat flux along the surface.

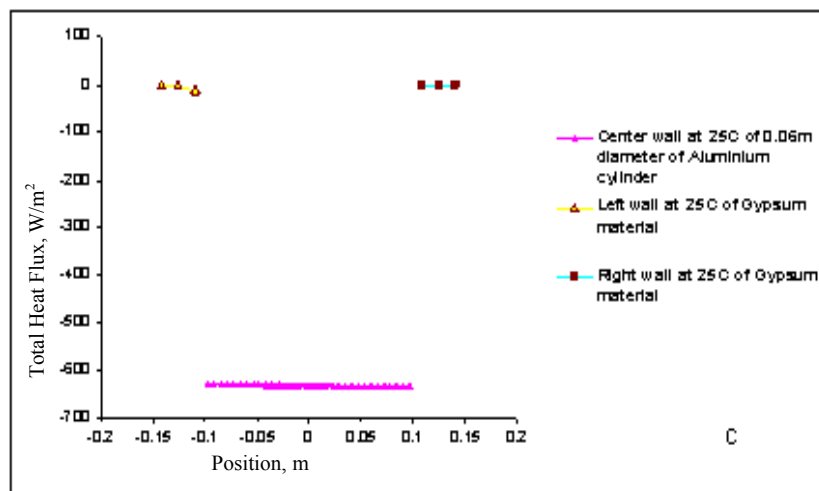
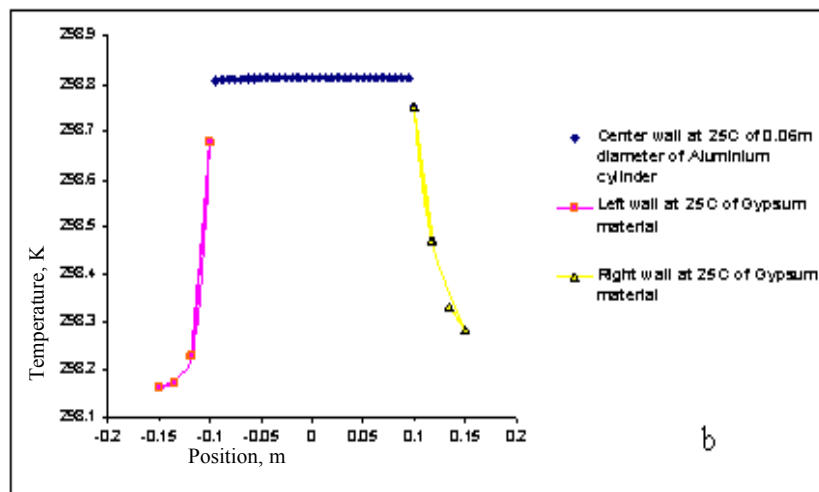
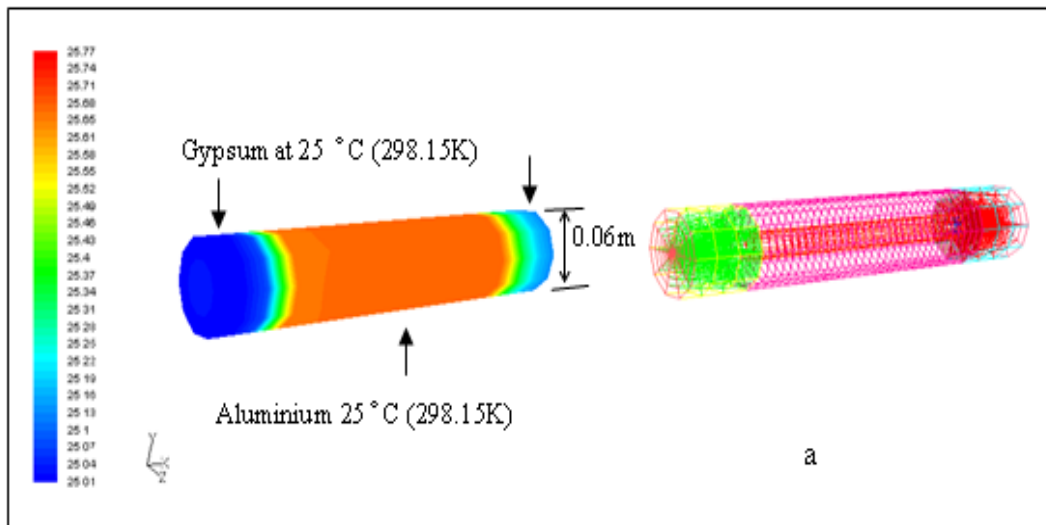


Figure A.14. Center wall region (irrigation) is made of Aluminium of 0.06m diameter at 25 °C. Two side regions are made of Gypsum at 25 °C; a) temperature contours for the three regions; b) temperature distribution along the cylinder; c) heat flux along the surface.

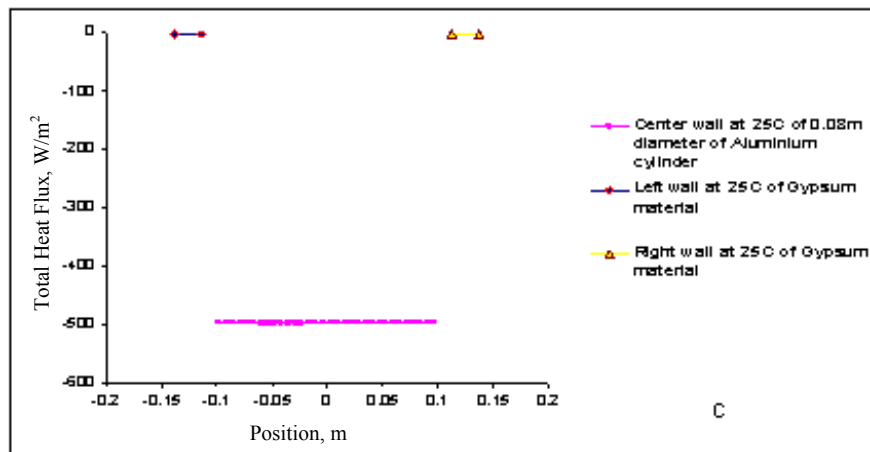
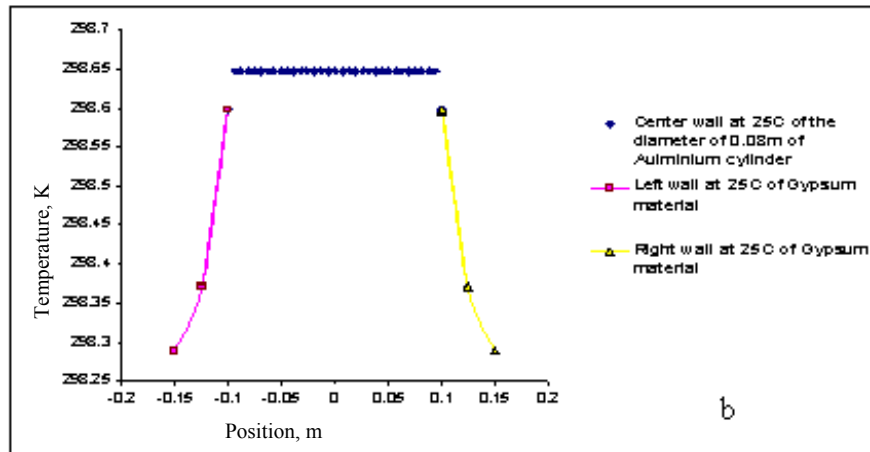
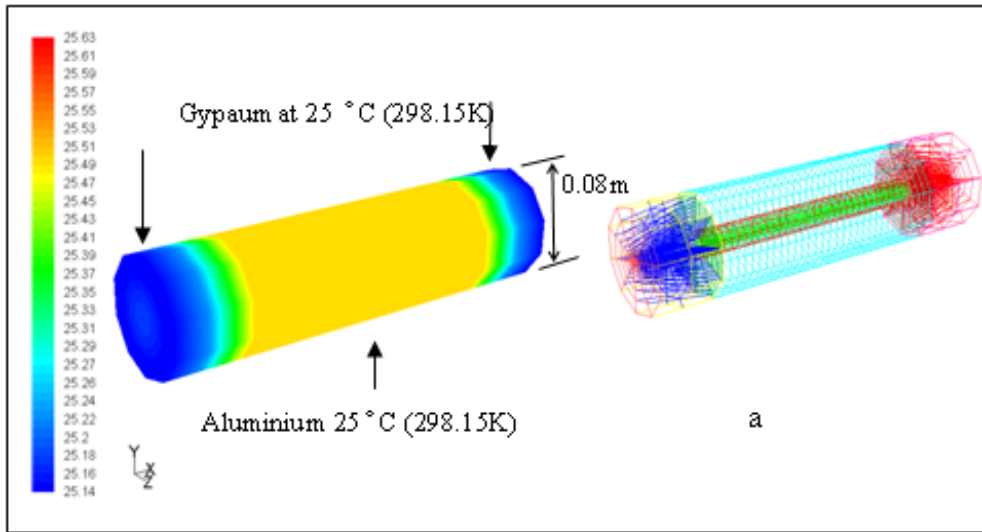


Figure A.15. Case 15 in Table A.1. Center wall region (irrigation) is made of Aluminium of 0.08m diameter at 25 °C. Two side regions are made of Gypsum at 25 °C; a) temperature contours for the three regions; b) temperature distribution along the cylinder; c) heat flux along the surface.

APPENDIX B

Falling Film over Cylinders in Random, Rectangular Pitch Arrangements and up to Ten Horizontal Cylinders: Flow Field

In addition to studying the falling film over three horizontal heated cylinders, the effect of bundles of cylinders has been investigated in this study. There are two types of cylinder bundle arrangements considered here, namely, the random and rectangular pitch arrangements. In addition, up to ten horizontal cylinders have been studied. The objective here is to investigate the flow field for these geometries towards the simulation of more realistic experiments in a hydrocooler system.

The random and rectangular cylinders arrangements are presented in Figures B.1 and B.2, respectively. It can be seen from these two figures that there more uniform liquid distribution in the case of the rectangular pitch arrangement than the random layout. The flow field with ten horizontal cylinders is shown in Figure B.3. It can be seen from Figure B.4 that the wetted area is a function of Reynolds number. When the liquid flow rate increases, wetted area appears occasionally at first and then continues on the surface with a further increasing of flow rate. Thus the wetted area is expected to increase with increasing initial flow rate and the location of cylinder.

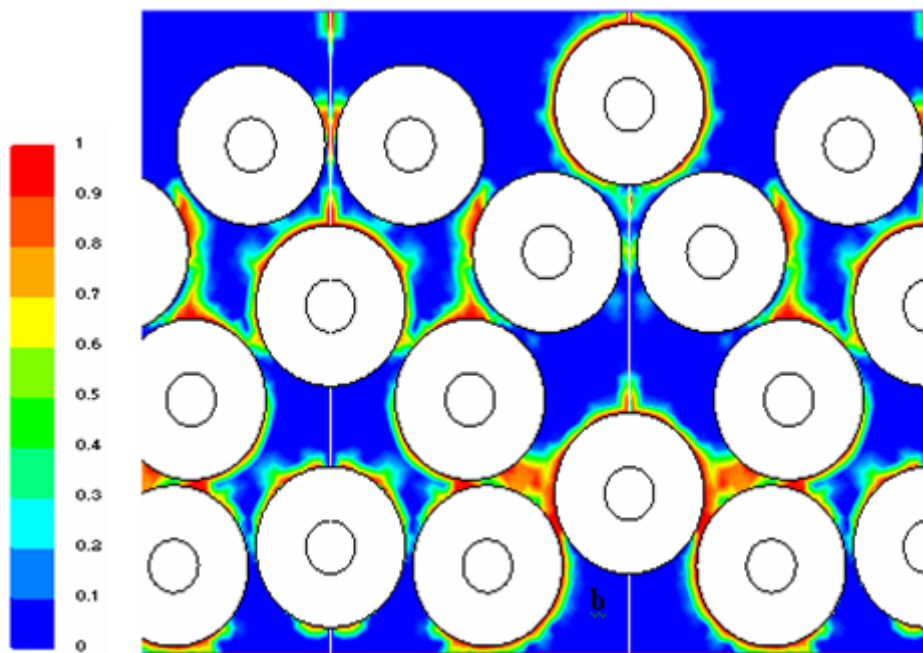
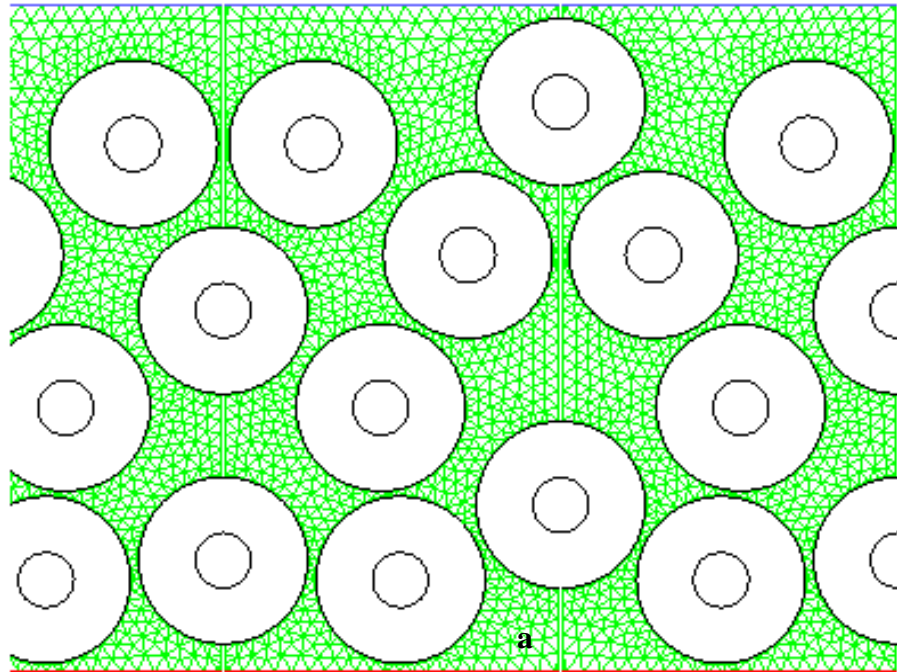


Figure B.1. Flow visualization of falling liquid film over random cylinders arrangement, a) the mesh and b) flow field around the liquid film falling over cylinders at $Re = 1300$.

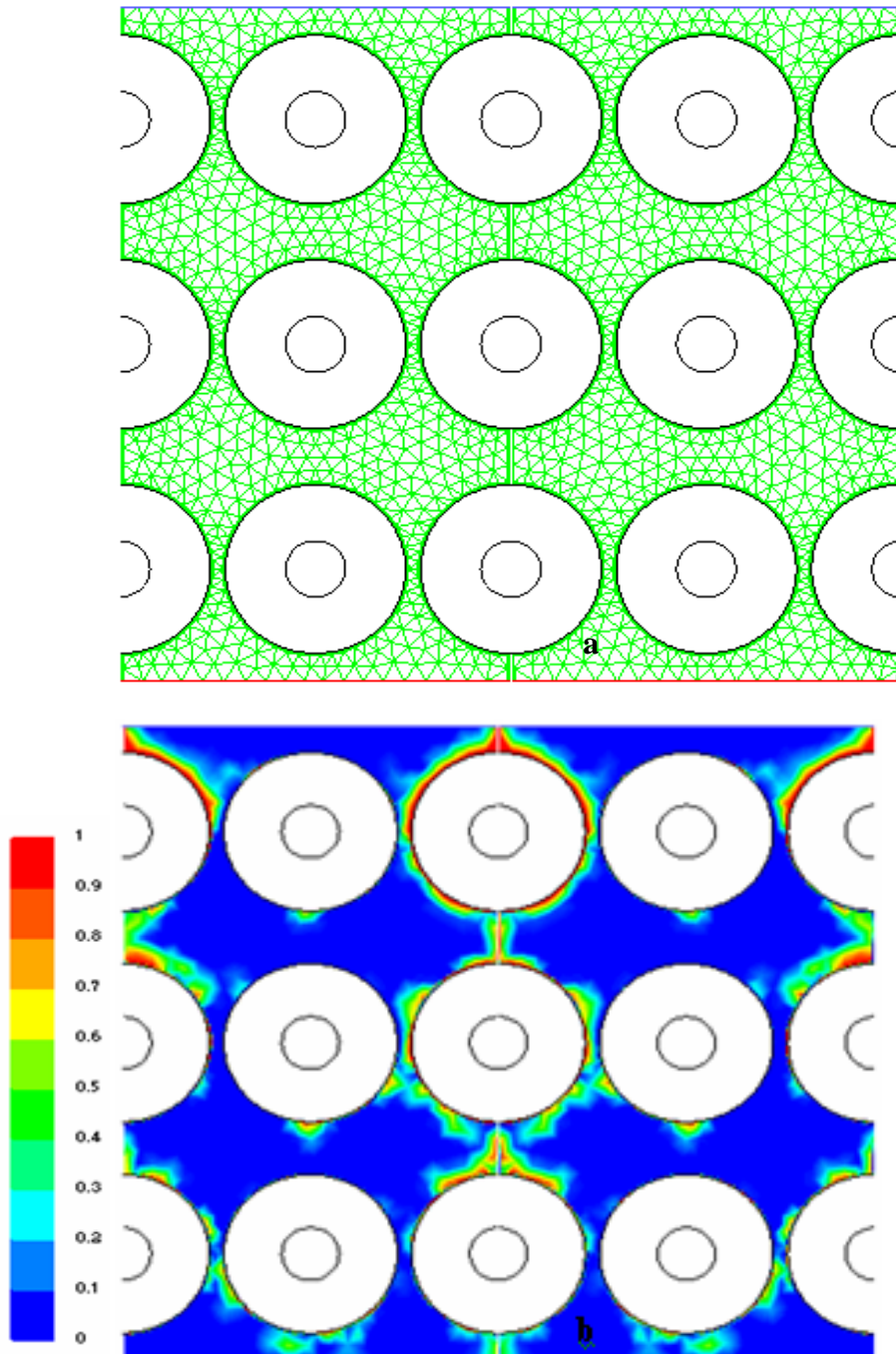


Figure B.2. Flow visualization of falling liquid film over rectangular cylinders arrangement, a) the mesh and b) flow field around the cylinders at $Re = 1300$.

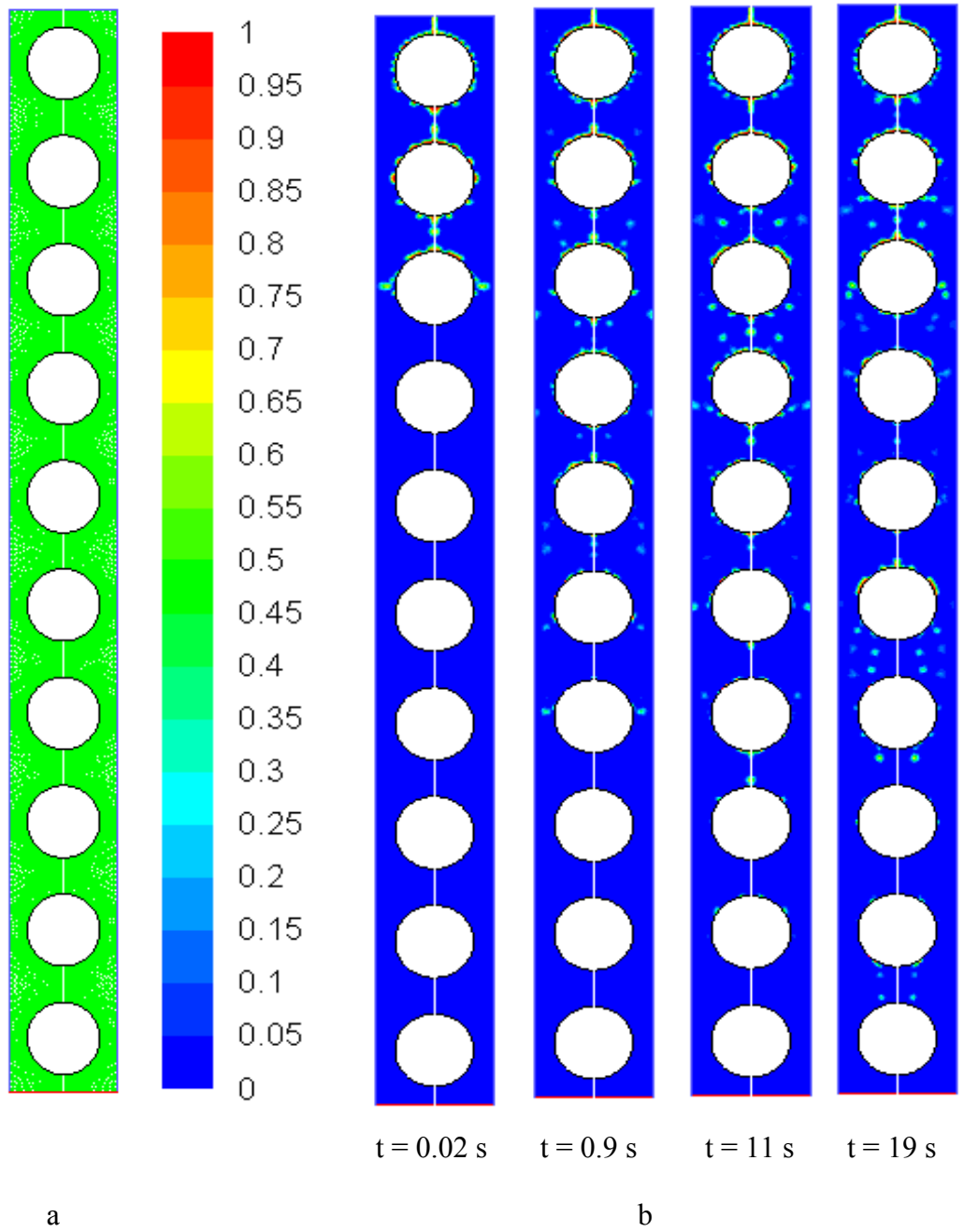


Figure B.3: Flow visualization of falling liquid film over ten cylinders. a) the mesh and b) flow field around the cylinders at different times at $Re = 1300$.

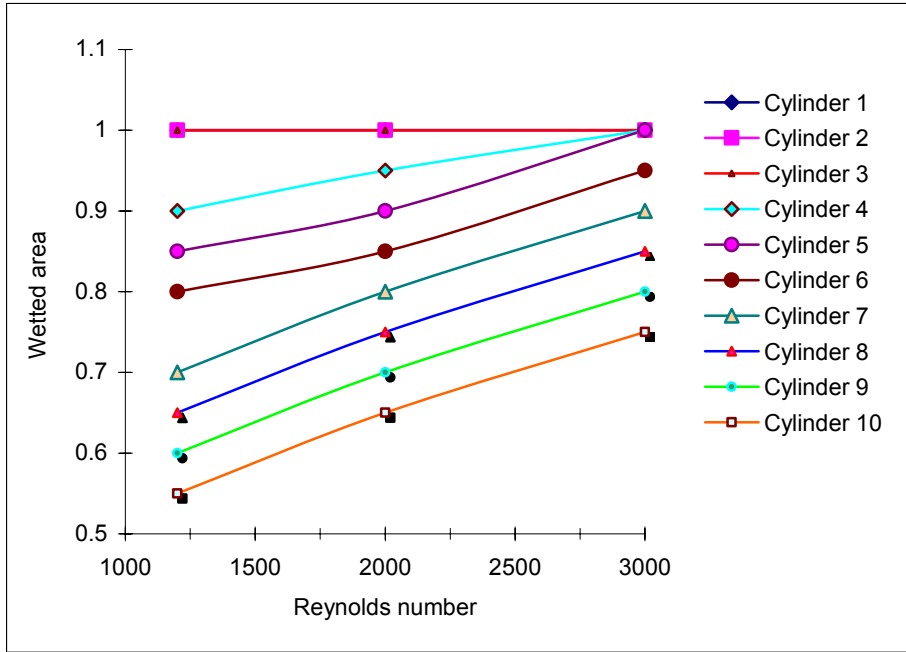


Figure B.4. Wetted area for ten horizontal cylinders at different Reynolds numbers.

APPENDIX C

Falling Film over Cylinders in Random, Rectangular Pitch Arrangements and up to Ten Horizontal Cylinders: Heat Transfer

In this appendix, the heat transfer results are presented for the cases introduced in Appendix B.

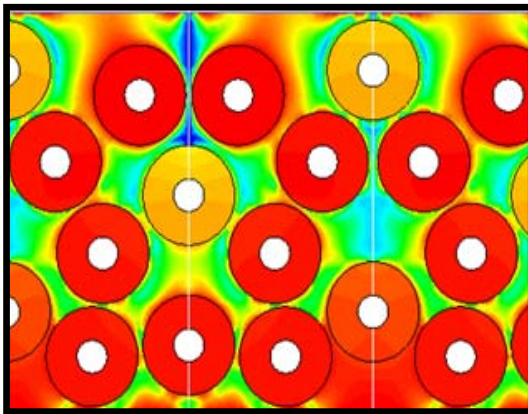
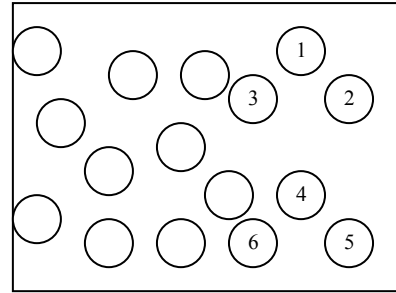
Moeykens *et al.* (1995) investigated the effect of the bundle of tube arrangements on heat transfer. They found that the heat transfer coefficient increases from row to row in a square pitch arrangement at low heat flux, due to the uniform irrigation. While in triangular pitch arrangements, the liquid flow rate distribution seems to be less uniform than in the square pitch. Therefore, row to row variation is larger in a square pitch arrangement. Also, they have found that the triangular pitch bundles provide higher average heat transfer coefficient than the square pitch bundles at high heat fluxes.

Zeng *et al.* (2001) studied the effect of heat transfer on triangular pitch plain tubes. Their results show that square pitch bundles seem to provide a higher performance than triangular pitch bundles at low saturation temperatures, and that a triangular pitch bundle is more likely to provide a better performance at high saturation temperatures.

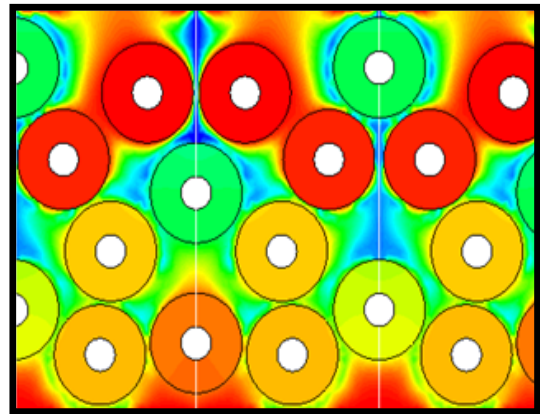
In Figures C.1 and C.2, the temperature distribution from the numerical simulation of the rectangular and random pitch arrangements are shown respectively. The inlet temperature for both arrangements is 5 °C. The cylinder diameter is 0.1 m, the height of the feeder from the first row of the cylinders is 0.01 m, and cylinder wall temperature assumed to be 27 °C at these start. It can be seen that the first row at all different times is cooled faster than the second row, and the second row faster than the third row, as expected.

In Figures C.3 and C.4, the cylinder wall temperature at different times for rectangular and random pitch arrangements are shown, respectively. It can be

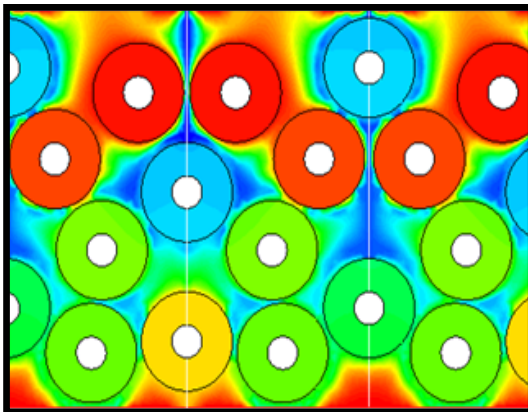
Random pitch arrangement



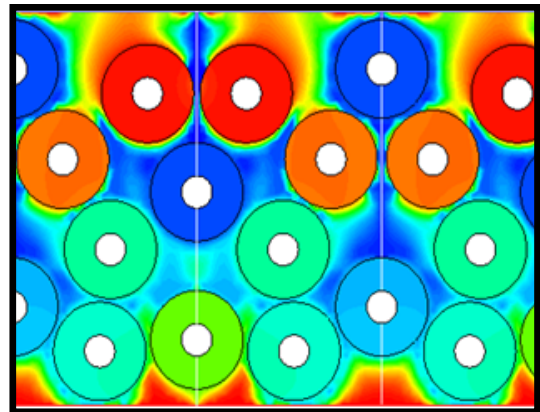
a



b



c



d

Figure C.2. Temperature distribution for the random pitch arrangement at different times.

a) $t = 30$ s, b) $t = 90$ s, c) $t = 150$, and d) $t = 200$ s.

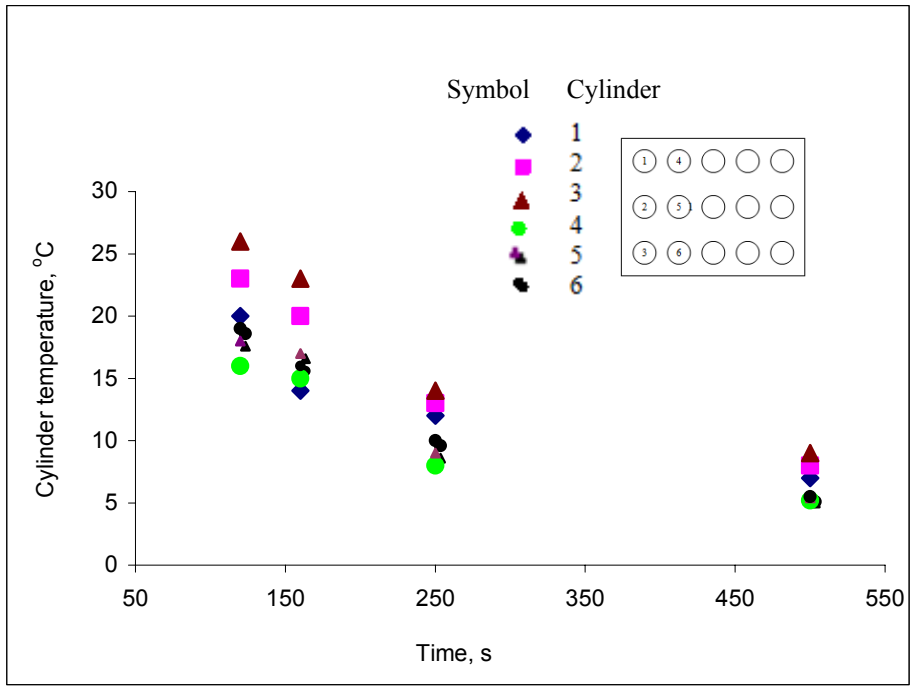


Figure C.3. Cylinder temperature for the rectangular pitch arrangement. Cylinders 4, 5 and 6 are below the nozzle.

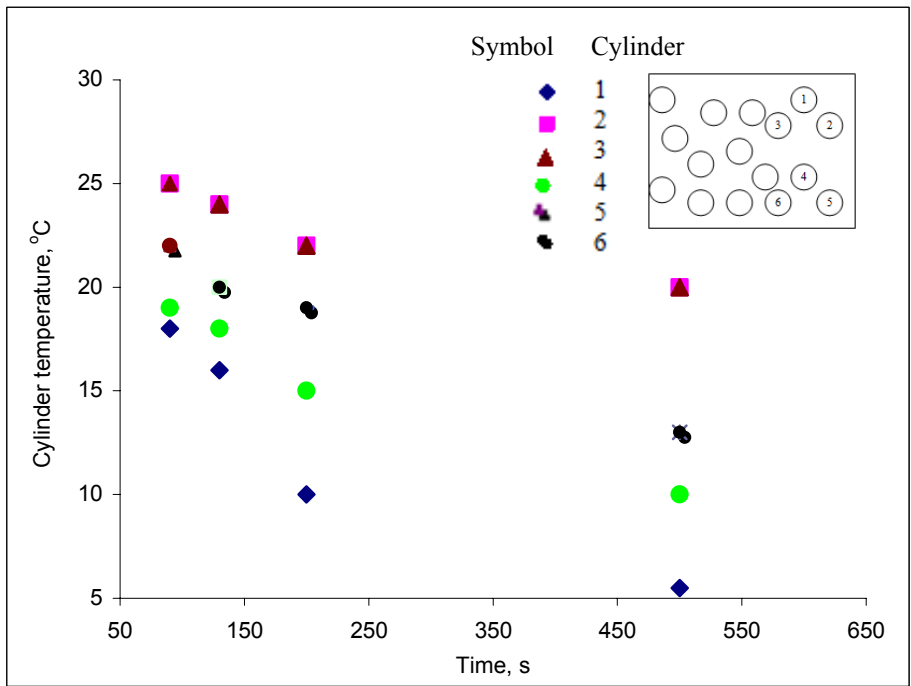


Figure C.4. Cylinder temperature for the random pitch arrangement. Cylinders 1 and 4 are below the nozzle.

For ten horizontal cylinders, the temperature distribution has been monitored similar to the 2D cases, as shown in Figure C.5. The top cylinder cools faster than the bottom ones, due to its closeness to the feeder, as discussed earlier in Section 5.6.2.

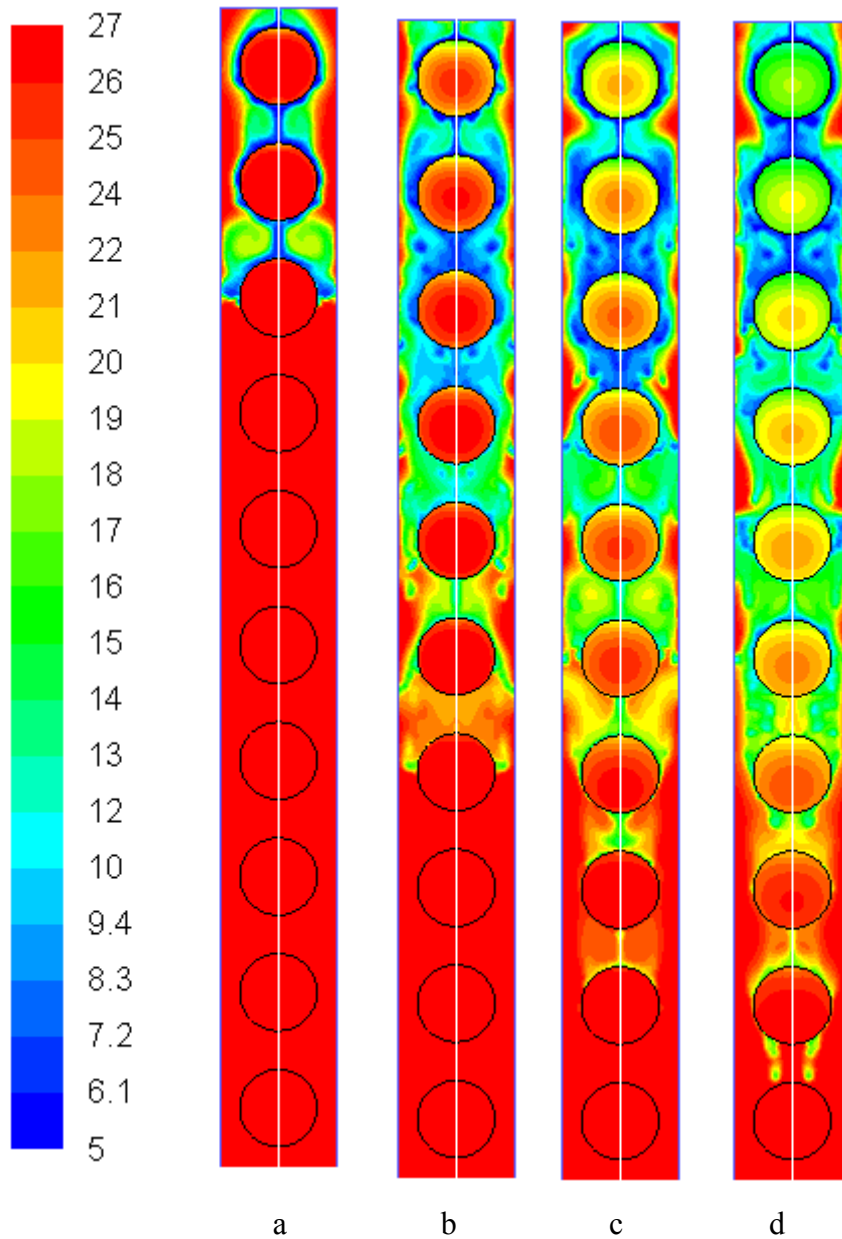


Figure C.5. Temperature distribution of 2D ten cylinders. a) 90 s, b) 250 s, c) 420 s and d) 950 s.

REFERENCES

- Anon 2007, *Hydrocoolers*, viewed 4 Nov. 2009
<<http://www.trj-inc.com/hydroCooler.html>>.
- Armbruster, R & Mitrovic, J 1994, 'Patterns of falling film flow over horizontal smooth tubes', *Proceedings of the Tenth International Heat Transfer Conference*, vol. 3, pp. 275-80.
- Baonga, JB, Louahlia-Gualous, H & Imbert, M 2006, 'Experimental study of the hydrodynamic and heat transfer of free liquid jet impinging a flat circular heated disk', *Applied Thermal Engineering*, vol. 26, no. 11-12, pp. 1125-38.
- Beitelmal, AH, Shah, AJ & Saad, MA 2006, 'Analysis of an impinging two dimensional jet', *Journal of Heat Transfer*, vol. 128, pp. 307-10.
- Bellman, RH & Pennington 1954, 'Effects of surface tension and viscosity on Taylor instability', *Appl. Math.*, vol. 12, pp. 151 - 62.
- Boyette, MD, Estes, EA & Rubin, AR 1992, *Hydrocooling*,
<<http://www.bae.ncsu.edu/programs/extension/publicat/postharv/ag-414-4/index.html>>.
- Boyette, MD, Estes, E. A, Rubin, A. R 1992, **Hydrocooling**, North Carolina State University, North Carolina A&T State University, U.S. Department of Agriculture, and local governments cooperating.
- Brumfield, LK & Theofanous, TG 1976, 'On the Prediction of Heat Transfer Across Turbulent Liquid Films', *Transactions of the ASME Journal of Heat Transfer* pp. 496-502.
- Bula A. J., Rahman, MM & Leland, JE 2000, 'Numerical modeling of conjugate heat transfer during impingement of free liquid jet issuing from a slot nozzle', *Numerical Heat Transfer – Part A- Applications*, vol. 38 no.1, pp. 45-66.
- Chan, TL, Leung, CW, Jambunathan, K, Ashforth-Frost, S, Y., Z & Liu, MH 2002, 'Heat transfer characteristics of a slot jet impinging on a semi-circular convex surface', *International Journal of Heat and Mass Transfer*, vol. 45, pp. 993 – 1006.
- Chun, KR & Seban, RA 1972, 'Performance Prediction of Falling Film Evaporators', *ASME Journal of Heat Transfer*, vol. 94, pp. 432-6.
- Chung, YM, Luo, KH & Sandham, ND 2002, 'Numerical study of momentum and heat transfer in unsteady impinging jets', *International Journal of Heat and Fluid Flow*, vol. 23, pp. 592 - 600.
- Chung, YM, Luo, KH & Sandham, NDC 2002, 'Numerical study of momentum and heat transfer in unsteady impinging jets', *International Journal of Heat and Fluid Flow*, vol. 23, pp. 592-600.
- Chyu, M-C & Bergles, AE 1987, 'An Analytical and Experimental Study of Falling-Film Evaporation on a Horizontal Tube', *Transactions of the ASME Journal of Heat Transfer*, vol. 109, pp. 983-90.
- Dirita, C, De Bonis, MV & Ruocco, G 2007, 'Analysis of food cooling by jet impingement, including inherent conduction', *Journal of Food engineering*, vol. 81, pp. 12-20.
- Fenot, M, Vullierme, JJ & Dorignac, E 2005, 'Local heat transfer due to several configurations of circular air jets impinging on a flat plate with and without

- semi-confinement,' *International Journal of Thermal Sciences*, vol. 44, pp. 665 – 75.
- Fletcher, LS, Sernas, V & Parken, WH 1975, 'Evaporation Heat Transfer Coefficients for Thin Sea Water Film on Horizontal tubes', *Industrial Engineering Chemistry*, vol. Vol. 14, pp. 411 – 6.
- Fujita, Y & Tsutsui, M 1995a, 'Evaporation Heat Transfer of Falling Film on Horizontal Tube - Part 1, Analytical Study', *Heat Transfer - Japanese Research*, vol. 24, no. 1.
- 1995b, 'Evaporation heat transfer of falling films on horizontal tube, Part 2, Experimental study', *Heat Transfer Journal* vol. 24, pp. 17 – 31.
- Ganic, EN & Roppo, MN 1980, 'An Experimental Study of Falling Liquid Film Breakdown on Horizontal Cylinder During Heat Transfer', *Journal of Heat Transfer*, vol. 102, pp. 342 – 6.
- Gardon, R & Akfirat, JC 1965, 'The role of turbulence in determining the heat-transfer characteristics of impinging jets', *Int. j. heat Mass Transfer*, vol. 8, pp. 101-8.
- Gardon, R & Akfirat, Jc 1966, 'Heat transfer characteristics of impinging two-dimensional air jets', *J. Heat Transfer*, vol. 86, no. 101-108.
- Goppert, S, Gurtler, T, Mocikat, H & Herwig, H 2004, 'Heat transfer under a processing jet: effects of unsteady jet impingement,' *International Journal of Heat and Mass Transfer*, vol. 47, pp. 2795 – 806.
- Hansen, LG & Webb, BW 1993, 'Air jet impingement heat transfer from modified surfaces', *J. Heat Mass Transfer*, vol. 36, pp. 989-97.
- Hirt, CW & Nichols, BD 1981, 'Volume of fluid method for the dynamics of free boundaries', *J. comput. Phys*, vol. 39, p. 201.
- Hofmann, HM, Kind, M & Martin, H 2007, 'Measurements on steady state heat transfer and flow structure and new correlations for heat and mass transfer in submerged impinging jets', *Int. J. Heat Mass Transfer*, vol. 50, pp. 3957-65.
- Honda, H, Nozu, S & Takeda, Y 1987, 'Flow Characteristics of Condensation on a Vertical Column of Horizontal Tubes', *ASME - JSME Thermal Engineering Joint Conference, Honolulu*, vol. 1, pp. 517 - 24.
- Hrycak, P 1983, 'Heat transfer from round impinging jets to flat plate', *International Journal of Heat and Mass Transfer*, vol. 26, pp. 1857-65.
- Hu, X & Jacobi, AM 1996, 'The Intertube Falling Film Part 1 - Flow Characteristics. Mode Transitions and Hysteresis.', *ASME J. Heat Transfer*, vol. 118, pp. 616 - 25.
- 1996, 'The Intertube Falling Film: Part 2 – Mode Effects on Sensible Heat Transfer to a Falling Liquid Film', *Journal of Heat Transfer*, vol. 118, pp. 626 – 33.
- 1998, 'Departure - site spacing for liquid droplets and jets falling between horizontal circular tubes.', *Experimental Thermal and Fluid Science*, vol. 16, pp. 322 - 31.
- Huang, L & El-Genk, MS 1994, 'Heat transfer of an impinging jet on a flat surface', *International Journal of heat and mass transfer* vol. 37, no. 13, pp. 1915 - 23.
- Incropera, FP & DeWitt, DP 1990, *Fundamentals of Heat and Mass Transfer*, 3rd edn, John Wiley and Sons, New York.

- Jafar, FA, Thorpe, GR & Turan, OF 2007, 'Liquid Film Falling on Horizontal Circular Cylinders', paper presented to 16th Australasian Fluid Mechanics Conference, Gold Coast, Queensland, Australia, 3-7 December.
- Jafar, FA, Thorpe, GR & Turan, ÖF 2009, 'Flow Mode Characterisation of Liquid Films Falling on Horizontal Plain Cylinders', paper presented to Seventh International Conference on CFD in the Minerals and Process Industries Melbourne, Australia, 9-11 December 2009.
- Jambunathan, K, Lai, E, Moss, MA & Button, BL 1992, 'A review of heat transfer data for single circular impingement', *Internat.J. Heat Fluid Flow.*, vol. 13, no. 2, pp. 106-15.
- Kanna, PR & Das, MK 2008, 'Heat transfer study of two-dimensional laminar incompressible offset jet flows', *International Journal of Thermal Sciences*, vol. 47, no. 12, pp. 1620-9.
- Katti, V & Prabhu, SV 2008, 'Experimental study and theoretical analysis of local heat transfer distribution between smooth flat surface and impinging air jet from a circular straight pipe nozzle', *International Journal of Heat and Mass Transfer*, *ARTICLE IN PRESS*.
- Larachi, F, Alix, C, Grandjean, BPA & Bernis, A 2003, "Nu/Sh correlation for particle – liquid heat and mass transfer coefficients in trickle beds on Peclet similarity", *Chem. Eng. Res. Dev. (Trans IChemE Part A)*, vol. 81, pp. 689 - 94.
- Lee, DH, Song, J & Jo, MC 2004, 'The effect of nozzle diameter on impinging jet heat transfer and fluid flow', *J. Heat Transfer*, vol. 126, pp. 554-7.
- Lee, SL 1963, 'Instability of a liquid film around a long, horizontal, circular cylindrical body in still air', *J. Appl. Mech. Trans. ASME* vol. 30, p. 443.
- Lienhard, JH & Wong, PTY 1964, 'The dominant useable wavelength and minimum heat flux during film boiling on a horizontal cylinder', *ASME Journal of Heat Transfer* vol. 86, pp. 220-6.
- Liu, X, Lienhard, VJH & Lombara, JS 1991, 'Convective heat transfer by impingement of circular liquid jets', *ASME J. Heat Transfer.*, vol. 113, pp. 571-82.
- Looney, MK & Walsh, JJ 1984, 'Mean-flow and turbulent characteristics of free and impinging jet flows', *J. Fluid Mech*, vol. 147, pp. 397-429.
- Lytle, D & Webb, BW 1994, 'Air jet impingement heat transfer at low nozzle plate spacing,' *Int. J. Heat Mass Transfer* vol. 37(12), pp. 1687-97.
- Maron-Moalem, D, Sideman, S & Dukler, AE 1978, 'Dripping characteristics in a horizontal tube film evaporator', *Desalination*, vol. 27, pp. 117-27.
- Martin, H 1977, 'Heat and mass transfer between impinging gas jets and solid surfaces', *Adv. Heat Transfer*, vol. 13, pp. 1-60.
- McDaniel, CS & Webb, BW 2000, 'Slot jet impingement heat transfer from circular cylinders', *Int. J. Heat Mass Transfer* vol. 43, pp. 1975-85.
- McMurray, DC, Myers, PS & Uyehara, OA 1966, 'Influence of Impinging Jet Variables on Local Heat Transfer Coefficients Along a Flat Surface With Constant Heat Flux', *Proceedings of the 3rd International Heat Transfer Conference*, vol. II, pp. 292-9.
- Mitrovic, J 1986, 'Influence of tube spacing and flow rate on heat transfer from a horizontal tube to a falling liquid film', *International Heat Transfer Conference San Francisco*, vol. 4, pp. 1949-56.
- Miyasaka, Y & Inada, S 1980, 'The Effect of Pure Forced Convection on the Boiling Heat Transfer Between a Two-Dimensional Subcooled Water Jet

- and Heated Surface', *Journal of Chemical Engineering in Japan*, vol. 13 no. 1, pp. 22-8.
- Moeykens, SA, Newton, BJ & Pate, MB 1995, 'Effects of surface enhancement film-feed supply rate, and bundle geometry spray evaporation heat transfer performance', *ASHRAE trans.*, vol. 101, no. 2, pp. 408-19.
- Moffat, RJ 1988, 'Describing the Uncertainties in Experimental. Results', *Experimental Thermal and Fluid Science*, vol. 1, pp. 3-17.
- Mohamed, AMI 2007, 'Flow behavior of liquid falling film on a horizontal rotating tube', *Experimental Thermal and Fluid Science*, vol. 31, pp. 325 - 32.
- Nakod, PM, Prabhu, SV & Vedula, RP 2008, 'Heat transfer augmentation between impinging circular air jet and flat plate using finned surfaces and vortex generators', *Experimental Thermal and Fluid Science*, vol. 32, pp. 1168 - 87.
- Narayanan, V, Seyed-Yagoobi, J & Page, RH 2004, 'An experimental study of fluid mechanics and heat transfer in an impinging slot jet flow', *International Journal of Heat and Mass Transfer* vol. 47, no. 1827–1845.
- Olsson, EEM, Ahrne, LM & Tragardh, AC 2004, 'Heat transfer from a slot air jet impinging on a circular cylinder ', *Journal of Food Engineering*, vol. 63, pp. 393-401.
- Ouldhadda, D, Idrissi, AI & Asbik, M 2002, 'Heat transfer in non-Newtonian falling liquid film on a horizontal circular cylinder', *Heat and Mass Transfer*, vol. 38, pp. 713 – 21.
- Parken, WH 1975, 'Heat Transfer to Thin Water Film on Horizontal Tubes', Rutgers University
- Ribatski, G & Jacobi, AM 2005, 'Falling – film evaporation on horizontal tubes – a critical review', *International Journal of Refrigeration*, vol. 28, pp. 635 – 53.
- Robinson, AJ & Schnitzler, E 2007, 'An experimental investigation of free and submerged miniature liquid jet array impingement heat transfer', *Experimental Thermal and Fluid Science*, vol. 32, pp. 1-13.
- Rogers, JT 1981, 'Laminar falling film flow and heat transfer characteristics on horizontal tubes', *Canadian Journal of Chemical Engineering* vol. 59, pp. 213-22.
- Rogers, JT & Goindi, SS 1989, 'Experimental laminar falling film heat transfer coefficient on a large diameter horizontal tube', *The Canadian Journal of Chemical Engineering* vol. 67, pp. 560-8.
- Roques, JF & Thome, JR 2007, 'Falling Films on Arrays of Horizontal Tubes with R – 134a, Part II: Flow Visualization, Onset of Dryout, and Heat Transfer Predictions', *Heat Transfer Engineering*, vol. 28 no. 5, pp. 415 – 34.
- Siba, EA, Ganesa-Pillai, M, Harris, KT & Haji-Sheikh, A 2003, 'Heat transfer in a high turbulence air jet impinging over a flat circular disk,' *J. Heat Transfer, ASME*, vol. 125, pp. 257-65.
- Slayzak, SJ, Viskanta, R & Incropera, FP 1994, 'Effects of interaction between adjacent free surface planar jets on local heat transfer from the impingement surface', *International Journal of Heat and Mass Transfer*, vol. 37, pp. 269-82.
- Stevens, J & Webb, BW 1989, 'Local heat transfer coefficients under an axisymmetric, single-phase liquid jet', *Am. Soc. Mech. Eng., Heat Transfer Divis.*, vol. 111, pp. 113-9.

- 1989, 'Local heat transfer coefficients under an axisymmetric, single-phase liquid jet', *Am. Soc. Mech. Eng., Heat Transfer Divis*, vol. 111 pp. 113-9.
- 1993, 'Measurements of flow structure in the radial layer of impinging free surface liquid jets,' *Int. J. Heat Mass Transfer* vol. 36, no. 15, pp. 3751-8.
- Sung, MK & Mudawar, I 2008, 'Effect of jet pattern on single-phase cooling performance of hybrid micro-channel/micro-circular-jet-impingement thermal management scheme', *International Journal of Heat and Mass Transfer*, vol. in press.
- Thorpe, GR 2006, 'Towards a semi – continuum approach to the design of hydrocoolers for horticultural produce', *Postharvest Biology and Technology*, vol. 46, pp. 280 – 9.
- 2008, *The design and operation of hydrocoolers, A Smart Water Funded Project.*,
<http://eprints.vu.edu.au/779/1/The_design_and_operation_of_a_hydrocooler11.pdf>.
- Tonini, G, Bertoloni, P & Cimino, A 1979, 'Controlled atmosphere storage of hydrocooled ', paper presented to Proceedings of the XVth International Congress of Refrigeration, Venezia, Italy.
- Watson, EJ 1964, 'The radial spread of a liquid jet over a horizontal plane,' *J. Fluid Mech.*, vol. 20 part 3, pp. 481-99.
- Wen, M-Y & Jang, K-J 2003, 'An impingement cooling on a flat surface by using circular jet with longitudinal swirling strips', *International Journal of Heat and Mass Transfer*, vol. 46, pp. 4657 – 67
- Wheeler, JP & Neti, S 1999, 'Heat transfer for a semi-confined impinging laminar jet', paper presented to ASME National Heat Transfer Albuquerque, New Mexico.
- Wikipedia® 2009, *Galilei number*, 23/05/2010,
<http://en.wikipedia.org/wiki/Galilei_number>.
- Yokobori, S, Kasagi, N, Hirata, M & Nishiwaki, N 1978, 'Role of large-scale eddy structure on enhancement of heat transfer in stagnation region of two-dimensional, submerged, impinging jet', paper presented to Proceedings of the Sixth International Heat Transfer Conference, , Toronto, Canada.
- Yoon, JI, Phan, TT, Moon, CG, Lee, HS & Jeong, SK 2008, 'Heat and mass transfer characteristics of a horizontal tube falling film absorber with small diameter tubes', *Heat Mass Transfer*, vol. 44, pp. 437-44.
- Yung, D, Lorentz, JJ & Ganic, EN 1980, 'Vapor/Liquid interface and entrainment in falling film evaporators', *Journal of Heat Transfer*, vol. 102, pp. 20-5.
- Zeng, X, Chyu, M & Ayub, ZH 2001, 'Experimental investigation on ammonia spray evaporator with triangular-pitch plain-tube bundle, Part I: tube bundle effect ', *International Journal of Heat and Mass Transfer*, vol. 44, pp. 2299-310.
- 2001, 'Experimental investigation on ammonia spray evaporator with triangular-pitch plain-tube bundle, Part II: evaporator performance', *International Journal of Heat and Mass Transfer*, vol. 44, pp. 2081-92.
- Zhang, L, Hu, G & Wang, Z 2008, 'Study on liquid-jet cooling and heating of the moving SMA actuator', *International Journal of Thermal Sciences*, vol. 47, pp. 306-14.